2000

Experimental and theoretical investigations in alkaline earth-zinc-aluminum intermetallic systems

Chi-Shen Lee
Iowa State University

INFORMATION TO USERS

This manuscript has been reproduced from the microfilm master. UMI films the text directly from the original or copy submitted. Thus, some thesis and dissertation copies are in typewriter face, while others may be from any type of computer printer.

The quality of this reproduction is dependent upon the quality of the copy submitted. Broken or indistinct print, colored or poor quality illustrations and photographs, print bleedthrough, substandard margins, and improper alignment can adversely affect reproduction.

In the unlikely event that the author did not send UMI a complete manuscript and there are missing pages, these will be noted. Also, if unauthorized copyright material had to be removed, a note will indicate the deletion.

Oversize materials (e.g., maps, drawings, charts) are reproduced by sectioning the original, beginning at the upper left-hand corner and continuing from left to right in equal sections with small overlaps.

Photographs included in the original manuscript have been reproduced xerographically in this copy. Higher quality 6" x 9" black and white photographic prints are available for any photographs or illustrations appearing in this copy for an additional charge. Contact UMI directly to order.

Bell & Howell Information and Learning
300 North Zeeb Road, Ann Arbor, MI 48106-1346 USA
800-521-0600

Experimental and theoretical investigations in alkaline earth - zinc -aluminum intermetallic systems

by

Chi-Shen Lee

A dissertation submitted to the graduate faculty

in partial fulfillment of the requirements for the degree of

DOCTOR OF PHILOSOPHY

Major: Inorganic Chemistry

Major Professor: Gordon J. Miller

Iowa State University

Ames, Iowa

2000

UMI Number: 9977335

Bell & Howell Information and Learning Company
300 North Zeeb Road
P.O. Box 1346
Ann Arbor, MI 48106-1346

Graduate College
Iowa State University

This is to certify that the Doctoral dissertation of

Chi-Shen Lee

has met the dissertation requirements of Iowa State University

Signature was redacted for privacy.

Major Professor

Signature was redacted for privacy.

For the Major Program

Signature was redacted for privacy.

For the Graduate College

"天行健 君子以自強不息"

-易經 乾卦 象辭

"The action of Heaven is strong and dynamic. In the same manner, the noble man never ceases to strengthen himself."

- I-Ching, Qian (No. 1), Commentary on the images (Translated by Richard John Lynn)

to my parents

TABLE OF CONTENTS

CHAPTER 1: GENERAL INTRODUCTION 1

Dissertation Organization 7
References 8

CHAPTER 2: EXPERIMENTAL AND THEORETICAL STUDIES OF $BaZn_{10}Al_2$: A $NaZn_{13}$-TYPE INTERMETALLIC COMPOUND 10

Abstract 10
References 16
Supplementary Material 26

CHAPTER 3: WHERE ARE THE ELEMENTS IN COMPLEX ALUMINIDES? AN EXPERIMENTAL AND THEORETICAL INVESTIGATION OF THE QUASICRYSTALLINE APPROXIMANTS, $Mg_{2-Y}(Zn_XAl_{1-X})_{3+Y}$ 31

Abstract 31
Introduction 32
Experimental 35
Results and Discussion 42
R-Phase Mg-Zn-Al: Where Are The Atoms? 53
Conclusions 54
References 56
Supplementary Material 81

CHAPTER 4: EXPERIMENTAL AND THEORETICAL STUDIES OF R-PHASE COMPOUNDS IN Li-Mg-Zn-Al SYSTEMS 95

Abstract 95
Introduction 96
The Theoretical Model 98
Experimental Studies of Quaternary Li-Mg-Zn-Al R-Phases 102
Results and Discussion 105
Conclusions 108
References 109
Supplementary Material 124

CHAPTER 5: SITE-PREFERENCE STUDY OF TERNARY ALKALINE EARTH-ZINC ALUMINIDES SYSTEM FORMING STRUCTURAL VARIANTS OF $BaAl_4$ 144

Abstract 144
Introduction 144
Experimental 146
Results 148
Discussion 151
Conclusion 155
References 155

CHAPTER 6: $Ba_{14}Zn_5Al_{22}$: A NEW TERNARY INTERMETALLIC COMPOUND WITH A NOVEL 2D NETWORK 171

Abstract 171
Introduction 171
Experimental 172
Results and Discussion 178
Conclusion 184
References 184

CHAPTER 7: GENERAL CONCLUSIONS 206

APPENDIX A. REACTION COMPOSITION AND PRODUCT IDENTIFICATION 210

APPENDIX B. SUMMARY OF SINGLE CRYSTAL REFINEMENTS ON VARIOUS REACTIONS 213

APPENDIX C. ELECTRONIC STRUCTURE STUDIES OF Ba_2PdP_3 AND RELATED COMPOUNDS 222

ACKNOWLEDGMENTS 251

CHAPTER 1

GENERAL INTRODUCTION

Understanding the structure and property relationships of intermetallic compounds has been a goal of solid state chemists for decades.[1-3] A great deal of synthetic effort has resulted in many new compounds with known or novel structure types.[4] Significant achievements in models for predicting structural features and properties of intermetallic compounds have been developed.[5,6] One of the thoroughly studied systems is the Hume-Rothery phases. These compounds are made up of late transition metals (groups 8-12) through the post-transition metals, and their structural types can be predicted by their average valence electron concentration per atom (*vec*) between 1.0 and 2.0 e^-/atom.[7] For example, In $Al_{1-x}Cu_x$ system, the *vec* of Al_2Cu_3 (ε-brass) is $(2\times3+3\times1)/5 = 1.8$ (d electrons of Cu are excluded) and the structure type of Al_2Cu_3 adopts the hexagonal close-pack (h.c.p.) structure (see Figure 1a). On the other hand, the β-brass ($Al_{1-x}Cu_x$, x = 0.70~0.82, vec = 1.36 ~1.6) adopts the body centered cubic (b.c.c.) structure type. Another example is Wade's rule that relates the structure of molecular cluster (e.g. borane clusters) with its "magic" electron count.[8] During the last decade, theoretical calculations have been extensively used to understand the electronic structures of solid state compounds.[9,10] One of the contributions was the application of the second-moment scaling to sort the relative stability of elements in different structure types.[11-13]

The concept of the valence electron concentration per atom (*vec*) has been applied to identify structure types of Hume-Rothery phases and may be used as an index to group intermetallic compounds. The *vec* can be calculated in two ways:

a) e^-/atom: The *vec* is calculated as the total number of valence electron divided by the number of atoms per formula. This definition includes every atom in the formula and was used in the Hume-Rothery phases. This counting scheme was applied to the Mg-Zn-Al system because of the similar electronegativities for Mg (1.31), Zn (1.65), and Al (1.61).

b) e^-/electronegative atom: The *vec* is calculated as the total number of valence electron per formula divided by the number of electronegative atoms per formula. This definition was used in Zintl phases because such compounds contain electropositive elements (e.g. alkali/alkaline earth metals). The electropositive elements are treated as electron donor and the *vec* does not include the contribution of such metal. For example, in the $BaZn_xAl_{4-x}$ ($0 \le x \le 2$), the *vec* range is between 3.0 ($BaZn_2Al_2$, *vec* = (2 + 2×2 + 2×3)/4 = 3.0) and 3.5 ($BaAl_4$) e^-/anions.

Three possible groups of intermetallic compounds can be categorized by different *vec* ranges and they are discussed below:

1) $1.0 \le vec \le 2.0$: Hume-Rothery phases represent compounds with such a *vec* range. As mentioned before, the structure types (e.g., h.c.p. or c.c.p.) of Hume-Rothery phases depend on the *vec* range. Their structures are more complex than corresponding elementals and their packing efficiencies are usually higher than that of the metal elements themselves due to different atomic sizes. The composition of Hume-Rothery phases is flexible resulting in phase widths. For example, the ε-brass phase (h.c.p.) is between 56 and 60 atom% Cu in $Al_{1-x}Cu_x$ binary system.

2) $vec \ge 4.0$: Zintl phases stand for the intermetallic compounds in such *vec* range. The Zintl phases usually contain two kinds of metals: one is an electropositive metal (i.e.,

group 1 or 2 element) and the other is a main group element from group 13-16.[14] To calculate the *vec* for Zintl compound, the electropositive metal is treated as an electron donor and the *vec* is calculated by the total number of valence electrons (per formula) divided by the number of main group metal atoms. For example, the *vec* of LiAl is equal to (1 + 3)/1 = 4.0. According to the Zintl-Klemm concept, the main-group element is reduced by the electropositive metal and the electronic configuration of the reduced atom fulfills the octet rule. Therefore, Al is reduced by Li and the ionic substructure of $^{3}_{\infty}[Al^{-}]$ is equivalent to the diamond network because Al^{-} has the same number of valence electrons as C (see Figure 1b).[15] Since each atom from the ionic network comply with the octet rule, the Zintl compounds are electron precise with fixed compositions.

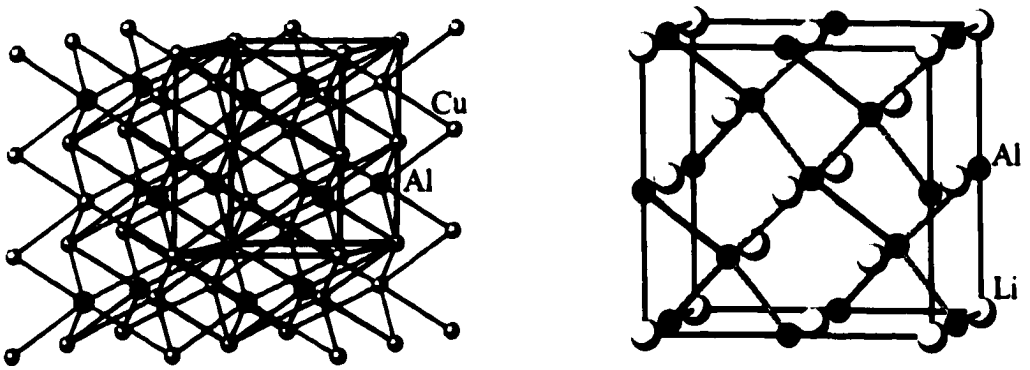

(a) Al_2Cu_3 (b) LiAl

Figure 1. The structures of Al_2Cu_3 (a) and LiAl (b)

3) $2.0 \leq vec \leq 4.0$: The structure types of compounds with this *vec* range are more complex than Hume-Rothery and Zintl phases, and classification of their relationship between *vec* and structure types is difficult. For example, the $NaZn_{13}$-type phase exists in the ternary Ba-Cu-Al and Ba-Zn-Al systems. The structure of $NaZn_{13}$-type phases are similar to close packed structure (average coordination numbers > 9), while the observed *vec* for both compounds are nearly fixed at *vec* ~ 2.35(3). Both compounds contains building blocks of icosahedral units, however, the $BaCu_5Al_8$ (*vec* = (2+1×5+3×8)/13 = 2.38) contains filled M_{13} icosahedra units while the $BaZn_{10}Al_2$ (*vec* = (2+2×10+3×2)/12 = 2.33) contains empty M_{12} icosahedra units. An electronic rationale for the formation of $BaZn_{10}Al_2$ is discussed in Chapter 2.

Intermetallic compounds from the third group ($2.0 \leq vec \leq 4.0$) show properties similar to both Hume-Rothery phases and Zintl phases. For example, the $Mg_{2-y}(Zn_xAl_{1-x})_{3+y}$ (R-phase) system not only exists in a phase width (similar to Hume-Rothery phases) but also shows brittle behavior that is common to Zintl phases. The coexistence of the above properties makes the third group of compounds ($2.0 \leq vec \leq 4.0$) interesting and worthwhile for further investigations to understand their structural (i.e., site preference, phase width, etc.) and physical properties (i.e., mechanical and thermoelectric behaviors). These studies may lead to the development of new functional materials for applications such as high temperature metallic alloys, high strength alloys, thermoelectric materials, and superconductors, or their structures may provide a possible model to understand the structure of quasicrystalline compounds.[16-18]

Our research on the third group of intermetallic systems ($2.0 \leq vec \leq 4.0$) has focused on compounds containing group 13 metals, especially the aluminum-based intermetallic compounds.[19] The structures of Al-based intermetallics are quite different compared with those of other group 13 intermetallics. Boron forms a rich variety of boron hydrides and boranes containing various cluster units.[8] The heavier elements of Ga, In, Tl also form polyatomic clusters when they are reduced by alkali or alkaline earth metals in binary and ternary intermetallic systems.[20,21] The structural features of Al-based intermetallics usually do not include isolated clusters but rather involve extended structures.[19,22] Some examples such as the $NaZn_{13}$-type phases and quasicrystalline approximants also contain fused cluster units including high-symmetry cluster units of icosahedra, pentagonal dodecahedra and fullerene-type polyhedra.[22] Another interesting Al-based intermetallic compounds is the quasicrystalline phases. The quasicrystalline compounds present unusual 5-fold symmetry in the diffraction pattern and the structure of quasicrystalline phases is still not well understood.[23-25]

In this study, the alkaline earth elements (Ae = Mg-Ba), the late transition metal, Zn, and group 13 element, Al, were used to synthesize new compounds. To date, the ternary Ae-Zn-Al system has not been thoroughly investigated: only three compounds (single crystal data), $Mg_{32}(Zn,Al)_{49}$[26], $Mg_4Zn_{11}Al$[27] and $CaZn_2Al_2$[28], were reported to date. Therefore, these systems provide good starting points to search for new ternary compounds with the *vec* falling between 2 and 4. The systems investigated are illustrated as dashed lines I-V in the ternary phase diagram (see Figure 2). The composition of alkaline earth metal on each dashed line is fixed and reactions with different Zn/Al ratios were carried out to identify new ternary phases. For example, dashed line V represents the $Mg_2(Zn_xAl_{1-x})_3$ system. The Mg

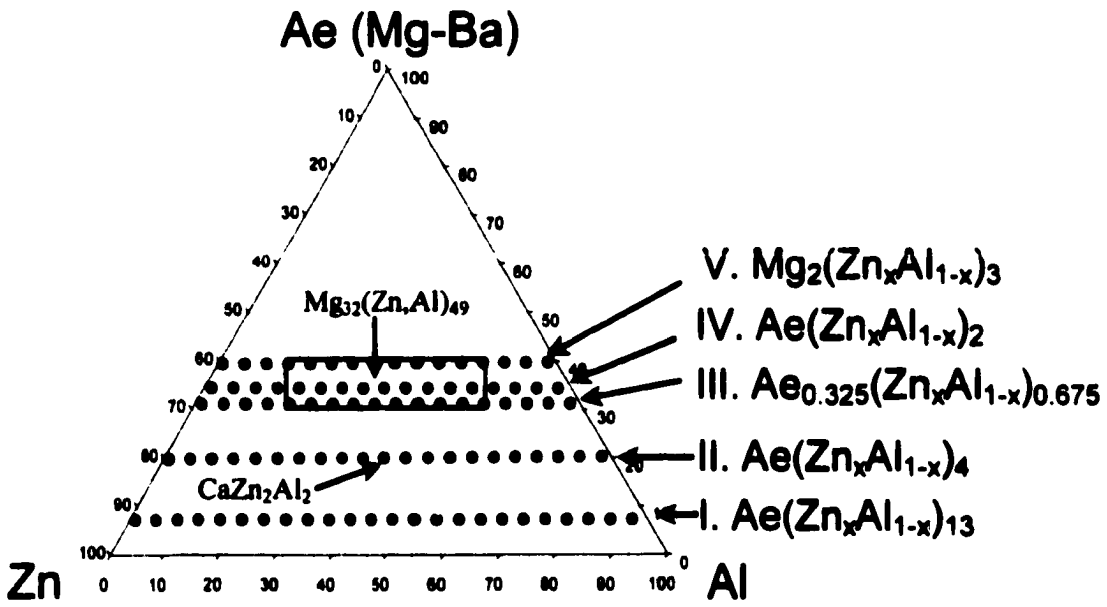

Figure 2. Ternary phase diagram of Ae-Zn-Al system. The gray area is the experimental phase width of the $Mg_{32}(Zn,Al)_{49}$ (R-phase).

content was fixed at 40 atom% and the Zn/Al ratio was varied from 0.0 to 1.0 (2.0 < *vec* < 2.6 e/atom).

Once the target system was chosen, the reaction was carried out by solid state methods using sealed Ta tubes as the reaction container. The reaction was heated under vacuum followed by a slow or fast cooling process. Detailed procedures are described in the following chapters. Products from each reaction were characterized by single crystal or powder X-ray and neutron diffractions, elemental analyses, and differential thermal analyses (DTA) to study their crystal structures, phase widths and compositions. For compounds that could be prepared in single phase, conductivity and magnetic susceptibility measurements were performed at low temperature (~ 5-10 K) and at room temperature (~ 300 K). The

electronic structures of these compounds were studied by theoretical band structure calculations (Extended Hückel Tight-Binding method)[29,30] to interpret the identified trends from experiments.

Dissertation Organization

During the course of this research, a broad spectrum of new compounds with different structure types, such as the $NaZn_{13}$-type, quasicrystalline approximants of the cubic R-phase type (Li/Mg/Zn/Al systems), $BaAl_4$-type, and a new derivative of the Ba_7Al_{13}-type structures, $Ba_{14}Zn_5Al_{22}$, have been characterized. A brief summary of each chapter is described below:

1) Synthesis and theoretical studies of $BaZn_{10}Al_2$ (*vec* ≅ 2.16, Chapter 2): The structure contains interconnected icosahedral (M_{12}) units ($NaZn_{13}$-type). Structural characterization and theoretical studies have been carried out to understand the factors for the formation of the filled/unfilled cluster units.

2) $(Li,Mg)_{52}(Zn,Al)_{108}$ ($2.0 \leq vec \leq 2.5$, Chapter 3, 4): This project focused on the experimental and theoretical investigation of ternary and quaternary Li-Mg-Zn-Al R-phase systems. Structure characterization, phase width and site-preference of the R-phases were reported.

3) $AeZn_xAl_{4-x}$ (Ae = Ca, Sr, Ba; $x = 0.0$-2.0; $3.0 \leq vec \leq 3.5$, Chapter 5): Intermetallics with the $BaAl_4$-type structure were synthesized to study the structure and site preference for Zn and Al atoms as well as the effect of alkaline earth metals.

4) $Ba_{14}Zn_5Al_{22}$ ($BaZn_{0.34(5)}Al_{1.59(5)}$; *vec* ≅ 3.85, Chapter 6): Compounds with high *vec* value (close to 4.0) were investigated in the $Ae(Zn_xAl_{1-x})_2$ systems. The investigations revealed a new ternary intermetallic compound $Ba_{14}Zn_5Al_{22}$ (*vec* = 3.85).

Chapter 2 to 6 are written in the form of journal papers and a general conclusion is given in chapter 7.

References

1)Westbrook, J. H.; Fleischer, R. L. *Intermetallic Compounds: Principles and Practice*; John Wiley & Sons: West Sussex, 1995; Vol. 1-2.

2)Sauthoff, G. *Intermetallics*; VCH Publishers Inc.: New York, 1995.

3)Hafner, J.; Hulliger, F.; Jensen, W. B.; Majewski, J. A.; Mathis, K.; Villars, P.; Vogl, P. *The Structures of Binary Compounds*; de Boer, F. R. and Pettifor, D. G., Ed.; Elsevier Science Publising Compony, Inc.: New York, 1989; Vol. 2.

4)Villars, P.; Calvert, L. D. *Pearson's Handbook of Crystallographic Data for Intermetallic Phases*; 2nd ed ed.; ASM International, Metals Park OH:, 1991.

5)Barrett, C. S.; Massalski, T. B. *Structure of metals : crystallographic methods, principles and data*; 3rd rev. ed.; Pergamon Press: Oxford ; New York, 1980.

6)Schaefer, H. *Annu. Rev. Mater. Sci.* **1985**, *15*, 1-41.

7)Hume-Rothery, W. *J. Inst. Metals* **1926**, *35*.

8)Wade, K. A. *Adv. Inorg. Chem. Radiochem.* **1976**, *18*, 1.

9)Miller, G. J. *Eur. J. Inorg. Chem.* **1998**, 523-536.

10)Miller, G. J. *Structure and bonding at the Zintl border*; Kauzlarich, S. M., Ed.; VCH, New York, N, 1996, pp 1-59.

11)Pettifor, D. G.; Podloucky, R. *Phys. Rev. Lett.* **1984**, *53*, 1080-3.

12)Burdett, J. K.; Lee, S. *J. Am. Chem. Soc.* **1985**, *107*, 3063-82.

13)Lee, S. *J. Am. Chem. Soc.* **1991**, *113*, 8611-14.

14)Zintl, E.; Woltersdorf, G. *Z. Electrochem* **1935**, *41*, 876.

15)Kishio, K.; Brittain, J. O. *J. Phys. Chem. Solids.* **1979**, *40*, 933.

16)Nesper, R. *Angew. Chem.* **1991**, *103*, 805-34 (See also Angew. Chem., Int. Ed. Engl., 1991, 30(7), 789-817).

17)Cheetham, A. K. *Solid State Chemistry Techniques*; Oxford Science Publications: Oxford, 1987.

18)Cheetham, A. K. *Solid State Chemistry Compounds*; Oxford Science Publications: Oxford, 1992.

19)Nordell, K. J.; Miller, G. J. *Inorg. Chem.* **1999**, *38*, 579-590.

20)Corbett, J. D. *Angew. Chem. Int. Ed. Engl.* **2000**, *39*, 670-690.

21)Belin, C.; Tillard-Charbonnel, M. *Prog. Solid State Chem.* **1993**, *22*, 59-109.

22)Lee, C.-S.; Miller, G. J. *manuscript in preparation* **1999**.

23)Goldman, A. I.; Kelton, R. F. *Rev. Modern Phys.* **1993**, *65*, 213.

24)Janot, C. *Quasicrystals: A Primer*; 2nd ed.; Oxford Univ. Press: Oxford, 1994.

25)Tsai, A. P. *MRS Bull.* **1997**, *22*, 43-47.

26)Bergman, G.; Waugh, J. L. T.; Pauling, L. *Acta Crystallogr.* **1957**, *10*, 254.

27)Auld, J. H.; Cousland, S. M. *J. Aust. Inst. Metals.* **1974**, *19*, 194.

28)Cordier, G.; Czech, E.; Schafer, S. *Z. Naturforsch., B: Anorg. Chem., Org. Chem.* **1984**, *39B*, 1629.

29)Hoffmann, R.; Lipscomb, W. N. *J. Chem. Phys.* **1962**, *36*, 2179, 3489.

30)Whangbo, M.-H.; Hoffmann, R.; Woodward, R. B. *Proc. R. Soc. London, Ser. A* **1979**, *366*, 23-46.

CHAPTER 2

EXPERIMENTAL AND THEORETICAL STUDIES OF $BAZn_{10}Al_2$, A $NaZn_{13}$-TYPE INTERMETALLIC COMPOUND

A paper to be submitted to *J. Solid State Chem.*
Chi-Shen Lee and Gordon J. Miller

Abstract

The new phase, $BaZn_{10}Al_2$, was synthesized during reactions used to explore the Ba-Zn-Al system. (a=12.267(2) Å, cubic, space group $Fm\bar{3}c$ (No. 226), Z = 8). $BaZn_{10}Al_2$ is a derivative of the $NaZn_{13}$ structure type containing empty icosahedral units of $[Zn_{10}Al_2]$. Magnetic susceptibility measurements of the title compound show diamagnetic behavior. Experimental and theoretical studies indicate that the formation of filled or unfilled clusters in the $NaZn_{13}$-type structure is affected by the size of the cluster, *vec* of the AM_{12+x} (A = alkaline earth element, M = late transition metal and Al; $0 \leq x \leq 1$), and the transition metal in the center of an icosahedral unit.

Communication

Compounds adopting the $NaZn_{13}$ structure type exist for a variety of binary and ternary phases.[1] The binary compounds of $AeZn_{13}$ (Ae = Ca, Sr and Ba) have been discovered from powder X-ray diffraction studies, but no ternary phase, $Ae(Zn_xAl_{1-x})_{13}$ has been reported. The structure of $NaZn_{13}$-type compounds contains a network of interconnected icosahedral units. Recent studies of ternary trielide (Al, Ga, In) systems indicate that this structure occurs in a narrow range of valence electron concentration (*vec*).[2,3] The experimental and theoretical study of the $Ba(Cu_xAl_{1-x})_{13}$ system suggests that the stable

phase in terms of optimized bonding is close to $BaCu_{5.25}Al_{7.75}$ (*vec* = 2.35). According to these results, a possible compound in Ba-Zn-Al systems would be close to $BaZn_{10}Al_3$ (*vec* = 2.38).[4] An attempt to prepare this hypothetical ternary phase yields a derivative of a $NaZn_{13}$-type compound, which contains, surprisingly, unfilled icosahedral units. In this paper, we report the synthesis and characterization of $BaZn_{10.13(5)}Al_{1.87(5)}$ and address factors influencing the insertion of similar atoms into the center of the icosahedra.

Three different compositions of Ba/Zn/Al mixtures (1:10:3, 1:8:5 and 1:5:8; *vec* = 2.38, 2.54, and 2.77) were prepared to study the possible $NaZn_{13}$-type phase in the $Ba(Zn_xAl_{1-x})_{13}$ system.[5] Guinier powder patterns indicate that the 1:5:8 and 1:8:5 products contained mixtures of $BaZn_5$, $BaAl_4$, $NaZn_{13}$-type phases and trace amounts of Al.[6] Single crystals for structural characterization cannot be found in these products. On the other hand, the powder pattern of the 1:10:3 system indicated a nearly pure phase of $NaZn_{13}$-type compound with a trace amount of Al. Single crystals were then selected for X-ray diffraction analysis and subsequent X-ray refinements revealed the formula of $BaZn_{10.13(5)}Al_{1.87(5)}$.[6] The pure phase, $BaZn_{10}Al_2$, was subsequently synthesized from a stoichiometric mixture of the elements in a sealed tantalum tube at 800 °C followed by slow cooling and was confirmed by X-ray analyses (single crystal and powder).[6] Four independent single crystals were collected from the $BaZn_{10}Al_2$ product, and the results show that the average formula is $BaZn_{10.4(3)}Al_{1.6(3)}$ (*vec* = 2.28~2.32 e/atom). Magnetic susceptibility was measured over the temperature range 6 ~ 300K and the data have been corrected by diamagnetic core correction of constituent atoms.[7] The result indicates that $BaZn_{10.13(5)}Al_{1.87(5)}$ is diamagnetic and the average magnetic susceptibility above 50K is $-1.65(3)\times10^{-3}$ emu/mole.

The important crystal data are listed in Table 1. A polyhedral representation of $BaZn_{10.13(5)}Al_{1.87(5)}$ in a direction nearly parallel to the [100] direction is shown in Figure 1. Its structure features interconnected, unfilled, icosahedral clusters (M_{12}) that can be grouped into two interpenetrating face centered cubic (fcc) networks (gray and white clusters in Figure 1). Each M_{12} cluster is surrounded by six adjacent M_{12} clusters along {100} directions, and the interstitial space is surrounded by a stella quadrangular, as shown in Figure 2a. Each Ba atom is surrounded by M_{12} units along {111} directions to form a 24-vertex snub cube coordination environment (Wyckoff site *8a*; Figure 2b). Each unit cell contains eight formula units of $BaZn_{10}Al_2$ (Pearson symbol cF104). The composition of a M_{12} unit (Wyckoff site *96i*) is close to the formula of $[Zn_{10}Al_2]$ (86%Zn/14%Al), and this particular unit was also found in the R-phase of the $Mg_{2-y}(Zn_xAl_{1-x})_{3+y}$ system.[8] The center of the icosahedron (Wyckoff site *8b*) is essentially empty. However, both partial and full data refinement generates a positive electron density ($\Delta\rho_{max}$) at this position: the average value over four crystals is 2.8(9) $e^-/Å^3$, and suggests that the central position may contain a small fraction of either Zn or Al (or impurities such as O). Therefore, the structure of $BaZn_{10.13(5)}Al_{1.87(5)}$ contains mostly unfilled icosahedra.

Unfilled icosahedral cluster units are found in many group 13 intermetallics such as $K_{34}Zn_{20}In_{85}$[9], $Na_{17}Zn_{12}Ga_{40.5}$[10], and the R-phase compounds.[8,11-15] On the other hand, filled icosahedral cluster units exist in $NaZn_{13}$-type compounds, Mg_2Zn_{11}[16] and various Hume-Rothery phases.[17] $BaZn_{10}Al_2$ is the only known example among $NaZn_{13}$-type compounds with unfilled cluster units. Comparing the crystal data of $BaZn_{10}Al_2$ and other $NaZn_{13}$-type compounds (see Table 2), the center of the M_{12} cluster prefers late transition metals (Co-

Zn)[3,18] or Li.[2] Furthermore, the size of the icosahedra is affected not only by atomic size but also by the *vec*. The radii of the M_{12} clusters in $BaZn_{10.13(5)}Al_{1.87(5)}$ (r = 2.58(1) Å, *vec* = 2.32) are similar to $BaCu_5Al_8$ (r = 2.571(1) Å, *vec* = 2.38) , whereas, the radii of the M_{12} units from other Zn-rich compounds (r > 2.6 Å) are larger than $BaZn_{10}Al_2$ due to the interstitial Zn or Li atoms.

Extended-Hückel tight-binding (EHTB) calculations were carried out to formulate a reason for the electronic structure for the preference of filled or unfilled icosahedra.[19-25] The relative stability of the $NaZn_{13}$ structure type with filled and unfilled icosahedra units has been examined theoretically, and the results indicate that the optimal *vec* value of AM_{13} (*vec* = 2.2, filled cluster) is lower than that of AM_{12} (*vec* = 2.3, unfilled cluster).[2] This result is consistent with the experiments on $BaZn_{12.77}$[18] (*vec* = 2.16) and $BaZn_{10}Al_2$ (*vec* = 2.33).

In this study, the interaction between a transition metal and an M_{12} unit to form a filled M_{13} cluster was studied by MO calculations using identical sizes of M_{12} and M_{13} fragments (point group T_h).[26] The *3d* parameters were included only for the central atom. The result, presented in an orbital interaction diagram of M_{12} (left), M_{13} (center), and M (right) is shown in Figure 3. According to Wade's rules, an isolated M_{12} cluster contains 26 electrons for cluster bonding (2n+2 e^- for *closo*-cluster) and 24 electrons for exo-bonding (like B-H bonding in *closo*-$B_{12}H_{12}$). The MO diagram of M_{12} cluster shows a energy gap between MO #25(e_g, E ~ -6.5 eV) and #26 (t_u, E ~ -5.0 eV). Therefore, a possible highest occupied molecular orbital (HOMO) is 50 e^-/M_{12} unit (left side of Figure 3). The orbital interaction between the *d* orbitals of the central atom and the e_g, t_g levels of the M_{12} unit is weak (ΔE < 0.01 eV). On the other hand, strong interactions between the M_{12} and the central atom were

observed from a_g-a_g and t_u-t_u levels (see Figure 3). A possible number of bonding orbitals for the M_{13} unit is 30 orbitals/formula (25 for s-, p- orbitals and 5 for d-orbitals from the central atom). The result indicates that M_{12} and M_{13} clusters contain the same the number of bonding orbitals. A similar result has been pointed out in the study of $K_8In_{10}Zn$ system.[27] The theoretical results for these cluster units are consistent with Wade's rules.

When the isolated cluster units are stacked to form the $NaZn_{13}$ structure type, the possible number of bonding orbitals (or bonding electrons) per formula is changed due to the interactions between clusters. The effect of the inter-cluster distance d (d = R – 2r; R = distance between centers of two clusters, r = radius of icosahedral cluster) to the stability of $NaZn_{13}$ structure was evaluated by plotting the "magic electron number" for $^3_\infty[M_{12}]$ and $^3_\infty[M_{13}]$ as a function of intercluster distances. The "magic electron number" for M_{12} and M_{13} clusters is calculated from the number of orbitals below the HOMO of M_{12}/M_{13} clusters (2×orbitals). The result is shown in Figure 4. The size of each icosahedral units was kept the same for each model (r = 2.60 Å). When the intercluster distances decrease, the intercluster interactions raise the high-lying crystal orbitals near the HOMO of M_{12} (50e/formula) or M_{13} (60 e/formula) and decrease the "magic electron number". The lowest e/formula is 32 for $^3_\infty[M_{12}]$ (d ≤ 0.92 Å) and 42 for $^3_\infty[M_{13}]$ (d ≤ 0.31 Å, including d electrons of the central atom). The d_{min} of $^3_\infty[M_{12}]$ is longer than $^3_\infty[M_{13}]$, a result that is consistent with the crystal data of $BaZn_{10}Al_2$ (d = 0.96 Å) and $BaZn_{12.75}$ (d = 0.88 Å). The minimum magic electron number for each model is comparable to that observed in the $NaZn_{13}$-type compounds such as $BaZn_{10}Al_2$ (28 e) and $BaCu_5Al_8$ (41 e).

The effect of atomic charge on the cluster size is determined by Madelung energy calculations.[28] This study assumes each position as a point charge and the effect of atomic size did not apply to each atom. The atomic charge on counter cations was fixed as +2 (Ba^{2+}) and the charge for the central atom of M_{12} unit was varied between -1.0 and 2.0. The charge on the M_{12} unit was adjusted to balance the charge. For each set of atomic charges, the radius of M_{12} was varied from 0.9r to 1.4r (r = 2.60 Å) and the Madelung calculations were performed to obtain the lowest Madelung energy. The radius of the most stable structure was plotted as a function of the central atom's charge (see Figure 5). The result suggests that clusters with more positive charge at the central atom tend to have smaller radii. Therefore, the radius of a M_{12} unit (zero charge in the center) is larger than that of an M_{13} cluster with positive charge in the center. The EHTB calculations on $^{3}_{\infty}[M_{13}]$ indicate that the central atom is more positively polarized than atoms on the cluster based on relative Mulliken population over the *vec* range between 2.0 and 3.0. The results from the crystal data of $BaZn_{10}Al_2$ (r = 2.58 Å) and $BaZn_{12.75}$ (r = 2.65 Å) suggest that the charge of the centeral atom in the $BaZn_{12.75}$ is less than zero comparing with vacancy in the structure of $BAZn_{10}Al_2$. The experiments suggest that the M_{12} unit in $BaZn_{10}Al_2$ is too small to accommodate a Zn atom (The van der Waals radius of the Zn atom is 1.37 Å).

Three-dimensional band calculations were performed to examine the relative stability of filled and unfilled units based on the hypothetical reaction:

$$M_{12} + M^{\bullet} \rightarrow M_{12}M^{\bullet} \quad (M_{12} = Zn_{12}^{2-}, Zn_{10}Al_2^{2-}, Cu_4Al_8^{2-}; M^{\bullet} = Al, Cu, Zn)^{26}$$

$$\Delta E = E(M_{12}M^{\bullet}) - E(M_{12} + M^{\bullet})$$

The atomic parameters were fixed for each calculation and the total energy of M^*, M_{12}, and $M_{12}M^*$ are calculated in different valence electrons to simulate Zn_{12}^{2-} (26 e^-), $Zn_{10}Al_2^{2-}$ (28 e^-) etc. The results indicate that the stability of $[M_{12}M^*]$ is affected by the electronic configuration of the central atom (see Table 3). The central atom is preferentially a late transition metal with fewer valence electrons than Zn or a main group metal with fewer valence electrons than Al.

In summary, $BaZn_{10.13(5)}Al_{1.87(5)}$ contains a Zn/Al network with unfilled icosahedra. Experimental and theoretical studies indicate that the formation of filled or unfilled clusters in the $NaZn_{13}$ structure type is affected by the size of the cluster, *vec* of the AM_{12+x} (A = alkaline earth element, M = late transition metal and Al; $0 \leq x \leq 1$), and the type of element at the center of an icosahedral unit.

References

1)Villars, P.; Calvert, L. D. *Pearson's Handbook of Crystallographic Data for Intermetallic Phases*; 2nd ed ed.; ASM International, Metals Park OH:, 1991.

2)Haeussermann, U.; Svensson, C.; Lidin, S. *J. Am. Chem. Soc.* **1998**, *120*, 3867-3880.

3)Nordell, K. J.; Miller, G. J. *Inorg. Chem.* **1999**, *38*, 579-590.

4)Note: The *vec* value of $BaZn_{10}Al_3$ is calculated from the total number of valence electrons divided by the number of atoms per formula unit excluding Ba atoms. The electropositive element Ba is treated as a two-electron donor and the d electrons of Zn are not included.

5)Syntheses: The preparations of ternary intermetallic phases were carried out under an Ar-filled glove box with the concentration of O_2 is lower than 10 ppm. Experimental starting materials were Ba rod (Johnson-Matthey, 99.5 %), Zn powder (Alfa, 99.9%), Al ingot (Alfa, 99.9999%), and Al foil. The BaO on the surface of Ba rod is removed by scalpel before use. The starting materials were put in a Ta tube that is sealed by Ar-melter under Ar. The reaction was first heated under vacuum to 850 °C for 6 hours and then slow cooled (20 °C/h) to room temperature. All reactions yield melted shiny silver metal alloy attached on the

inside wall of Ta tube. All products are not air nor moisture sensitive but decomposed readily with weak acid (1N HCl).

6)X-ray Analyses: (1) Powder x-ray analysis: Powder patterns were obtained from ground samples fixed by tape on a sample holder. An Enraf-Nonius Guinier camera with Cu Kal radiation (λ = 1.54056 Å) and Si powder as the internal standard was used to obtain diffraction film. The detail line positions were measured with an LS20 line scanner (KEJ instrument, Stockholm, Sweden) using the Si standard lines as reference and processed with the program SCAPI8. Least-square refinement of unit cell with observed intensity positions were calculated. (2) Single crystal analysis: Small crushed product was picked for single crystal structure analysis. For all single crystal x-ray analysis, the intensity data were collected under room temperature of 25(2) °C. Instruments used were Siemens P4 diffractometer. The X-ray source is Mo Ka (λ = 0.71073 Å). Detail data collection conditions are listed in Table 1.

7)Physical Measurements: 28.7 mg of powder sample was packed tightly in a silica tube (~ 16 cm) by two silica rods in a glove box. The sample tube was sealed outside by O_2/H_2 torch. Temperature-dependent magnetic susceptibility measurements with field strength of 3 Tesla over the temperature range 6 - 300K were performed using a SQUID magnetometer. Data were corrected for the diamagnetic contributions of the constituent atomic cores and the sample holder.

8)Lee, C.-S.; Miller, G. J. *manuscript in preparation* **1999**.

9)Cordier, G.; Mueller, V. *Z. Naturforsch., B: Chem. Sci.* **1995**, *50*, 23-30.

10)Tillard-Charbonnel, M.; Chouaibi, N. E.; Belin, C. *C. R. Acad. Sci., Ser. II* **1992**, *315*, 661-5.

11)Bergman, G.; Waugh, J. L. T.; Pauling, L. *Acta Crystallogr.* **1957**, *10*, 254.

12)Audier, M.; Pannetier, J.; Leblanc, M.; Janot, C.; Lang, J.-M.; Dubost, B. *Physica B (Amsterdam)* **1988**, *153*, 136.

13)Tillard-Charbonnel, M.; Belin, C. *J. Solid State Chem.* **1991**, *90*, 270-8.

14)Bergman, G.; Waugh, J. L. T.; Pauling, L. *Nature* **1952**, *169*, 1057.

15)Todorov, E.; Sevov, S. C. *Inorg. Chem.* **1997**, *36*, 4298.

16)Samson, S. *Acta. Chem. Scan.* **1949**, *3*, 835.

17)Hume-Rothery, W.; Raynor, G. V. *The structure of metals and alloys*; <4th , rev.> ed.; Institute of Metals: London,, 1962.

18)Lee, C.-S. M., G. J. , unpublished results: (a) $BaZn_{12.77}$(1): a=12.3364(18) Å, cF110. (b) $BaZn_{12}Fe$: a=12.3299(15) Å, cF112. (c) $BaZn_{12}Co$: a=12.333(3) Å, cF112. (d) $Ba(Cu,Ni)_6Al_7$: a = 12.056(1) Å, cF112.

19)Hoffmann, R.; Lipscomb, W. N. *J. Chem. Phys.* **1962**, *36*, 2179, 3489.

20)Hoffmann, R. *J. Chem. Phys* **1963**, *39*, 1397.

21)Ammeter, J. H.; Buergi, H. B.; Thibeault, J. C.; Hoffmann, R. *J. Am. Chem. Soc.* **1978**, *100*, 3686-92.

22)Whangbo, M.-H.; Hoffmann, R.; Woodward, R. B. *Proc. R. Soc. London, Ser. A* **1979**, *366*, 23-46.

23)Hughbanks, T.; Hoffmann, R. *J. Am. Chem. Soc.* **1983**, *105*, 3528-37.

24)Wijeyesekera, S. D.; Hoffmann, R. *Organometallics* **1984**, *3*, 949-61.

25)Chadi, D. J.; Cohen, M. L. *Phys. Rev. B* **1973**, *8*, 5474.

26)The Zn paremeters were used for the MO calculations. The Cu, Zn, Al and two new atomic parameters (M and M') for $Zn_{10}Al_2^{2-}$ and $Cu_4Al_8^{2-}$ were applied for 3D band calulations. The atomic parameters for the calculations were listed in the supplmentary material.

27)Sevov, S. C.; Corbett, J. D. *Inorg. Chem.* **1993**, *32*, 1059-61.

28)Ziman, J. M. *Principles of the Theory of Solids*; Cambridge University Press: London, 1964, pp p39.

Table 1. Selected crystal data and conditions of data collection for $BaZn_{10.13(5)}Al_{1.87(5)}$

Formula	$BaZn_{10}Al_2$
Refined Composition	$BaZn_{10.13(5)}Al_{1.87(5)}$
Formula Weight	871.98
Space Group , Z	$Fm\bar{3}c$ (No. 226), 8
a(Å)[a], V(Å^3)	A = 12.267(2), V = 1846.0(5)
D_{calc} (g/cm^3)	3.156
Radiation, λ (Å)	Mo Kα, 0.71073
Abs Coeff. (mm^{-1})	15.026
Temperature, K	298(2)
Crystal Size, mm	0.075 × 0.1 × 0.1
R_{int}	0.0466
R1/wR2 ($I>2\sigma_I$)[b]	0.0168/0.0486
R1/wR2 (All Data), GOF	0.0178/0.0509, 1.049
Extinction Coefficient	0.00018(9)

[a] Cell parameters were calculated from powder X-ray data.

[b] $R1 = \sum\|F_o\|-|F_c\|\Big/\sum|F_0|$; $wR2 = \left[\sum\left[w\left(F_o^2-F_c^2\right)^2\right]\Big/\sum\left[w\left(F_o^2\right)^2\right]\right]^{1/2}$,

$w = 1\Big/\left[s^2F_0^2+(0.04P)^2\right], P = \left(F_o^2+2F_c^2\right)/3$

Table 2. Radius of icosahedron (Å) in various $NaZn_{13}$-type compounds

Compounds	*vec*	Radius(Å)	Composition	Ref.
$BaLi_7Al_6$	2.08	2.732(2)	$[Li_7Al_6]$, filled	2
$BaZn_{12.77(1)}$	2.17	2.6451(9)	$[Zn_{12}]$, $[Zn_{13}]$, mixture	18
$BaZn_{10.6(4)}Al_{1.6(4)}$[†]	2.33	2.58(1)	$[Zn_{10.6(4)}Al_{1.6(4)}]$, unfilled	This work
$BaCu_5Al_8$	2.38	2.571(1)	$[Cu_5Al_8]$, filled	3

[†] The composition is obtained from average results of four crystal data.

Table 3. Summary of band calculations

	M_{12}^{2-}	+	M	→	M_{13}^{2-}	ΔE, eV
1)	$Cu_4Al_8^{2-}$	+	Cu	→	$Cu_5Al_8^{2-}$	-2.62
2)	$Cu_4Al_8^{2-}$	+	Al	→	$Cu_4Al_9^{2-}$	0.57
3)	$Zn_{10}Al_2^{2-}$	+	Zn	→	$Zn_{11}Al_2^{2-}$	1.76
4)	$Zn_{10}Al_2^{2-}$	+	Al	→	$Zn_{10}Al_3^{2-}$	0.62
5)	Zn_{12}^{2-}	+	Zn	→	Zn_{13}^{2-}	0.40

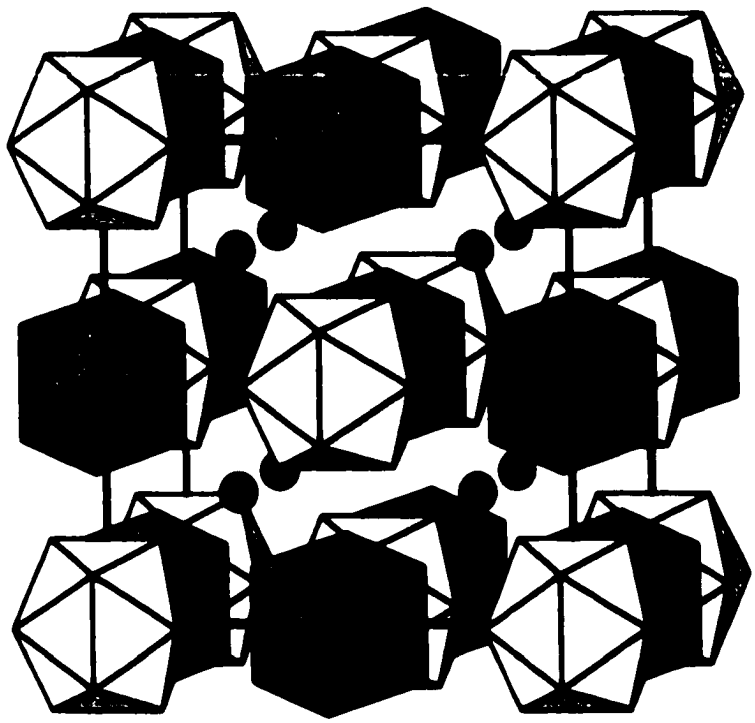

Figure 1. The crystal structure of $BaZn_{10.13(5)}Al_{1.87(5)}$. Large filled circles are Ba atoms. Gray and white icosahedral units representing two fcc network. Note: The gray and white icosahedral units are only used to identify two fcc networks. These two icosahedral units (gray and white) are symmetry equivalent.

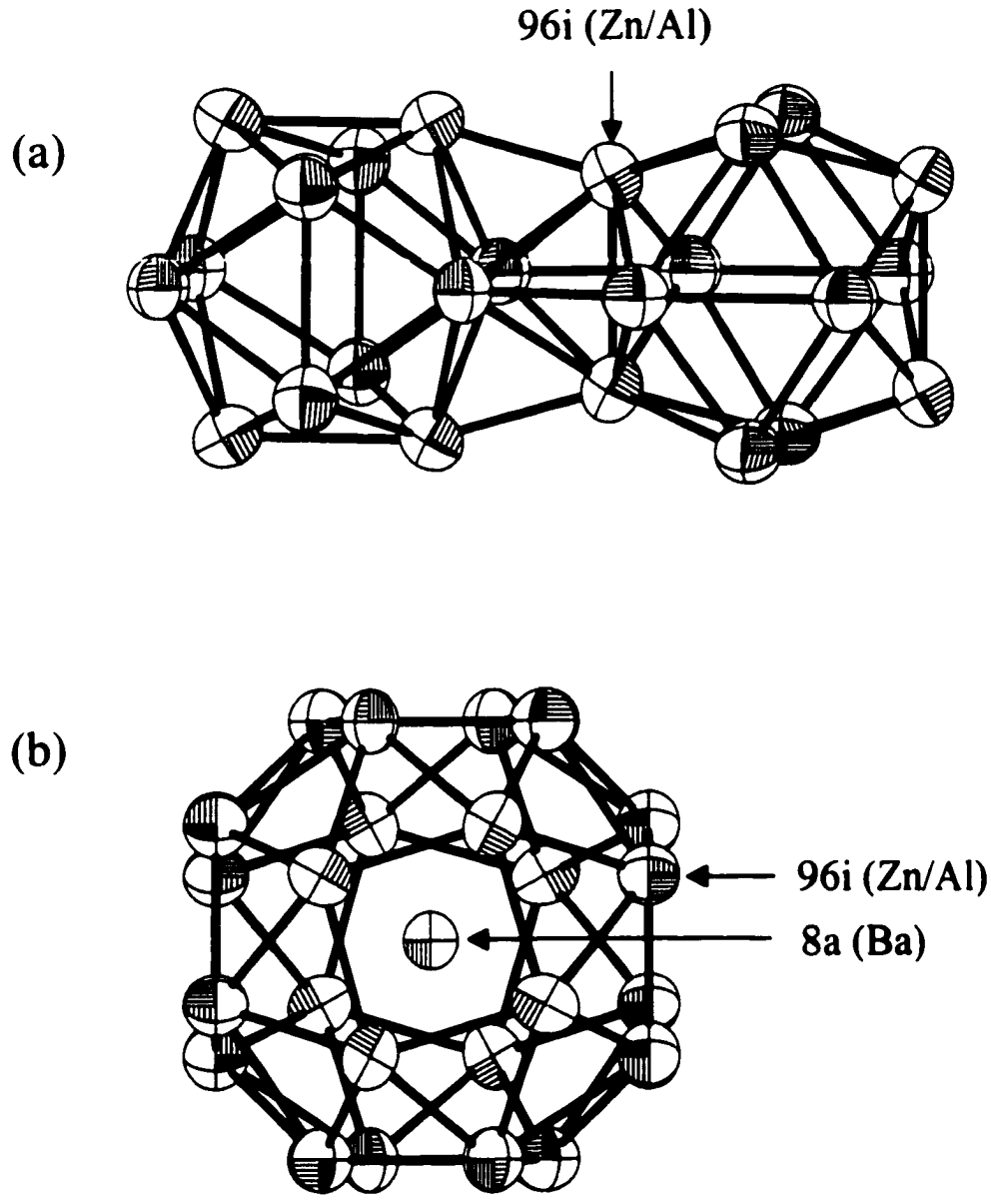

Figure 2. ORTEP drawing (99.9 % thermal ellipsoids) of (a) Two adjacent M12 unit (Stella quadrangula) (b) Snub cube containing Ba (center) and twenty-four vertexes polyhedron.

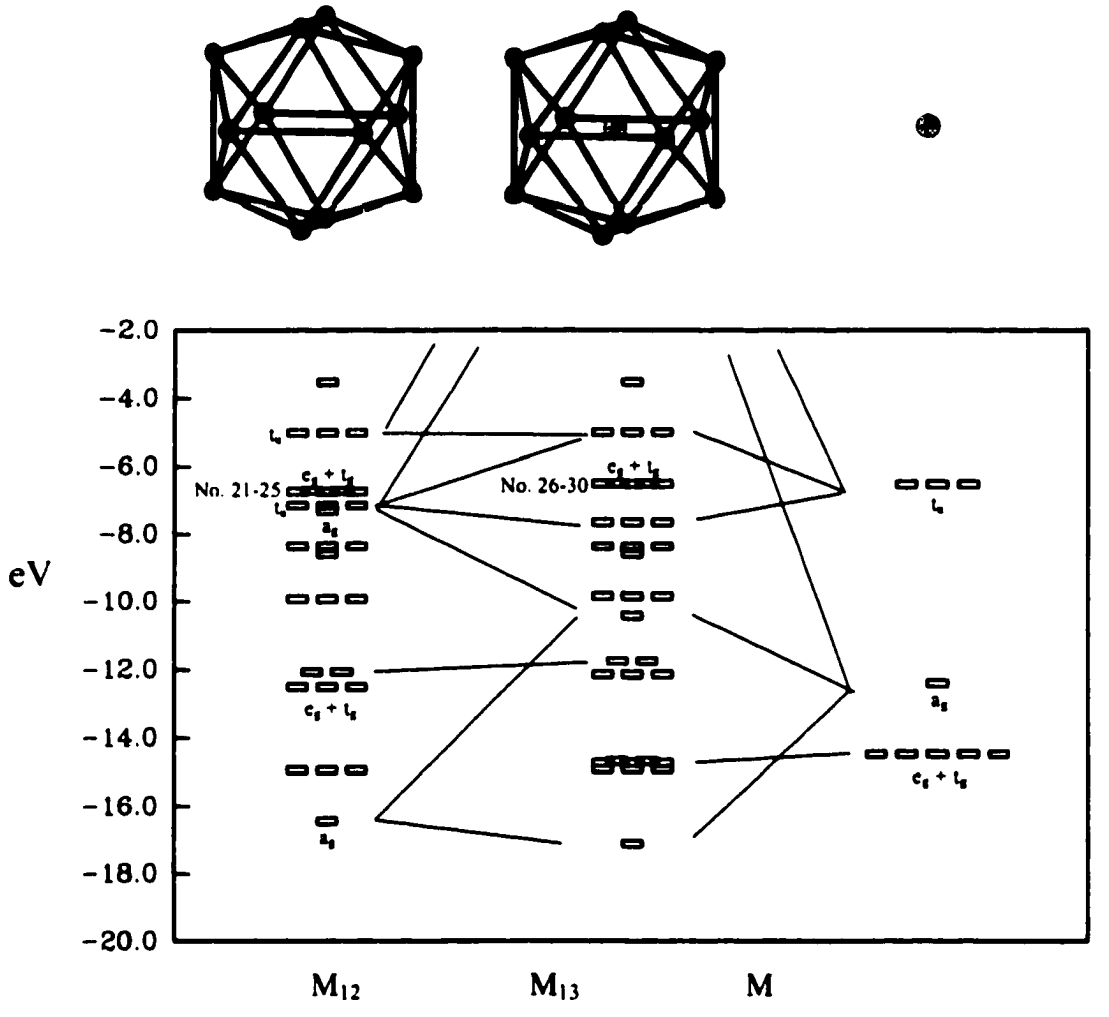

Figure 3. Extended-Hückel MO calculations of M_{12} and M_{13} fragments (T_h) and isolated M atom. The correlation orbitals between the central atom and the M_{12} unit are labeled.

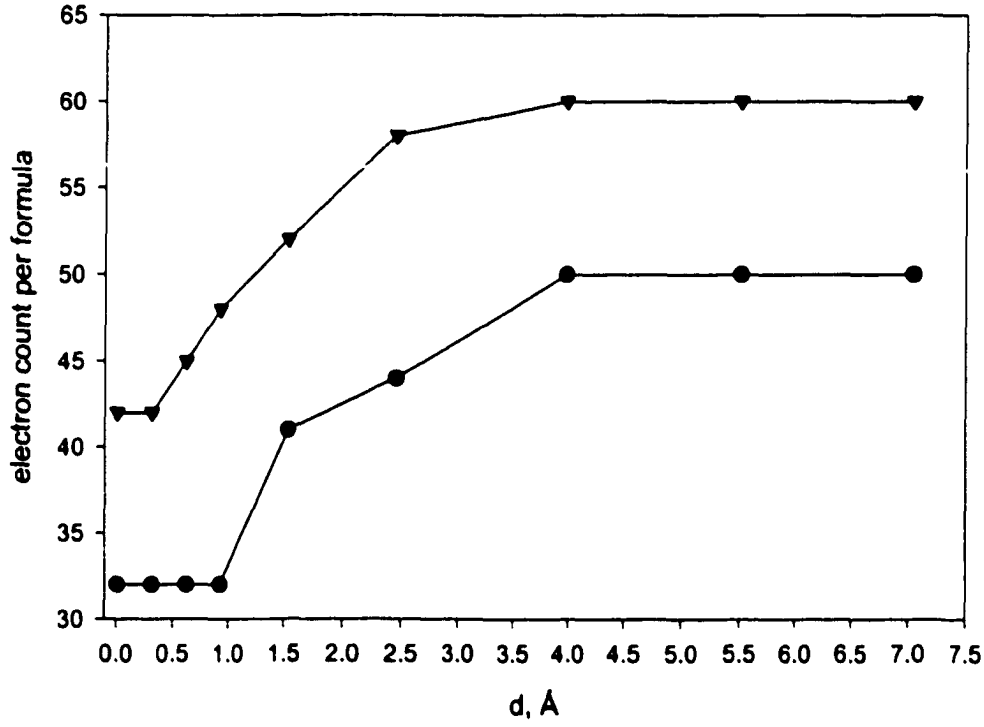

Figure 4. The "magic electron count" for [M12] and [M13] as a function of intercluster distance d.

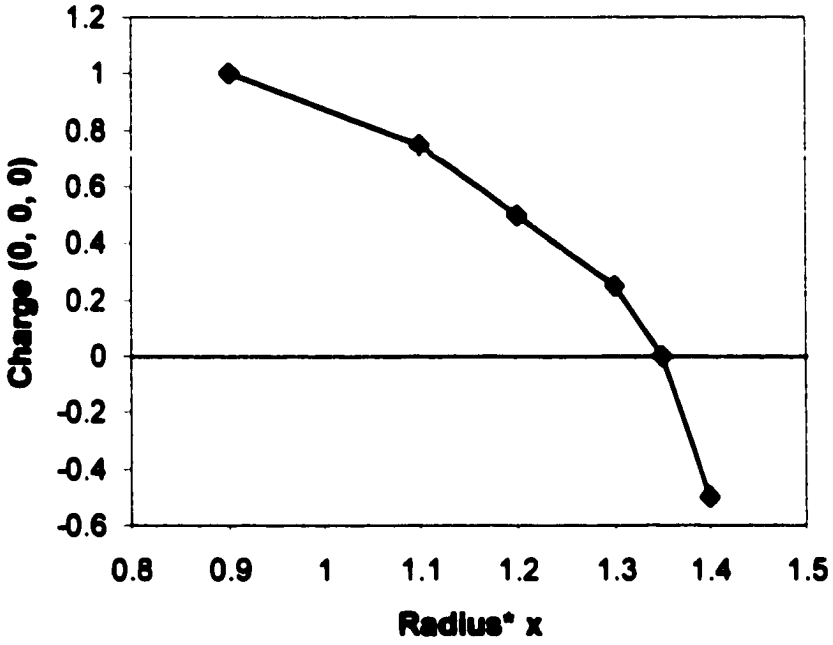

Figure 5. The radius of the most stable [M13] structure as a function of the charge for central atom.

Supplementary Material

Appendix 1. Crystal Data and Conditions of Data Collection for $BaZn_{10}Al_2$

Compound	$BaZn_{10}Al_2$
Refined Composition	$BaZn_{10.13(5)}Al_{1.87(5)}$
Formula weight	871.98
Radiation	0.71073 Å
Space group , Z	$Fm\bar{3}c$(No. 226), 8
unit cell params[a]	a = 12.267(2) Å, V = 1846.0(5) Å^3
d_{calc} (g/cm^3)	3.156
Radiation (Å)	Mo Kα, 0.71073
Abs Coeff (Mm^{-1})	15.026
Abs.Corr.	ψ-Scan
T_{min}, T_{max}	0.510, 0.964
Temperature, C	25(2)
Crystal Size, mm	0.075 × 0.1 × 0.1
Diffractometer, Collection Method	Siemens P4, ω-Scan
$2\theta_{Max}$ (°)	54.8°
H_{min}, H_{max}	-19, 19
K_{min}, L_{max}	-13, 13
L_{min}, L_{max}	-11, 11
Reflections Collected, R_{int}	3927, 0.0466
Unique Data / Parameters Refined	106, 10
R1/Wr2 ($I>2\sigma_I$)[B]	0.0168/0.0486
R1/Wr2 (All Data)	0.0178/0.0509
Goodness-Of-Fit On F^2	1.049
Extinction Coefficient	0.00018(9)
(Δρ) Max, Min (E.Å^{-3})	1.807, -0.593

[a] Cell parameters were calculated from powder x-ray data.[8]

[b] $R1 = \sum \| F_0 - F_c \| / \sum |F_0|$; $wR2 = \left[\sum \left[w\left(F_o^2 - F_c^2\right)^2 \right] / \sum \left[w\left(F_o^2\right)^2 \right] \right]^{1/2}$,

$w = 1/\left[s^2 F_0^2 + (0.04P)^2 \right]$, $P = \left(F_o^2 + 2F_c^2\right)/3$

Appendix 2. Summary of single crystal refinement

No.	Reactions	Refined Comp.	a (Å)	R/ wR/GOF(all data)	$\Delta\rho_{max}$ (e/Å^3)†
1	$BaZn_{10}Al_3$	$BaZn_{10.13(5)}Al_{1.87(5)}$	12.267(2)	0.0214/0.0560/1.049	1.81
2	$BaZn_{10}Al_3$	$BaZn_{10.16(7)}Al_{1.84(7)}$	12.2300(10)	0.0257/0.0809/1.082	2.24
3	$BaZn_{10}Al_2$	$BaZn_{10.68(7)}Al_{1.32(7)}$	12.2483(11)	0.0232/0.0582/1.052	3.76
4	$BaZn_{10}Al_2$	$BaZn_{10.68(7)}Al_{1.32(7)}$	12.2425(15)	0.0388/0.0907/1.064	3.20

†: Electron density at 8b(0,0,0) position.

Appendix 3. Atomic Coordinates (x 10^4) and Equivalent Isotropic Displacement parameters (Å^{2}x 10^3) for $BaZn_{10}Al_2$ (Crystal No 1.). U_{eq} is defined as one third of the trace of the orthogonalized U_{ij} tensor.

Atom	Site	x	y	z	U_{eq}	Site occ.
Ba(1)	8a	2500	2500	2500	15(1)	1.0
Zn(2)	96i	1177(1)	1756(1)	0	18(1)	0.844(4)
Al(2)	96i	1177(1)	1756(1)	0	18(1)	0.156(4)

Appendix 4. Anisotropic displacement parameters (Å^{2}x 10^3).

Atom	U_{11}	U_{22}	U_{33}	U_{23}	U_{13}	U_{12}
Ba(1)	15(1)	15(1)	15(1)	0	0	0
Zn(2)	19(1)	17(1)	17(1)	0	0	3(1)
Al(2)	19(1)	17(1)	17(1)	0	0	3(1)

$U_{ij} = -2\pi^2 [h^2 a^{*2} U_{11} + ... + 2 h k a^* b^* U_{12}]$

Appendix 5. Interatomic distances (Å) in $BaZn_{10}Al_2$.

contacts	distances, Å
8a-96i (24×)	3.5809(5)
8b-96i (12×)	NA
96i-96i(intraicosahedral contacts)	
(4×)	2.6833(8)
(1×)	2.8812(15)
96i-96i(intericosahedral contacts)	
(2×)	2.6286(11)
(2×)	2.7330(15)

Appendix 6. Atomic orbital energy parameters for extended Hückel calculations

ATOM	Orbital	H_{ii} (eV)	ζ_1	c_1	ζ_2	c_2
Cu	4s	-11.4	2.2			
	4p	-6.06	2.2			
	3d	-14.0	5.95	0.5933	2.3	0.5744
Zn[a]	4s	-12.41	2.01			
	4p	-6.53	1.7			
	3d	-14.493	6.3	0.6148	2.25	0.646
Al	3s	1.37	-12.3			
	3p	1.36	-6.5			
$M(Zn_{10}Al_2)$[b]	4s	-12.36	1.77			
	4p	-6.52	1.61			
$M(Cu_4Al_8)$[b]	3s	-11.85	1.49			
	3p	-6.28	1.69			

[a] The d orbital parameters were obtained from the extrapolation of the last four transition metals (Fe, Co, Ni, Cu).

[b] The H_{ii} values were obtained from the average of (Cu/Zn) and Al based on their relative composition in M_{12} unit. The ζ_1 parameters were obtained from the curve fits of the equation: $x\zeta_1(Cu/Zn) + (1-x)\zeta_1(Al) = \exp(-\zeta_M \times r)$; r = 2.0-4.0 Å.

Appendix 7. Analysis of Guinier powder X-ray diffraction film of $BaZn_{10}Al_2$. Input reflections were corrected by interpolation of Si lines

	Parameters
a(Å)	12.267(2)
Volume (Å^3)	1846.0(5)
Radiation, λ (Å)	Cu Kα$_1$, 1.54056

The error of fit is 4.146

Refl #	h	k	l	J	I	sin^2×1000	d calc.	2θ calc.	2θ corr.	diff
1	2	2	2	8	213.4	47.39	3.5412	25.15	25.1	0.05
2	4	2	0	24	867.8	78.98	2.743	32.64	32.64	0.01
3	4	2	2	24	546.2	94.78	2.504	35.86	35.79	0.07
4	5	3	1	48	1000.0	138.22	2.0735	43.65	43.69	-0.04
5	6	0	0	6	91.0	142.17	2.0445	44.3	44.29	0.01
6	6	2	0	24	129.9	157.97	1.9396	46.84	46.82	0.01
7	4	4	4	8	115.1	189.56	1.7706	51.62	51.62	0.01
8	6	4	0	24	242.6	205.36	1.7012	53.89	53.87	0.02
9	6	4	2	48	73.6	221.15	1.6393	56.1	56.1	0.01
10	8	0	0	6	73.3	252.75	1.5334	60.36	60.34	0.03
11	8	2	0	24	108.6	268.54	1.4876	62.42	62.41	0.02
12	6	6	0	12	42.0	284.34	1.4457	64.45	64.41	0.04
13	6	6	2	24	26.4	300.14	1.4071	66.44	66.39	0.04
14	7	5	3	48	149.6	327.78	1.3465	69.85	69.88	-0.03
15	9	3	1	48	128.7	359.38	1.2859	73.67	73.71	-0.04
16	8	4	4	24	110.3	379.12	1.252	76.01	76.1	-0.09

Appendix 7. Molar magnetic susceptibility data for $BaZn_{10}Al_2$.

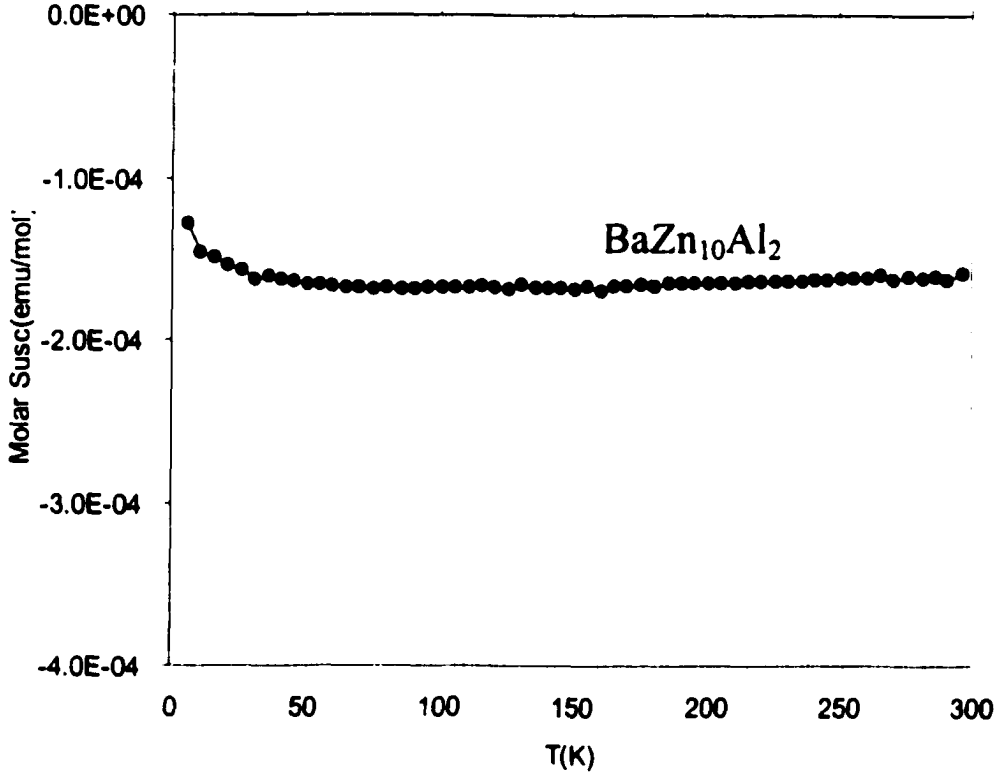

CHAPTER 3

WHERE ARE THE ELEMENTS IN COMPLEX ALUMINIDES? AN EXPERIMENTAL AND THEORETICAL INVESTIGATION OF THE QUASICRYSTALLINE APPROXIMANTS, $Mg_{2-y}(Zn_xAl_{1-x})_{3+y}$

A paper published in the *J. Am. Chem. Soc.* **2000**, *122*, 4937-4947
Chi-Shen Lee and Gordon J. Miller

Abstract

The first detailed investigation of the crystalline R-phases in the Mg-Zn-Al ternary system is reported, which will assist with the interpretation and understanding of similar quasicrystalline phases in this phase diagram. Although "$Mg_{32}(Zn,Al)_{49}$" was originally reported by Bergman and Pauling in 1956, some details regarding its structure and the atomic arrangement remain to be solved. Single phase product can be obtained from reaction compositions "$Mg_{1.63}(Zn_xAl_{1-x})_{3.37}$," $0.35 \le x \le 0.65$. A combination of single crystal X-ray diffraction, powder neutron diffraction, energy dispersive spectroscopy, densities, and theoretical modeling are needed to elucidate a complete structural model for these phase. Single crystal X-ray diffaction gave the R-phase structure (space group $Im\bar{3}$, Z = 32) for three difference samples: $Mg_{1.76(1)}Zn_{1.46(6)}Al_{1.65(3)}$ (a = 14.364(3) Å), $Mg_{1.75(1)}Zn_{1.80(2)}Al_{1.31(1)}$ (a = 14.212(1) Å), $Mg_{1.73(1)}Zn_{2.46(6)}Al_{0.69(3)}$ (a = 14.131(1) Å). Neutron powder diffraction on three similar bulk samples gave: $Mg_{1.76(1)}Zn_{1.34(5)}Al_{1.76(5)}$ (a = 14.2697(1) Å), $Mg_{1.75(1)}Zn_{1.76(5)}Al_{1.34(6)}$ (a = 14.1804(1) Å), $Mg_{1.73(1)}Zn_{2.06(3)}Al_{1.09(3)}$ (a = 14.11247(6) Å). For all phases in this Mg-Zn-Al system, one crystallographic site (M4) has ca. 33% vacancies, and shows a mixture of Mg and Zn atoms. Mg atoms occur next to vacancies on these sites. Theoretical calculations are used to explain the observed phase width involving Zn and Al,

the trend in observed site occupancies, and the occurrence of vacancies in this structure. A range of nonbonding states near the Fermi level account for the phase width, and allow a range in valence electron concentration between 2.07 and 2.48 for the existence of this structure. Valence electron concentrations in Mg-Zn-Al, however, necessitate the occupation of some metal-metal antibonding orbitals, which creates a driving force for vacancies. Since Mg can replace atoms in the (Zn,Al) framework, the R-phases are true intermediates between Zintl phases, on the one hand, and Hume-Rothery intermetallic phases, on the other.

Introduction

Intermetallic compounds provide a rich source of different structure types and special physical properties (electronic, magnetic, thermal, and mechanical) for both potential applications as new functional materials (e.g., as permanent magnets or thermoelectric materials) as well as studying the fundamental relationships among composition, structure, and properties.[1-9] An important component of many intermetallics is aluminum due to its light atomic weight and conductivity properties, and it also deserves exceptional chemical interest. In the periodic table of elements, aluminum borders the transition from metallic to nonmetallic elements in the third period, while, among the Group 13 elements, it is the most electropositive.[10] In fact, the ground state structure of each Group 13 element differs from each of the others; the structure adopted by a given element is governed by the amount of valence *s*, *p* orbital mixing.[11,12]

Aluminum combines with few other main group metals, viz. Li, Mg, Ca, Sr and Ba, to form intermetallic compounds whose structures and properties follow simple valence rules.

LiAl is a classic Zintl phase, with Al forming the diamond network.[13,14] Other examples, like $CaAl_2$,[15,16] $CaAl_4$[17] and Ba_7Al_{13},[2,18] show electronic structures similar to Zintl phases: there is a distinct minimum in the total electronic densities of states (DOS) at the Fermi level, which is indicative of weakly conducting behavior. Orbitals at and below the Fermi level have bonding and nonbonding characteristics; those above the Fermi level are antibonding.[4,19] These intermetallics are usually brittle, diamagnetic, and weakly conducting.[5,19,20] On the other hand, with Group 11 or 12 elements, aluminum forms Hume-Rothery phases, which are typically soft metals with close packed structures.[21] For Hume-Rothery phases, chemical bonding properties are not readily discerned from the generally featureless DOS curves, but instead require details of the energy band structure in reciprocal space.[22] The structures within these two classes of intermetallic compounds follow simple electron counting schemes based upon the average number of valence electrons per atom, called the valence electron concentration (*vec*): (1) Hume-Rothery phases occur for total *vec* less than or equal to two electrons per atom; (2) Zintl phases are valence compounds in which the *vec* of the electronegative component exceeds four electrons per atom. A gap in our understanding of the relationships among *vec*, structure and properties exists between these two classes of intermetallic compounds.

As part of a research program to elucidate structural, electronic and chemical bonding properties in complex aluminides and other intermetallics, our group is systematically investigating "hybrid" materials, $A_xT_yAl_z$, that involve components of both the Zintl-type and Hume-Rothery-type phases (A = alkaline earth or rare earth element; T = late transition element).[23-25] Experimental and theoretical results on A-Cu-Al, A-Au-Al, and A-Zn-Al

systems indicate that compositions and structures lead to filled bonding and nonbonding orbitals of the $[T_yAl_z]$ framework, just as in Zintl phases, but with no energy gap in the total DOS.[23] The *vec*'s of these aluminide substructures vary between two and four electrons per atom, and allow a systematic study of the transition from Hume-Rothery to Zintl-type intermetallic compounds. Among the alkaline earth elements, magnesium represents a significant decrease in size and increase in electronegativity from calcium, strontium or barium.[10] Consequently, Mg can contribute to the network of strong orbital interactions and become more involved in the $[T_yAl_z]$ frameworks of ternary aluminides than its heavier analogues. This paper reports on a specific collection of substances in the Mg-Zn-Al system.

The title compounds were identified during a systematic investigation of the Mg-Zn-Al system with the reaction composition of $Mg_2(Zn_xAl_{1-x})_3$, $0 \le x \le 3$. Over thirty years ago, Bergman and Pauling reported the crystal structure of $Mg_{32}(Zn,Al)_{49}$, which is currently used as a model to discuss the atomic structure of quasicrystalline phases in the Mg-Zn-Al system.[26,27] Accordingly, this phase belongs to a collection of crystalline intermetallic phases called "quasicrystalline approximants," and the structure of $Mg_{32}(Zn,Al)_{49}$ is labeled the R-phase.[28,29] Thermodynamic investigations of the Mg-Zn-Al phase diagram indicate that the R-phase exists for a range of compositions close to $Mg_2(Zn_xAl_{1-x})_3$ and $Mg(Zn_xAl_{1-x})_2$ ($0.3 < x < 0.65$),[30] but no structural characterizations exist. The quasicrystalline phases of this system have been prepared at compositions close to $Mg_{32}(Zn_xAl_{1-x})_{49}$ using a rapid-quench method.[31-34] However, a systematic study of the relationship among composition, crystal structure, chemical bonding and physical properties of the crystalline phases has not been reported.

In this paper, we report the synthesis and detailed characterization of a series of crystalline R-phases in the Mg-Zn-Al system. The major goals of this work are: (1) to determine the phase-width of the R-phase structure and to establish its relationship to the total *vec* of the substance; (2) to elucidate unequivocally the distribution of the elements in this structure, which is frequently cited to model quasicrystalline phases; (3) to evaluate the chemical bonding characteristics of these phases to establish a link between electronic structure and composition; and (4) to characterize the physical properties of these crystalline phases. The difficulty to differentiate Mg and Al in X-ray diffraction experiments necessitates neutron diffraction as an alternative method to assist in solving the site preference problem in these structures. However, since the elastic scattering factors for Mg and Zn are close to one another, a thorough structural chemical analysis of this system requires information from both techniques.

Experimental

Synthesis

All materials were handled in an Ar-filled glovebox (O_2 concentration < 10 ppm) and prepared from the elements. Starting materials were Mg turnings (Johnson-Matthey, 99.9 %), Zn powder (Alfa, 99.9%), Al ingots (Alfa, 99.9999%), and Al foil. Reactions were carried out in sealed Ta ampoules (Alfa, 99.99%; washed with 15% HF/ 35% HNO_3/50% H_2SO_4 solution and dried), that were either sealed in fused silica tubes or placed in a fused silica Schlenk tube under reduced pressure. Reactant mixtures were heated to 1123 K for 24 hours to insure complete melting, followed by either quenching to room temperature, or annealing at 768 K for four weeks. The title compounds were initially identified by X-ray

powder diffraction patterns on products from target compositions of $Mg_2(Zn_xAl_{1-x})_3$ (x = 0, 0.33, 0.67, 1.0; *vec* = 2.0-2.6[35]). The binary systems (x = 0 and 1) showed mixtures of known elemental and binary phases, while the powder patterns of the x = 0.33 and 0.67 samples matched the theoretical pattern of $Mg_{32}(Zn,Al)_{49}$ with slightly different 2θ values to suggest a possible phase width for $Mg_{32}(Zn,Al)_{49}$. Crystals were selected from these two products for single crystal X-ray diffraction and led us to investigate the phase width of the system $Mg_{2-y}(Zn_xAl_{1-x})_{3+y}$ in detail, based on the formula $Mg_{1.625}(Zn_xAl_{1-x})_{3.375}$ (≡ $Mg_{52}(Zn_xAl_{1-x})_{108}$).

Eight reactions with different Zn:Al stoichiometric ratios in $Mg_{1.625}(Zn_xAl_{1-x})_{3.375}$ were carried out and these results are summarized in Table 1. For each sample, the weighing error for each element is less than 0.5% by mass. The phases were identified by Guinier X-ray powder diffraction using an Enraf-Nonius Guinier camera with Cu $K\alpha_1$ radiation (λ = 1.54056 Å) and Si (NBS) as an internal standard. The products of every reaction were silvery, brittle ingots that were neither air nor moisture sensitive, but decomposed readily in dilute acid (1.00 M HCl). According to X-ray photoelectron spectroscopy (XPS), Al_2O_3 and ZnO covered the surface of each product.

------ Table 1 ------

Since X-ray diffraction data and elemental analyses (discussed in the following paragraphs) could not provide a definitive picture of the Mg content and placement in the R-phases, three different compositions of $Mg_{1.625}(Zn_xAl_{1-x})_{3.375}$ samples (x = 0.63, 0.50 and 0.37) were prepared for neutron powder diffraction experiments. The previous reaction conditions were used, except that the final annealing procedure was changed to 768 K for 2

days. High, middle and low Zn:Al molar ratios were chosen based on reactions that could be prepared in nearly single phase.

Structural Characterization by X-ray Diffraction

Needle-shaped crystals for single crystal X-ray diffraction experiments were selected from crushed products, mounted on glass fibers, and checked by means of rotation photographs and data collections on a Siemens P4 or a Rigaku AFC6R diffractometer using monochromatic Mo Kα radiation. On these instruments, the intensities for every crystal were very weak for angles $2\theta > 40°$ ($I/\sigma < 10$) and the ratios of unique reflections to independent parameters were low because the higher angle data were missed. These data are important because they are more sensitive to the chemical composition of a single crystal.

To improve the quality of the high angle intensity data, a Bruker CCD-1000 diffractometer with monochromatic Mo K_α radiation, λ=0.71073 Å, and a detector to crystal distance of 5.08 cm was used for subsequent structural analyses at 298(2) K. For each crystal, data were collected in at least a quarter hemisphere, and were harvested by collecting three sets of frames with 0.3° scans in ω for an exposure time of 30-60 sec per frame. The ranges in 2θ values varied between 3.0° and values from 56.0° to 108.0°. The data were corrected for Lorentz and polarization effects. Absorption corrections were based on fitting a function to the empirical transmission surface as sampled by multiple equivalent measurements.

The unit cell parameters were indexed by peaks obtained from 90 frames of reciprocal space images and then refined using all observed diffraction peaks after data integration. Systematic absences and Wilson plots[36] revealed a centrosymmetric, body-centered cubic

crystal system with the Laue group $m\bar{3}$. Therefore, the space group $Im\bar{3}$ was chosen for subsequent structural analysis.

Structures of the R-phases were obtained by direct methods and refined by full-matrix least-squares refinement of F^2 using the SHELXTL 5.12 package.[37-39] At least two individual single crystal data sets were collected for each reaction to check the variation of the refined composition. Results of all single crystal studies are available from the author. Table 2 summarizes the crystallographic data of three samples (**1**, **2** and **3**) for which Guinier X-ray powder diffraction indicated that the R-phase is the only product. These samples represent the two extremes in Zn:Al ratios plus one intermediate composition. Table 3 gives atomic coordinates, site occupancies and isotropic displacement parameters; Table 4 lists relevant internuclear distances.

------ Tables 2, 3, 4 ------

Elemental Analysis

Energy dispersive spectroscopy (EDS) was performed on the same samples used for single crystal X-ray diffraction experiments, and on corresponding bulk samples using a Hitachi S-2460N scanning electron microscope. Internal standards of elemental Mg, Zn and Al were included to determine the composition of each sample. At least 4 different points on each sample were measured to obtain the average chemical composition and standard deviations. Results for three different single crystal and three different bulk samples are listed in Table 5.

------ Table 5 ------

Neutron Powder Diffraction

Micrometer-sized powder (less than 100 mesh) of "$Mg_{1.625}Zn_{1.25}Al_{2.125}$" (**4**), "$Mg_{1.625}Zn_{1.688}Al_{1.688}$" (**5**) and "$Mg_{1.625}Zn_{2.125}Al_{1.25}$" (**6**) were prepared for neutron diffraction studies as described above. The purity of each sample was checked by Guinier X-ray powder diffraction. Each sample was placed in a vanadium container and mounted on the general-purpose powder diffractometer (GPPD) at the Intense Pulsed Neutron Source (IPNS), Argonne National Laboratory.[40,41] Time-of-flight neutron diffraction data were collected at 10(2) K and $2\theta = \pm 148.88°$. The data were analyzed by Rietveld refinement with the GSAS software system.[42-44] The lowest d-spacing for all data was set at 0.8 Å.

The starting structural model of each sample came from the corresponding single crystal X-ray diffraction study. Refined structural parameters included overall scale factors, lattice parameters, fractional coordinates, anisotropic thermal displacement parameters (only applied on Mg sites) and site occupancies. Absorption parameters and an extinction coefficient were also refined. Backgrounds were fit using a six-parameter analytical function, and peak shapes were fit using exponential pseudo-Voigt functions.[45] Contributions to the total pattern from impurity phases were also included in the refinement. The experimental and Rietveld refined profiles of these data are shown in Figure 1. Final compositions for each sample were ultimately set from a combination of elemental analyses, X-ray diffraction, and neutron diffraction refinements. Summaries of the crystallographic data and refinement, atomic positions, site occupancies and isotropic displacement parameters, and interatomic distances for each sample are listed in Tables 6, 7 and 8. The

refined compositions from neutron diffraction for each bulk product are also included in Table 5.

------ Figure 1 and Tables 6, 7, 8 ------

After the structure of the main phase was determined, refinements including impurities from the starting elements and possible binary phases were included. In addition to the three elements, an $AuCu_3$-type phase is present. The product of the "$Mg_{1.625}Zn_{2.125}Al_{1.25}$" reaction contains trace amounts of Al, while the other two samples contain trace amounts of Mg, Zn, Al and an $AuCu_3$-type compound. The $AuCu_3$-type compound was indexed based on six unidentified peaks (two independent + four overlapped peaks) and the composition was set at "MgZn."

Physical properties measurements

Density: Densities of single-phase products used for neutron diffraction and EDS investigations were measured pycnometrically in triplicate using 100 mesh powders and He as the displacement fluid on a multipycnometer (Quanta Chrome Corp.). The results are tabulated with the crystallographic data from powder neutron diffraction in Table 6.

Differential Thermal Analysis: Several powdered samples were used to perform differential thermal analysis (DTA) on a Perkin-Elmer DTA 7 running Pyris software version 3. The sample holder was purged with Ar for at least 30 minutes to remove oxygen and hydrogen before each measurement. Preliminary experiments indicated that all samples decomposed when the temperature is raised above 1023 K because elemental Zn vaporizes. Each powder sample (ca. 30 mg) was heated from 473 to 973 K at a rate of 5 K/min, and then

cooled at the same rate to 473 K under Ar atmosphere. Guinier powder X-ray diffraction was performed before and after the DTA experiment on each sample. Table 1 lists some DTA results for each sample.

Magnetic Susceptibility Measurements: Temperature-dependent magnetic susceptibility measurements were conducted using a Quantum Design SQUID magnetometer operated at 3 Tesla over the temperature range 6-300 K. Data were collected for the samples "$Mg_{1.625}Zn_{1.375}Al_{2.00}$," "$Mg_{1.625}Zn_{1.688}Al_{1.688}$" and "$Mg_{1.625}Zn_{2.125}Al_{1.25}$." All three samples showed temperature independent susceptibilities over the range 50-250 K. After corrections for the diamagnetic contributions of the constituent atomic cores and the sample holder,[46] all samples show Pauli paramagnetic behavior with average susceptibilities of $3.4(3) \times 10^{-3}$, $1.5(2) \times 10^{-3}$, and $3.0(2) \times 10^{-3}$ emu/mole, respectively.

Electrical Resistivity Measurements: A standard four-probe technique was used to measure the temperature dependent resistivity for the "$Mg_{1.625}Zn_{1.688}Al_{1.688}$" sample from 1.8 to 300 K in fields of both 0 T and 5.5 T. The irregular shape of the polycrystalline sample was first polished to form a metal plate and then cut into a rectangular bar by using a wire saw. The dimensions of the sample was $1 \times 1 \times 3$ mm^3. Electrical contact was made to the sample using Epo-tek H2OE silver epoxy, with typical contact resistances of 1-2 Ω. The resistivity at 298(2) K is 62.47(1) μΩ·cm and decreases nearly linearly toward low temperatures, which is consistent with typical metallic behavior. At 5.5 T, the shape of the resistivity vs. temperature curve did not change, but the resistivity measured at each

temperature is 0.2-0.3 μΩ·cm higher than the zero field value (e.g., 62.67(6) μΩ·cm at 298(2) K).

Electronic Structure Calculations

The electronic structures of various models of R-phases were calculated using the LCAO (tight-binding) approximation with the Extended Hückel theory (EHT).[47-50] Mg atomic orbital parameters were used for the three A sites (A1-A3) and Al atomic orbital parameters were used for the four M sites (M1-M4). Calculations using both Al and Zn atomic orbital parameters were also performed, but the results were essentially the same as for calculations with just Al parameters. A primitive cell of 80 atoms (26 A + 54 M) was used for calculations of total and partial densities of states (DOS), crystal orbital overlap population curves (COOP), Mulliken populations, and Fermi energies.[51,52] A special points set of 60 **k** points in the irreducible wedge of the first Brillouin zone was chosen to perform the integrations.[53] Atomic orbital parameters are as follows (all single-ζ STO functions). Mg: $H_{ii}(3s) = -9.00$ eV, $H_{ii}(3p) = -4.50$ eV, $\zeta(3s) = \zeta(3p) = 0.95$. Al: $H_{ii}(3s) = -12.3$ eV, $H_{ii}(3p) = -6.5$ eV, $\zeta(3s) = \zeta(3p) = 1.167$.

Results and Discussion

In the following discussion, we summarize the experimental and theoretical results relevant to an understanding of how Mg, Zn, and Al distribute themselves in the cubic R-phase structure. Although there are other examples adopting this structure type in the literature,[26,54-58] these results comprise the first thorough investigation of a ternary system that shows a phase width for this structure. Furthermore, to elucidate the distribution of

elements in this structure, not only were detailed structural assessments necessary, but thorough elemental analyses of single crystal and bulk samples were crucial to reach the conclusions. The final model, which we present in the next section, relies on using a combination of diffraction methods, density measurements, and elemental analyses.

Structure Determination

Structure: The body-centered cubic, R-phase structure adopted by several examples in the Mg-Zn-Al system involves seven crystallographic sites (A1-A3, M1-M4; these labels are selected to reflect the results of evaluating the atomic site distributions) that form three shells of polyhedra containing 12, 32 and 60 vertices surrounding the center and corners of the cubic unit cell with additional A atoms filling voids as the 60-vertex polyhedra condense to form the three-dimensional structure. A perspective view of this structure along the [100] direction is shown in Figure 2. This structure is one of three types adopted by Group 13 intermetallic compounds with large polyhedra as building units: (1) the cubic (R-phase) structure, e.g. $Mg_{2-y}(Zn,Al)_{3+y}$,[26] Li_3CuAl_5,[54] $Li_{13}Cu_6Ga_{21}$,[55] $Na_{13}Cd_{20}E_7$ (E = Pb, Sn),[56] $K_{49}Tl_{108}$;[57] (2) the hexagonal (stuffed boron) structure, e.g., $K_{34}Zn_{20}In_{85}$,[58] $Na_{17}Zn_{12}Ga_{40.5}$;[59] and (3) condensed fullerene-like cage structures, e.g., $LiMgAl_2$,[3,60] $Na_{96}In_{97}Z_2$ (Z=Ni, Pd, Pt),[61] and $Na_{\sim 172}In_{\sim 197}Z_2$ (Z=Ni, Pd).[62] Derivative structures of these three types also exist, but may be considered superstructures, as for example, Z-$Al_{59}Cu_5Li_{26}Mg_{10}$, which is related to the R-phase.[63] Although each structure type is different, the atomic networks contain common polyhedral building blocks such as icosahedra and truncated tetrahedra (Friauf

polyhedra).[64] In the following discussion, the distances reported are for Mg-Zn-Al systems in our study.

------ Figure 2 ------

The first shell of atoms is an icosahedron of twelve M2 atoms with a radius of 2.53(1) Å and M2–M2 distances between 2.63 and 2.68 Å. No atomic density is detected at the center of the cluster (Wyckoff site 2a) according to both X-ray and neutron diffraction experiments, which disagrees with the original report for $Mg_{32}(Zn,Al)_{49}$ by Pauling and Bergman,[26,27] who assigned this site to be 80% Al (Note: while finishing this manuscript, an abstract of a report of a X-ray diffraction study of crystalline $Mg_{32}(Zn,Al)_{49}$ indicated the same result as ours,[65] and a similar conclusion was also achieved for a Na-Mg-Zn-Al R-phase[66]).

The second shell of atoms contains a large icosahedron of twelve M1 sites, and a pentagonal dodecahedron of eight A2 sites and twelve A3 atoms, which together form a 32-vertex triacontahedron. Each M1 atom is connected to a vertex of the inner M2 icosahedron at distances between 2.53 and 2.56 Å (the radius of the M1 icosahedron is 5.06(2) Å). Each of the twenty A2 and A3 atoms caps a triangular face of the inner M2 icosahedron (the radius of the pentagonal dodecahedron is 5.61(3) Å). The average A–M1 and A–M2 distances are, respectively, 3.20(2) and 3.02(1) Å.

The third shell of atoms contains 48 M3 sites and twelve M4 sites to form a buckminsterfullerene-type polyhedron (truncated icosahedron) with an average radius of 6.88(5) Å. Every atom on the third shell is shared with the third shell of an adjacent unit: M3

atoms are shared along the {111} directions and M4 sites are shared along the {100} directions.

------ Figure 3 ------

The M1-M4 sites form a large M_{84} cluster called a Samson polyhedron.[67] The Al sites occupy all "tetrahedral holes" created by the body-centered condensed packing of these Samson polyhedra, shown in Figure 3. The local environment is a 13-vertex Friauf-type polyhedron around each Al atom. Finally, with respect to the seven crystallographic sites in the R-phase structure, the general formula can be written as:

$$\{[(M2)_{12}(M1)_{12}(A2)_8(A3)_{12}][(M3)_{48/2}(M4)_{12/2}]\}(Al)_{24/4} \equiv A_{26}M_{54} = A_{1.625}M_{3.375}$$

Site Occupancies: In the Mg-Zn-Al system, it is difficult to distinguish Mg and Al unequivocally using the results of electron density distributions from X-ray diffraction data. On the other hand, the coherent scattering lengths[68] for Mg (5.375 fm), Al (3.449 fm) and Zn (5.680 fm) allow excellent differentiation of Mg and Al, but now a problem to resolve Mg from Zn emerges. Nevertheless, the metallic radii of Mg, Al and Zn for coordination number 12 are, respectively, 1.60 Å, 1.43 Å and 1.37 Å, which are sufficiently different to allow atomic assignments based on: (1) inter-atomic distances; and (2) coordination environments of each site. The final structural model from both single crystal X-ray and powder neutron diffraction, which takes these distance criteria into account, divides the seven atomic sites into three distinct sets: (1) three sites occupied solely by Mg atoms (A1, A2 and A3), (2) three mixed-occupied sites involving Zn and Al (M1, M2, and M3), and (3) one site (labeled

M4) that could involve any assortment of Zn, Al, Mg and vacancies. In the Bergman and Pauling model, the M4 site is exclusively assigned to Mg atoms.

Atomic site occupancies were first refined on each independent crystallographic site. The Mg sites (A1, A2 and A3) remained essentially unchanged (variations were less than 2%) and were fixed at 100% Mg for all subsequent single crystal and powder refinements. The compositions of the other metal sites (M1-M4) were then refined using constrained fractional occupancies of Zn and Al. To determine the final "composition" (i.e., average electron density or elastic scattering length) on each M1-M4 site, three different initial Zn:Al ratios (0:100, 50:50 and 100:0) were assigned on each individual site to refine. For each sample, these refinements for each Zn/Al site gave the same final composition and the thermal displacement parameters for all atomic sites could be refined anisotropically.

------ Figure 4 ------

Figure 4 illustrates the results of refinements of the M1-M4 sites in two plots: (1) from single crystal X-ray diffraction, the average electron density for each site vs. lattice constant; and (2) from powder neutron diffraction, the average elastic scattering factor for each site vs. lattice constant. The occupation of the M2 site remains essentially constant and Zn rich for all examples. Since the inter-atomic M2–M2 and M2–M1 distances are appropriate just for Zn or Al, we assign M2 as a mixture of Al and Zn, which refines to 83(3)% Zn for all compositions. The average formula of the M2 icosahedron, therefore, is close to $[Zn_{10}Al_2]$ (83.3% Zn), which is similar to a $NaZn_{13}$-type compound, $BaZn_{10}Al_2$.[69] These two independent results suggest that the $[Zn_{10}Al_2]$ icosahedron is a stable building unit in these intermetallic phases. The M1 and M3 sites increase in Zn content as the lattice

constant decreases. According to the distance criteria, therefore, these two sites are also assigned as mixtures of Zn and Al, which change composition by identical relations with total composition of the sample (M1 varies from 19.5(4)% to 72.0(6)% Zn; M3 varies from 19.7(4)% and 73.2(5)% Zn). The composition of the M4 site is nearly insensitive for all samples except at low lattice constants, but neither X-ray nor neutron diffraction results lead to a single conclusion. Nevertheless, the combination of these experimental results strongly suggests that Mg and Zn atoms occupy this site. Other than the M4–M4 distances (2.6-2.7 Å), all other contacts to the M4 site exceed 2.90 Å. Therefore, if a Mg atom occupies one M4 site, we hypothesize that the adjacent M4 site must be vacant. To reach a definite conclusion, we need to incorporate results from additional elemental analyses.

Elemental Analysis

The results of EDS analyses performed on three different single crystal samples (used for single crystal X-ray diffraction) and three bulk samples (used for powder neutron diffraction) are summarized in Table 5. In every case except one bulk sample, the Mg content exceeds 32.5 atomic percent (52 Mg atoms on the A1-A3 sites out of 160 total sites in the unit cell). Furthermore, the Mg content never reaches 40.0 atomic percent (64 Mg atoms on the A1-A3 and M4 sites), but monotonically increases as the Al content increases. In addition to the analytical results, the experimental densities for the three bulk samples are also listed in Table 5, and are consistent with the analytical results.

To reach conclusions for the final compositions at the M4 sites in these R-phase structures, we carried out seven different refinement strategies of the X-ray and neutron diffraction data to achieve the best overall agreement with the elemental analysis and density.

These models involved refining the M4 site for occupation by (1) Mg only; (2) Zn only; (3) Al only; (4) a mixture of Mg and Zn; (5) a mixture of Mg and Al; (6) a mixture of Zn and Al; and (7) a mixture of Mg, Al and Zn. The model that provided the best overall agreement with all data for all samples was (4), refining a mixture of Mg and Zn at the M4 site. The total occupancies for each sample refine to ca. 67%, so that 33% of the M4 sites remain vacant. These results of the "analysis" from refinements of single crystal X-ray diffraction and powder neutron diffraction experiments are also listed in Table 5 to compare with EDS measurements. Furthermore, the various site occupancies from this model are included in Table 3 (X-ray diffraction) and Table 7 (neutron diffraction), and plotted with respect to *vec* in Figure 5. These refinements show that the M4 site is approximately 33% Zn, 33% Mg, and 33% vacancies. Since the M4 site has 12 positions in the unit cell, there are four vacancies (on average) per unit cell. Among the eight remaining sites, we hypothesize four Mg adjacent to vacancies and four Zn atoms forming two Zn–Zn pairs. In the section on theoretical calculations, we describe a model to account for this pattern of site occupancies and the presence of vacancies.

------ Figure 5 ------

Phase Width Investigations

Table 1 summarizes the results of powder and single crystal studies as well as DTA measurement on $Mg_{2-y}(Zn_xAl_{1-x})_{3+y}$ samples for $y = 0.33$ and 0.40, $0 \le x \le 1$. According to X-ray powder diffraction patterns, the R-phase was observed for x between 0.19 (*vec* = 2.55) and 0.74 (*vec* = 2.18). Mixtures of an R-phase and other binary or elemental phases were observed for $x < 0.41$ (*vec* > 2.40) and $x > 0.63$ (*vec* < 2.25) reactions. Also, no binary phase

adopting the R-phase structure was found. For $0.41 < x < 0.63$ ($2.25 < vec < 2.40$), nearly single phase products were identified. DTA experiments on "$Mg_{1.625}Zn_{1.375}Al_{2.0}$," which is the single phase sample with the highest Al content, revealed a congruently melting sample, with endothermic and exothermic events observed, respectively, at 780.1 K (heating) and 768.7 K (cooling). X-ray powder diffraction patterns from this sample, taken before and after the DTA measurements, showed no decomposition of the sample.

Physical properties

The "$Mg_{1.625}Zn_{1.688}Al_{1.688}$" polycrystalline sample shows metallic behavior ($d\rho/dT > 0$) throughout the temperature range 1.8 to 300 K, and its room temperature resistivity of 62.5 $\mu\Omega$·cm is higher than resistivities reported for each of the component elements, Mg (4.45 $\mu\Omega$·cm), Zn (5.9 $\mu\Omega$·cm) and Al (2.65 $\mu\Omega$·cm).[70] Furthermore, this resistivity value is close to reports of room temperature resistivities of the quasicrystalline phases, *i*-$Mg_{32}(Zn_xAl_{1-x})_{49}$ ($x = 0.50$ and 0.69), which are, respectively, 59(5) and 90(10) $\mu\Omega$·cm.[31] In addition, magnetic susceptibility measurements at 3 T for "$Mg_{1.625}Zn_{1.375}Al_{2.00}$," "$Mg_{1.625}Zn_{1.688}Al_{1.688}$" and "$Mg_{1.625}Zn_{2.125}Al_{1.25}$" demonstrate Pauli paramagnetic behavior, which is also consistent with metallic character.

Theoretical Calculations

Figure 6 illustrates the DOS and COOP curves for the R-phase structure using the atomic orbital parameters associated with the model $Mg_{52}Al_{108}$ ($A_{52}M_{108}$). The Fermi energy (E_F) calculated to give the optimized total bonding within the M1-M4 network (as given by the total overlap population for all M–M interactions) is indicated by the dashed line.

------ Figure 6 ------

The DOS curve shows no band gap within the *vec* range between 2.07 and 2.25 e^-/atom (−7.8 eV ≤ E_F ≤ −6.1 eV), although this region has significantly lower DOS values than the surrounding energy regions, which is consistent with the resistivity measurements on the Mg-Zn-Al phases. According to the COOP curve, this part of the DOS is nearly nonbonding for the total M–M interaction (the total overlap population varies by less 0.6% throughout the range). The peak between −8 and −10 eV comes mostly from Al 3*p* orbitals, while below this peak, the DOS curve is featureless and approximates a nearly free electron distribution of electronic states.

The total overlap population of the $^3_\infty[M_{108}]$ network is maximized at *vec* = 2.18 e^-/atom. The overlap populations of individual M–M contacts, however, indicate optimal bonding interactions at different *vec* values for each contact, which agrees with the computational results on $Na_{13}Cd_{20}Pb_7$ (these calculations were performed without atomic orbitals at the Na (A) positions).[56] The M2–M2 contacts in the first shell and the M1–M4 contacts between the second and third shells are optimized at *vec* = 2.14 e^-/atom. Other inter-shell contacts, viz. M1–M2 and M1–M3, are optimized, respectively, at *vec* = 2.36 and 2.20 e^-/atom. Within the third shell, the largest overlap populations for M3–M3, M3–M4 and M4–M4 interactions and are observed at *vec* = 2.29, 2.25 and 2.50 e^-/atom, respectively. Therefore, to optimize various M–M interactions in the R-phases, values of the *vec* should range between 2.14 and 2.50 e^-/atom. These results are in good agreement to the observed range of *vec* values in the single crystal study (*vec* = 2.17-2.41 e^-/atom). Like the total

overlap population for all M–M interactions in this structure, each M–M contact shows essentially nonbonding character between –6.1 and –7.8 eV. These results suggest that the *vec* can be varied without significantly changing the bond strength of the M–M contacts by adjusting the molar ratio of Zn to Al, and, therefore, producing an observable phase width (i.e., variable x) in $Mg_{2-y}(Zn_xAl_{1-x})_{3+y}$.

------ Figure 7 ------

This distinctive, nonbonding region ($2.07 < vec < 2.25$) in the DOS, however, is nonzero. Decompositions of the total DOS into contributions from each of the M1-M4 sites are illustrated in Figure 7. From these results, we can now understand the trends between site preference and x in $Mg_{2-y}(Zn_xAl_{1-x})_{3+y}$ that are shown in Figure 5. These DOS curves indicate that:

(1) The Mulliken populations (MP's) of the M1 and M3 sites are sensitive to *vec* across this nonbonding range (the variations of MP's are 10% for M1 and 11% for M4). Therefore, the chemical compositions of these two sites will change when the *vec* is altered.

(2) The M2 and M4 sites essentially do not contribute to the electronic states in this nonbonding region of the DOS. The MP's at these two sites, therefore, remain constant for changes in *vec* (the MP's for M2 and M4 increase by 4% and 2% across the range). Therefore, as the *vec* of the Mg-Zn-Al R-phase is varied by changing the Zn:Al molar ratio, the chemical composition of the M2 and M4 sites should remain nearly fixed in this *vec* region. When *vec* exceeds 2.25 e^-/atom, the M2 and M4 sites contribute orbitals to the total DOS, and the chemical compositions at these sites will begin to change. The values of the

MP's for the M2 (2.4-2.5) and M4 (2.3-2.4) sites also agree with the diffraction results: the M2 site attracts more Zn (the most electronegative element) than the M4 site.

The best model that accounts for our diffraction and analytical data places four vacancies per unit cell at the M4 site. Our theoretical calculations have shown that M–M bonding in the $A_{52}M_{108}$ model is optimized at *vec* = 2.18 e^-/atom, which is close to the "magic number" of electrons for this structure predicted by King (340 e^-/unit cell or *vec* = 2.125 e^-/atom).[71] Increasing the *vec* by increasing the Al content will push the Fermi level up to some M–M antibonding orbitals once the *vec* exceeds ca. 2.25 e^-/atom, according to a rigid band model applied to the DOS and COOP curves in Figure 6. To alleviate such antibonding interactions, extended solids can either undergo a structural distortion (e.g., the puckering of the honeycomb network in α-As[72]), or create vacancies in the network. In the R-phase structure, therefore, a model with vacancies incorporated into the network becomes favored. Figure 8 illustrates the trend in total valence electron energy per atom with changes in the average number of valence electrons per atom for various vacancy models at the M4 site in the R-phase structure, i.e., $Mg_{52}(Al_w\square_{1-w})_{12}Al_{96}$. When *vec* exceeds ca. 2.28 e^-/atom, structural models with vacancies in the M4 position become preferred. According to our simple model, there is a narrow range of stability ($2.28 < vec < 2.33$) for four vacancies per unit cell. For larger *vec* values, six vacancies per unit cell are favored. The seven structural models we examined are summarized in Table 9, which also describes how the vacancies are distributed in each model: since the M4 position involves six M4–M4 pairs, vacancies can either occur together (□–□) or isolated (M–□).

------ Figure 8 and Table 9 ------

This argument is similar to accounting for vacancies in the network of tetrahedral semiconductors using the Grimm-Sommerfeld valence rule or for "missing" cluster atoms in carborane deltahedra using Wade's rules.[72] For tetrahedral frameworks, the average valence electron count per site is four; if there are vacancies in the structure, the valence electron count per atom (i.e., *vec*) is greater than four. In carborane chemistry, a *closo*-deltahedron with n cluster atoms needs $n+1$ pairs of skeletal electrons. The *nido*-cluster based upon the same deltahedron needs the same number of skeletal electron pairs, but has one less atom. Therefore, *vec* increases from *closo*- to *nido*- (and to *arachno*-) deltahedra.

R-Phase Mg-Zn-Al: Where Are The Atoms?

All data from X-ray and neutron diffraction as well as EDS and density measurements lead to the general formulation for the Mg-Zn-Al R-phases as $Mg_{52}[(Mg_uZn_v\square_z]_{12}(Zn_wAl_{1-w})_{96}$ in which the occupancy of the 12-fold M4 site is emphasized. According to this formulation, the valence electron count per site is 2.45 + 0.15(u + v) – 0.6w; u + v = total fraction of M4 sites occupied and w = fraction of Zn on the remaining 96 M1-M3 sites. The range in *vec* observed for Mg-Zn-Al phases exceeds the values appropriate for complete occupation of all crystallographic sites, and thus leads to the creation of vacancies. In this ternary system, the Al content must be less than ca. 20 atomic % to eliminate vacancies (w > 0.67 with u + v = 1), but these synthetic targets, e.g., "$Mg_{52}(Mg_uZn_v)_{12}(Zn_{0.90}Al_{0.10})_{96}$ = $Mg_{1.625+0.375u}Zn_{2.70+0.375v}Al_{0.30}$," will compete against the formation of $MgZn_2$. Nevertheless, the report of quasicrystalline phases in the Mg-Zn-Al systems obtained by splat quenching melted mixtures of these elements suggest that quasicrystalline structures may arise when such vacancies are eliminated.

------ Figure 9 ------

Figure 9a shows a fragment of the crystalline R-phase containing three shells of M1-M4 sites and two shells of the A sites (A1-A3 sites) projected along a pseudo fivefold axis, $[\sqrt{3}, 1, 0]$, of the cluster. The point group of this fragment is T_h based on the space group of $Im\bar{3}$, which is the highest point symmetry allowed for an icosahedron in a crystalline structure. Figure 9b illustrates the same type of fragment, but with I_h point symmetry. In this model, each shell of atoms corresponds to a single atom type (M3 and M4 become symmetry equivalent; A1-A3 become symmetry equivalent). When superimposed, the two images show the most pronounced difference in the buckminsterfullerene-type (outermost) cage. In the cubic R-phase structures, the M3 and M4 sites are not only crystallographically inequivalent, but also contain different elemental compositions, which included vacancies at the M4 position. These sites prevent the formation of fivefold symmetry that can lead to the formation of a quasicrystalline phase, and suggests that the M4 sites may play a crucial role in the formation of quasicrystalline phases in the Mg-Zn-Al system.

Conclusions

This study reports the first detailed and systematic experimental and theoretical investigation of the crystalline R-phases in the Mg-Zn-Al system, which have been used to model quasicrystalline materials in the same ternary system. Elemental analyses coupled with X-ray and neutron diffraction experiments were necessary to elucidate the structural chemistry at the various sites in the R-phase structure. Theoretical calculations provided models to interpret some exceptional features of these materials: (1) nonbonding character of

the M–M contacts exists over a range of *vec*, which can account for the observed phase width; (2) two M sites (M1 and M3) are responsible for the phase width, while the other two M sites (M2 and M4) are essentially fixed in chemical composition (or in *vec*); (3) the M4 site allows occupation by vacancies, Zn and Mg atoms; and (4) vacancies arise in the structure because the *vec* exceeds the value that optimizes M–M bonding. Since the vacancy concentration is linked to both *vec* and the observation of quasicrystalline phases, we continue to investigate the chemistry and properties of these materials.

Acknowledgments

This work was supported by the NSF DMR 96-27161 and DMR 99-81766. The authors gratefully thank Dr. R. A. Jacobson for the use of X-ray diffractometers, Dr. Ilia Guzei for training on the Bruker CCD-1000 diffractometer (which was purchased by the grant NSF 97-11121), Dr. J. Richardson at Argonne National Laboratory for neutron powder diffraction experiments, Dr. I. A. Fisher for conductivity measurements, A. W. Straszheim for EDS experiments, R. Terpstra for pycnometric measurements, and J. Ostenson for magnetic susceptibility measurements.

Supplementary Material Available

The following tables and figures are available from the author:

1) Tables listing detailed crystallographic data, aniostropic thermal displacement parameters, and observed and calculated structure factors of the three single crystals from single crystal X-ray diffraction.

2) X-ray powder diffraction line refinements of Mg_2ZnAl_2 and Mg_2Zn_2Al products.

3) Tables listing crystallographic data and aniostropic thermal displacement parameters from neutron powder diffraction.

4) Figures of COOP curves for Mg-Mg, Mg-Al and Al-Al contacts calculated from the EHT method based on the model $Mg_{52}Al_{108}$.

5) Figures of magnetic susceptibility measurements for "$Mg_{52}Zn_{44}Al_{64}$," "$Mg_{52}Zn_{44}Al_{64}$," and "$Mg_{52}Zn_{44}Al_{64}$".

6) Figures of resistivity measurements at 0 and 5T for "$Mg_{52}Zn_{44}Al_{64}$".

References

1)Westbrook, J. H.; Fleischer, R. L. *Intermetallic Compounds: Principles and Practice*; John Wiley & Sons: West Sussex, 1995; Vol. 1-2.

2)Villars, P.; Calvert, L. D. *Pearson's Handbook of Crystallographic Data for Intermetallic Phases*; 2nd ed ed.; ASM International, Metals Park OH:, 1991.

3)Nesper, R. *Angew. Chem.* **1991**, *103*, 805-34 (See also Angew. Chem., Int. Ed. Engl., 1991, 30(7), 789-817).

4)Miller, G. J. *Eur. J. Inorg. Chem.* **1998**, 523-536.

5)Nesper, R. *Prog. Solid State Chem.* **1990**, *20*, 1-45.

6)Belin, C.; Tillard-Charbonnel, M. *Coord. Chem. Rev.* **1998**, *178-180*, 529-564.

7)Schaefer, H. *Annu. Rev. Mater. Sci.* **1985**, *15*, 1-41.

8)Belin, C.; Tillard-Charbonnel, M. *Prog. Solid State Chem.* **1993**, *22*, 59-109.

9)Corbett, J. D. *Struct. Bonding (Berlin)* **1997**, *87*, 157-193.

10)Huheey, J. E.; Keiter, E. A.; Keiter, R. L. *Inorganic Chemistry : Principles of Structure and Reactivity*; 4th ed.; Harper Collins College Publishers: New York, NY, 1993.

11)Häussermann, U.; Simak, S. I.; Abrikosov, I. A.; Sven, L. *Chem. Eur. J.* **1997**, *3*, 904.

12)Häussermann, U.; Simak, S. I.; Ahuja, R.; Johansson, B.; Sven, L. *Angew. Chem. Int. Ed. Engl.* **1999**, *38*, 2017.

13)Zintl, E. *Naturwiss* **1929**, *17*, 782.

14)Kishio, K.; Brittain, J. O. *J. Phys. Chem. Solids.* **1979**, *40*, 933.

15)Iandelli, A. *J. Less-Common Met.* **1987**, *135*, 195.

16)Nesper, R.; Miller, G. J. *J. Alloys Compd.* **1993**, *197*, 109-21.

17)Miller, G. J.; Li, F.; Franzen, H. F. *J. Am. Chem. Soc.* **1993**, *115*, 3739-45.

18)Fornasini, M. L.; Bruzzone, G. *J. Less-Common Metals* **1975**, *40*, 335.

19)Miller, G. J. *Chemistry, Structure, and Bonding of Zintl Phases and Ions*; Kauzlarich, S. M., Ed.; VCH, New York, 1996, pp 1-59.

20)Schaefer, H.; Eisenmann, B.; Mueller, W. *Angew. Chem.* **1973**, *85*, 742-60.

21)Barrett, C. S.; Massalski, T. B. *Structure of Metals: Crystallographic Methods, Principles and Data*; 3rd ed.; Pergamon Press: Oxford ; New York, 1980.

22)Hume-Rothery, W. *The Metallic State*; Oxford: Clarendon, 1931, 328.

23)Nordell, K. J.; Miller, G. J. *Inorg. Chem.* **1999**, *38*, 579-590.

24)Nordell, K. J.; Miller, G. J. *Angew. Chem., Int. Ed. Engl.* **1997**, *36*, 2008-2010.

25)Nordell, K. J.; Miller, G. J. *Croat. Chem. Acta* **1995**, *68*, 825-35.

26)Bergman, G.; Waugh, J. L. T.; Pauling, L. *Acta Crystallogr.* **1957**, *10*, 254.

27)Bergman, G.; Waugh, J. L. T.; Pauling, L. *Nature* **1952**, *169*, 1057.

28)Goldman, A. I.; Kelton, R. F. *Rev. Modern Phys.* **1993**, *65*, 213.

29)Janot, C. *Quasicrystals: A Primer*; 2nd ed.; Oxford Univ. Press: Oxford, 1994.

30)Deshpande, N. U.; Ray, K. K.; Mallik, A. K. *J. Alloy. Phase. Diag.* **1986**, *2*, 108.

31)Baxter, D. V.; Richter, R.; Strom-Olsen, J. O. *Phys. Rev. B* **1987**, *35*, 4819.

32)Shen, Y.; Shiflet, G. J. *Phys. Rev. B* **1988**, *38*, 5332.

33)Cassada, W. A.; Shen, Y.; Poon, S. J.; Shiflet, G. J. *Phys. Rev. B* **1986**, *34*, 7413.

34)Rajasekharan, T.; Akhtar, D.; Gopalan, R.; Muraleedharan, K. *Nature* **1986**, *322*, 528.

35)Note: The vec value is calculated from the total number of valence electrons divided by the total number of atoms per formula unit. Mg is included because the electronegativity of Mg is similar to Al and Zn. The d electrons of Zn are not included.

36)Wilson, A. J. C. *Nature* **1942**, *150*, 151.

37)*SAINT*; Version 4 ed.; Siemens Analytical X-ray Instruments Inc.: Madison, WI., 1995.

38)Sheldrick, G. M. *SHELXTL. Structure Determination Programs*; Version 5.12 ed.; Siemens Analytical X-ray Instruments Inc.: Madison, WI., 1995.

39)Sheldrick, G. M. *Crystallographic Computing 3*; Sheldrick, G. M., Kruger, C. and Goddard, R., Ed.; Oxford University Press: Oxford, 1985, pp 175.

40)Von Dreele, R. B.; Jorgensen, J. D.; Windsor, C. G. *J. Appl. Crystallogr.* **1982**, *15*, 581.

41)Jorgensen, J. D.; Rotella, F. J. *J. Appl. Crystallogr.* **1982**, *15*, 27.

42)Rietveld, H. M. *J. Appl. Crystallogr.* **1969**, *2*, 65.

43)Young, R. A. *The Rietveld Method*; Oxford Univ. Press: Oxford OX2 6DP, 1995.

44)Larson, L. C.; Von Dreele, R. B. *Generalized Structural Analysis System (GSAS)*; LANSCE, MSH805, Los Alamos National Laboratory, NM 87545, USA, 1995.

45)Von Dreele, R. B. *Unpublished work.* **1990**.

46)Mulay, L. N.; Boudreaux. , E. A. *Theory and Applications of Molecular Diamagnetism*; Wiley: New York, 1976.

47)Hoffmann, R.; Lipscomb, W. N. *J. Chem. Phys.* **1962**, *36*, 2179, 3489.

48)Hoffmann, R. *J. Chem. Phys* **1963**, *39*, 1397.

49)Ammeter, J. H.; Buergi, H. B.; Thibeault, J. C.; Hoffmann, R. *J. Am. Chem. Soc.* **1978**, *100*, 3686-92.

50)Whangbo, M.-H.; Hoffmann, R.; Woodward, R. B. *Proc. R. Soc. London, Ser. A* **1979**, *366*, 23-46.

51)Hughbanks, T.; Hoffmann, R. *J. Am. Chem. Soc.* **1983**, *105*, 3528-37.

52)Wijeyesekera, S. D.; Hoffmann, R. *Organometallics* **1984**, *3*, 949-61.

53)Chadi, D. J.; Cohen, M. L. *Phys. Rev. B* **1973**, *8*, 5474.

54)Audier, M.; Pannetier, J.; Leblanc, M.; Janot, C.; Lang, J.-M.; Dubost, B. *Physica B* **1988**, *153*, 136.

55)Tillard-Charbonnel, M.; Belin, C. *J. Solid State Chem.* **1991**, *90*, 270-8.

56)Todorov, E.; Sevov, S. C. *Inorg. Chem.* **1997**, *36*, 4298.

57)Cordier, G.; Mueller, V. *Z. Naturforsch., B* **1993**, *48*, 1035-40.

58)Cordier, G.; Mueller, V. *Z. Naturforsch., B* **1995**, *50*, 23-30.

59)Tillard-Charbonnel, M.; Chouaibi, N. E.; Belin, C. *C. R. Acad. Sci., Ser. II* **1992**, *315*, 661-5.

60)Nesper, R. *Angew. Chem. Int. Ed. Engl.* **1994**, *33*, 843.

61)Sevov, S. C.; Corbett, J. D. *Science (Washington, D. C., 1883-)* **1993**, *262*, 880-3.

62)Sevov, S. C.; Corbett, J. D. *J. Solid State Chem.* **1996**, *123*, 344-370.

63)Le Bail, A.; Leblanc, M.; Audier, M. *Acta Crystallogr., Sect. B: Struct. Sci.* **1991**, *B47*, 451-7.

64)Friauf, J. B. *J. Am. Chem. Soc.* **1927**, *49*, 3107-3114.

65)Sun, W.; J., L. F.; Sugiyama, K.; Hiraga, K. *Structure of $(Al,Zn)_{49}Mg_{32}$-type phase by single-crystal X-ray diffraction*: Abstract PB23 from 7th International Conference on Quasicrystals, Stuttgart, Germany, 1999, pp 37.

66)Elding-Ponten, M.; Lidin, S. *J. Solid State Chem.* **1995**, *115*, 270-3.

67)Samson, S. *Structure Chemistry and Molecular Biology*; Rich, A. and Davidson, N., Ed.; Freeman: San Francisco, 1968, pp 687-717.

68)Sears, V. F. *Neutron News* **1992**, *3*, 26.

69)Lee, C.-S.; Miller, G. J. *manuscript in preparation.* **2000**.

70)Ashcroft, N. W.; Mermin, N. D. *Solid State Physics*; Saunders College Publishing: Orlando, 1976.

71)King, R. B. *Inorganica Chimica Acta* **1991**, *181*, 217-225.

72)Burdett, J. K. *Molecular Shapes: Theoretical Models of Inorganic Stereochemistry*; Wiley, New York, 1980.

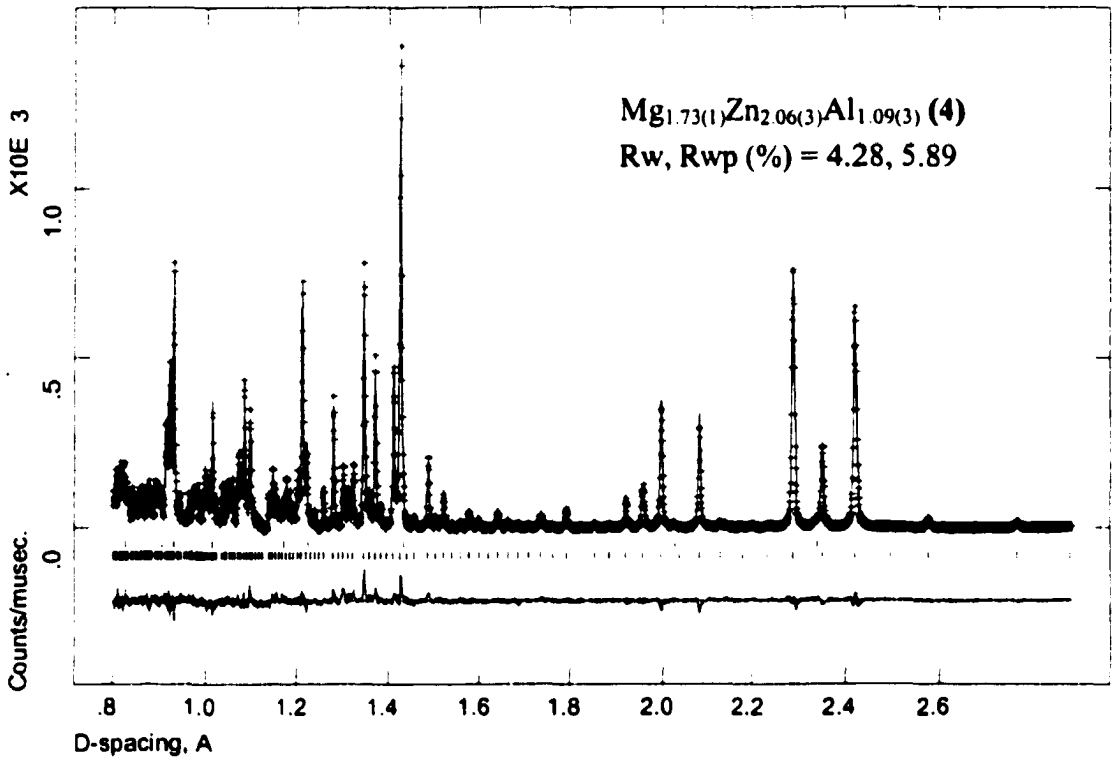

(a)

Figure 1. The observed (+) and refined powder neutron diffraction profiles (solid line) of samples (a) **4**; (b) **5**; and (c) **6** from Rietveld refinements. The refined compositions for each sample are labeled on each plot and the Bragg peaks (R-phase and impurities) are noted by tick marks below each profile. A difference curve (raw data minus calculated data) is shown at the bottom and a background correction has been applied to each curve.

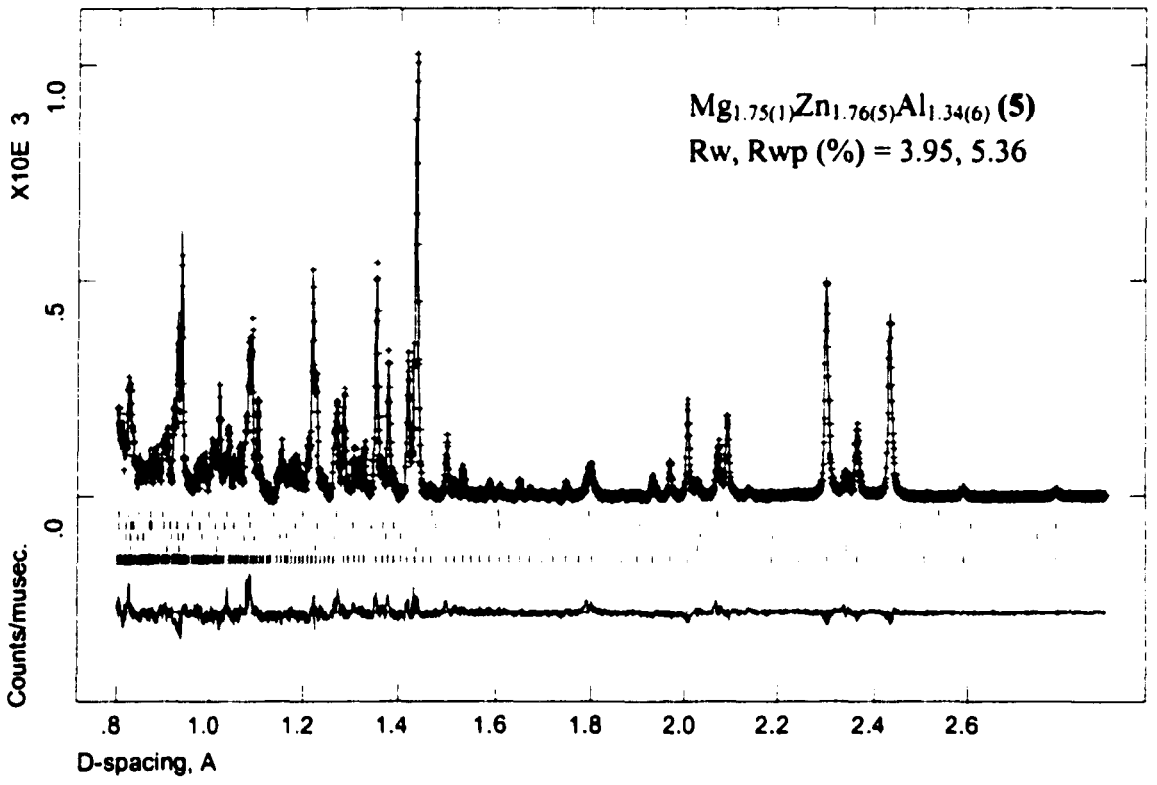

(b)

Figure 1. Continued

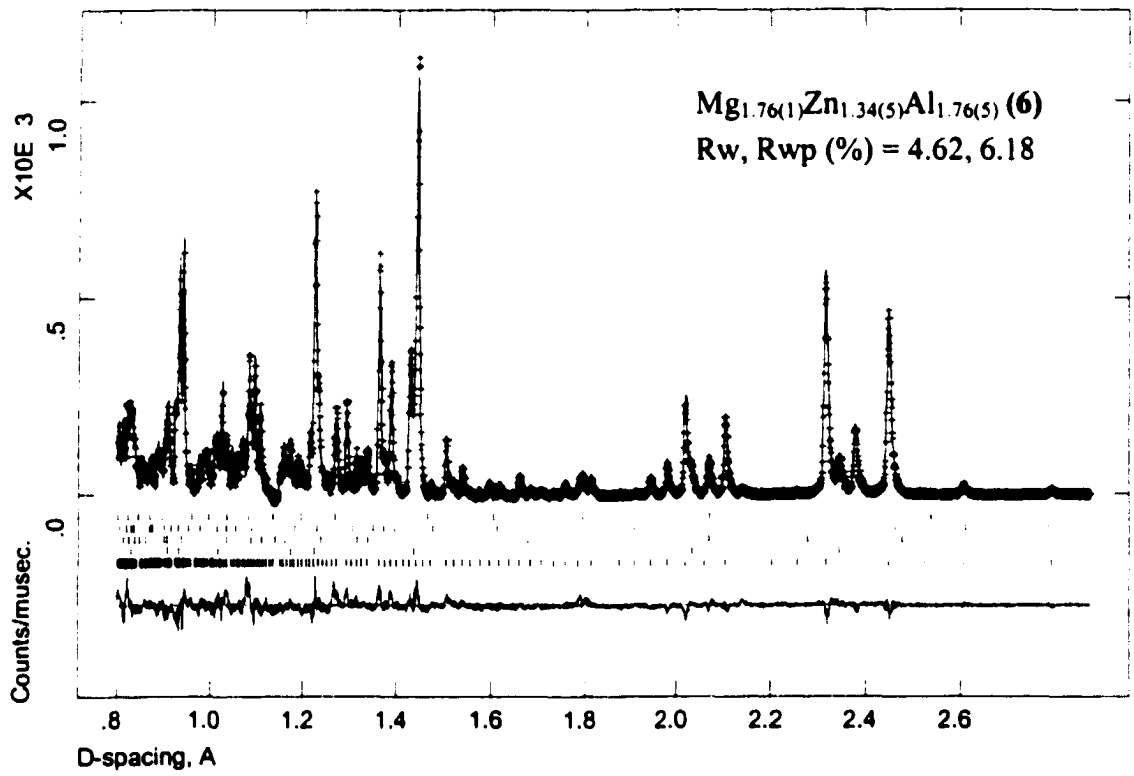

(c)

Figure 1. Continued

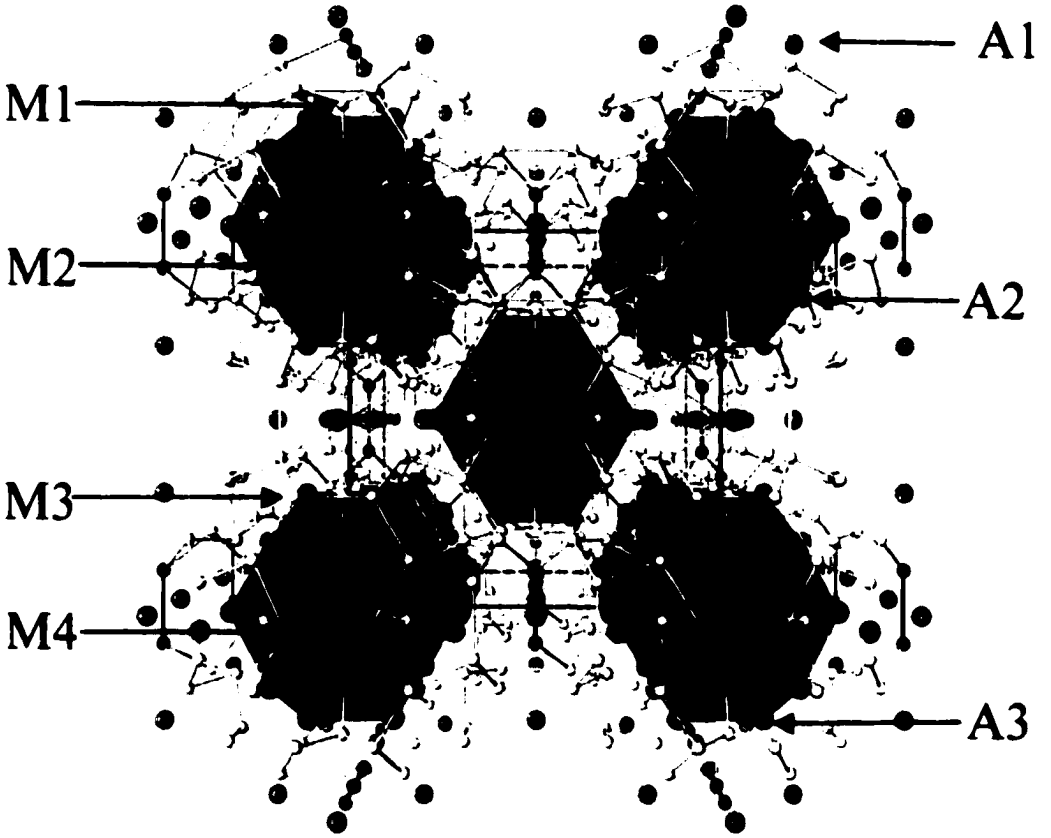

Figure 2. The crystal structure (ATOMS 5.0) of the R-phase structure for $Mg_{2-y}(Zn_xAl_{1-x})_{3+y}$ projected in perspective along [100]. The Mg atoms (A1, A2, A3) are drawn as blue circles; the M1, M3 and M4 atoms are drawn as small circles with different gray scales; the M2 atoms are drawn as red circles. Yellow, red and black lines indicate M–M contacts with distances less than 3.10 Å. A_{20} pentagonal dodecahedra are represented in blue.

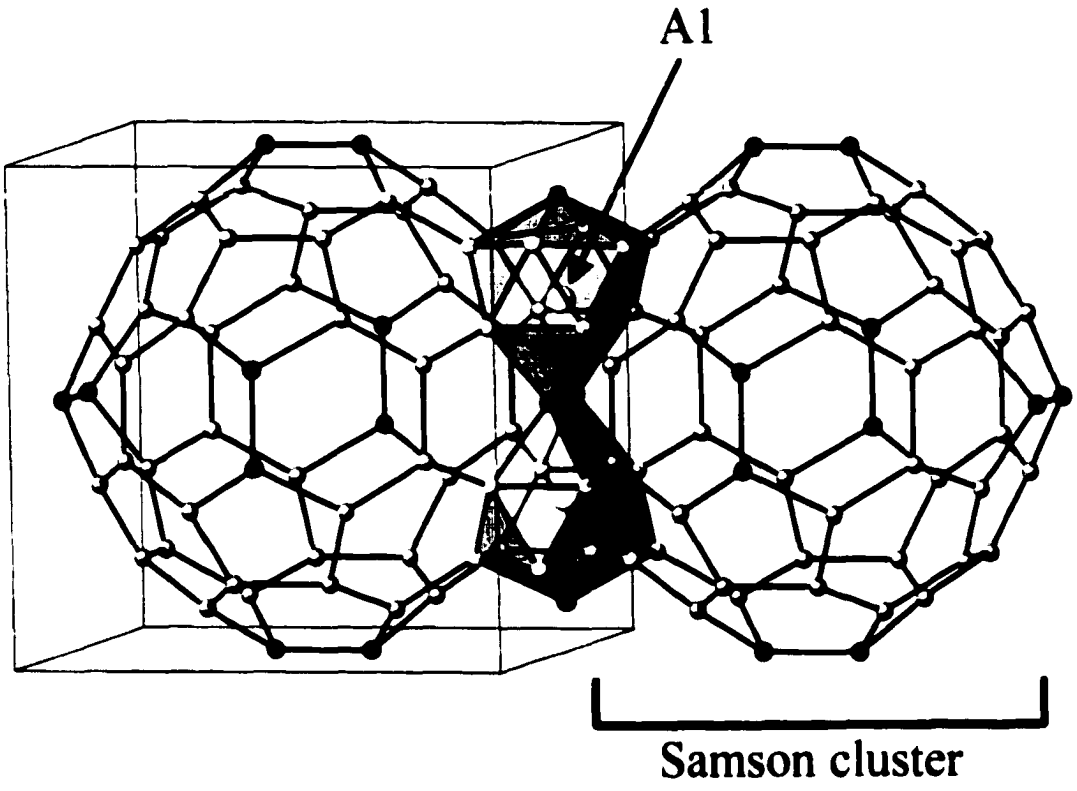

Figure 3. The Al crystallographic site in the R-phase structure. The outer shell of the Samson polyhedron and the 13-vertex coordination environment for the Al site are emphasized.

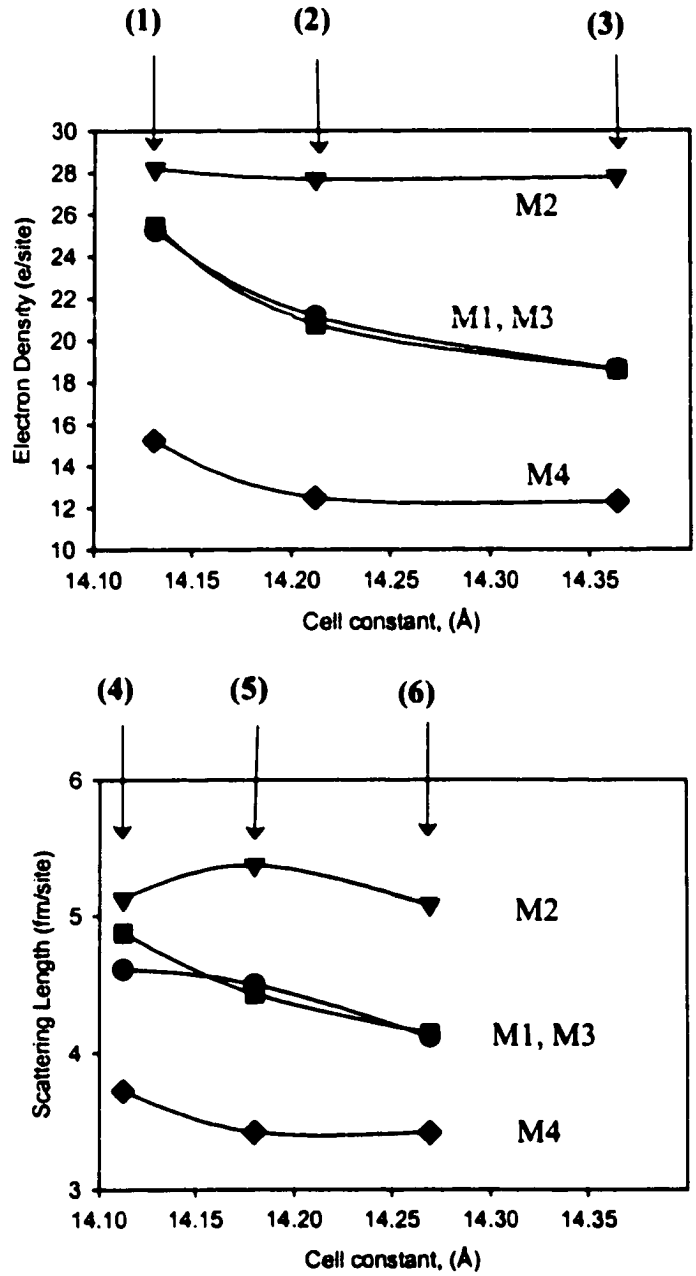

Figure 4. (Top) Refined electron densities vs. lattice constants for the M1-M4 sites from single crystal X-ray diffraction experiments for three samples, **1**, **2** and **3**; (Bottom) Refined elastic scattering lengths vs. lattice constants for the M1-M4 sites from powder neutron diffraction experiments for three samples, **4**, **5** and **6**.

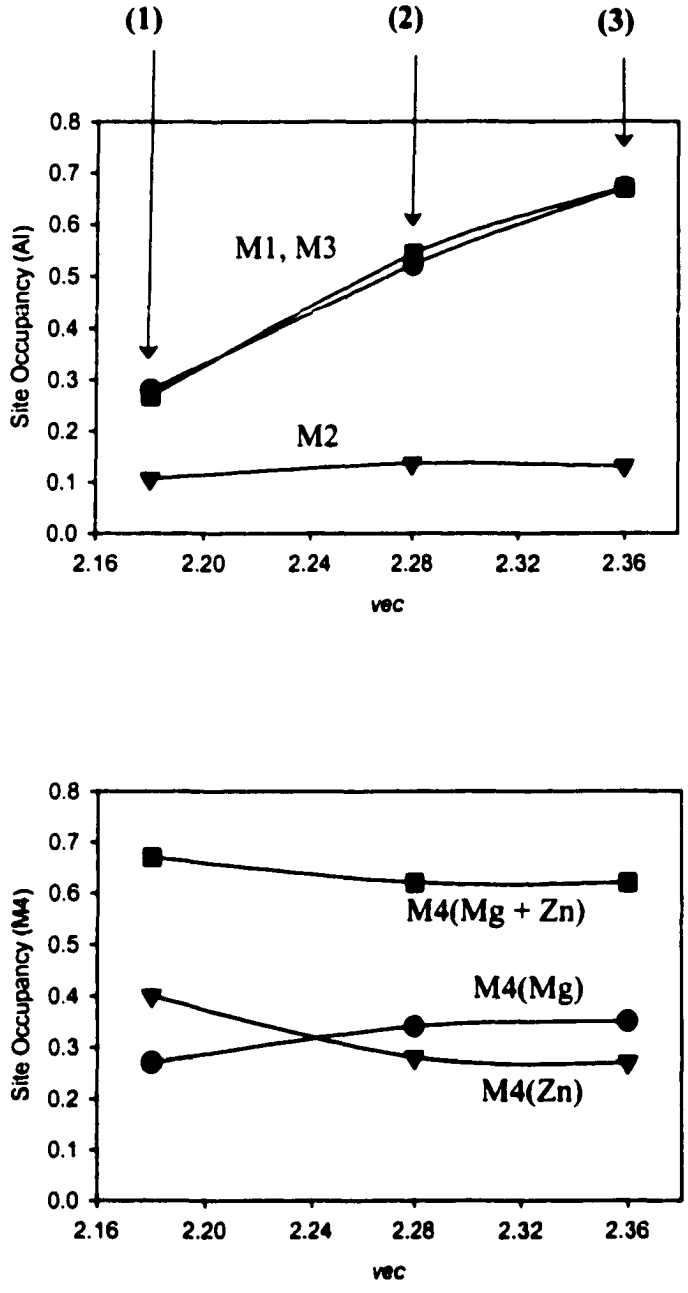

Figure 5. Variations in site occupancies by Zn vs. valence electron concentration (*vec*).

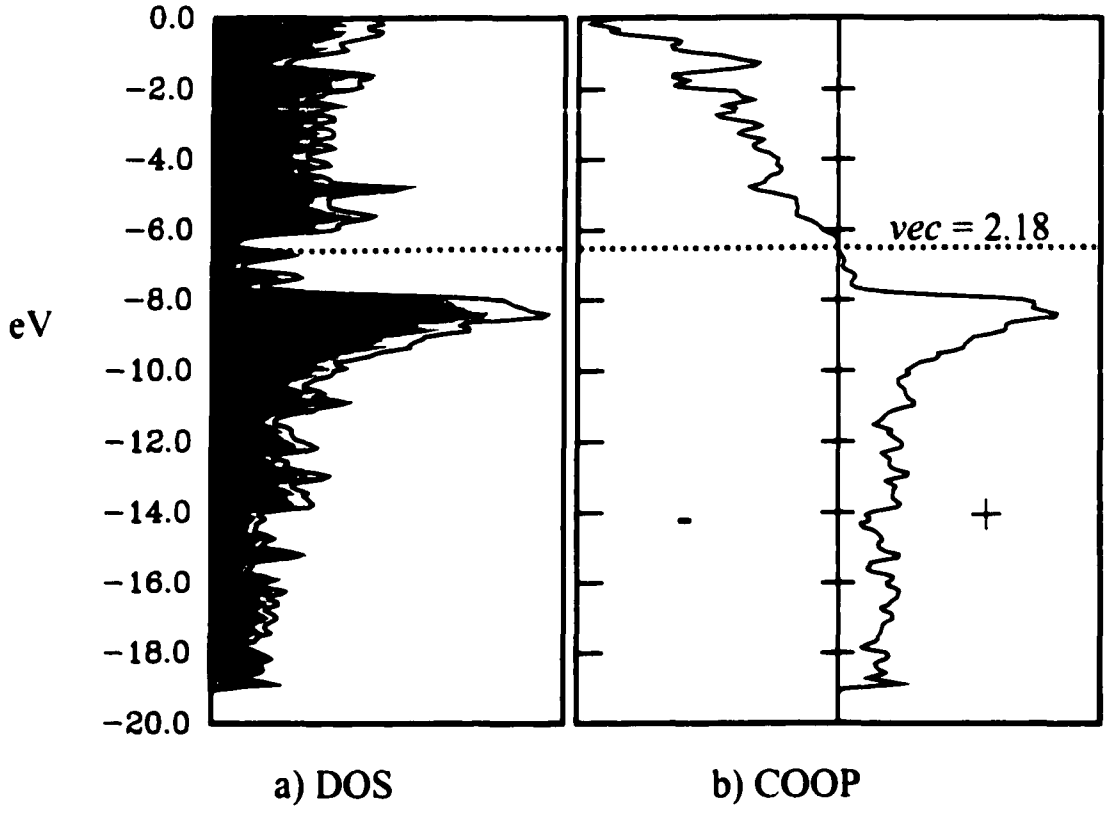

Figure 6. a) Total density of states (solid line) and partial DOS curves (PDOS) of Mg (black) and Al (gray) for the R-phase model "$Mg_{52}Al_{108}$." b) COOP curve for all Al-Al contacts less than 3.10 Å. The dashed line indicates the Fermi level for *vec* = 2.18, the value at which the total Al–Al overlap population is optimized.

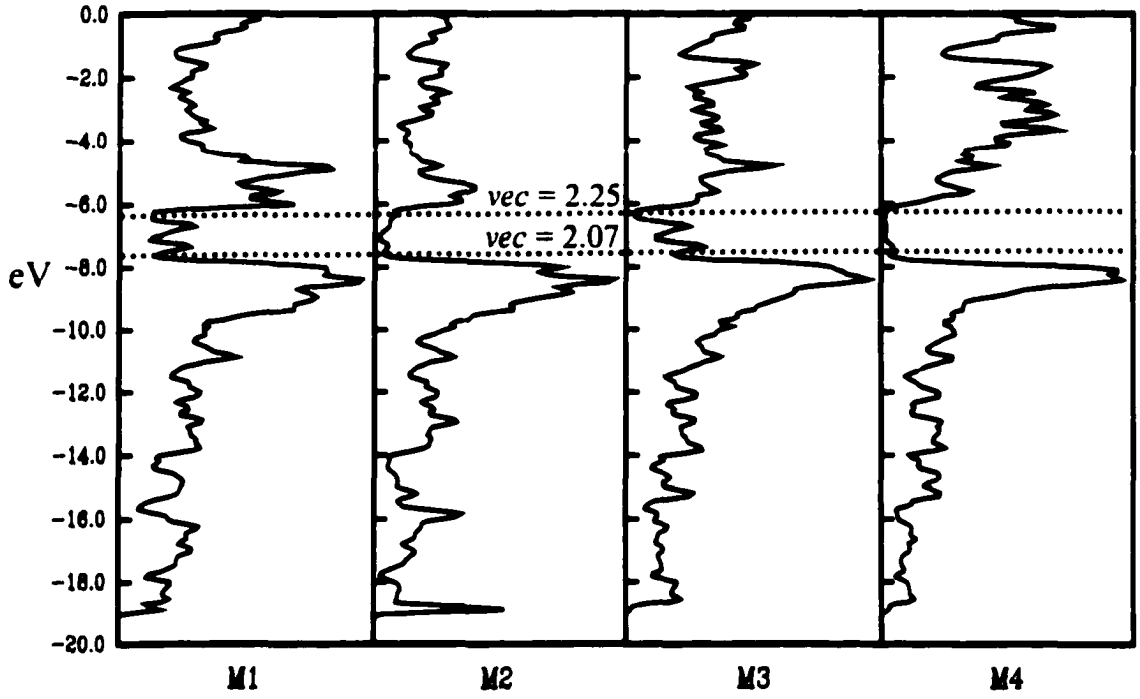

Figure 7. PDOS curves for the M1, M2, M3 and M4 sites from the results of EHT calculations. The dashed lines indicate the minimum and maximum Fermi energies ($2.07 \leq vec \leq 2.25$) for which the M–M contacts show essentially nonbonding interactions.

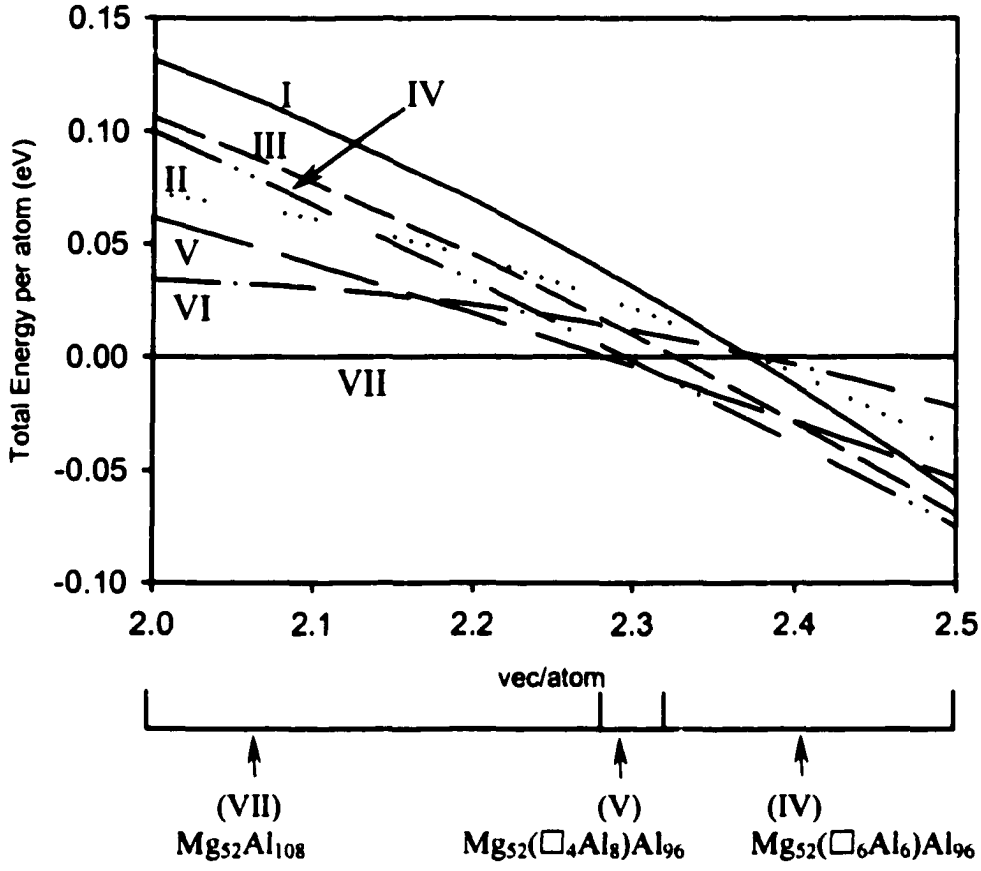

Figure 8. Variations in total energy per atom with *vec* for various R-phase models including vacancies at the M4 sites. The seven models are summarized in Table 9. Below the graph, the lowest energy vacancy model is labeled over the range of *vec* plotted.

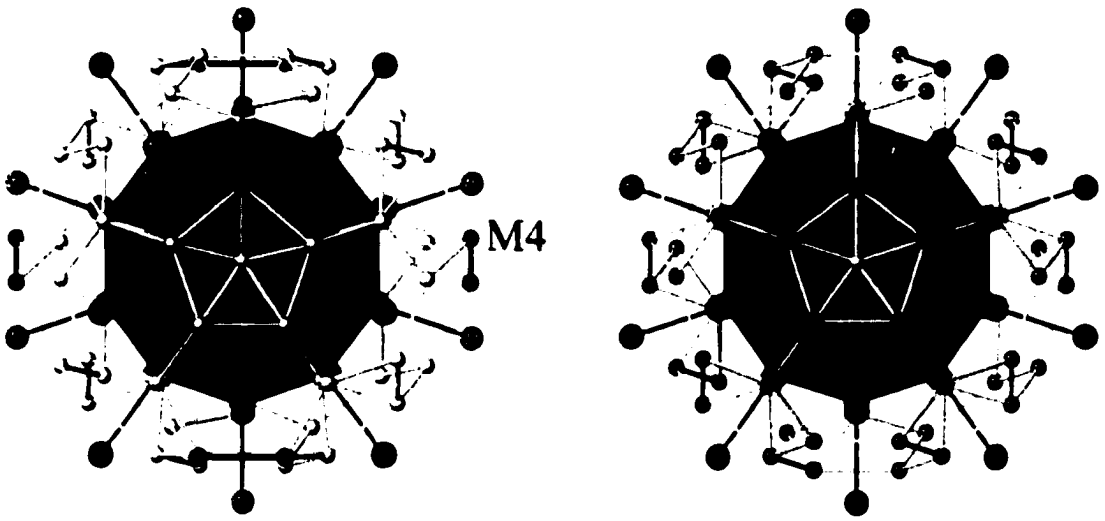

Figure 9. (a) A fragment of the R-phase structure (point group T_h) showing three shells of M sites and two shells of A sites projected down a pseudo 5-fold axis [$\sqrt{3}$, 1, 0]. (b) The same fragment as in (a) with the point group of I_h (the average interatomic distances were obtained from the R-phase structure).

Table 1. Summary of reaction compositions and products identified by Guinier X-ray powder diffraction and single crystal X-ray diffraction for various Mg:Zn:Al reactions.

I.Guinier Powder X-ray			
Reactions	x	Identified Phase[a]	mp. (K)[b]
1. $Mg_2(Zn_xAl_{1-x})_3$			
Mg_2Al_3	0.00	Mg_2Al_3 + Al	722.2
Mg_2Zn_2Al	0.33	R-phase + Zn	790.5
Mg_2ZnAl_2	0.67	R-phase + Al	780.8
Mg_2Zn_3	1.00	$MgZn_2$ + Al(tr)	NA
2. $Mg_{1.63}(Zn_xAl_{1-x})_{3.37}$			
$Mg_{1.63}Al_{3.37}$	0.00	$Mg_{17}Al_{12}$ + unknown phase	723.8
$Mg_{1.63}Zn_{0.64}Al_{2.73}$	0.19	R-Phase + $Mg_{17}Al_{12}$	722.6
$Mg_{1.63}Zn_{1.25}Al_{2.12}$	0.37	R-phase + Al(tr)	NA
$Mg_{1.63}Zn_{1.42}Al_{1.95}$	0.42	R-Phase	780.1
$Mg_{1.63}Zn_{1.72}Al_{1.65}$	0.51	R-Phase	763.2
$Mg_{1.63}Zn_{2.16}Al_{1.21}$	0.64	R-Phase	765.5
$Mg_{1.63}Zn_{2.76}Al_{0.61}$	0.82	$MgZn_2$ + Zn + R-phase	794.3
$Mg_{1.63}Zn_{3.37}$	1.00	$MgZn_2$ + Zn	834.9
II. Single Crystal Data			
Reaction	x	Crystal data	R1/wR2, %
3. $Mg_2(Zn_xAl_{1-x})_3$			
$Mg_2Zn_1Al_2$	0.33	$Mg_{1.76(1)}Zn_{1.46(3)}Al_{1.63(3)}$ (**3**) a = 14.364(3) Å	6.64/3.03
$Mg_2Zn_2Al_1$	0.67	$Mg_{1.73(1)}Zn_{2.46(6)}Al_{0.69(3)}$ (**1**) a = 14.131(1) Å	4.17/3.11
4. $Mg_{1.63}(Zn_xAl_{1-x})_{3.37}$			
$Mg_{1.63}Zn_{0.64}Al_{2.73}$	0.19	$Mg_{1.76(1)}Zn_{1.14(2)}Al_{1.97(2)}$ a = 14.412(1) Å	2.11/4/01
$Mg_{1.63}Zn_{1.42}Al_{1.95}$	0.42	$Mg_{1.76(1)}Zn_{1.76(1)}Al_{1.36(1)}$ a = 14.297(1) Å	2.42/3.19
$Mg_{1.63}Zn_{1.72}Al_{1.65}$	0.51	$Mg_{1.75(1)}Zn_{1.84(2)}Al_{1.31(1)}$ (**2**) a = 14.212(3) Å	2.27/3.40
$Mg_{1.63}Zn_{2.16}Al_{1.21}$	0.64	$Mg_{1.78(1)}Zn_{2.29(4)}Al_{0.81(4)}$ a = 14.138(1) Å	2.34/3.72

[a] All products identified by Guinier Powder X-ray diffraction.
[b] Only melting point of major phase is presented.
[c] tr = trace amounts

Table 2. Crystallographic data for three samples of "$Mg_{2-y}(Zn_xAl_{1-x})_{3+y}$" from single crystal X-ray diffraction.

Reactions	$Mg_2Zn_2Al_1$	$Mg_{1.64}Zn_{1.68}Al_{1.68}$	$Mg_2Zn_1Al_2$
Refined Composition	$Mg_{1.73(1)}Zn_{2.46(6)}Al_{0.69(3)}$ (1)	$Mg_{1.75(1)}Zn_{1.84(2)}Al_{1.31(1)}$ (2)	$Mg_{1.76(1)}Zn_{1.46(3)}Al_{1.63(3)}$ (3)
Space group, Z	$Im\bar{3}$, 32	$Im\bar{3}$, 32	$Im\bar{3}$, 32
Color of crystal	Silver	silver	silver
Temperature, K	298(2)	298(2)	163(2)
Formula wt (g/mol)	$7.08(6) \times 10^3$	$6.35(3) \times 10^3$	$5.82(5) \times 10^3$
a(Å)[a]	14.131(1)	14.212(3)	14.364(3)
V(Å^3)	2822.0(4)	2871(1)	2963(1)
d_{calc} (g/cm^3)	4.17(4)	3.67(2)	3.26(3)
Abs coeff. (mm^{-1})	16.69	11.58	9.419
F(000)	3327.0	2950.4	2765
θ_{min}, θ_{max} (°)	2.03, 28.93	2.03, 28.30	2.01, 28.23
Reflections collected	9324	5450	6350
Unique Data ($I \geq 2\sigma(I)$)	777	681	675
Radiation (Å)	0.71073	0.71073	0.71073
Refinement Method		Full-matrix least-squares on F^2	
R1, wR2 (all data)[b]	0.0417, 0.0311	0.0227, 0.0340	0.0664, 0.0303
Goodness-of-fit on F^2	0.986	1.012	0.924
Largest hole and peaks, e/Å^3	0.699 and –0.555	0.353 and –0.580	0.621 and –0.554

[a] From Guinier powder patterns (room temperature).

[b] $R1 = \sum|F_o - F_c| \Big/ \sum|F_o|$; $wR2 = \left[\sum\left[w\left(F_o^2 - F_c^2\right)^2\right] \Big/ \sum\left[w\left(F_o^2\right)^2\right]\right]^{1/2}$, $w = \sigma_F^{-2}$

Table 3. Atomic positional coordinates, isotropic displacement parameters ($Å^2$) and site occupancies for "$Mg_{2-y}(Zn_xAl_{1-x})_{3+y}$."

Atom	Site	x	y	z	U_{eq}[a]		Site occ.
$Mg_{1.73(1)}Zn_{2.46(6)}Al_{0.69(3)}$ **(1)**							
A1	12e	0.1991(1)	0	1/2	0.17(1)	Mg	1.000(1)
A2	16f	0.1862(1)	0.1862(1)	0.1862(1)	0.16(1)	Mg	1.000(1)
A3	24g	0	0.3005(1)	0.1167(1)	0.16(1)	Mg	1.000(1)
M1	24g	0	0.1795(1)	0.3074(1)	0.14(1)	Al	0.280(6)
						Zn	0.720(6)
M2	24g	0	0.929(1)	0.1514(1)	0.12(1)	Al	0.106(6)
						Zn	0.894(6)
M3	48h	0.1577(1)	0.1904(1)	0.4037(1)	0.15(1)	Al	0.268(5)
						Zn	0.732(5)
M4	12e	0.4032(1)	0	1/2	0.15(1)	Mg	0.27(2)
						Zn	0.40(1)
$Mg_{1.75(1)}Zn_{1.84(2)}Al_{1.31(1)}$ **(2)**							
A1	12e	0.1970(1)	1/2	0	0.016(1)	Mg	1.000(1)
A2	16f	0.1860(1)	0.1860(1)	0.1860(1)	0.015(1)	Mg	1.000(1)
A3	24g	0.1163(1)	0.3007(1)	0	0.015(1)	Mg	1.000(1)
M1	24g	0.3063(1)	0.1788(1)	0	0.013(1)	Al	0.521(2)
						Zn	0.479(2)
M2	24g	0.1508(1)	0.926(1)	0	0.011(1)	Al	0.136(3)
						Zn	0.864(3)
M3	48h	0.3088(1)	0.3422(1)	0.968(1)	0.014(1)	Al	0.542(2)
						Zn	0.458(2)
M4	12e	0.4021(1)	1/2	0	0.015(1)	Mg	0.34(2)
						Zn	0.28(1)
$Mg_{1.76(1)}Zn_{1.46(3)}Al_{1.63(3)}$ **(3)**							
A1	12e	0.1963(2)	0	1/2	0.010(1)	Mg	1.000(1)
A2	16f	0.1860(1)	0.1860(1)	0.1860(1)	0.010(1)	Mg	1.000(1)
A3	24g	0	0.3009(1)	0.1161(1)	0.011(1)	Mg	1.000(1)
M1	24g	0	0.1782(1)	0.3061(1)	0.010(1)	Al	0.672(5)
						Zn	0.328(5)
M2	24g	0	0.924(1)	0.1506(1)	0.009(1)	Al	0.159(5)
						Zn	0.841(5)
M3	48h	0.1578(1)	0.1915(1)	0.4034(1)	0.010(1)	Al	0.682(4)
						Zn	0.318(4)
M4	12e	0.4019(2)	0	1/2	0.010(1)	Mg	0.35(2)
						Zn	0.27(1)

[a] U_{eq} is defined as one third of the trace of the orthogonalized U_{ij} tensor.

Table 4. Selected interatomic distances (Å) for $Mg_{1.73(1)}Zn_{2.46(6)}Al_{0.69(3)}$ **(1)**, $Mg_{1.75(1)}Zn_{1.84(2)}Al_{1.31(1)}$ **(2)** and $Mg_{1.76(1)}Zn_{1.46(3)}Al_{1.63(3)}$ **(3)**.

		(1)	(2)	(3)
A1	A3 (2x)	3.059(1)	3.0754(9)	3.077(2)
	M1 (4x)	3.225(1)	3.2918(7)	3.311(2)
	M3 (4x)	3.050(1)	3.0927(7)	3.101(1)
	M3 (4x)	3.0797(5)	3.1162(4)	3.1227(7)
	M4	2.891(2)	2.933(2)	2.948(3)
	M4 (2x)	3.137(2)	3.147(1)	3.145(2)
A2	A2	3.133(3)	3.170(2)	3.178(4)
	A3 (3x)	3.248(1)	3.2806(6)	3.289(1)
	M1 (3x)	3.1491(5)	3.1698(4)	3.1750(6)
	M2 (3x)	2.991(1)	3.0196(9)	3.027(2)
	M3 (3x)	3.0935(8)	3.1150(6)	3.121(1)
	M3 (3x)	3.1089(9)	3.1339(6)	3.143(1)
A3	A3	3.306(3)	3.328(2)	3.329(3)
	M1	3.0351(8)	3.0517(6)	3.049(1)
	M1 (2x)	3.200(1)	3.228(1)	3.241(2)
	M2	2.981(1)	3.0170(9)	3.027(1)
	M2 (2x)	2.988(1)	3.0194(7)	3.028(2)
	M3 (2x)	3.111(1)	3.1376(8)	3.142(2)
	M3 (2x)	3.1235(8)	3.1597(5)	3.170(1)
	M4 (2x)	3.550(1)	3.5857(9)	3.590(2)
M1	M2	2.5286(7)	2.5418(5)	2.545(1)
	M3 (2x)	2.6225(5)	2.6551(4)	2.664(1)
	M3 (2x)	2.6793(6)	2.7170(5)	2.728(1)
	M4	2.9693(8)	3.0027(6)	3.007(1)
M2	M2	2.6330(9)	2.6487(6)	2.649(1)
	M2 (4x)	2.6491(6)	2.6651(4)	2.666(1)
M3	M3	2.7284(7)	2.7679(6)	2.6995(7)
	M3 (2x)	2.6767(4)	2.6928(4)	2.768(1)
	M4	2.9348(7)	2.9648(6)	2.970(1)
M4	M4	2.743(3)	2.801(2)	2.811(4)

Table 5. Summary of chemical compositions for single crystal and bulk materials from X-ray, neutron, and EDS experiments.

No.		Mg	Zn	Al	d(g/cm^3)	*vec*	Remarks
Single Crystal							
(1)	X-Ray	0.354(1)	0.504(1)	0.142(3)	4.17(4)[a]	2.14	2.2×10^{-2} mm^3
	EDS	0.350(6)	0.487(2)	0.163(3)		2.16	
(2)	X-Ray	0.359(1)	0.378(2)	0.268(1)	3.67(2)[a]	2.28	4.4×10^{-3} mm^3
	EDS	0.346(5)	0.384(2)	0.270(3)		2.27	
(3)	X-Ray	0.360(1)	0.299(3)	0.334(3)	3.26(3)[a]	2.32	1.3×10^{-2} mm^3
	EDS	0.397(5)	0.287(2)	0.316(3)		2.32	
Bulk Product							
		Mg	Zn	Al	d(g/cm^3)	*vec*	Remarks
(4)	neutron	0.35(2)	0.43(1)	0.22(1)	3.90(6)[b]	2.22	powder (< 100 mesh)
	EDS	0.32(1)	0.48(1)	0.20(1)	4.10(3)[c]	2.20	
(5)	neutron	0.36(1)	0.36(1)	0.28(1)	3.62(9)[b]	2.28	powder (< 100 mesh)
	EDS	0.34(1)	0.40(2)	0.26(2)	3.75(4)[c]	2.26	
(6)	neutron	0.36(1)	0.28(1)	0.36(1)	3.25(6)[b]	2.36	powder (< 100 mesh)
	EDS	0.36(1)	0.30(2)	0.34(2)	3.4(1)[c]	2.34	

[a] Calculated density from single crystal X-ray data.

[b] Calculated density from neutron diffraction data.

[c] Pycnometer measurements.

Table 6. Crystallographic Data for "$Mg_{1.63}(Zn_xAl_{1-x})_{3.37}$" from neutron powder diffraction.

Reactions	$Mg_{1.63}Zn_{2.16}Al_{1.21}$	$Mg_{1.63}Zn_{1.72}Al_{1.65}$	$Mg_{1.63}Zn_{1.21}Al_{2.16}$
Refined Composition	$Mg_{1.73(1)}Zn_{2.06(3)}Al_{1.09(3)}$ (4)	$Mg_{1.75(1)}Zn_{1.76(5)}Al_{1.34(6)}$ (5)	$Mg_{1.76(1)}Zn_{1.34(5)}Al_{1.76(5)}$ (6)
Space group, Z	$Im\bar{3}$, 32	$Im\bar{3}$, 32	$Im\bar{3}$, 32
Color	gray powder	gray powder	gray powder
Temperature, K	10(2)	10(2)	10(2)
Formula wt (g/mol)	$6.6(1) \times 10^3$	$6.2(2) \times 10^3$	$5.7(1) \times 10^3$
A(Å)	14.11247(6)	14.1804(1)	14.2697(1)
V(Å^3)	2810.66(2)	2851.48(5)	2905.66(4)
d_{calc} (g/cm^3)	3.90(6)	3.62(9)	3.25(6)
d_{exp} (g/cm^3)	4.10(3)	3.75(4)	3.4(1)
Scattering angle	145.88°	145.88°	145.88°
d-spacing range, Å	0.8-2.8	0.8-2.8	0.8-2.8
No. data points	4335	4335	4335
No. Bragg reflections	610	687	689
No. parameters	53	56	56
R_p, R_{wp} (%)	4.28, 5.89	3.95, 5.36	4.62, 6.18
Goodness of fit (χ)[b]	1.43	1.53	1.71

[a] $R_p = \sum|Y_o - Y_c| \Big/ \sum|Y_o|$; $R_{wp} = \left[\sum\left[w\left(Y_o^2 - Y_c^2\right)^2\right] \Big/ \sum\left[w\left(Y_o^2\right)^2\right]\right]^{1/2}$, Y_o and Y_c are observed and calculated counts.

[b] $\chi = \left[\sum\left[w\left(Y_o^2 - Y_c^2\right)^2\right] \Big/ (N_{obs} - N_{var})\right]^{1/2}$, N_{obs} is the number of observations and N_{var} is the number of parameters.

Table 7. Atomic positions, U_{eq}(× 100 Å^2)[a] and site occupancies for refined structures of $Mg_{1.73(1)}Zn_{2.06(3)}Al_{1.09(3)}$ (**4**), $Mg_{1.75(1)}Zn_{1.76(5)}Al_{1.34(6)}$ (**5**) and $Mg_{1.76(1)}Zn_{1.34(5)}Al_{1.76(5)}$ (**6**) from neutron powder diffraction.

atom	Site	x	y	z	U_{eq}		Site occ.
$Mg_{1.73(1)}Zn_{2.06(3)}Al_{1.09(3)}$ (**4**)							
A1	12e	0.2022(3)	1/2	0	0.94(8)	Mg	1.00(1)
A2	16f	0.1861(2)	0.1861(2)	0.1861(2)	0.93(8)	Mg	1.00(1)
A3	24g	0.1190(2)	0.3011(2)	0	0.75(5)	Mg	1.00(1)
M1	24g	0.3100(2)	0.1772(2)	0	0.76(5)	Al	0.48(1)
						Zn	0.52(1)
M2	24g	0.1527(2)	0.0941(3)	0	0.77(5)	Al	0.25(1)
						Zn	0.75(1)
M3	48h	0.3137(2)	0.3411(2)	0.0962(2)	0.79(4)	Al	0.36(1)
						Zn	0.64(1)
M4	12e	0.4075(4)	1/2	0	0.7(1)	Mg	0.27(2)
						Zn	0.40(1)
$Mg_{1.75(1)}Zn_{1.76(5)}Al_{1.34(6)}$ (**5**)							
A1	12e	0.1970(5)	1/2	0	1.0(1)	Mg	1.00(2)
A2	16f	0.1866(2)	0.1866(2)	0.1866(2)	1.0(1)	Mg	1.00(2)
A3	24g	0.1191(3)	0.2999(3)	0	1.08(8)	Mg	1.00(1)
M1	24g	0.3090(4)	0.1769(3)	0	0.62(9)	Al	0.53(2)
						Zn	0.47(2)
M2	24g	0.1516(3)	0.0933(4)	0	0.69(9)	Al	0.14(2)
						Zn	0.86(2)
M3	48h	0.3132(3)	0.3396(3)	0.0971(3)	0.73(7)	Al	0.56(2)
						Zn	0.44(2)
M4	12e	0.4076(7)	1/2	0	0.7(2)	Mg	0.34(2)
						Zn	0.28(1)
$Mg_{1.76(1)}Zn_{1.34(5)}Al_{1.76(5)}$ (**6**)							
A1	12e	0.1944(7)	1/2	0	1.0(1)	Mg	1.00(1)
A2	16f	0.1852(2)	0.1852(2)	0.1852(2)	1.0(1)	Mg	1.00(1)
A3	24g	0.1177(4)	0.2994(4)	0	1.14(7)	Mg	1.00(1)
M1	24g	0.3084(4)	0.1805(4)	0	0.82(8)	Al	0.70(2)
						Zn	0.30(2)
M2	24g	0.1515(3)	0.0924(4)	0	0.74(8)	Al	0.27(2)
						Zn	0.73(2)
M3	48h	0.3103(3)	0.3415(4)	0.0972(4)	0.82(6)	Al	0.69(1)
						Zn	0.31(1)
M4	12e	0.4045(8)	1/2	0	0.8(2)	Mg	0.35(2)
						Zn	0.27(1)

[a] $U_{eq} = (1/3)\sum_i\sum_j U_{ij}a^i a^j a_i a_j$

Table 8. Bond lengths (Å) for $Mg_{1.73(1)}Zn_{2.06(3)}Al_{1.09(3)}$ **(4)**, $Mg_{1.75(1)}Zn_{1.76(5)}Al_{1.34(6)}$ **(5)** and $Mg_{1.76(1)}Zn_{1.34(5)}Al_{1.76(5)}$ **(6)** with estimated standard deviations in parentheses.

		(4)	(5)	(6)
A1	A3 (2x)	3.039(3)	3.046(4)	3.073(4)
	M1 (4x)	3.179(4)	3.245(6)	3.259(6)
	M3 (4x)	3.060(4)	3.128(6)	3.124(6)
	M3 (4x)	3.021(3)	3.031(4)	3.084(4)
	M4	2.898(7)	2.99(1)	3.00(1)
	M4 (2x)	3.136(5)	3.086(8)	3.103(7)
A2	A2	3.114(7)	3.12(1)	3.198(9)
	A3 (3x)	3.232(2)	3.240(3)	3.254(3)
	M1 (3x)	3.158(2)	3.168(3)	3.179(3)
	M2 (3x)	2.972(3)	2.999(5)	2.999(4)
	M3 (3x)	3.102(3)	3.089(5)	3.116(5)
	M3 (3x)	3.092(3)	3.089(5)	3.123(5)
A3	A3	3.361(6)	3.38(1)	3.350(9)
	M1	3.212(4)	3.209(7)	3.228(7)
	M1 (2x)	3.016(3)	3.027(5)	3.058(4)
	M2	2.964(4)	2.965(6)	2.995(6)
	M2 (2x)	2.994(4)	3.003(5)	3.006(4)
	M3 (2x)	3.117(4)	3.129(6)	3.145(6)
	M3 (2x)	3.052(2)	3.082(4)	3.133(4)
	M4 (2x)	3.522(3)	3.552(5)	3.577(5)
M1	M2	2.508(5)	2.527(8)	2.571(7)
	M3 (2x)	2.684(4)	2.687(6)	2.697(5)
	M3 (2x)	2.606(3)	2.639(5)	2.638(5)
	M4	2.935(4)	2.962(6)	2.985(5)
M2	M2	2.665(3)	2.657(5)	2.660(4)
	M2 (4x)	2.652(7)	2.65(1)	2.634(9)
M3	M3	2.718(5)	2.755(9)	2.781(8)
	M3 (2x)	2.678(2)	2.668(4)	2.679(4)
	M4	2.934(4)	2.977(6)	2.988(6)
M4	M4	2.62(1)	2.62(2)	2.69(2)

Table 9. Models of $Mg_{52}(Al_w\square_{1-w})_{12}Al_{96}$ (w = 0-1). □ denotes a vacancy on the M4 site.

Model	Formula	M4–M4 contact		
		Al–Al	Al–□	□–□
I	$Mg_{52}(\square_{12}Al_0)Al_{96}$	0	0	6
II	$Mg_{52}(\square_8Al_4)Al_{96}$	2	0	4
III	$Mg_{52}(\square_8Al_4)Al_{96}$	0	4	2
IV	$Mg_{52}(\square_6Al_6)Al_{96}$	0	6	0
V	$Mg_{52}(\square_4Al_8)Al_{96}$	4	0	2
VI	$Mg_{52}(\square_4Al_8)Al_{96}$	2	4	0
VII	$Mg_{52}(\square_0Al_{12})Al_{96}$	6	0	0

Supplementary Materials

Appendix 1.

(a) X-ray single crystal data and structure refinements for $Mg_{1.73(1)}Zn_{2.46(2)}Al_{0.69(2)}$ (1), $Mg_{1.75(1)}Zn_{1.84(2)}Al_{1.31(1)}$ (2) and $Mg_{1.76(1)}Zn_{1.46(6)}Al_{1.63(3)}$ (3).

Compound	(1)	(2)	(3)
I. Crystal Data.			
form wt (g/mol)	7.08(6)x10^3	6.35(3)x10^3	5.82(2)x10^3
Color, habit	silver, needle	silver, needle	silver, needle
Crystal size, mm	0.03 x 0.05 x 0.1	0.13 x 0.13 x 0.25	0.07 x 0.02 x 0.02
Crystal system	Cubic	Cubic	Cubic
Space group	*Im*$\bar{3}$	*Im*$\bar{3}$	*Im*$\bar{3}$
a(Å)[a]	14.131(1)	14.212(3)	14.364(3)
V(Å^3)	2822.0(4)	2871(1)	2963(1)
d_{calc} (g/cm^3)	4.17(3)	3.67(2)	3.26(3)
Abs coeff. (mm^{-1})	16.69	11.58	9.419
F(000)	3327.0	2950.4	2765
II. Data Collections.			
Diffractometer	Siemens Smart CCD		
Radiation (Å)	0.71073	0.71073	0.71073
Temperature, K	298(2)	298(2)	163(2)
θ_{min}, θ_{max} (°)	2.03, 28.93	2.03, 28.30	2.01, 28.23
hkl range			
h	-10, 18	-10, 18	-18,18,
k	-18, 18	-6, 19	-18, 18,
l	-18, 16	-18, 15	-8, 17
Reflections collected	9324	5450	6350
Unique Data	777	681	675
Absorption corrections	SADABS	SADABS	SADABS
Transmission range	0.43, 1.0	0.61, 1.0	0.54, 0.86
III. Solution and Refinement.			
Structure solution	Direct methods		
Refinement Method	Full-matrix least-squares on F^2		
Goodness-of-fit on F^2	0.986	1.012	0.962
R1, wR2 ($I>2\sigma_I$)[b]	0.0209, 0.0388	0.0168, 0.0326	0.0262, 0.0277
R1, wR2 (all data)	0.0417, 0.0311	0.0227, 0.0340	0.0664, 0.0303
Extinction coefficient	0.00086(3)	0.00020(2)	0.00005(1)
($\Delta\rho$) max, min (e/Å^3)	0.699, -0.555	0.353, –0.580	0.621, –0.554

[a] From Guinier powder pattern (room temperature).

[b] $R1 = \sum\|F_o - F_c\| / \sum|F_o|$; $wR2 = \left[\sum\left[w(F_o^2 - F_c^2)^2\right] / \sum\left[w(F_o^2)^2\right]\right]^{1/2}$, $w = \sigma_F^{-2}$

Appendix 1. (Continued)

(b) Anisotropic displacement parameters ($Å^2 x\ 10^3$) for "$Mg_{2-y}(Zn_xAl_{1-x})_{3+y}$" from X-ray single crystal data. The anisotropic displacement factor exponent takes the form: $-2\pi^2[h^2 a^2 U_{11} + ... + 2\ h\ k\ a\ b\ U_{12}]$

		U_{11}	U_{22}	U_{33}	U_{23}	U_{13}	U_{12}
$Mg_{1.73(1)}Zn_{2.46(2)}Al_{0.69(2)}$ **(1)**							
A1	12e	15(1)	21(1)	16(1)	0	0	0
A2	16f	16(1)	16(1)	16(1)	-1(1)	-1(1)	-1(1)
A3	24g	15(1)	16(1)	16(1)	-3(1)	0	0
M1	24g	14(1)	15(1)	15(1)	-3(1)	0	0
		14(1)	15(1)	15(1)	-3(1)	0	0
M2	24g	12(1)	12(1)	12(1)	0(1)	0	0
M3	48h	13(1)	18(1)	15(1)	1(1)	-1(1)	1(1)
$Mg_{1.75(1)}Zn_{1.84(2)}Al_{1.31(1)}$ **(2)**							
A1	12e	13(1)	14(1)	21(1)	0	0	0
A2	16f	15(1)	15(1)	15(1)	-1(1)	-1(1)	-1(1)
A3	24g	16(1)	14(1)	15(1)	0	0	-2(1)
M1	24g	13(1)	14(1)	13(1)	0	0	-3(1)
M2	24g	11(1)	11(1)	11(1)	0	0	-1(1)
M3	48h	16(1)	11(1)	13(1)	-1(1)	1(1)	1(1)
$Mg_{1.76(1)}Zn_{1.46(6)}Al_{1.63(3)}$ **(3)**							
A1	12e	7(1)	13(2)	11(1)	0	0	0
A2	16f	10(1)	10(1)	10(1)	-1(1)	-1(1)	-1(1)
A3	24g	9(1)	10(1)	12(1)	-3(1)	0	0
M1	24g	10(1)	10(1)	11(1)	-2(1)	0	0
M2	24g	10(1)	9(1)	9(1)	0	0	0
M3	48h	9(1)	12(1)	10(1)	1(1)	-1(1)	1(1)

Appendix 2.

(a) Analysis of Guinier Powder X-ray Diffraction Film of "Mg_2Zn_2Al"

- Input reflections were corrected by interpolation of Si Lines
- Wavelength used is 1.54180 Å
- Single Crystal data $Mg_{1.73(1)}Zn_{2.46(2)}Al_{0.69(2)}$ **(1)**

Space group	$Im\bar{3}$
a	14.131(1)
V(Å^3)	2822.0(4)
Error of fit	2.535

Refl #	h	k	l	J	I	$\sin^2 x10^3$	d calc.	2θ calc.	2θ corr.	diff.
1	1	1	0	12	779.9	5.95	9.9924	8.85	8.89	-0.04
2	2	1	1	24	232.4	17.86	5.7691	15.36	15.36	0
3	3	1	0	12	104.4	29.76	4.4687	19.87	19.87	0
4	2	3	1	24	267.8	41.66	3.7768	23.56	23.59	-0.04
5	3	3	0	12	61.2	53.57	3.3308	26.76	26.73	0.03
6	2	4	0	12	71	59.52	3.1599	28.24	28.22	0.02
7	5	1	0	12	25.2	77.38	2.7714	32.3	32.29	0.01
8	3	5	0	12	671.7	101.18	2.4235	37.1	37.08	0.02
9	6	0	0	6	320.6	107.13	2.3552	38.21	38.21	0
10	5	3	2	24	1000	113.09	2.2924	39.3	39.29	0.01
11	6	3	1	24	588.3	136.89	2.0836	43.43	43.41	0.02
12	5	4	3	24	405.5	148.8	1.9985	45.38	45.38	0
13	4	6	0	12	182.2	154.75	1.9597	46.33	46.31	0.02
14	7	2	1	24	93.4	160.7	1.923	47.27	47.25	0.02
15	6	4	2	24	13.6	166.65	1.8884	48.19	48.19	0
16	5	6	1	24	76.5	184.51	1.7947	50.88	50.85	0.02
17	4	7	1	24	69.8	196.41	1.7395	52.61	52.59	0.02
18	8	5	3	24	350.6	291.64	1.4275	65.37	65.35	0.02
19	10	0	0	6	99.4	297.6	1.4131	66.12	66.1	0.02
20	5	9	0	12	44.2	315.45	1.3726	68.34	68.32	0.02
21	5	9	2	24	91.8	327.36	1.3474	69.8	69.78	0.02
22	10	4	0	12	43	345.21	1.3121	71.97	72.01	-0.05
23	6	9	1	24	40.2	351.16	1.3009	72.68	72.71	-0.02
24	9	5	4	24	66	363.07	1.2794	74.11	74.15	-0.04
25	5	10	1	24	9.3	374.97	1.2589	75.52	75.56	-0.04

Appendix 2. (Continued)

(b) Analysis of Guinier Powder X-ray Diffraction Film of "$Mg_{1.625}Zn_{1.688}Al_{1.687}$"

- Input reflections were corrected by interpolation of Si Lines
- Wavelength used is 1.54180 Å
- Single Crystal data $Mg_{1.75(1)}Zn_{1.84(2)}Al_{1.31(1)}$ **(2)**

Space group	$Im\bar{3}$
a	14.212(3)
V(Å^3)	2871(1)
Error of fit	5.529

Refl #	h k l	J	I	$\sin^2 x10^3$	d calc.	2θ calc.	2θ corr.	diff.
1	2 1 1	24	231.4	17.65	5.8021	15.27	15.22	0.05
2	3 1 0	12	104	29.42	4.4943	19.75	19.66	0.09
3	2 3 1	24	266.9	41.19	3.7984	23.42	23.36	0.06
4	2 4 0	12	70.8	58.84	3.1779	28.08	28.03	0.05
5	5 1 0	12	25.1	76.5	2.7872	32.11	32.09	0.02
6	3 5 0	12	671.5	100.04	2.4374	36.88	36.81	0.06
7	6 0 0	6	320.6	105.92	2.3687	37.99	37.96	0.02
8	5 3 2	24	1000	111.8	2.3055	39.07	39.03	0.04
9	6 3 1	24	588.8	135.34	2.0955	43.17	43.11	0.06
10	5 4 3	24	406	147.11	2.0099	45.11	45.07	0.03
11	4 6 0	12	182.5	153	1.9709	46.05	46.03	0.02
12	7 2 1	24	93.5	158.88	1.934	46.98	46.95	0.03
13	5 6 1	24	76.7	182.42	1.8049	50.57	50.51	0.06
14	4 7 1	24	70	194.19	1.7494	52.29	52.27	0.03
15	8 5 3	24	350.9	288.34	1.4356	64.96	64.98	-0.02
16	10 0 0	6	99.5	294.22	1.4212	65.7	65.78	-0.08
17	5 9 0	12	44.2	311.88	1.3804	67.9	67.99	-0.09
18	5 9 2	24	91.8	323.64	1.3551	69.35	69.37	-0.03
19	5 10 1	24	9.3	370.72	1.2661	75.02	75.09	-0.07

Appendix 2. (Continued)

(c) Analysis of Guinier Powder X-ray Diffraction Film of "Mg_2ZnAl_2"

- Input reflections were corrected by interpolation of Si Lines
- Wavelength used is 1.54180 Å
- Single Crystal data $Mg_{1.76(1)}Zn_{1.46(6)}Al_{1.63(3)}$ **(3)**

Space group	$Im\bar{3}$
a	14.364(3)
V(Å^3)	2963(1)
Error of fit	4.943

Refl #	h k l	J	I	$\sin^2 x10^3$	d calc.	2θ calc.	2θ corr.	diff.
1	2 1 1	24	229.4	17.28	5.8641	15.11	15.07	0.04
2	2 3 1	24	265.3	40.32	3.839	23.17	23.12	0.05
3	5 1 0	12	25.1	74.89	2.817	31.76	31.75	0.02
4	3 5 0	12	671.1	97.93	2.4634	36.47	36.43	0.04
5	6 0 0	6	320.5	103.69	2.394	37.57	37.54	0.03
6	5 3 2	24	1000.0	109.45	2.3302	38.64	38.65	-0.01
7	6 3 1	24	589.8	132.49	2.1179	42.69	42.66	0.03
8	7 1 0	12	176.8	144.02	2.0314	44.6	44.57	0.03
9	4 6 0	12	182.9	149.78	1.9919	45.54	45.51	0.03
10	7 2 1	24	93.8	155.54	1.9547	46.45	46.42	0.04
11	6 4 2	24	13.7	161.3	1.9195	47.36	47.35	0.01
12	5 6 1	24	77.0	178.58	1.8242	50	49.97	0.02
13	4 7 1	24	70.3	190.1	1.7681	51.7	51.69	0.00
14	8 5 3	24	351.6	282.27	1.451	64.19	64.16	0.03
15	10 0 0	6	99.6	288.03	1.4364	64.92	64.9	0.01
16	5 9 0	12	44.2	305.31	1.3952	67.08	67.07	0.02
17	6 7 5	24	88.7	316.83	1.3696	68.51	68.5	0.01
18	9 5 4	24	65.9	351.4	1.3005	72.71	72.75	-0.04
19	6 10 0	12	212.8	391.72	1.2317	77.49	77.66	-0.17

Appendix 3.

(a) Crystallographic Data from neutron diffraction study of $Mg_{1.73(1)}Zn_{2.06(3)}Al_{1.09(3)}$ (**4**), $Mg_{1.75(1)}Zn_{1.76(5)}Al_{1.34(6)}$ (**5**), $Mg_{1.76(1)}Zn_{1.34(5)}Al_{1.76(5)}$ (**6**).

Compound	(4)	(5)	(6)
I. Crystal data			
form wt (g/mol)	$6.7(3)\times10^3$	$6.2(5)\times10^3$	$5.7(2)\times10^3$
Cell system	Cubic	Cubic	Cubic
Space group	$Im\bar{3}$	$Im\bar{3}$	$Im\bar{3}$
a(Å)	14.11247(6)	14.1804(1)	14.2697(1)
V(Å^3)	2810.66(2)	2851.48(5)	2905.66(4)
d_{calc} (g/cm^3)	3.90(6)	3.62(9)	3.25(6)
Specimen shape, color	powder, gray	powder, gray	powder, gray
Radiation type	neutron	neutron	neutron
Temperature, K		10(2)	
II. Data Collection			
Diffractometer		GPPD	
Data collection method		Time-of-flight scans	
Specimen mounting		Vanadium can	
Structure refinements		GSAS	
Profile function		Pseudo-Voigt	
Background function		polynomial function with 6 variables	
Scattering angle		145.88°	
d-spacing range, Å		0.8-2.8	
Data points		4335	
R_p, R_{wp} (%)[a]	4.28, 5.89	3.95, 5.36	4.62, 6.18
Goodness of fit (χ)[b]	1.43	1.53	1.71
Diffraction	610	687	689
Variable parameters	53	55	55

[a] $R_p = \sum|Y_o - Y_c| / \sum|Y_o|$; $R_{wp} = \left[\sum\left[w\left(Y_o^2 - Y_c^2\right)^2\right] / \sum\left[w\left(Y_o^2\right)^2\right]\right]^{1/2}$, Y_o and Y_c are observed and calculated counts.

[b] $\chi = \left[\sum\left[w\left(Y_o^2 - Y_c^2\right)^2\right] / (N_{obs} - N_{var})\right]^{1/2}$, N_{obs} is the number of observations and N_{var} is the number of parameters.

Appendix 3. (Continued)

(b) Anisotropic thermal displacement parameters (U^{ij} x 100 Å^2) for Rietveld-refined structure for "$Mg_{2-y}(Zn_xAl_{1-x})_{3+y}$" (**4-6**)from neutron powder diffraction.

I. $Mg_{1.73(1)}Zn_{2.06(3)}Al_{1.09(3)}$ (**4**)

atom	site	U_{11}	U_{22}	U_{33}	U_{12}	U_{13}	U_{23}
A1	12e	1.4(3)	0.7(2)	0.7(2)	0	0	0
A2	16f	0.93(8)	0.93(8)	0.93(8)	-0.1(1)	-0.1(1)	-0.1(1)
A3	24g	1.0(2)	0.7(2)	0.6(1)	-0.3(1)	0	0

II. $Mg_{1.75(1)}Zn_{1.76(5)}Al_{1.34(6)}$ (**5**)

atom	site	U_{11}	U_{22}	U_{33}	U_{12}	U_{13}	U_{23}
A1	12e	1.5(5)	0.8(4)	0.6(4)	0	0	0
A2	16f	0.9(1)	0.9(1)	0.9(1)	-0.1(2)	-0.1(2)	-0.1(2)
A3	24g	1.1(3)	0.7(2)	0.5(2)	-0.3(2)	0	0

III. $Mg_{1.76(1)}Zn_{1.34(5)}Al_{1.76(5)}$ (**6**)

atom	site	U_{11}	U_{22}	U_{33}	U_{12}	U_{13}	U_{23}
A1	12e	1.8(4)	0.7(3)	1.8(4)	0	0	0
A2	16f	0.9(1)	0.9(1)	0.9(1)	-0.4(1)	-0.4(1)	-0.4(1)
A3	24g	2.4(3)	1.2(2)	0.8(2)	-1.9(2)	0	0

Appendix 4. COOP curves of Mg-Mg, Mg-M and M-M contacts from theoretical calculations of "$Mg_{52}Al_{108}$". The Fermi levels with their *vec* values are labeled. The value in the parentheses are overlap coefficients.

(a) Mg-Mg contacts

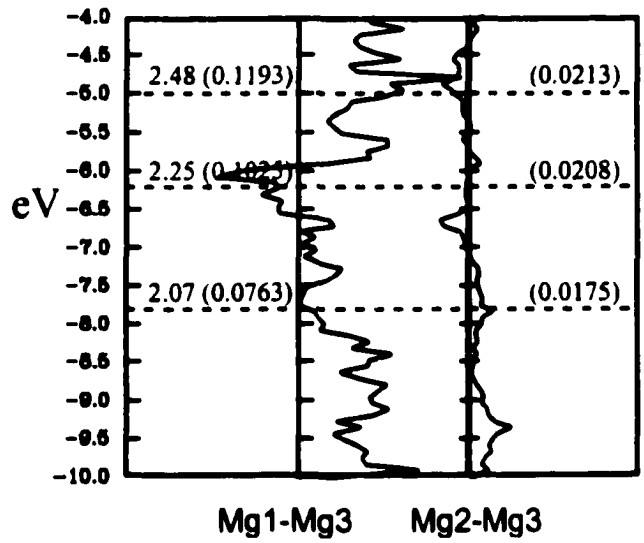

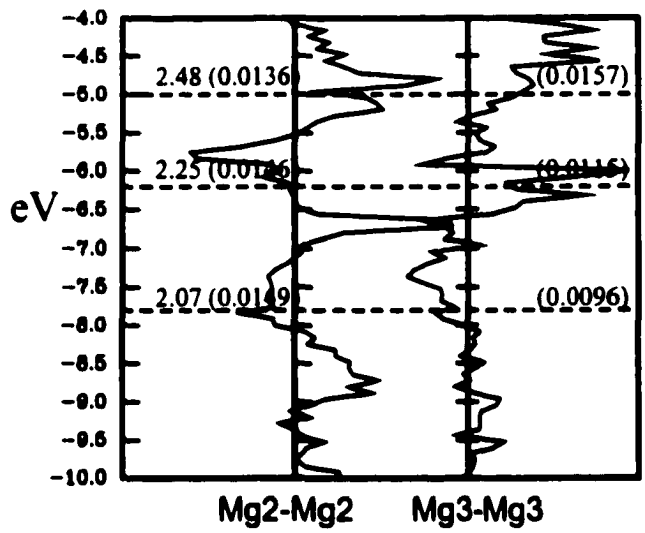

Appendix 4. (Continued)

(b) Mg-M contacts

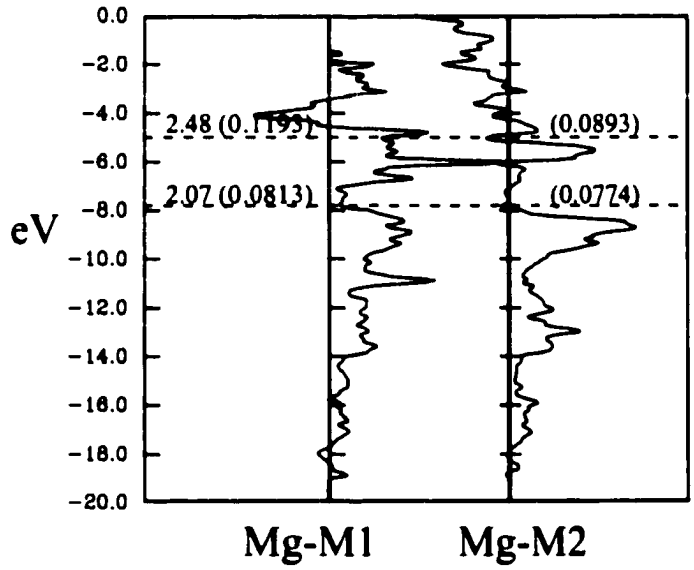

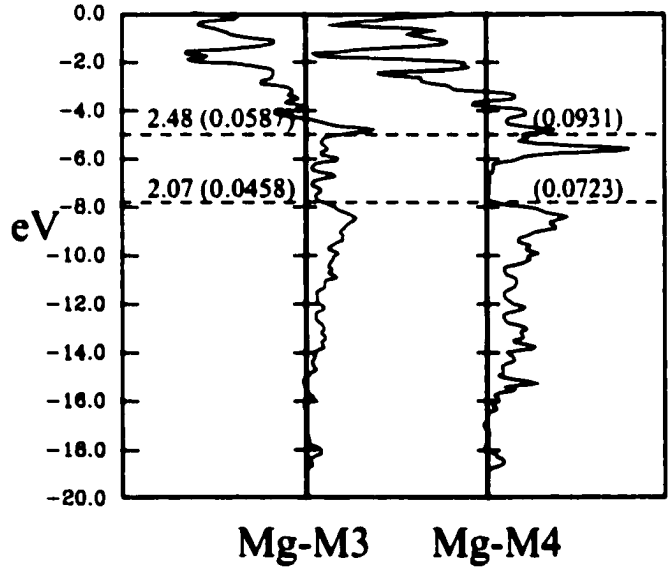

Appendix 4. (Continued)

(c) M-M contacts

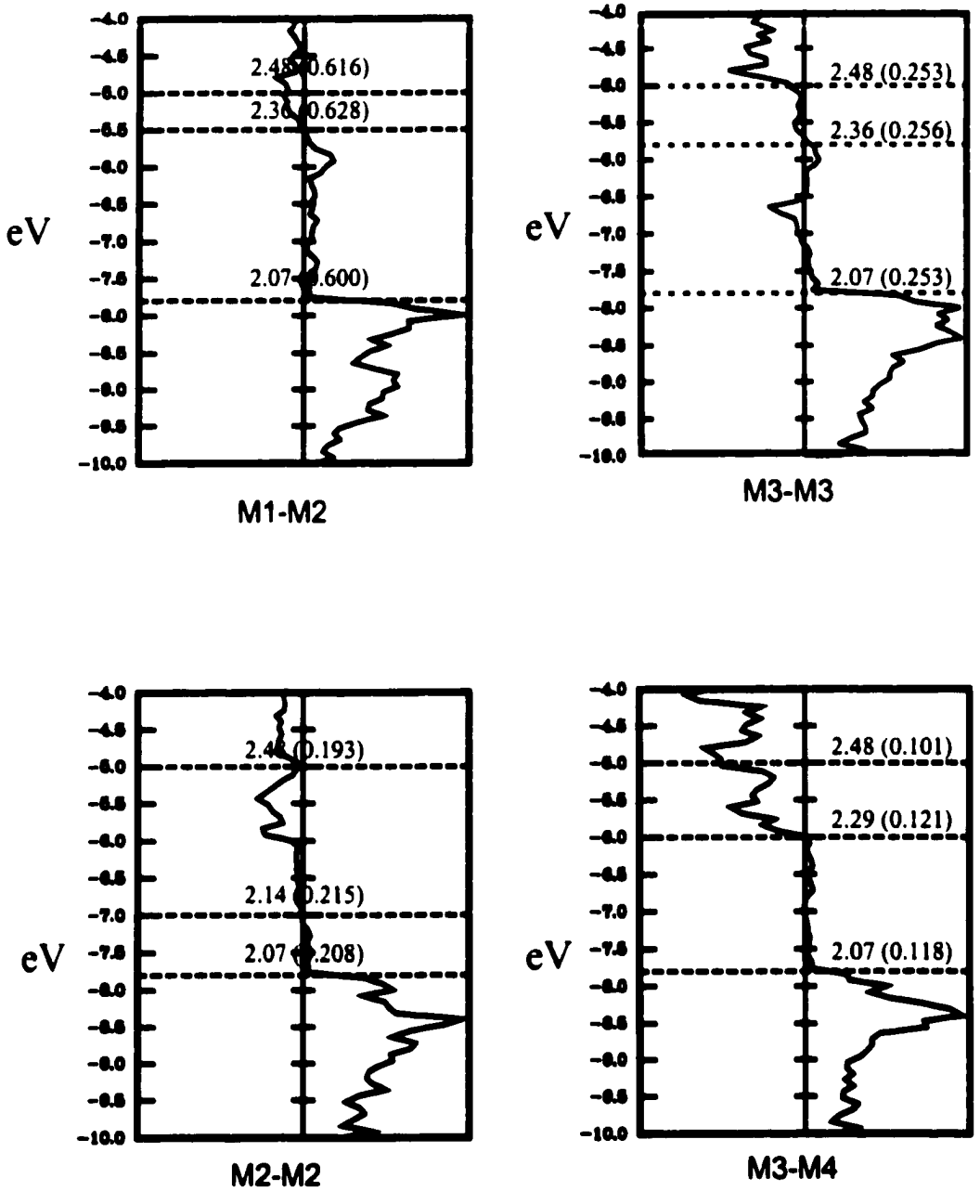

Appendix 4. (Continued)

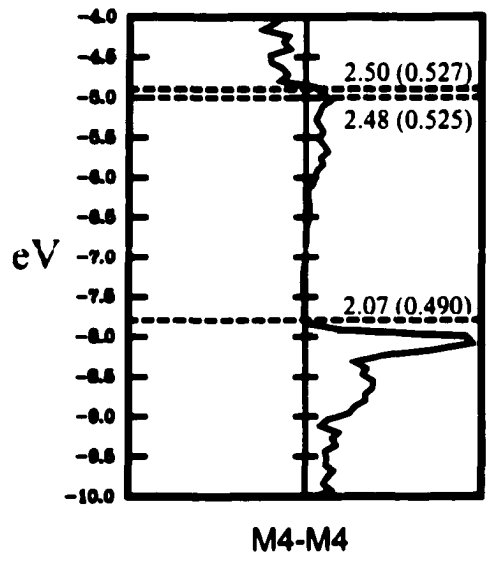

M4-M4

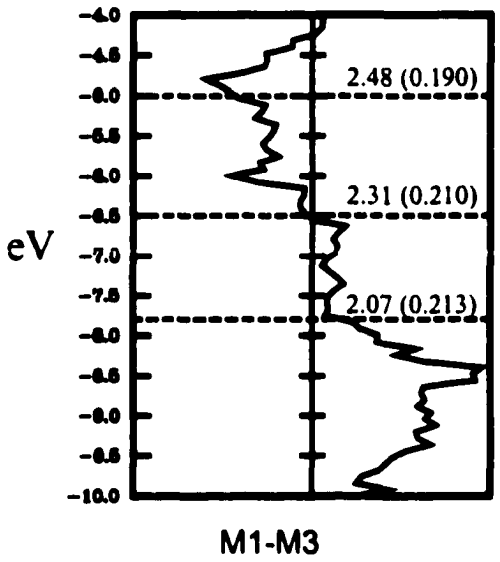

M1-M3

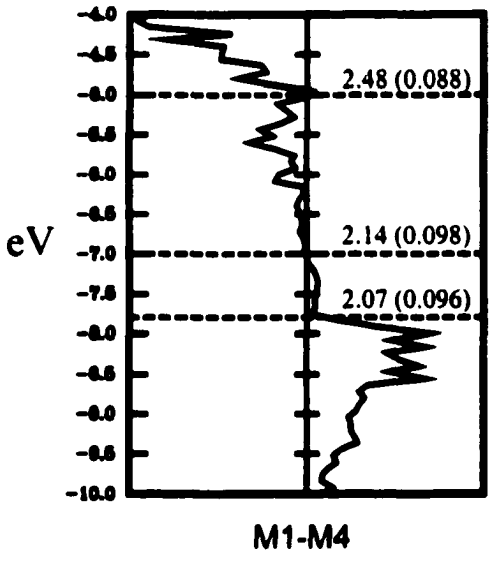

M1-M4

Appendix 5. Magnetic susceptibility measurements of "$Mg_{1.625}Zn_{1.25}Al_{2.125}$", "$Mg_{1.625}Zn_{1.688}Al_{1.687}$" and "$Mg_{1.625}Zn_{2.125}Al_{1.25}$". Two independent measurements were performed for each product.

(a)

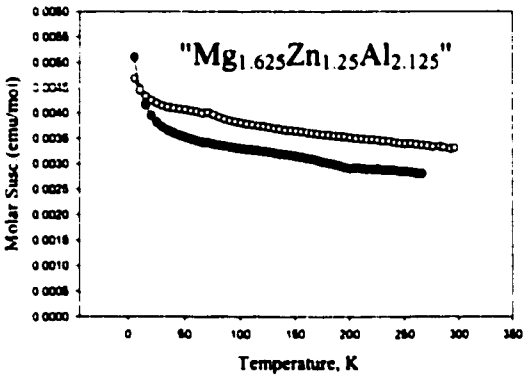

(b)

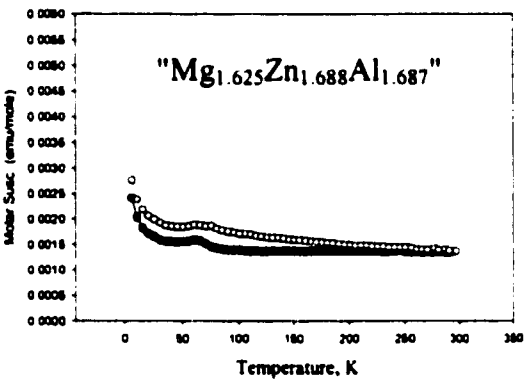

(c)

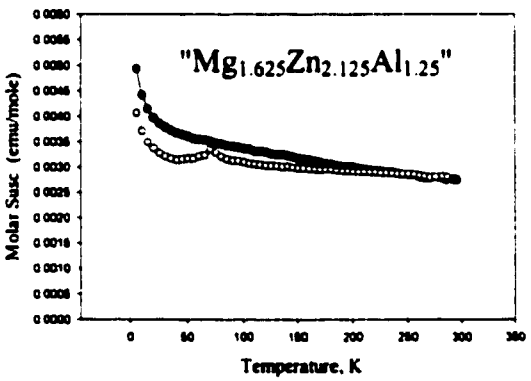

Appendix 6. Temperature-dependent Resistivity Measurements of "$Mg_{1.625}Zn_{1.25}Al_{2.125}$" under zero and 5.5 T of magnetic field.

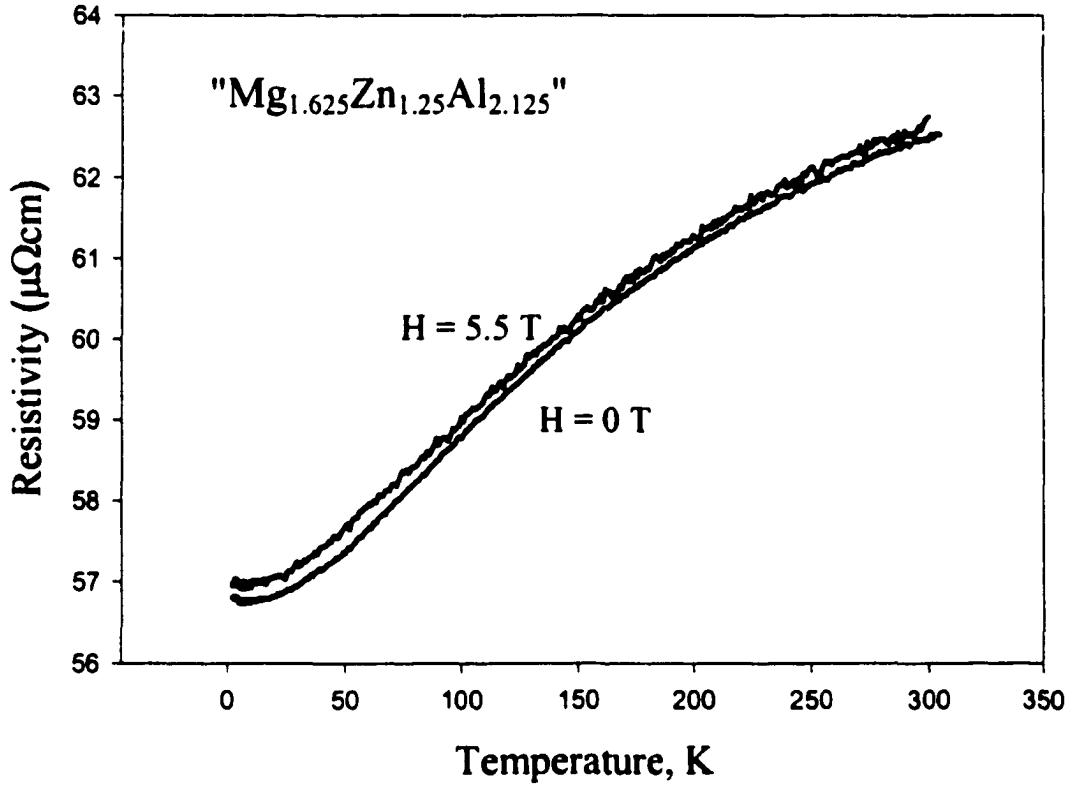

Appendix 7. The composition of M4 site from neutron data using different models of Mg/Zn/Al/v combinations. The model in bold characters is the best model to match EDS experiment. (v: vacancy, NA: the model has no meaningful solution)

	Atomic Composition			*vec*	#atom/cell	M4						
	Mg	Zn	Al			Mg	Zn	Al	Mg/Zn	Mg/Al	Zn/Al	Mg/Zn/Al/v
"$Mg_{0.33}Zn_{0.43}Al_{0.24}$"												
reaction	0.33	0.43	0.24	2.25	160							
neutron-1	**0.35**	**0.43**	**0.22**	**2.22**	**156**				**0.27/0.40**			
neutron-2										NA		
neutron-3	0.33	0.41	0.26	2.26	160						0.23/0.77	
neutron-4	0.39	0.40	0.21	2.21	157	0.75						
neutron-5	0.33	0.46	0.21	2.21	157		0.72					
neutron-6								NA				
neutron-7												
EDS	0.32	0.48	0.20	2.20								NA
"$Mg_{0.33}Zn_{0.335}Al_{0.335}$"												
reaction	0.33	0.335	0.335	2.34	160							
neutron-1	**0.36**	**0.36**	**0.28**	**2.28**	**155**				**0.34/0.28**			
neutron-2	0.34	0.34	0.32	2.32	160					0.27/0.73		
neutron-3											NA	
neutron-4	0.39	0.34	0.27	2.27	156	0.64						
neutron-5	0.34	0.39	0.27	2.27	156		0.67					
neutron-6	0.33	0.33	0.34	2.34	160			1				
neutron-7												
EDS	0.34	0.40	0.26	2.26								NA
"$Mg_{0.33}Zn_{0.24}Al_{0.43}$"												
reaction	0.33	0.450	0.43	2.43	160							
neutron-1	**0.36**	**0.28**	**0.36**	**2.36**	**155**				**0.35/0.27**			
neutron-2	0.35	0.25	0.40	2.40	160					0.67/0.33		
neutron-3											NA	
neutron-4	0.39	0.25	0.36	2.36	156	0.67						
neutron-5	0.33	0.31	0.36	2.36	156		0.63					
neutron-6	0.33	0.25	0.42	2.43	160			1				
neutron-7												
EDS	0.35	0.30	0.34	2.32								NA

CHAPTER 4

EXPERIMENTAL AND THEORETICAL STUDIES OF QUASICRYSTALLINE APPROXIMANTS IN LI-MG-ZN-AL SYSTEMS

A paper to be submitted to *Inorg. Chem.*
Chi-Shen Lee and Gordon J. Miller

Abstract

A series of ternary and quaternary R-phase compounds in the Li-Mg-Zn-Al system were synthesized from pure elements in sealed Ta tubes with starting compositions based on the suggestions from electronic structure calculations using relative Mulliken populations to quantify the site preference for the various elements. Single crystal structural analyses revealed new R-phase compounds with various (Li/Mg) and (Zn/Al) ratios. The space group of all compounds is cubic $Im\bar{3}$ (No. 204). Five quaternary ($Li_{1.00(1)}Mg_{0.63(2)}$-$Zn_{1.23(1)}Al_{2.14(1)}$(**1**), a = 14.073(3) Å; $Li_{1.00(1)}Mg_{0.63(1)}Zn_{1.42(1)}Al_{1.96(1)}$(**2**), a = 14.088(3) Å; $Li_{1.01(1)}Mg_{0.62(1)}Zn_{1.31(1)}Al_{2.06(1)}$(**3**), a = 14.096(5) Å; $Li_{1.03(1)}Mg_{0.60(1)}Zn_{1.78(3)}Al_{1.59(3)}$(**4**), a = 13.993(5) Å; and $Li_{0.78(2)}Mg_{0.85(2)}Zn_{2.47(1)}Al_{0.94(1)}$(**5**), a = 13.933(2) Å) and four ternary ($Li_{1.63}Zn_{0.81(1)}Al_{2.56(1)}$(**6**), a = 14.135(3) Å; $Li_{1.63}Zn_{1.42(1)}Al_{1.95(1)}$(**7**), a = 13.966(5) Å; $Li_{1.63}Zn_{1.59(1)}Al_{1.78(1)}$(**8**), a = 13.947(2) Å; and $Li_{1.63}Zn_{1.77(1)}Al_{1.60(1)}$(**9**), a = 13.933(4) Å) R-phase compounds were identified. The crystal structure exhibits an Al/Zn (M sites) network constructed from M_{12} icosahedra and M_{60} buckyball-type clusters. Li/Mg atoms (A sites) fill cavities within the Al/Zn network to give pentagonal dodecahedra (A_{20}). The site-potential studies (relative Mulliken populations) indicate two groups of atomic sites (positively and negatively polarized) and these results are consistent with the single crystal studies.

Introduction

Quasicrystalline phases are a young class of solid state compounds that contains noncrystallographic rotational symmetries in their diffraction patterns.[1-3] Compositions (including phase widths), structures and physical properties have been studied intensively for a variety of quasicrystalline phases in binary and ternary intermetallic systems.[4-7] To date, however, the actual structures of most quasicrystals are still a mystery. On the other hand, some crystalline intermetallic compounds are considered "quasicrystalline approximants," because their building blocks contain high-symmetry polyhedra that can be used as possible models for components of quasicrystalline structures.[2,3,8-10] One of these quasicrystalline approximants is the $Mg_{32}(Zn,Al)_{49}$-type structure (also called the R-phase structure, Pearson symbol *cI160*) that was first reported by Bergman and Pauling.[8,9] Its structure features a network of fused polyhedra with icosahedra, pentagonal dodecahedra and truncated icosahedra (C_{60}-type cages). This particular structure type is only found in ternary or higher order intermetallic systems.[11-16]

We have recently reported a detailed, systematic investigation of the phase width, elemental site preferences, physical properties and electronic structure of the ternary Mg-Zn-Al R-phase system.[11] According to our results, the seven crystallographic sites in the R-phase structure separate into three distinct sets: (1) three sites (52 atoms per unit cell) exclusively contain the electropositive Mg atoms (we will call these A sites: A1, A2, A3); (2) three sites (96 atoms per unit cell) have mixtures of Zn and Al (we will call these M sites: M1, M2, M3); and (3) one site, called M4 (12 atoms per unit cell), contains a mixture of Zn and Mg atoms with ca. 33% vacancies. Electronic structure calculations can rationalize the observed

phase width in this system due to a region of M–M nonbonding levels in the densities of states (DOS) occurring over a range in valence electron concentration between ca. 2.1 and 2.3 (*vec* = the total number of valence electrons divided by the total number of atoms in the formula unit). Vacancies occur in the Mg-Zn-Al R-phases because the observed compositions set *vec* values that lead to the occupation of some M–M antibonding levels when all sites are completely occupied. This explanation of vacancies in an intermetallic system is similar to the Grimm-Sommerfeld model of tetrahedral semiconductors.[17] Therefore, the crystalline, cubic R-phase structure presents numerous possibilities for elemental site preferences and vacancy distributions in an intermetallic structure.

In this paper, we discuss a further theoretical study of the R-phase structure, revealing that the site potentials of the three A sites are not equal. This result inspired us to introduce other electropositive elements, like Li, Ca, or Eu, into the Mg-Zn-Al system to form possible quaternary R-phases. To our knowledge, the only quaternary R-phase system to be reported is in the Na-Mg-Zn-Al system, but the relative site occupancies of Na, Mg and Al atoms could not be definitely characterized due to their similar scattering of X-rays. Our previous results in the ternary Mg-Zn-Al R-phase system and the significant differences in X-ray scattering between Mg and Li, Ca, or Eu make it possible to completely investigate the "coloring problem"[18] in this system of quasicrystalline approximants. Therefore, we also report the synthesis and the first single crystal structural characterizations of ternary and quaternary R-phases in the Li-Zn-Al and Li-Mg-Zn-Al systems.

The Theoretical Model

Before we discuss the theoretical model of site potentials in the R-phase structure, we show its beautiful structure in Figure 1.[19] According to crystallographic studies on diverse intermetallic systems adopting the R-phase structure, four distinct positions (M1-M4 sites) create a network of pentagonal pyramids, icosahedra and buckminsterfullerene-type clusters (truncated icosahedra), and three other positions (A1-A3 sites) fill interstices in the M1-M4 network. The coordination environments of the three A sites are shown in Figure 2. Environments for A2 (Wyckoff site *16f*) and A3 (Wyckoff site *24g*) are Friauf polyhedra, which are common structural elements in binary Mg-Zn and Mg-Al system.[20,21] The four hexagonal faces are all capped by other A-site atoms. Eight A2 and twelve A3 environments fuse to form the "Samson polyhedron,"[22] which contains 84 M atoms from a central icosahedron surrounded by twelve pentagonal pyramids. Adjacent Samson polyhedra share hexagons along {111} directions and M4–M4 edges along {100} directions to create the condensed, body-centered cubic packing of these building blocks.

------ Figures 1 and 2 ------

The environment surrounding each A1 site consists of 13 M atoms (2 M1 + 8 M3 + 3 M4 sites) with A3 atoms capping two hexagonal faces and a M4 site capping the third hexagonal face, as shown in Figure 2a. This particular interstitial site connects four adjacent Samson polyhedra in a tetrahedral arrangement – these sites are the tetrahedral holes in a bcc packing.[14]

To study the site preference problem in R-phase compounds, Extended Hückel tight-binding band calculations were performed on a model in which all seven crystallographic sites[23-26] were assigned the same atomic orbital parameters (Al). The primitive unit cell containing 80 atoms was used and a special points set of 60 **k** points in the irreducible wedge of the first Brillouin zone of a bcc lattice was chosen to perform the integrations[27] for calculations of Mulliken populations, total/partial densities of states (DOS and PDOS), crystal orbital overlap populations (COOP) and Fermi energies.[28,29] Atomic orbital parameters for Al are: $H_{ii}(3s) = -12.3$ eV, $H_{ii}(3p) = -6.5$ eV, $\zeta(3s) = \zeta(3p) = 1.167$.

------ Figure 3 ------

The total DOS and the COOP curves for M–M, A–M and A–A interactions are illustrated in Figure 3 for the model described above. The contributions to the total density of states (PDOS) curves from the M1-M4 and A1-A3 sites are represented, respectively, as gray and black shades. Two Fermi energies (E_F) are marked by dashed lines and represent the observed range in *vec* for R-phase structures: $2.00 \leq vec \leq 2.34$. The DOS curve shows a significant drop in the number of electronic states between −5.8 and −8.0 eV ($2.10 < vec < 2.70$), but no band gap occurs in this energy region. Furthermore, the relative contributions of orbitals from the M1-M4 and the A1-A3 sites are essentially equal in this region of the DOS. On the other hand, the M1-M4 orbitals have greater contribution at lower (occupied) energies ($E < -8.0$ eV), while the A1-A3 orbitals have larger contributions at higher (unoccupied) energies ($E > -6.0$ eV). Therefore, the density of valence electrons on the M1-M4 network is greater than the A1-A3 sites from the characteristics of the occupied energy

bands in the R-phase. Since this calculation was carried out with the same atomic orbital parameters at each site in the structure, the resulting Mulliken populations are affected by the atomic coordination environment and the strengths of the various interatomic orbital interactions.

The COOP curves for A···A (dashed line), A–M (dotted line) and M–M (solid line) contacts are illustrated in Figure 3. For $2.00 \leq vec \leq 2.25$, the integrated overlap population of each contact is essentially optimized, since the orbital interactions for all metal-metal contacts in this region of the DOS are nearly nonbonding. Moreover, there are electronic states contributing to this nonbonding region, and R-phases should be metallic conductors. These COOP curves also suggest that the total strength of all chemical bonds in the R-phase structure is weakly sensitive to *vec* values in the range between 2.00 and 2.50, and that unit cell sizes will be controlled by the average atomic sizes than by special chemical bonding forces.

------ Figure 4 ------

To elucidate the site potentials for the different crystallographic positions in the R-phase framework, we can compare the calculated Mulliken populations for each crystallographic site. These results are plotted in Figure 4 as the relative Mulliken population for each independent crystallographic site vs. total *vec* over a range of *vec* values in which the R-phase structure is observed for ternary and quaternary systems (indicated by the two dashed lines). The relative Mulliken population for a site equals the difference between the average *vec* and the calculated Mulliken population for that site. The Extended Hückel method allows such an analysis because the energy DOS is constructed solely from atomic

orbital interactions; valence electrons are then placed in these orbitals according to the *aufbau principle*, and several different electron counts can be examined. For a given *vec*, a positive (negative) value of the relative Mulliken population means an atomic site is positively (negatively) polarized. According to the concept of topological charge stabilization in a chemical structure with inequivalent positions[30], the atomic sites with high Mulliken populations (negative relative Mulliken populations) are favored for the more electronegative atoms and the sites with low Mulliken populations (positive relative Mulliken populations) are favored for the more electropositive atoms. Figure 4 shows some important features:

(1) The relative charges of the seven crystallographic sites divide into two groups. The M1-M4 sites are negatively polarized and the A1-A3 sites are positively polarized. This is consistent with the relative electronegativities of the elements found on these two sets of positions for various ternary R-phase materials listed in Table 1: more electronegative elements occupy the M1-M4 sites.

------ Table 1 ------

(2) The A3 site shows significantly lower positive charge than both the A1 and A2 sites to suggest that two different electropositive metallic elements may occupy the A1-A3 sites in a nonrandom fashion. In this case, the more electropositive atoms would preferentially segregate to the A1 and A2 positions in the R-phase structure.

(3) For the M1-M4 sites, the M4 site is the least negatively polarized (closest to zero) when $2.12 \leq vec \leq 2.50$, and there is a crossover point between M4 and M3 when $vec = 2.12$. Our

previous studies on the ternary Mg-Zn-Al R-phase system indicated that Zn and Mg atoms as well as vacancies occurred at the M4 position for higher Al content (*vec* ≥ 2.28).

These theoretical results, especially points (2) and (3), inspired us to investigate various quaternary derivatives of the R-phase structure in the Mg-Zn-Al system by introducing other electropositive elements to the reactant mixture. We limited our search to monovalent and divalent elements, i.e., alkali, alkaline earth, and divalent rare earth elements (Eu and Yb), and made initial trials with those elements that were closest to Mg in size and electronegativity. We avoided Na because it would be difficult to differentiate Na from Mg using diffraction techniques. Among these elements, Eu has the closest electronegativity value to Mg and Li has the closest atomic radius to Mg. Therefore, to take into account potential size and electrochemical effects, our targets involved quaternary systems with Li, Ca and Eu. Size seemed to played a decisive role, as well as competing thermodynamic stability of binary aluminides, e.g., $CaAl_4$ and $EuAl_4$, which contributed to the result that Li was the only element among these three that would form new quaternary derivatives of the R-phase structure.

Experimental Studies of Quaternary Li-Mg-Zn-Al R-Phases

Synthesis All materials were handled in an Ar-filled glovebox in which the concentration of O_2 is lower than 10 ppm. Starting materials included Li ingots (Johnson-Matthey, 99.5 %), Mg turnings (Johnson-Matthey, 99.98 %), Zn powder (Alfa, 99.9%), Al ingots (Alfa, 99.9999%), and Al foil. Maximum weighing errors were less than 1%. All reactant mixtures were sealed in cleaned Ta tubes (Alfa, 99.99%; washed with 15% HF/35% HNO_3/50%

H_2SO_4 solution and dried) that were placed in fused silica Schlenk tubes under reduced pressure. The ampoules were heated to 1070-1120 K for six hours, and then cooled to 670 K at a rate of 5 K/hr, and finally quenched to room temperature. Several different reactant mixtures were designed and measured to give targets of $(Li_uMg_{1-u})_{52}(Zn_xAl_{1-x})_{108}$, $0 < u \leq 1$. These reactions are summarized in Table 2. All products were silvery and brittle, and sensitivity to moisture and air increased as the Li content increased. Reaction products were characterized by Guinier X-ray powder patterns using Cu K_α radiation (λ = 1.54056 Å). In all but one condition, reaction (f), the R-phase structure was the major crystalline product, although subsequent single crystal diffraction showed that there were subtle differences between the composition of the R-phase and the reactant composition. Reaction (f) produced a novel intermetallic structure, which we report elsewhere.[31]

------ Table 2 ------

Single Crystal X-ray Diffraction Single crystals suitable for X-ray diffraction analysis were selected from small amounts of crushed product. Crystals in the Li-Mg-Zn-Al system showed needle-like morphologies, and were mounted on the tips of glass fibers. Crystal quality was checked by rotation photographs on a Siemens P4 single crystal diffractometer with Mo K_α radiation (λ = 0.71073 Å) at room temperature (298(2) K). Diffraction data for detailed structural analyses were collected at 298(2) K using a Bruker CCD-1000 diffractometer with monochromatic Mo K_α radiation, λ = 0.71073 Å, and a detector to crystal distance of 5.08 cm. At least two independent single crystal data sets were collected for each sample. For each crystal, the data were collected in at least a quarter hemisphere, and

harvested by collecting three sets of frames with 0.3° scans in ω for an exposure time of 30-60 sec per frame. The range of 2θ values was 3.0° to 58.0°. The data were corrected for Lorentz and polarization effects. Absorption corrections were based on fitting a function to the empirical transmission surface as sampled by multiple equivalent measurements. The unit cell parameters were determined from 90 frames of reciprocal space images and then least squares refined with all observed intensity data. Systematic absences revealed a body-centered cubic crystal system, Laue group $m\bar{3}$, and space group $Im\bar{3}$. Structures were solved by direct methods (SHELXTL-V5.12[32,33]) and subsequently refined by full-matrix least-squares refinement of F^2 using a model based upon $Mg_{1.63}(Zn_xAl_{1-x})_{3.37}$.[34] An abbreviated summary of the crystallographic data is listed in Table 3. The detail crystallographic data including atomic positions, site occupancies, and internuclear separations for all compounds are available as Supporting Information.

------ Table 3 ------

Magnetic susceptibility measurements Magnetic susceptibility measurements were carried out at 3T using a Quantum Design SQUID magnetometer for product (c), $Li_{1.00}Mg_{0.63}Zn_{1.22}Al_{2.15}$ (5-260 K) and product (i), $Li_{1.63}Zn_{1.50}Al_{1.87}$ (5-150 K). After diamagnetic core corrections, both compounds show temperature independent susceptibilities above ca. 50 K. $Li_{1.00}Mg_{0.63}Zn_{1.22}Al_{2.15}$ exhibits paramagnetic behavior and the average magnetic susceptibility above 50 K is 8.51×10^{-6} emu/mole. On the other hand, $Li_{1.63}Zn_{1.50}Al_{1.87}$ shows diamagnetic behavior and the average susceptibility above 50 K is -1.9×10^{-4} emu/mole.

Results and Discussion

Composition, structure, site occupancies and properties of intermetallic compounds in general are closely interrelated aspects of such compounds, and really cannot be considered separately. Nevertheless, to facilitate the discussion of our results, we will address each area in its own section and conclude with an overview of these relationships.

Composition in Li-Mg-Zn-Al R-phases

Figure 5 summarizes the compositional results in a pseudo-ternary (isothermal) phase diagram based upon *vec*. Different starting compositions involving five quaternary mixtures (a-f, see Table 1) and four ternary Li-Zn-Al mixtures (g-j, see Table 1) are indicated by open circles in the diagram. Compositions based upon refinements of site occupancies from single crystal X-ray diffraction experiments are shown by filled circles on the same diagram. Although starting compositions give a range in *vec* from ca. 1.8 to 2.3, the single crystal results produced a narrower range between 2.00 and 2.25, which is in excellent agreement with our findings from electronic structure calculations. The observed minimum *vec* value require that the maximum Li:Al ratio be 1.0. Also, the maximum Li content is 0.325, which is exactly in accord with 52 A sites per unit cell.

------ Figure 5 ------

Structure and Site Occupancies in Li-Mg-Zn-Al R-phases

The positional parameters and site occupancies in the structures of quaternary Li-Mg-Zn-Al crystals were first refined by placing Mg atoms on the A1-A3 sites and Al atoms on the M1-M4 sites and fixing isotropic thermal displacement parameters. After a few cycles of

least-squares refinements, the site occupancies indicated that the A1-A3 sites (Wyckoff sites *12h* and *16d*) were electron deficient compared to Mg and should be partially occupied by Li. On the other hand, the refined electron densities on the M1-M4 sites were larger than Al and should be refined as a mixture of Zn and Al. Once the possible atom types were determined for each site, subsequent refinements included anisotropic displacement parameters.

------ Figures 6 and 7 ------

Figures 6 and 7 illustrate results concerning structure and site occupancies in quaternary and ternary R-phase systems. Figures 6a and 6b show the correlations between unit cell volumes and, respectively, average atomic volume and *vec*. Included in these graphs are results from our earlier work with ternary Mg-Zn-Al R-phases.[11] Clearly, the unit cell volumes increase as both the average size and electron count of the component elements increases. Although the correlation with average atomic volume is clear, the correlation with *vec* is require exploration. Throughout the range of observed *vec* values (2.00-2.35 for all examples in Figure 6), the orbitals near the corresponding Fermi levels show an overall nonbonding character with respect to M–M, A–M, and A–A contacts (see COOP curves in Figure 3). Therefore, the trend in unit cell volume should follow the changes in atomic volumes associated with the elements controlling the *vec*. In the ternary classes of R-phases, i.e., the Li-Zn-Al and Mg-Zn-Al systems, *vec* values increase as the Al:Zn stoichiometric ratio increases. Since the metallic radius of Al (1.43 Å) exceeds that of Zn (1.34 Å), as *vec* increases in these two systems, the average atomic volume increases, and the unit cell volume also increases. In the quaternary Li-Mg-Zn-Al system, crystallographic experiments

demonstrated that the Li:Mg stoichiometric ratio also did not change. Thus, again, *vec* values increase as the Al:Zn ratio increases, and the same trend will occur.

Site occupancies among the different A and M sites in the quaternary crystals also show interesting variations. Figure 7a reveals the Li site occupancies at the three different A sites in the quaternary systems. The A1 site is completely occupied by Li, whereas the A2 and A3 sites are occupied by a mixture of Li and Mg. Since the experimental *vec* values in the Li-Mg-Zn-Al system lie between 2.00 and 2.25 e^-/atom, the relative site occupancies follow theoretical expectations for the three A sites exactly (see Figure 4). The A2 and A3 sites constitute pentagonal dodecahedra that cap the faces of the internal icosahedra (M2 sites) in the Samson cluster. Figures 7b and 7c illustrate how the Al contents vary among the crystals in the Li-Zn-Al and Li-Mg-Zn-Al systems. In all Li-Zn-Al crystals and in the quaternary system when *vec* is between ca. 2.15 and 2.25 e^-/atom, the M4 site is exclusively occupied by Al atoms (there are no vacancies apparent in our refinements, which is consistent with our conclusions from the Mg-Zn-Al system that introduced vacancies on the M4 sites when *vec* exceeds 2.28 e^-/atom). When *vec* drops below 2.15 e^-/atom in the Li-Mg-Zn-Al crystals, a small amount of Zn also occupies this M4 site. All other M sites (M1, M2 and M3) show a monotonic increase in Al content with lattice constant for both systems. Unlike in the ternary Mg-Zn-Al systems, the Al content at the M2 site varies among the different crystals.

------ Figure 8 ------

The effect of replacing Mg with Li in the electronic structure of the R-phases is to introduce high energy atomic orbitals at the Li sites. To investigate the change in site potentials throughout the R-phase structure, we treated the Li sites as vacant (i.e., no atomic orbitals were positioned at these sites, which is equivalent to placing a negative potential at these sites that repels electrons), but included its one valence electron to the total valence electron count. Figure 8 illustrates the variation in relative Mulliken populations with *vec* for the model $\square_{12}A_{40}M_{108}$ (A2, A3 and all M sites are given Al parameters; the A1 site is vacant). From this calculation, we observe the following results:

(1) The M4 site clearly becomes the most negatively polarized and highly attractive for the Al atoms. Such sites are also not well suited to accommodate vacancies.

(2) The A2 site is definitely more positively polarized than the A3 site. In the quaternary Li-Mg-Zn-Al crystals, the A2 site obtains significantly more Li than the A3 site, which agrees with these theoretical results.

Conclusions

In this study, ternary and quaternary R-phases were characterized and the results revealed a nonrandom site preference for Li and Mg atoms among the A1-A3 sites in the structure. A Mulliken population analysis from Extended-Hückel tight-binding band calculations on the R-phase structure separates the atomic positions into two groups of positively and negatively polarized sites, whose site occupancies follow elemental electronegativities. The site potential of different atomic positions depends on the various coordination environments, and leads to a difference among the three "cation" sites, A1-A3. A subsequent X-ray diffraction study on quaternary samples indicated that Li more readily

occupies the isolated A1 sites than the A2 and A3 positions that generate pentagonal dodecahedra. The behavior of the M1-M4 sites towards Zn/Al ratios are also affected by the Li atoms. The M1-M4 sites are all completely occupied as the *vec* values remain below 2.25 e^-/atom for the quaternary examples. Earlier work in Mg-Zn-Al revealed vacancies at the M4 site when *vec* exceeds 2.25 e^-/atom, and this work also showed that *vec* remains below 2.15 in the Li-Zn-Al R-phase system. Therefore, the additional flexibility in composition in the quaternary Li-Mg-Zn-Al crystals allows the system to achieve an optimal valence electron concentration near 2.25 e^-/atom (360 electrons per unit cell; King cited 340 electrons per unit cell using simple electron counting schemes.[35]). Theoretical calculations of the relative Mulliken populations for the different crystallographic sites in these intermetallic phases provided a beautiful model for predicting site preferences. These calculations can be used with X-ray diffraction data to provide models for structural refinements. We are pursuing this technique in related intermetallics and quasicrystalline phases.

Acknowledgments

This work was supported by the NSF DMR 96-27161 and DMR 99-81766. The authors gratefully thank Dr. R. A. Jacobson for the use of X-ray diffractometers, Dr. Ilia Guzei for training on the Bruker CCD-1000 diffractometer (which was purchased by the grant NSF 97-11121), and J. Ostenson for magnetic susceptibility measurements.

References

1) Shechtman, D.; Blech, I.; Gratias, D.; Cahn, J. W. *Phys. Rev. Lett.* **1984**, *53*, 1951-3.

2) Goldman, A. I.; Kelton, R. F. *Rev. Modern Phys.* **1993**, *65*, 213.

3) Janot, C. *Quasicrystals: A Primer*; 2nd ed.; Oxford Univ. Press: Oxford, 1994.

4) Tsai, A. P. *MRS Bull.* **1997**, *22*, 43-47.

5) Steurer, W. *Z. Kristallogr.* **1990**, *190*, 179-234.

6) Yamamoto, A. *Acta Crystallogr., Sect. A: Found. Crystallogr.* **1996**, *A52*, 509-560.

7) Fournee, V.; Belin-Ferre, E.; Sadoc, A.; Donnadieu, P.; Flank, A. M.; Muller, H. *J. Phys.: Condens. Matter* **1999**, *11*, 191-208.

8) Bergman, G.; Waugh, J. L. T.; Pauling, L. *Nature* **1952**, *169*, 1057.

9) Bergman, G.; Waugh, J. L. T.; Pauling, L. *Acta Crystallogr.* **1957**, *10*, 254.

10) Cooper, M.; Robinson, K. *Acta Cryst* **1966**, *20*, 614.

11) Lee, C.-S.; Miller, G. J. *J. Am. Chem. Soc.* **2000**, *122*, 4937-4947.

12) Elding-Ponten, M.; Lidin, S. *J. Solid State Chem.* **1995**, *115*, 270-3.

13) Audier, M.; Pannetier, J.; Leblanc, M.; Janot, C.; Lang, J.-M.; Dubost, B. *Physica B* **1988**, *153*, 136.

14) Tillard-Charbonnel, M.; Belin, C. *J. Solid State Chem.* **1991**, *90*, 270-8.

15) Doering, W.; Seelentag, W.; Buchholz, W.; Schuster, H. U. *Z. Naturforsch., B: Anorg. Chem., Org. Chem.* **1979**, *34B*, 1715-18.

16) Todorov, E.; Sevov, S. C. *Inorg. Chem.* **1997**, *36*, 4298.

17) Burdett, J. K. *Molecular Shapes: Theoretical Models of Inorganic Stereochemistry*; Wiley, New York, N. Y.:, 1980.

18) Miller, G. J. *Eur. J. Inorg. Chem.* **1998**, 523-536.

19) Dowty, E. Atoms; 5.0 ed., 1999.

20) Friauf, J. B. *Phys. Rev. B* **1927**, *29*, 34-40.

21) Friauf, J. B. *J. Am. Chem. Soc.* **1927**, *49*, 3107-3114.

22) Samson, S. *Structure Chemistry and Molecular Biology*; Rich, A. and Davidson, N., Ed.; Freeman: San Francisco, 1968, pp 687-717.

23) Hoffmann, R.; Lipscomb, W. N. *J. Chem. Phys.* **1962**, *36*, 2179, 3489.

24) Hoffmann, R. *J. Chem. Phys* **1963**, *39*, 1397.

25) Ammeter, J. H.; Buergi, H. B.; Thibeault, J. C.; Hoffmann, R. *J. Am. Chem. Soc.* **1978**, *100*, 3686-92.

26) Whangbo, M.-H.; Hoffmann, R.; Woodward, R. B. *Proc. R. Soc. London, Ser. A* **1979**, *366*, 23-46.

27) Chadi, D. J.; Cohen, M. L. *Phys. Rev. B* **1973**, *8*, 5474.

28) Hughbanks, T.; Hoffmann, R. *J. Am. Chem. Soc.* **1983**, *105*, 3528-37.

29) Wijeyesekera, S. D.; Hoffmann, R. *Organometallics* **1984**, *3*, 949-61.

30) Gimarc, B. M. *J. Am. Chem. Soc.* **1983**, *105*, 1979-84.

31) Lee, C.-S.; Miller, G. J. *Manuscript in preparation.* **2000**.

32) Sheldrick, G. M. *SHELXTL. Structure Determination Programs*; Version 5.12 ed.; Siemens Analytical X-ray Instruments Inc.: Madison, WI., 1995.

33) *SAINT*; Version 4 ed.; Siemens Analytical X-ray Instruments Inc.: Madison, WI., 1995.

34) Sheldrick, G. M. *Crystallographic Computing 3*; Sheldrick, G. M., Kruger, C. and Goddard, R., Ed.; Oxford University Press: Oxford,, 1985, pp 175.

35) King, R. B. *Inorganica Chimica Acta* **1991**, *181*, 217-225.

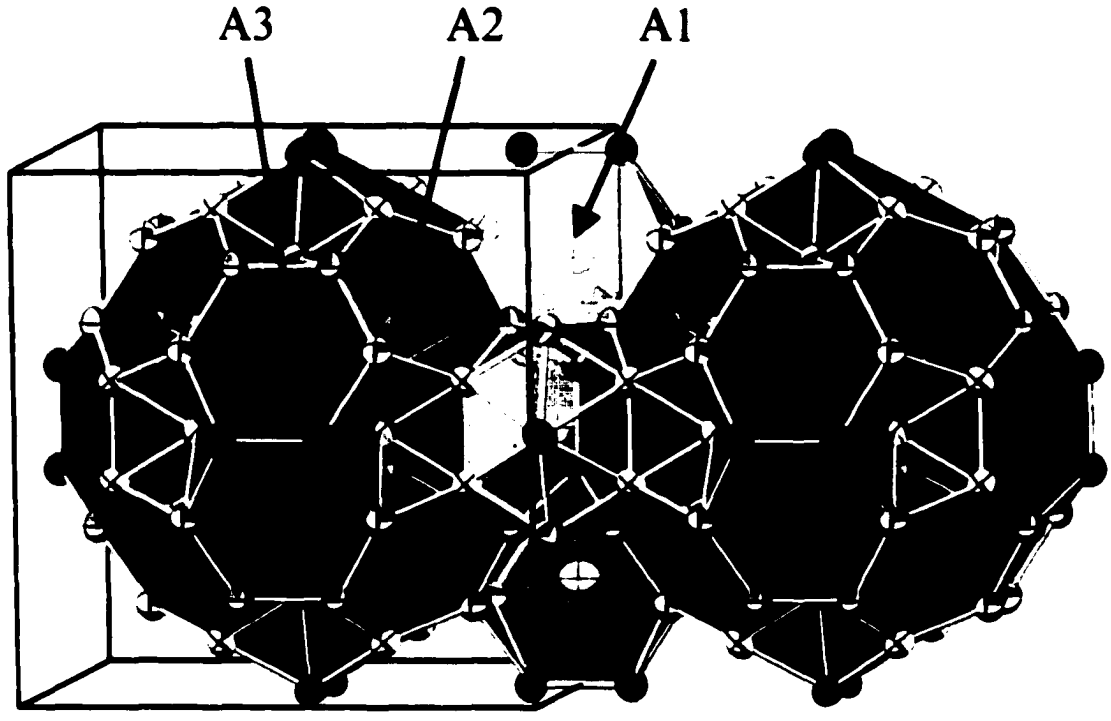

Figure 1. The crystal structure of the R-phase compound projected near [100]. The A1-A3 sites are drawn as isolated ellipsoids inside the clusters with different gray scales (A1: dark gray, A2: gray, A3: light gray). White sticks connect Zn/Al atoms (M1-M4). The thermal ellipsoid parameters are drawn as 99% probability from the data for $Li_{1.00(1)}Mg_{0.63(2)}Zn_{1.23(1)}Al_{2.14(1)}$ (**1**).

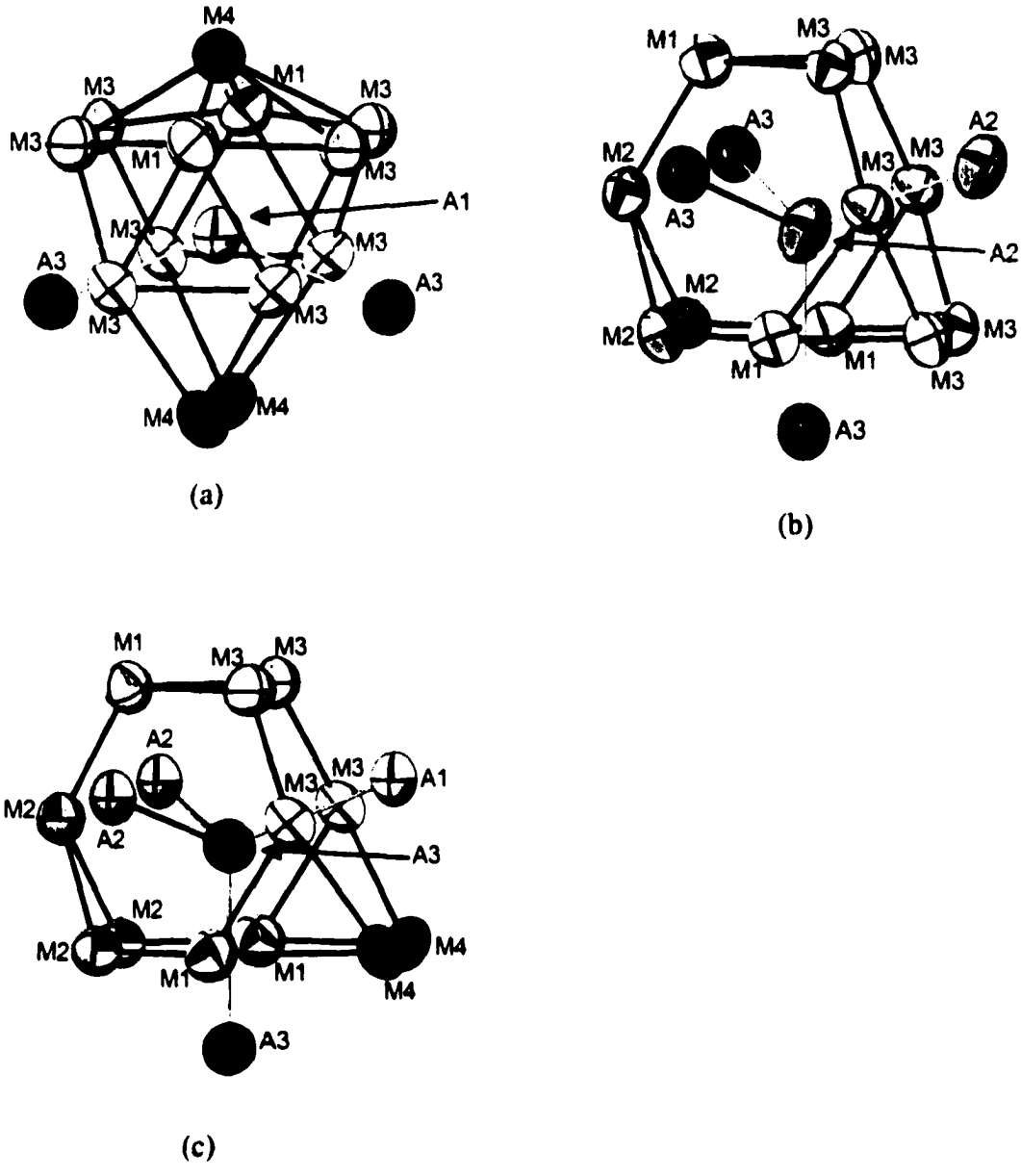

Figure 2. Three coordination environments for the A atoms in the R-phase structure. The thermal ellipsoid parameters are taken fron $Li_{1.00(1)}Mg_{0.63(2)}Zn_{1.23(1)}Al_{2.14(1)}$ (**1**). Gray sticks identify the shortest A-A contact. (a) A1-type: 13-vertex cluster. (b) A2-type: Truncated tetrahedron. (c) A3-type: Truncated tetrahedron.

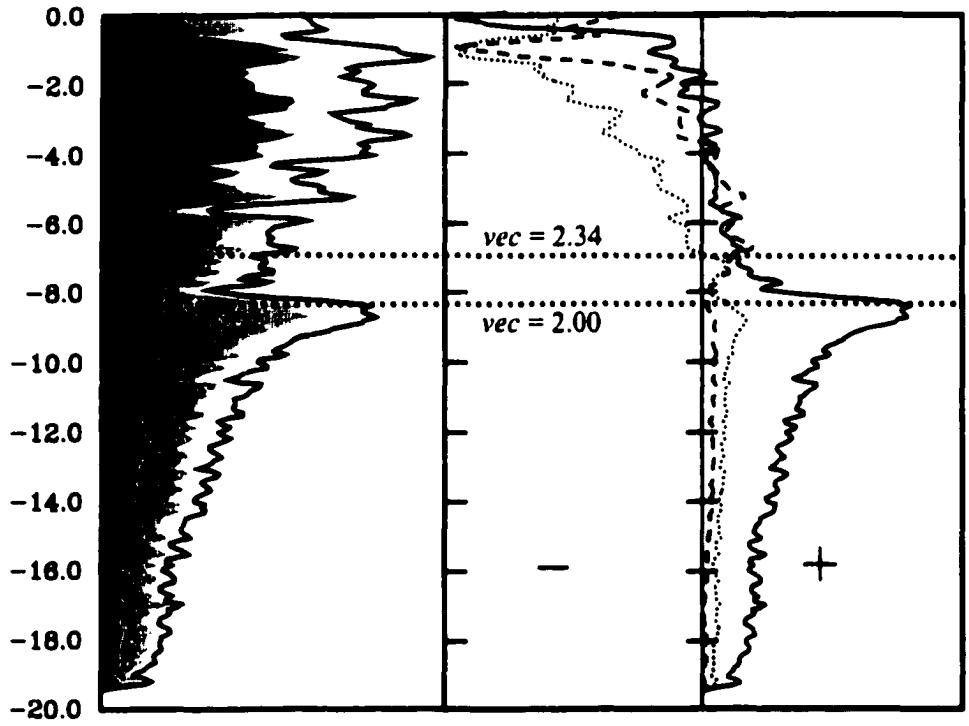

Figure 3. The DOS and COOP curves from the model formula of $[Al_{26}][Al_{54}]$ for the R-phase. Two dashed lines denote the Fermi energies corresponding to the observed *vec* range in the Li-Mg-Zn-Al R-phases. (a) Total DOS (solid line), PDOS from A1-A3 sites (black shadow) and PDOS from M1-M4 sites (gray shadow). (b) COOP curves from contacts of A-A (dashed), A-M (dotted) and M-M (solid).

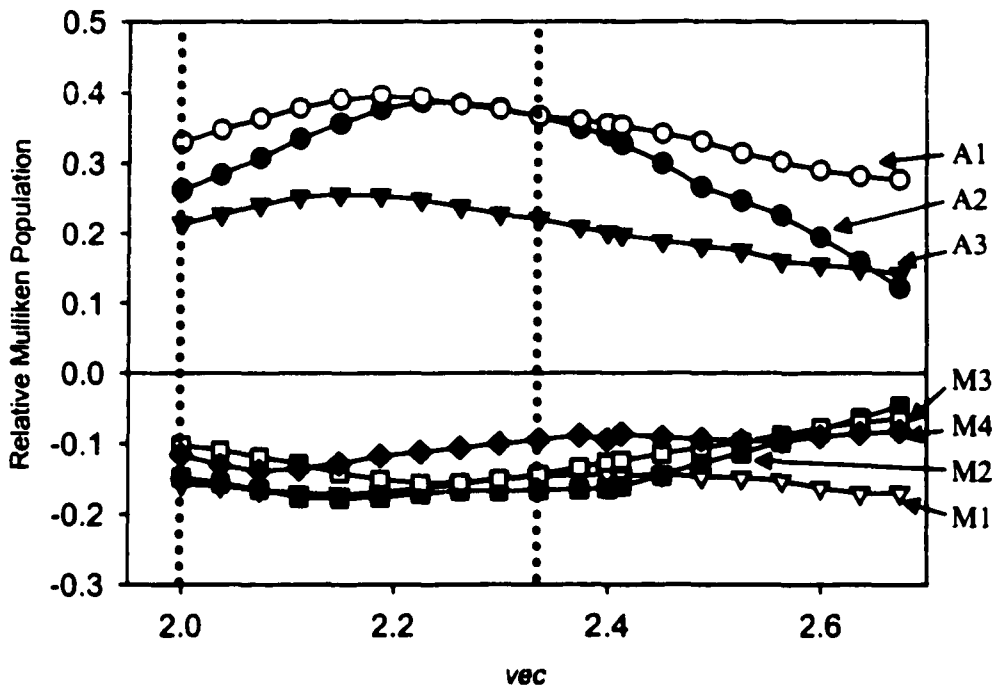

Figure 4. The relative Mulliken populations of the A1-A3 and M1-M4 sites as a function of *vec* range from 2.0 ("$Mg_{52}Zn_{108}$") to 2.68 ("$Mg_{52}Al_{108}$"). The two dashed lines indicate the lower and higher limit of *vec* for ternary and quaternary Li-Mg-Zn-Al R-phases. A1: filled circle. A2: empty circle. A3: filled inverse triangle. M1: empty inverse triangle. M2: filled square. M3: empty square. M4: filled diamond.

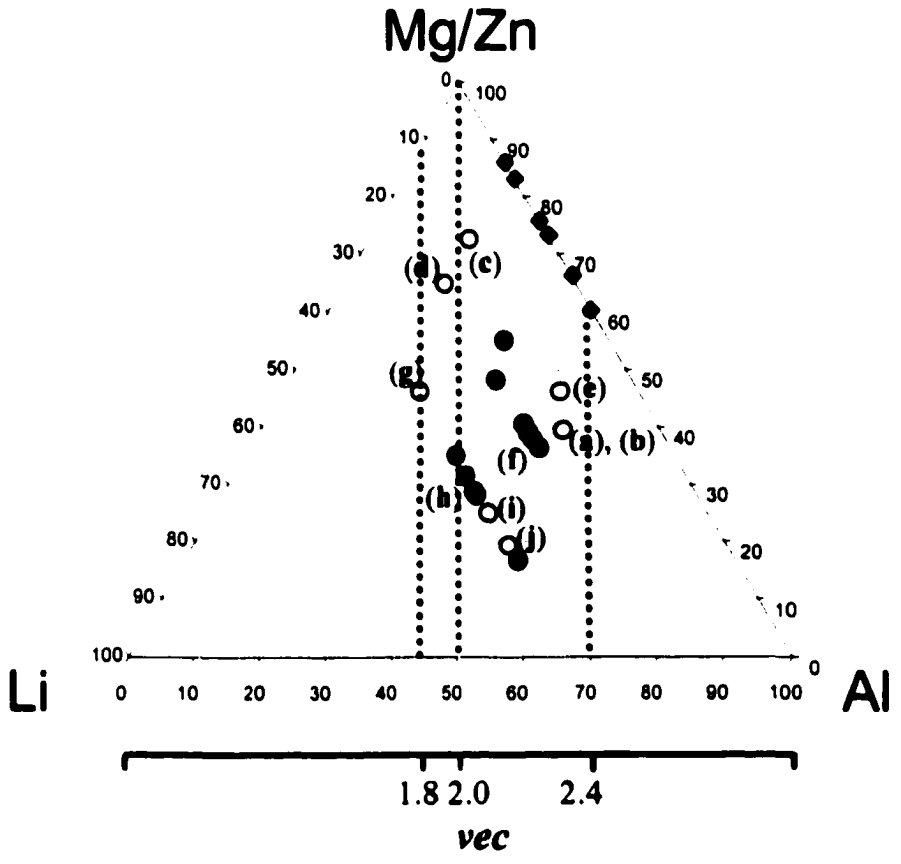

Figure 5. Phase diagram representing varies ternary and quaternary Li-Mg-Zn-Al reactions (open circles, **a** - **j**, see Table 1), and refined compositions (filled circles). Filled diamonds are single crystal results from ternary Mg-Zn-Al R-phase compounds.

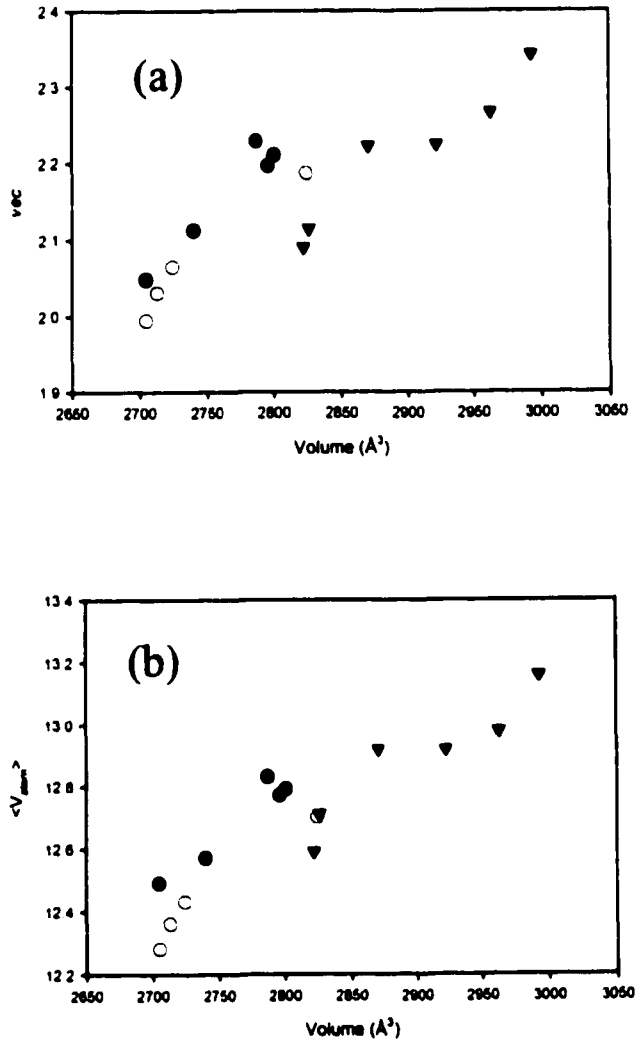

Figure 6. Unit cell volume (Å^3; x-axis) vs. *vec* (a), and average atomic volume (b) for ternary and quaternary R-phase systems. Filled circles: Li-Mg-Zn-Al. Empty circles: Li-Zn-Al. Inverse filled triangles: Mg-Zn-Al.

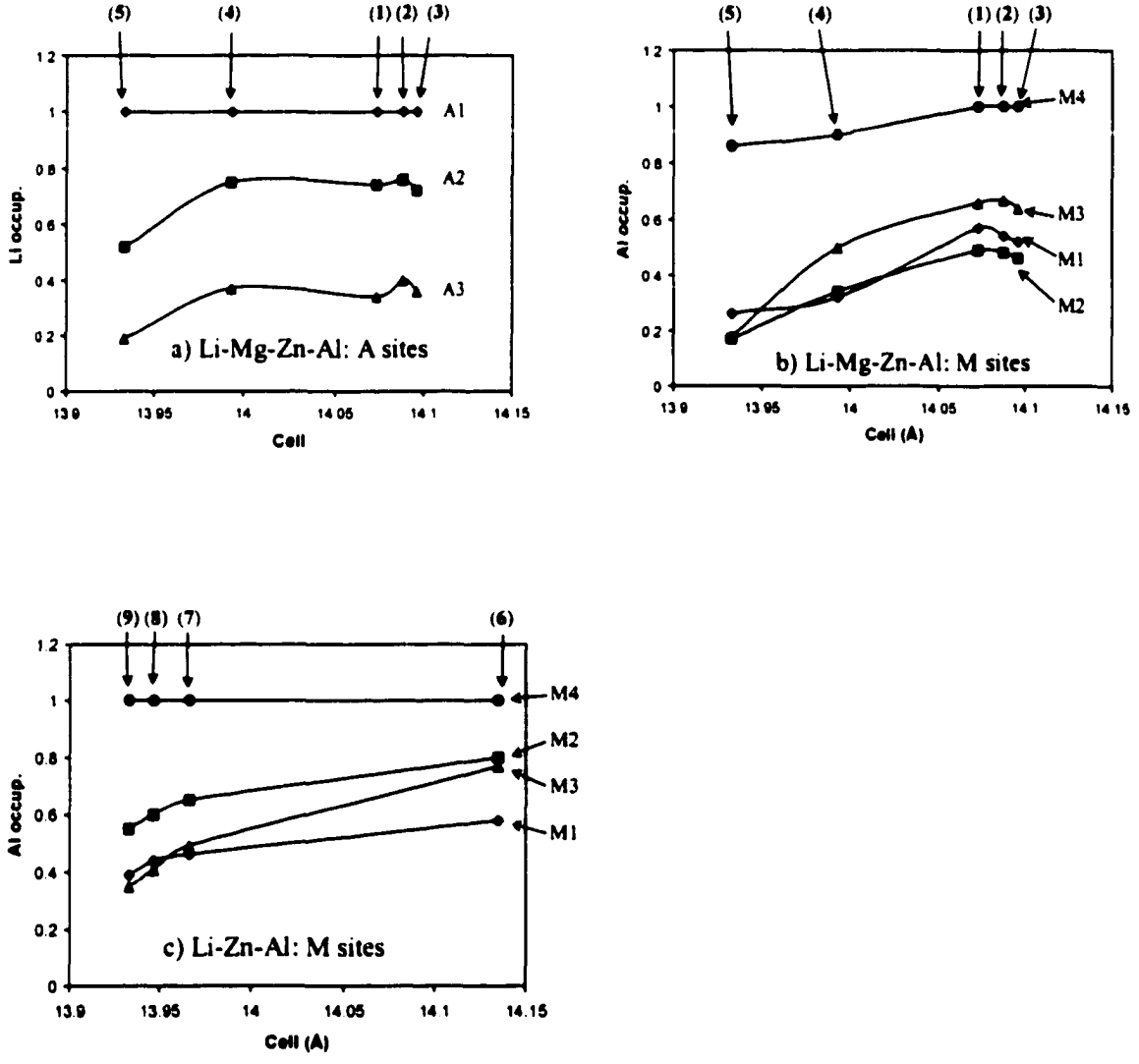

Figure 7. The relationship between site occupancies (Li :A sites, Al: M sites) and unit cell constants (Å) for ternary and quaternary R-phase compounds.

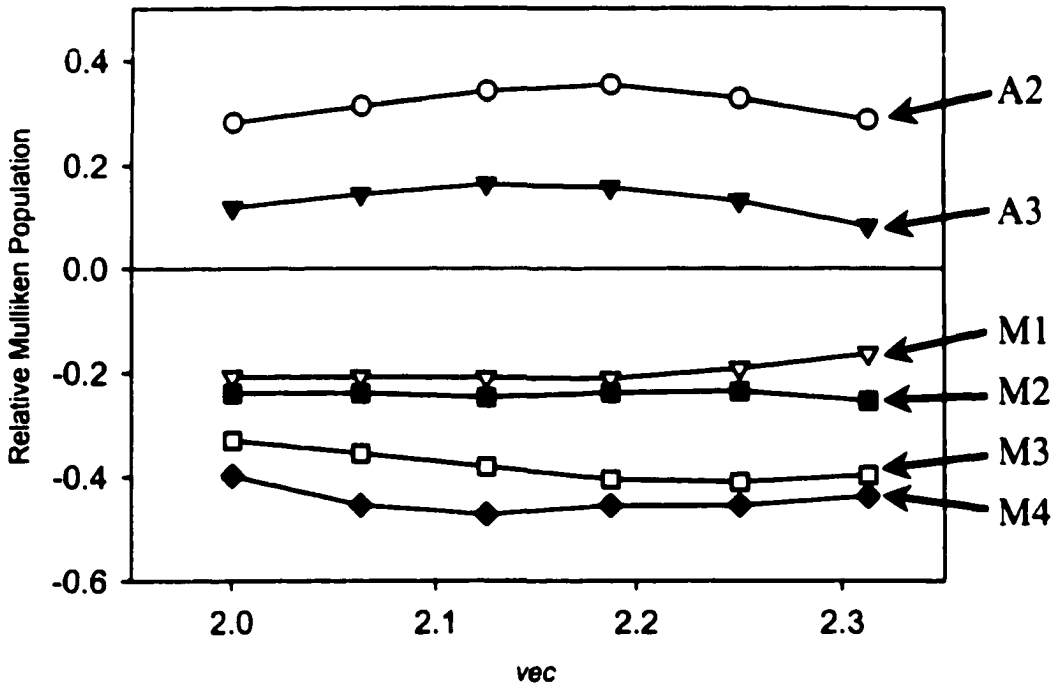

Figure 8. The relative Mulliken populations of A2-A3 and M1-M4 sites as a function of *vec* range based on the model $(\square_{12}Al_{40})Al_{108}$. The x-axis indicates the observed *vec* range for ternary and quaternary R-phases. A2: empty circle. A3: filled inverse triangle. M1: empty inverse triangle. M2: filled square. M3: empty square. M4: filled diamond.

Table 1. Summary of known R-phases with the site preference on each atomic site.

		M0	M1	M2	M3	M4	A1	A2	A3	
Formula	***a* (Å)**	**2a**	**24c**	**24b**	**48f**	**12g**	**12h**	**16d**	**24e**	**Ref.**
$Mg_{32}(Zn,Al)_{49}$	14.16(3)	Al	Zn/Al	Zn/Al	Zn/Al	Mg	Mg	Mg	Mg	11
$Mg_{1.63}(Zn,Al)_{3.37}$	14.13~14.41		Zn/Al	Zn/Al	Zn/Al	Mg/Zn/Al	Mg	Mg	Mg	11
$(Li,Mg)_{1.63}(Zn,Al)_{3.37}$	13.93~14.10		Zn/Al	Zn/Al	Zn/Al	Zn/Al	Li	Li/Mg	Li/Mg	[a]
$Li_{1.63}(Zn,Al)_{3.37}$	13.93~14.14		Zn/Al	Zn/Al	Zn/Al	Al	Li	Li	Li	[a]
$Li_{52}Ni_{37}Si_{72}$	12.741		Ni/Si	Ni/Si	Ni/Si	Ni/Si	Li	Li	Li	15
$Li_{52}Cu_{57}Si_{51}$	12.933		Cu/Si	Cu/Si	Cu/Si	Cu/Si	Li	Li	Li	15
$Li_{13}Cu_6Ga_{21}$	13.568(2)		Cu	Ga	Ga	Ga	Li	Li	Li	14
Li_3CuAl_5	13.9056(3)		Cu/Al	Cu/Al	Cu/Al	Al	Li	Li	Li	13
$Na_{52}Au_{81}Si_{29}$	14.138	Au	Si	Au	Au	Au/Si	Na	Na	Na	15
$Mg_{36}Na_{16}Zn_{68}Al_{40}$	14.2173(7)		Zn/Al	Zn/Al	Zn/Al	Al	Mg/Na	Mg/Na	Mg/Na	12
$Na_{52}Au_{80}Ge_{30}$	14.620	Au	Ge	Au	Au	Au/Ge	Na	Na	Na	15
$Na_{15}Au_{17}Sn_6$	14.989	Au	Sn	Au	Au	Au/Na	Na	Na	Na	15
$Na_{13}Cd_{20}Pb_7$	15.992(2)		Cd	Cd/Pb	Cd/Pb	Cd/Pb	Na	Na	Na	16

[a] This work. [b] Wyckoff site *2a* (0, 0, 0).

Table 2. Labeled summary of reaction compositions and products identified by Guinier X-ray powder diffraction and single crystal X-ray diffraction for various Li:Mg:Zn:Al reactions.

Reactions	*vec*	a[b]	Identified Minor Phase(s)[a]	Refined Formula[d]	*vec*
1. $(Li_xMg_{1-x})_{1.63}(Zn_yAl_{1-y})_{3.37}$					
(a) $Li_{0.88}Mg_{0.75}Zn_{1.13}Al_{2.24}$	2.272	14.073(3)	$MgZn_2$(t) + Mg_2Zn_{11}(t) + Al(t)	$Li_{1.00(1)}Mg_{0.63(2)}Zn_{1.23(1)}Al_{2.14(1)}$ **(1)**	2.23(2)
(b) $Li_{0.88}Mg_{0.75}Zn_{1.13}Al_{2.24}$	2.272	14.088(3)	Al (t) +Zn(t)	$Li_{1.00(1)}Mg_{0.63(1)}Zn_{1.42(1)}Al_{1.96(1)}$ **(2)**	2.20(2)
(c) $Li_{0.63}Mg_{1.00}Zn_{1.22}Al_{2.15}$	2.304	14.096(5)	NA	$Li_{1.01(1)}Mg_{0.62(1)}Zn_{1.31(1)}Al_{2.06(1)}$ **(3)**	2.21(2)
(d) $Li_{1.00}Mg_{0.63}Zn_{1.22}Al_{2.15}$	2.230	13.993(5)	NA	$Li_{1.03(1)}Mg_{0.60(1)}Zn_{1.78(3)}Al_{1.59(3)}$ **(4)**	2.11(4)
(e) $Li_{0.63}Mg_{1.00}Zn_{2.66}Al_{0.71}$	2.016	13.933(3)	$MgZn_2$(t) + Mg_2Zn_{11}(t) + Al(t)	$Li_{0.78(2)}Mg_{0.85(2)}Zn_{2.47(1)}Al_{0.94(1)}$ **(5)**	2.05(2)
(f) $Li_{1.00}Mg_{0.63}Zn_{2.66}Al_{0.71}$	1.942	13.951(4)	R-phase (m) + Al(t)	$Li_{1.00(2)}Mg_{0.60(2)}Zn_{3.09(1)}Al_{0.31(1)}$[c]	1.86(2)
2. $Li_{1.63}(Zn_xAl_{1-x})_{3.37}$					
(g) $Li_{1.63}Zn_{1.00}Al_{2.37}$	2.148	14.135(3)	LiZn(t) + LiAl(t) + Al(t)	$Li_{1.63}Zn_{0.81(1)}Al_{2.56(1)}$ **(6)**	2.19(1)
(h) $Li_{1.63}Zn_{1.22}Al_{2.15}$	2.104	13.966(5)	NA	$Li_{1.63}Zn_{1.42(1)}Al_{1.95(1)}$ **(7)**	2.06(1)
(i) $Li_{1.63}Zn_{1.50}Al_{1.87}$	2.048	13.947(2)	NA	$Li_{1.63}Zn_{1.59(1)}Al_{1.78(1)}$ **(8)**	2.03(1)
(j) $Li_{1.63}Zn_{2.25}Al_{1.17}$	1.928	13.933(4)	Zn(t)	$Li_{1.63}Zn_{1.77(1)}Al_{1.60(1)}$ **(9)**	1.99(1)

[a] From Guinier powder patterns, m= minor phase, tr = trace amounts.

[b] From Guinier powder X-ray diffractions.

[c] Ref 31.

[d] From single crystal refimenets.

Table 3a. Crystallographic data for five quaternary samples: $Li_{1.00(1)}Mg_{0.63(2)}Zn_{1.23(1)}Al_{2.14(1)}$ (1), $Li_{1.00(1)}Mg_{0.63(1)}Zn_{1.42(1)}Al_{1.96(1)}$ (2), $Li_{1.01(1)}Mg_{0.62(1)}Zn_{1.31(1)}Al_{2.06(1)}$ (3), $Li_{1.03(1)}Mg_{0.60(1)}Zn_{1.78(3)}Al_{1.59(3)}$ (4), and $Li_{0.78(2)}Mg_{0.85(2)}Zn_{2.47(1)}Al_{0.94(1)}$ (5) from single crystal X-ray diffraction.

Identification code	(1)	(2)	(3)	(4)	(5)
Formula weight	160.16	167.63	163.26	181.51	211.44
Space group , Z	$Im\bar{3}$, 32	$Im\bar{3}$, 32	$Im\bar{3}$, 32	$Im\bar{3}$, 32	$Im\bar{3}$, 32
a (Å)[a]	14.073(3)	14.088(3)	14.096(5)	13.993(5)	13.933(2)
V, Å^3	2787.1(5)	2807.0(4)	2801.8(7)	2806.2(6)	2699.3(8)
λ(Mo Kα), Å	0.71073	0.71073	0.71073	0.71073	0.71073
Temp, K	293(2)	293(2)	293(2)	293(2)	293(2)
μ, cm^{-1}	8.893	10.116	9.416	12.501	17.478
d_{calc} (g/cm^3)	3.040	3.173	3.096	3.437	4.162
R1, wR2 [I>2σ(I)][b]	0.0224, 0.0307	0.0194, 0.0348	0.0169, 0.0295	0.0157, 0.0385	0.0240, 0.0498
R1, wR2 (all data)[b]	0.0381, 0.0322	0.0272, 0.0360	0.0229, 0.0305	0.0178, 0.0391	0.0304, 0.0517

[a] From Guinier powder patterns (298(2) K).

[b] $R1 = \sum||F_o|-|F_c||/\sum|F_o|$; $wR2 = \left[\sum\left[w\left(F_o^2-F_c^2\right)^2\right]/\sum\left[w\left(F_o^2\right)^2\right]\right]^{1/2}$, $w=\sigma_F^{-2}$

Table 3b. Crystallographic data for four quaternary samples: $Li_{1.63}Zn_{0.81(1)}Al_{2.56(1)}$ (**6**), $Li_{1.63}Zn_{1.42(1)}Al_{1.95(1)}$ (**7**), $Li_{1.63}Zn_{1.59(1)}Al_{1.78(1)}$ (**8**), and $Li_{1.63}Zn_{1.77(1)}Al_{1.60(1)}$ (**9**) from single crystal X-ray diffraction.

Identification code	(6)	(7)	(8)	(9)
Formula weight	133.53	157.22	163.76	179.37
Space group , Z	$Im\bar{3}$, 32	$Im\bar{3}$, 32	$Im\bar{3}$, 32	$Im\bar{3}$, 32
a (Å)[a]	14.135(3)	13.966(5)	13.947(2)	13.933(4)
V, Å^3	2759.4(10)	2721.1(5)	2717.3(6)	2704.4(5)
λ(Mo Kα), Å	0.71073	0.71073	0.71073	0.71073
Temp, K	293(2)	293(2)	293(2)	293(2)
μ, cm^{-1}	6.206	10.381	11.525	12.727
d_{calc} (g/cm^3)	2.571	3.070	3.202	3.347
R1, wR2 [I>2σ(I)][b]	0.0247, 0.0376	0.0199, 0.0367	0.0262, 0.0453	0.0176, 0.0306
R1, wR2 (all data)[b]	0.0429, 0.0395	0.0277, 0.0374	0.0421, 0.0474	0.0262, 0.0314

[a] From Guinier powder patterns (298(2) K).

[b] $R1 = \sum\left||F_o|-|F_c|\right| \Big/ \sum|F_o|$; $wR2 = \left[\sum\left[w\left(F_o^2-F_c^2\right)^2\right] \Big/ \sum\left[w\left(F_o^2\right)^2\right]\right]^{1/2}$, $w=\sigma_F^{-2}$

Supplementary Materials

Appendix 1.

I. Analysis of Guinier Powder X-ray Diffraction Film of "(a)$Li_{0.88}Mg_{0.75}Zn_{1.13}Al_{2.24}$"

- Input reflections were corrected by interpolation of Si Lines
- Wavelength used is 1.54180 Å
- Single Crystal data $Li_{1.00(1)}Mg_{0.63(2)}Zn_{1.23(1)}Al_{2.14(1)}$ (1)

Space group	$Im\bar{3}$
a	14.073(3)
V(Å^3)	2787.4(9)
Error of fit	3.813

Refl #	h	k	l	J	I	$\sin^2 x10^3$	d calc.	2θ calc.	2θ corr.	diff.
1	2	1	1	24	258.5	18	5.7454	15.42	15.38	0.04
2	2	2	0	12	188.4	24	4.9757	17.83	17.78	0.04
3	1	3	0	12	538.7	30.01	4.4504	19.95	19.92	0.03
4	2	2	2	8	133.5	36.01	4.0626	21.88	21.84	0.04
5	2	3	1	24	82	42.01	3.7613	23.65	23.58	0.08
6	3	3	0	12	81.1	54.01	3.3171	26.88	26.81	0.06
7	5	2	1	24	37	90.02	2.5694	34.92	34.89	0.03
8	3	5	0	12	132.5	102.02	2.4136	37.25	37.22	0.03
9	6	0	0	6	381.7	108.02	2.3456	38.38	38.36	0.02
10	5	3	2	24	3.5	114.02	2.283	39.47	39.5	-0.03
11	3	6	1	24	896.4	138.03	2.075	43.62	43.64	-0.02
12	4	5	3	24	569.5	150.03	1.9903	45.58	45.56	0.02
13	6	4	0	12	190.6	156.03	1.9516	46.53	46.52	0.01
14	7	2	1	24	35.1	162.03	1.9151	47.47	47.48	0
15	5	6	1	24	43.1	186.03	1.7873	51.1	51.09	0.01
16	7	4	1	24	74.2	198.04	1.7323	52.85	52.83	0.02
17	8	2	2	24	38.3	216.04	1.6586	55.39	55.39	0
18	5	8	3	24	370.5	294.05	1.4216	65.68	65.73	-0.05
19	10	0	0	6	81	300.05	1.4073	66.43	66.45	-0.03
20	9	5	0	12	57.3	318.06	1.3669	68.66	68.72	-0.06

Appendix 1. (Continued)

II. Analysis of Guinier Powder X-ray Diffraction Film of "(b)$Li_{0.88}Mg_{0.75}Zn_{1.13}Al_{2.24}$"

- Input reflections were corrected by interpolation of Si Lines
- Wavelength used is 1.54180 Å
- Single Crystal data $Li_{1.00(1)}Mg_{0.63(1)}Zn_{1.42(1)}Al_{1.96(1)}$ (2)

Space group	$Im\bar{3}$
a	14.088(3)
V(Å^3)	2796(1)
Error of fit	4.543

Refl #	h k l	J	I	$\sin^2 x10^3$	d calc.	2θ calc.	2θ corr.	diff.
1	2 1 1	24	258.3	17.97	5.7514	15.41	15.34	0.06
2	2 2 0	12	188.3	23.95	4.9809	17.81	17.83	-0.02
3	1 3 0	12	538.3	29.94	4.455	19.93	19.9	0.03
4	2 2 2	8	133.5	35.93	4.0669	21.85	21.83	0.02
5	2 3 1	24	81.9	41.92	3.7652	23.63	23.55	0.08
6	3 3 0	12	81.1	53.9	3.3206	26.85	26.81	0.03
7	5 2 1	24	37	89.83	2.5721	34.88	34.91	-0.03
8	3 5 0	12	132.4	101.81	2.4161	37.21	37.26	-0.05
9	6 0 0	6	381.7	107.79	2.348	38.33	38.24	0.09
10	5 3 2	24	3.5	113.78	2.2854	39.43	39.42	0.01
11	3 6 1	24	896.6	137.74	2.0772	43.57	43.58	-0.01
12	4 5 3	24	569.6	149.71	1.9924	45.53	45.48	0.05
13	6 4 0	12	190.6	155.7	1.9537	46.48	46.41	0.07
14	7 2 1	24	35.1	161.69	1.9171	47.42	47.42	0
15	5 6 1	24	43.1	185.64	1.7892	51.04	51.05	0
16	7 4 1	24	74.3	197.62	1.7341	52.79	52.8	-0.01
17	8 2 2	24	38.3	215.59	1.6603	55.33	55.34	-0.01
18	5 8 3	24	370.6	293.44	1.4231	65.6	65.61	-0.01
19	10 0 0	6	81	299.43	1.4088	66.35	66.38	-0.03
20	9 5 0	12	57.3	317.39	1.3684	68.58	68.65	-0.07

Appendix 1. (Continued)

III. Analysis of Guinier Powder X-ray Diffraction Film of "(c)$Li_{0.63}Mg_{1.00}Zn_{1.22}Al_{2.15}$"

- Input reflections were corrected by interpolation of Si Lines
- Wavelength used is 1.54180 Å
- Single Crystal data $Li_{1.01(1)}Mg_{0.62(1)}Zn_{1.31(1)}Al_{2.06(1)}$ (3)

Space group	$Im\bar{3}$
a	14.096(3)
$V(Å^3)$	2801(1)
Error of fit	4.856

Refl #	h	k	l	J	I	sin^2x10^3	d calc.	2θ calc.	2θ corr.	diff.
1	1	1	0	12	483.1	5.98	9.9672	8.87	8.84	0.03
2	2	1	1	24	258.2	17.95	5.7546	15.4	15.39	0.01
3	3	1	0	12	35.2	29.91	4.4575	19.92	19.94	-0.02
4	2	3	1	24	81.9	41.87	3.7673	23.62	23.56	0.05
5	3	3	0	12	81.1	53.84	3.3224	26.83	26.97	-0.14
6	3	5	0	12	132.4	101.69	2.4174	37.19	37.19	0
7	6	0	0	6	381.7	107.68	2.3493	38.31	38.25	0.06
8	5	3	2	24	3.5	113.66	2.2866	39.4	39.38	0.02
9	6	3	1	24	0.9	137.59	2.0783	43.55	43.51	0.03
10	5	4	3	24	118.9	149.55	1.9934	45.5	45.47	0.04
11	4	6	0	12	28.6	155.53	1.9547	46.45	46.43	0.03
12	7	2	1	24	35.1	161.51	1.9182	47.39	47.41	-0.01
13	5	6	1	24	43.1	185.44	1.7902	51.02	51.02	-0.01
14	5	8	3	24	370.7	293.12	1.4239	65.56	65.56	0
15	10	0	0	6	81.1	299.1	1.4096	66.31	66.29	0.02
16	9	5	0	12	57.3	317.05	1.3691	68.54	68.61	-0.07
17	9	5	2	24	104.6	329.01	1.344	70	70.01	0

Appendix 1. (Continued)

IV. Analysis of Guinier Powder X-ray Diffraction Film of "(d)$Li_{1.00}Mg_{0.63}Zn_{1.22}Al_{2.15}$"

- Input reflections were corrected by interpolation of Si Lines
- Wavelength used is 1.54180 Å
- Single Crystal data $Li_{1.03(1)}Mg_{0.60(1)}Zn_{1.78(3)}Al_{1.59(3)}$ (4)

Space group	$Im\bar{3}$
a	13.933(3)
V(Å^3)	2705(1)
Error of fit	4.991

Refl #	h	k	l	J	I	$\sin^2 x10^3$	d calc.	2θ calc.	2θ corr.	diff.
1	1	1	0	12	326.7	6.12	9.8521	8.98	9.06	-0.08
2	2	1	1	24	225.8	18.37	5.6881	15.58	15.67	-0.1
3	2	2	0	12	91.7	24.49	4.9261	18.01	18.11	-0.1
4	3	1	0	12	526.5	30.61	4.406	20.15	20.2	-0.04
5	2	2	2	8	130.4	36.74	4.0221	22.1	22.14	-0.04
6	2	3	1	24	343.6	42.86	3.7238	23.9	23.91	-0.01
7	4	0	0	6	90.4	48.98	3.4833	25.57	25.57	0
8	3	3	0	12	90.4	55.1	3.284	27.15	27.07	0.08
9	3	5	0	12	444.8	104.08	2.3895	37.64	37.7	-0.05
10	6	0	0	6	399.5	110.21	2.3222	38.78	38.8	-0.02
11	5	3	2	24	893.3	116.33	2.2602	39.88	39.9	-0.02
12	6	3	1	24	1000	140.82	2.0543	44.08	44.07	0.01
13	5	4	3	24	574.2	153.06	1.9704	46.06	46.08	-0.01
14	4	6	0	12	202.2	159.19	1.9322	47.03	47.04	-0.01
15	7	2	1	24	47.1	165.31	1.896	47.98	48.01	-0.03
16	5	6	1	24	75.6	189.8	1.7695	51.65	51.67	-0.02
17	4	7	1	24	43.6	202.05	1.715	53.42	53.43	-0.01
18	5	8	3	24	7.2	300.01	1.4074	66.42	66.42	0
19	10	0	0	6	89.5	306.13	1.3933	67.19	67.16	0.03
20	10	2	0	12	0.7	318.37	1.3662	68.7	68.72	-0.02
21	9	5	0	12	44.6	324.5	1.3533	69.45	69.38	0.07
22	9	5	2	24	1.2	336.74	1.3285	70.94	70.88	0.06

Appendix 1. (Continued)

V. Analysis of Guinier Powder X-ray Diffraction Film of "(e) $Li_{0.63}Mg_{1.00}Zn_{2.66}Al_{0.71}$"

- Input reflections were corrected by interpolation of Si Lines
- Wavelength used is 1.54180 Å
- Single Crystal data $Li_{0.78(2)}Mg_{0.85(2)}Zn_{2.47(1)}Al_{0.94(1)}$ (5)

Space group	$Im\bar{3}$
a	13.992(3)
V(Å^3)	2740(1)
Error of fit	5.445

Refl #	h	k	l	J	I	$\sin^2 x10^3$	d calc.	2θ calc.	2θ corr.	diff.
1	2	1	1	24	259.8	18.21	5.7124	15.51	15.66	-0.15
2	2	2	0	12	189.1	24.28	4.9471	17.93	18	-0.07
3	3	1	0	12	35.5	30.35	4.4248	20.07	20.14	-0.07
4	2	2	2	8	134	36.42	4.0393	22	22.09	-0.09
5	2	3	1	24	82.2	42.49	3.7396	23.79	23.81	-0.02
6	4	0	0	6	105.8	48.57	3.4981	25.46	25.49	-0.03
7	3	3	0	12	81.3	54.64	3.2981	27.04	27.07	-0.03
8	3	5	0	12	132.5	103.2	2.3997	37.48	37.43	0.05
9	6	0	0	6	381.8	109.27	2.3321	38.61	38.63	-0.02
10	5	3	2	24	3.5	115.34	2.2699	39.71	39.73	-0.02
11	6	3	1	24	0.9	139.63	2.0631	43.88	43.9	-0.02
12	5	4	3	24	118.7	151.77	1.9788	45.86	45.87	-0.01
13	4	6	0	12	28.5	157.84	1.9404	46.82	46.85	-0.04
14	7	2	1	24	35	163.91	1.9041	47.76	47.73	0.04
15	5	6	1	24	43	188.19	1.777	51.42	51.37	0.05
16	4	7	1	24	15.6	200.33	1.7224	53.18	53.2	-0.02
17	5	8	3	24	370.1	297.46	1.4135	66.1	66.06	0.04
18	10	0	0	6	80.9	303.53	1.3992	66.86	66.8	0.06
19	10	2	0	12	33.4	315.68	1.3721	68.37	68.33	0.04
20	9	5	0	12	57.2	321.75	1.3591	69.11	69.13	-0.01
21	9	5	2	24	104.5	333.89	1.3341	70.6	70.6	-0.01

Appendix 1. (Continued)

VI. Analysis of Guinier Powder X-ray Diffraction Film of "(g) $Li_{1.63}Zn_{1.00}Al_{2.37}$"

- Input reflections were corrected by interpolation of Si Lines
- Wavelength used is 1.54180 Å
- Single Crystal data $Li_{1.63}Zn_{0.81(1)}Al_{2.56(1)}$ (**6**)

Space group	$Im\bar{3}$
a	14.135(3)
V(Å^3)	2824(1)
Error of fit	3.502

Refl #	h	k	l	J	I	$\sin^2 x10^3$	d calc.	2θ calc.	2θ corr.	diff.
1	2	1	1	24	379.8	17.85	5.7705	15.35	15.39	-0.04
2	3	1	0	12	605.3	29.75	4.4698	19.86	19.92	-0.05
3	2	3	1	24	493.2	41.64	3.7776	23.55	23.6	-0.05
4	4	0	0	6	97.2	47.59	3.5337	25.2	25.19	0.01
5	3	3	0	12	101.1	53.54	3.3316	26.76	26.78	-0.02
6	3	5	0	12	326.7	101.14	2.4241	37.09	37.1	-0.01
7	6	0	0	6	354.2	107.08	2.3558	38.2	38.19	0.01
8	5	3	2	24	762.9	113.03	2.2929	39.29	39.29	0
9	6	3	1	24	1000	136.83	2.084	43.42	43.43	-0.01
10	5	4	3	24	573.9	148.73	1.9989	45.37	45.36	0.01
11	4	6	0	12	191.6	154.68	1.9601	46.32	46.36	-0.04
12	7	2	1	24	57.8	160.63	1.9235	47.25	47.27	-0.01
13	5	6	1	24	92.9	184.42	1.7951	50.86	50.8	0.06
14	4	7	1	24	57.6	196.32	1.7399	52.6	52.54	0.06
15	8	5	3	24	285.5	291.51	1.4278	65.36	65.38	-0.02

Appendix 1. (Continued)

VII. Analysis of Guinier Powder X-ray Diffraction Film of "(h) $Li_{1.63}Zn_{1.22}Al_{2.15}$"

- Input reflections were corrected by interpolation of Si Lines
- Wavelength used is 1.54180 Å
- Single Crystal data $Li_{1.63}Zn_{1.42(1)}Al_{1.95(1)}$ (7)

Space group	$Im\bar{3}$
a	13.966(5)
V(Å^3)	2724(2)
Error of fit	6.944

Refl #	h	k	l	J	I	$\sin^2 x10^3$	d calc.	2θ calc.	2θ corr.	diff.
1	2	1	1	24	383.8	18.28	5.7017	15.54	15.65	-0.11
2	3	1	0	12	610.6	30.47	4.4165	20.1	20.16	-0.06
3	2	3	1	24	497.1	42.65	3.7326	23.84	23.87	-0.03
4	3	3	0	12	101.7	54.84	3.2919	27.09	27.1	-0.02
5	3	5	0	12	327.4	103.59	2.3952	37.55	37.56	-0.01
6	6	0	0	6	354.8	109.68	2.3277	38.68	38.67	0.01
7	5	3	2	24	763.9	115.78	2.2656	39.79	39.81	-0.03
8	6	3	1	24	1000	140.15	2.0592	43.97	43.76	0.21
9	5	4	3	24	573.6	152.34	1.9751	45.95	45.96	-0.02
10	4	6	0	12	191.4	158.43	1.9368	46.91	46.91	0
11	7	2	1	24	57.8	164.52	1.9006	47.86	47.87	-0.01
12	5	6	1	24	92.7	188.9	1.7737	51.52	51.56	-0.04
13	8	5	3	24	285.3	298.58	1.4108	66.24	66.22	0.03
14	5	9	0	12	42.7	322.95	1.3565	69.26	69.26	0
15	5	9	2	24	109.9	335.14	1.3316	70.75	70.8	-0.05

Appendix 1. (Continued)

VIII. Analysis of Guinier Powder X-ray Diffraction Film of "(i) $Li_{1.63}Zn_{1.50}Al_{1.87}$"

- Input reflections were corrected by interpolation of Si Lines
- Wavelength used is 1.54180 Å
- Single Crystal data $Li_{1.63}Zn_{1.59(1)}Al_{1.78(1)}$ **(8)**

Space group	$Im\bar{3}$
a	13.947(2)
V(Å^3)	2712.7(8)
Error of fit	3.271

Refl #	h	k	l	J	I	$\sin^2 x10^3$	d calc.	2θ calc.	2θ corr.	diff.
1	2	1	1	24	384.2	18.33	5.6936	15.56	15.5	0.06
2	3	1	0	12	611.2	30.55	4.4103	20.13	20.08	0.05
3	2	3	1	24	497.5	42.78	3.7274	23.87	23.81	0.06
4	3	3	0	12	101.8	55	3.2872	27.13	27.13	0
5	2	4	0	12	129.3	61.11	3.1185	28.62	28.61	0.02
6	3	5	0	12	327.5	103.88	2.3918	37.61	37.59	0.02
7	6	0	0	6	354.9	109.99	2.3244	38.74	38.69	0.04
8	5	3	2	24	764.1	116.1	2.2624	39.84	39.82	0.02
9	5	4	1	24	40.1	128.33	2.152	41.98	42.01	-0.02
10	6	3	1	24	1000	140.55	2.0563	44.04	44.03	0.01
11	5	4	3	24	573.5	152.77	1.9723	46.02	46.03	-0.01
12	4	6	0	12	191.4	158.88	1.934	46.98	46.99	-0.01
13	4	6	2	24	31.5	171.1	1.8637	48.87	48.87	-0.01
14	5	6	1	24	92.7	189.43	1.7712	51.6	51.59	0.01
15	4	7	1	24	57.4	201.65	1.7167	53.37	53.39	-0.03
16	5	6	3	24	69.1	213.88	1.6669	55.09	55.12	-0.02
17	4	7	3	24	18	226.1	1.6212	56.78	56.77	0.01
18	8	5	3	24	285.3	299.43	1.4088	66.35	66.4	-0.05

Appendix 1. (Continued)

IX. Analysis of Guinier Powder X-ray Diffraction Film of "(j) $Li_{1.63}Zn_{2.25}Al_{1.17}$"

- Input reflections were corrected by interpolation of Si Lines
- Wavelength used is 1.54180 Å
- Single Crystal data $Li_{1.63}Zn_{1.77(1)}Al_{1.60(1)}$ **(9)**

Space group	$Im\bar{3}$
a	13.938(4)
V(Å^3)	2708(1)
Error of fit	4.524

Refl #	h	k	l	J	I	$\sin^2 x10^3$	d calc.	2θ calc.	2θ corr.	diff.
1	2	1	1	24	384.4	18.35	5.6903	15.57	15.66	-0.09
2	3	1	0	12	611.5	30.59	4.4077	20.15	20.17	-0.03
3	2	3	1	24	497.7	42.83	3.7251	23.89	23.93	-0.05
4	3	5	0	12	327.5	104.01	2.3904	37.63	37.61	0.02
5	6	0	0	6	354.9	110.12	2.323	38.76	38.78	-0.02
6	5	3	2	24	764.1	116.24	2.2611	39.87	39.89	-0.02
7	6	3	1	24	1000	140.71	2.0551	44.06	44.05	0.01
8	5	4	3	24	573.5	152.95	1.9712	46.04	46.11	-0.06
9	7	2	1	24	57.7	165.19	1.8968	47.96	47.96	0.01
10	5	6	1	24	92.7	189.66	1.7702	51.63	51.59	0.04
11	8	5	3	24	285.3	299.78	1.408	66.39	66.35	0.05

Appendix 2. (a) Crystallographic data for three samples of $Li_{1.00(1)}Mg_{0.63(2)}Zn_{1.23(1)}Al_{2.14(1)}$ (1), $Li_{1.00(1)}Mg_{0.63(1)}Zn_{1.42(1)}Al_{1.96(1)}$ (2), $Li_{1.01(1)}Mg_{0.62(1)}Zn_{1.31(1)}Al_{2.06(1)}$ (3), $Li_{1.03(1)}Mg_{0.60(1)}Zn_{1.78(3)}Al_{1.59(3)}$ (4), and $Li_{0.78(2)}Mg_{0.85(2)}Zn_{2.47(1)}Al_{0.94(1)}$ (5) from single crystal X-ray diffraction.

Identification code	(1)	(2)	(3)	(4)	(5)
Crystal size (mm^3)	0.19× 0.12× 0.10	0.12× 0.21× 0.20	0.33× 0.29× 0.19	0.40× 40× 33	0.30× 0.27× 0.14
Formula weight	160.16	167.63	163.26	181.51	211.44
Crystal system	Cubic (no. 204)	Cubic (no. 204)	Cubic (no. 204)	Cubic (no. 204)	Cubic (no. 204)
a (Å)[a]	14.073(3)	14.088(3)	14.096(5)	13.993(5)	13.933(2)
V, $Å^3$	2787.1(5)	2807.0(4)	2801.8(7)	2806.2(6)	2699.3(8)
Space group , Z	$Im\bar{3}$, 32	$Im\bar{3}$, 32	$Im\bar{3}$, 32	$Im\bar{3}$, 32	$Im\bar{3}$, 32
d_{calc} (g/cm^3)	3.040	3.173	3.096	3.437	4.162
λ(Mo Kα), Å	0.71073	0.71073	0.71073	0.71073	0.71073
μ, cm^{-1}	8.893	10.116	9.416	12.501	17.478
Temp, K	293(2)	293(2)	293(2)	293(2)	293(2)
θ_{max} (°)	28.24°.	28.21°.	29.52°.	29.16°.	29.23°.
Extinction coeff	0.00030(2)	0.00025(3)	0.00018(3)	0.00026(4)	0.00015(4)
no. of Reflns colld	2641	2559	5311	5242	5138
no. of unique reflns	645 [R_i = 0.0394]	643 [R_i = 0.0270]	685 [R_i = 0.0318]	680 [R_i = 0.0225]	648 [R_i = 0.0263]
Data / restraints / parameters	645 / 0 / 47	643 / 0 / 47	685 / 0 / 46	680 / 0 / 47	648 / 0 / 47
R1, wR2 [$I>2\sigma(I)$][b]	0.0224, 0.0307	0.0194, 0.0348	0.0169, 0.0295	0.0157, 0.0385	0.0240, 0.0498
R1, wR2 (all data)[b]	0.0381, 0.0322	0.0272, 0.0360	0.0229, 0.0305	0.0178, 0.0391	0.0304, 0.0517
Goodness of fit (F^2)	0.948	1.043	1.057	1.051	1.068
(Δρ) max, min ($e/Å^3$)	0.480, -0.553	0.287, -0.429 e	0.849,-0.283	0.492, -0.421	0.691, -0.554

[a] From Guinier powder patterns (298(2) K). [b] $R1 = \sum\left||F_o|-|F_c|\right| / \sum|F_o|$; $wR2 = \left[\sum\left[w\left(F_o^2-F_c^2\right)^2\right] / \sum\left[w\left(F_o^2\right)^2\right]\right]^{1/2}$,

$w = \sigma_F^{-2}$

Appendix 2. (Continued)

(b). Crystallographic data for three samples of $Li_{1.63}Zn_{0.81(1)}Al_{2.56(1)}$ (6), $Li_{1.63}Zn_{1.42(1)}Al_{1.95(1)}$ (7), $Li_{1.63}Zn_{1.59(1)}Al_{1.78(1)}$ (8), and $Li_{1.63}Zn_{1.77(1)}Al_{1.60(1)}$ (9) from single crystal X-ray diffraction.

Identification code	(6)	(7)	(8)	(9)
Crystal size (mm^3)	0.30× 0.12× 0.11	0.34× 0.25× 0.19	0.20× 0.18× 0.10	0.31× 0.24× 0.23
Formula weight	133.53	157.22	163.76	179.37
Crystal system	Cubic	Cubic	Cubic	Cubic
a (Å)[a]	14.135(3)	13.966(5)	13.947(2)	13.933(4)
V, $Å^3$	2759.4(10)	2721.1(5)	2717.3(6)	2704.4(5)
Space group , Z	$Im\bar{3}$, 32	$Im\bar{3}$, 32	$Im\bar{3}$, 32	$Im\bar{3}$, 32
d_{calc} (g/cm^3)	2.571	3.070	3.202	3.347
λ(Mo Kα), Å	0.71073	0.71073	0.71073	0.71073
μ, cm^{-1}	6.206	10.381	11.525	12.727
Temp, K	293(2)	293(2)	293(2)	293(2)
θ_{max} (°)	29.42°.	26.35°.	28.27°.	29.56°.
Extinction coeff	0.00042(5)	0.00030(4)	0.00056(5)	0.00020(3)
no. of Refins colld	5041	2344	2520	5142
no. of unique refins	666 [R_i = 0.0526]	526 [R_i = 0.0305]	610 [R_i = 0.0426]	661 [R_i = 0.0313]
Data / restraints / parameters	666 / 0 / 47	526 / 0 / 46	610 / 0 / 47	661 / 0 / 47
R1, wR2 [I>2σ(I)][b]	0.0247, 0.0376	0.0199, 0.0367	0.0262, 0.0453	0.0176, 0.0306
R1, wR2 (all data)[b]	0.0429, 0.0395	0.0277, 0.0374	0.0421, 0.0474	0.0262, 0.0314
Goodness of fit (F^2)	1.042	1.087	1.062	1.028
(Δρ) max, min ($e/Å^3$)	0.436, -0.391	0.920, -0.357	1.143, -0.589	1.499, -0.387

[a] From Guinier powder patterns (298(2) K).

[b] $R1 = \sum||F_o| - |F_c|| / \sum|F_o|$; $wR2 = \left[\sum\left[w\left(F_o^2 - F_c^2\right)^2\right] / \sum\left[w\left(F_o^2\right)^2\right]\right]^{1/2}$, $w = \sigma_F^{-2}$

Appendix 3. (a) Atomic coordinates and equivalent isotropic displacement parameters ($Å^2$) for (**1**)~(**5**). U(eq) is defined as one third of the trace of the orthogonalized U^{ij} tensor.

atom	site	x	y	z	U(eq)		site occ.
$Li_{1.00(1)}Mg_{0.63(2)}Zn_{1.23(1)}Al_{2.14(1)}$ (**1**)							
A1	12h	0.2014(7)	0.0000	0.5000	0.034(3)	Li	1
A2	16d	0.18742(15)	0.18742(15)	0.18742(15)	0.02(1)	Mg	0.256(6)
						Li	0.74
A3	24e	0.0000	0.30263(11)	0.12095(12)	0.0162(6)	Mg	0.655(5)
						Li	0.34
M1	24c	0.0000	0.17632(4)	0.30982(4)	0.0131(2)	Zn	0.432(4)
						Al	0.57
M2	24b	0.0000	0.09344(4)	0.15265(4)	0.0107(2)	Zn	0.515(4)
						Al	0.49
M3	48f	0.15848(3)	0.18781(3)	0.40437(3)	0.0128(2)	Zn	0.343(3)
						Al	0.66
M4	12g	0.40457(10)	0.0000	0.5000	0.0169(5)	Al	1
$Li_{1.00(1)}Mg_{0.63(1)}Zn_{1.42(1)}Al_{1.96(1)}$ (**2**)							
A1	12h	0.2011(5)	0.5000	0.0000	0.030(2)	Li	1
A2	16d	0.18734(12)	0.18734(12)	0.18734(12)	0.019(1)	Mg	0.236(5)
						Li	0.76
A3	24e	0.12071(9)	0.30270(9)	0.0000	0.0177(5)	Mg	0.604(4)
						Li	0.40
M1	24c	0.30930(3)	0.17663(3)	0.0000	0.0150(2)	Zn	0.459(3)
						Al	0.54
M2	24b	0.15269(3)	0.09342(3)	0.0000	0.0125(2)	Zn	0.517(3)
						Al	0.48
M3	48f	0.31143(3)	0.34175(3)	0.09561(3)	0.0143(1)	Zn	0.333(3)
						Al	0.67
M4	12g	0.40400(8)	0.5000	0.0000	0.0180(4)	Al	1
$Li_{1.01(1)}Mg_{0.62(1)}Zn_{1.31(1)}Al_{2.06(1)}$ (**3**)							
A1	12h	0.2003(4)	0.0000	0.5000	0.027(1)	Li	1.00
A2	16d	0.18719(9)	0.18719(9)	0.18719(9)	0.0210(8)	Mg	0.279(4)
						Li	0.72
A3	24e	0.0000	0.30277(7)	0.12050(7)	0.0171(4)	Mg	0.635(4)
						Li	0.36
M1	24c	0.0000	0.17725(3)	0.30894(2)	0.0131(1)	Zn	0.479(3)
						Al	0.52
M2	24b	0.0000	0.09352(2)	0.15271(2)	0.0104(1)	Zn	0.537(3)
						Al	0.46
M3	48f	0.157956(19)	0.18924(2)	0.40442(2)	0.0127(1)	Zn	0.365(2)
						Al	0.64
M4	12g	0.40359(6)	0.0000	0.5000	0.0170(3)	Al	1.00

Appendix 3. (a) (Continued)

atom	site	x	y	z	U(eq)		site occ.
$Li_{1.03(1)}Mg_{0.60(1)}Zn_{1.78(3)}Al_{1.59(3)}$ (4)							
A1	12h	0.0000	0.5000	0.2990(4)	0.0175(15)	Li	1.00
A2	16d	0.18724(11)	0.18724(11)	0.18724(11)	0.0238(9)	Mg	0.254(7)
						Li	0.75
A3	24e	0.12036(8)	0.30283(8)	0.0000	0.0170(4)	Mg	0.63(1)
						Li	0.37
M1	24c	0.0000	0.30889(2)	0.17725(2)	0.0133(1)	Zn	0.68(1)
						Al	0.32
M2	24b	0.0000	0.15269(2)	0.09351(2)	0.0106(1)	Zn	0.66(1)
						Al	0.34
M3	48f	0.095337(18)	0.31003(2)	0.34231(2)	0.0129(1)	Zn	0.50(1)
						Al	0.50
M4	12g	0.0000	0.5000	0.09666(6)	0.0164(3)	Zn	0.100(7)
						Al	0.90
$Li_{0.78(2)}Mg_{0.85(2)}Zn_{2.47(1)}Al_{0.94(1)}$ (5)							
A1	12h	0.0000	0.2032	0.5000	0.012(2)	Li	1
A2	16d	0.1876(1)	0.1876(1)	0.1876(1)	0.018(1)	Mg	0.48(1)
						Li	0.52
A3	24e	0.0000	0.11907(11)	0.30387(11)	0.0165(6)	Mg	0.81(2)
						Li	0.19
M0	2a	0.0000	0.0000	0.0000	0.015	Zn	0.077(5)
M1	24c	0.0000	0.31252(4)	0.17814(4)	0.0131(2)	Zn	0.74(2)
						Al	0.26
M2	24b	0.0000	0.15441(3)	0.09441(3)	0.0117(2)	Zn	0.83(2)
						Al	0.17
M3	48f	0.09439(3)	0.31230(3)	0.34192(3)	0.0135(2)	Zn	0.82(2)
						Al	0.18
M4	12g	0.0000	0.40690(9)	0.5000	0.0143(4)	Zn	0.14(1)
						Al	0.86

Appendix 3. (Continued)

(b) Atomic coordinates and equivalent isotropic displacement parameters ($Å^2$) for (**6**)~(**9**). U(eq) is defined as one third of the trace of the orthogonalized U^{ij} tensor.

atom	site	x	y	z	U(eq)		site occ.
$Li_{1.63}Zn_{0.81(1)}Al_{2.56(1)}$ (**6**)							
A1	12h	0.0000	0.5000	0.3018(6)	0.036(2)	Li	1
A2	16d	0.1872(3)	0.1872(3)	0.1872(3)	0.035(2)	Li	1
A3	24c	0.1201(4)	0.3028(4)	0.0000	0.031(2)	Li	1
M1	24c	0.0000	0.31123(4)	0.17589(4)	0.0148(2)	Zn	0.425(3)
						Al	0.58
M2	24b	0.0000	0.15348(4)	0.09373(5)	0.0128(2)	Zn	0.201(2)
						Al	0.80
M3	48f	0.09428(3)	0.30950(3)	0.34213(3)	0.0143(2)	Zn	0.229(3)
						Al	0.77
M4	12g	0.40400(8)	0.5000	0.0000	0.0180(4)	Al	1
$Li_{1.63}Zn_{1.42(1)}Al_{1.95(1)}$ (**7**)							
A1	12h	0.0000	0.2001(8)	0.5000	0.031(3)	Li	1
A2	16d	0.1880(4)	0.1880(4)	0.1880(4)	0.034(2)	Li	1
A3	24e	0.0000	0.1176(5)	0.3028(6)	0.031(2)	Li	1
M1	24c	0.0000	0.31271(5)	0.17716(4)	0.0171(2)	Zn	0.536(4)
		0.0000	0.31271(5)	0.17716(4)	0.0171(2)	Al	0.46
M2	24b	0.0000	0.15429(5)	0.09410(5)	0.0145(3)	Zn	0.348(3)
		0.0000	0.15429(5)	0.09410(5)	0.0145(3)	Al	0.65
M3	48f	0.09379(3)	0.30967(3)	0.34224(3)	0.0167(2)	Zn	0.511(4)
						Al	0.49
M4	12g	0.0000	0.4050(1)	0.5000	0.0144(6)	Al	1
$Li_{1.63}Zn_{1.59(1)}Al_{1.78(1)}$ (**8**)							
A1	12h	0.0000	0.3007(9)	0.5000	0.026(3)	Li	1
A2	16d	0.1880(5)	0.1880(5)	0.1880(5)	0.027(3)	Li	1
A3	24e	0.0000	0.3020(7)	0.1172(6)	0.024(2)	Li	1
M1	24c	0.0000	0.17741(5)	0.31301(6)	0.0132(3)	Zn	0.560(5)
		0.0000	0.17741(5)	0.31301(6)	0.0132(3)	Al	0.44
M2	24b	0.0000	0.09407(6)	0.15450(6)	0.0119(3)	Zn	0.403(4)
		0.0000	0.09407(6)	0.15450(6)	0.0119(3)	Al	0.60
M3	48f	0.09370(4)	0.34217(3)	0.30989(4)	0.0136(2)	Zn	0.585(5)
		0.09370(4)	0.34217(3)	0.30989(4)	0.0136(2)	Al	0.41
M4	12g	0.0000	0.0950(1)	0.5000	0.0115(6)	Al	1

Appendix 3. (b) (Continued)

atom	site	x	y	z	U(eq)	site occ.
$Li_{1.63}Zn_{1.77(1)}Al_{1.60(1)}$ (**9**)						
A1	12h	0.2002(5)	0.0000	0.5000	0.023(2)	Li 1
A2	16d	0.1883(2)	0.1883(2)	0.1883(2)	0.023(1)	Li 1
A3	24e	0.0000	0.3028(3)	0.1180(3)	0.019(1)	Li 1
M1	24c	0.0000	0.17754(3)	0.31359(3)	0.0142(2)	Zn 0.608(3)
						Al 0.39
M2	24b	0.0000	0.09428(3)	0.15464(3)	0.0121(2)	Zn 0.449(3)
						Al 0.55
M3	48f	0.157909(19)	0.18973(2)	0.40630(2)	0.0142(1)	Zn 0.653(3)
						Al 0.35
M4	12g	0.40525(8)	0.0000	0.5000	0.0122(4)	Al 1

Appendix 4.

(a) Anisotropic displacement parameters ($Å^2 x\ 10^3$) for (**1**) - (**5**) from X-ray single crystal data. The anisotropic displacement factor exponent takes the form:
$-2\pi^2[h^2 a^2 U_{11} + ... + 2\ h\ k\ a\ b\ U_{12}]$

		U_{11}	U_{22}	U_{33}	U_{23}	U_{13}	U_{12}
$Li_{1.00(1)}Mg_{0.63(2)}Zn_{1.23(1)}Al_{2.14(1)}$ (**1**)							
A1	12e	37(6)	39(6)	28(6)	0	0	0
A2	16f	20(1)	20(1)	20(1)	-1(1)	-1(1)	-1(1)
A3	24g	15(1)	18(1)	16(1)	-3(1)	0	0
M1	24g	12(1)	14(1)	13(1)	-3(1)	0	0
M2	24g	12(1)	10(1)	10(1)	0(1)	0	0
M3	48h	11(1)	15(1)	12(1)	1(1)	-1(1)	2(1)
M4	12g	17(1)	18(1)	16(1)	0	0	0
$Li_{1.00(1)}Mg_{0.63(1)}Zn_{1.42(1)}Al_{1.96(1)}$ (**2**)							
A1	12e	27(4)	24(4)	40(5)	0	0	0
A2	16f	19(1)	19(1)	19(1)	-2(1)	-2(1)	-2(1)
A3	24g	19(1)	18(1)	16(1)	0	0	-3(1)
M1	24g	15(1)	16(1)	14(1)	0	0	-3(1)
M2	24g	12(1)	12(1)	13(1)	0	0	-1(1)
M3	48h	17(1)	13(1)	14(1)	-2(1)	0(1)	2(1)
M4	12g	17(1)	17(1)	20(1)	0	0	0
$Li_{1.01(1)}Mg_{0.62(1)}Zn_{1.31(1)}Al_{2.06(1)}$ (**3**)							
A1	12e	19(3)	33(3)	29(3)	0	0	0
A2	16f	21(1)	21(1)	21(1)	-1(1)	-1(1)	-1(1)
A3	24g	16(1)	18(1)	18(1)	-5(1)	0	0
M1	24g	13(1)	14(1)	13(1)	-3(1)	0	0
M2	24g	11(1)	10(1)	10(1)	-1(1)	0	0
M3	48h	11(1)	15(1)	12(1)	1(1)	-1(1)	1(1)
M4	12g	15(1)	20(1)	15(1)	0	0	0
$Li_{1.03(1)}Mg_{0.60(1)}Zn_{1.78(3)}Al_{1.59(3)}$ (**4**)							
A1	12e	17(3)	26(3)	10(2)	0	0	0
A2	16f	24(1)	24(1)	24(1)	-1(1)	-1(1)	-1(1)
A3	24g	17(1)	18(1)	16(1)	0	0	-5(1)
M1	24g	13(1)	13(1)	14(1)	-3(1)	0	0
M2	24g	11(1)	10(1)	10(1)	-1(1)	0	0
M3	48h	12(1)	15(1)	11(1)	2(1)	-1(1)	1(1)
M4	12g	15(1)	19(1)	15(1)	0	0	0
$Li_{0.78(2)}Mg_{0.85(2)}Zn_{2.47(1)}Al_{0.94(1)}$ (**5**)							
A1	12e	9(4)	17(5)	9(4)	0	0	0
A2	16f	18(1)	18(1)	18(1)	-2(1)	-2(1)	-2(1)
A3	24g	14(1)	18(1)	17(1)	-4(1)	0	0
M1	24g	12(1)	14(1)	13(1)	-3(1)	0	0
M2	24g	12(1)	11(1)	12(1)	-1(1)	0	0
M3	48h	13(1)	16(1)	12(1)	2(1)	-2(1)	0(1)

Appendix 4. (Continued)

M4	12g	19(1)	10(1)	15(1)	0	0	0

(b) Anisotropic displacement parameters ($Å^2 x\ 10^3$) for (**6**) - (**9**) from X-ray single crystal data. The anisotropic displacement factor exponent takes the form:
$-2\pi^2[h^2 a^2 U_{11} + ... + 2\ h\ k\ a\ b\ U_{12}]$

		U_{11}	U_{22}	U_{33}	U_{23}	U_{13}	U_{12}
$Li_{1.63}Zn_{0.81(1)}Al_{2.56(1)}$ (**6**)							
A1	12e	47(6)	32(5)	30(5)	0	0	0
A2	16f	35(2)	35(2)	35(2)	0(2)	0(2)	0(2)
A3	24g	33(4)	34(4)	27(3)	0	0	-7(3)
M1	24g	14(1)	15(1)	15(1)	-4(1)	0	0
M2	24g	14(1)	12(1)	13(1)	-1(1)	0	0
M3	48h	13(1)	17(1)	13(1)	3(1)	-1(1)	1(1)
M4	12g	14(1)	19(1)	12(1)	0	0	0
$Li_{1.63}Zn_{1.42(1)}Al_{1.95(1)}$ (**7**)							
A1	12e	27(6)	28(6)	37(6)	0	0	0
A2	16f	34(2)	34(2)	34(2)	-5(3)	-5(3)	-5(3)
A3	24g	29(4)	30(4)	33(4)	-15(4)	0	0
M1	24g	17(1)	18(1)	17(1)	-4(1)	0	0
M2	24g	16(1)	13(1)	14(1)	-1(1)	0	0
M3	48h	16(1)	20(1)	15(1)	2(1)	-2(1)	1(1)
M4	12g	16(1)	12(1)	16(1)	0	0	0
$Li_{1.63}Zn_{1.59(1)}Al_{1.78(1)}$ (**8**)							
A1	12e	25(7)	22(7)	33(8)	0	0	0
A2	16f	27(3)	27(3)	27(3)	2(3)	2(3)	2(3)
A3	24g	22(5)	34(5)	16(5)	-8(4)	0	0
M1	24g	13(1)	13(1)	14(1)	-3(1)	0	0
M2	24g	13(1)	13(1)	10(1)	-1(1)	0	0
M3	48h	13(1)	12(1)	16(1)	2(1)	1(1)	-2(1)
M4	48h	13(1)	8(1)	13(1)	0	0	0
$Li_{1.63}Zn_{1.77(1)}Al_{1.60(1)}$ (**9**)							
A1	12e	21(4)	24(4)	25(4)	0	0	0
A2	16f	23(1)	23(1)	23(1)	-3(2)	-3(2)	-3(2)
A3	24g	18(3)	18(2)	21(3)	-10(2)	0	0
M1	24g	14(1)	14(1)	15(1)	-3(1)	0	0
M2	24g	14(1)	12(1)	11(1)	-1(1)	0	0
M3	48h	12(1)	17(1)	13(1)	1(1)	-2(1)	2(1)
M4	12g	9(1)	14(1)	13(1)	0	0	0

Appendix 5.

(a) Bond lengths [Å] for (1) ~ (5).

		(1)	(2)	(3)	(4)	(5)
A1	A3×2	3.004(4)	3.005(3)	3.000(2)	3.005(2)	2.9714(16)
	M1×2	3.186(5)	3.196(4)	3.199(3)	3.196(3)	3.1121(8)
	M3×4	3.031(2)	3.037(4)	3.033(3)	3.020(3)	2.9797(6)
	M3×4	3.040(5)	3.0430(15)	3.0478(12)	3.0596(11)	2.9920(6)
	M4×1	2.863(10)	2.862(7)	2.866(6)	2.854(5)	2.8362(14)
	M4×2	3.141(9)	3.143(7)	3.134(5)	3.145(5)	3.0893(7)
A2	A2	3.055(7)	3.062(6)	3.067(4)	3.066(5)	3.011(6)
	A3×3	3.1586(8)	3.2427(13)	3.1511(6)	3.1526(7)	3.1409(8)
	M1×3	2.995(3)	3.1569(7)	2.9906(19)	2.993(2)	2.953(3)
	M2×3	3.0792(19)	2.996(2)	3.0771(12)	3.0763(14)	3.0524(16)
	M3×3	3.0846(19)	3.0795(15)	3.0901(12)	3.0952(14)	3.0634(16)
	M3×3	3.2388(17)	3.0893(15)	3.2408(11)	3.2439(12)	3.2176(15)
A3	A3	3.409(3)	3.406(3)	3.397(2)	3.395(2)	3.316(3)
	M1×2	3.0150(11)	3.0193(9)	3.0164(10)	3.0177(10)	2.9677(15)
	M1×1	3.2022(18)	3.1999(15)	3.1919(12)	3.1951(12)	3.2125(18)
	M2×1	2.9818(17)	2.9864(14)	2.9846(11)	2.9874(12)	2.9576(17)
	M2×2	3.0177(15)	3.0190(13)	3.0228(8)	3.0232(8)	2.9858(11)
	M3×2	3.0564(10)	3.0594(13)	3.0524(11)	3.0455(11)	3.0219(10)
	M3×2	3.0627(16)	3.0682(8)	3.0740(7)	3.0856(7)	3.0408(16)
	M4×2	3.5286(17)	3.5327(13)	3.5305(11)	3.5321(12)	3.4476(17)
M0	M2					2.5200(6)
M1	M2	2.5042(9)	2.5017(7)	2.4988(6)	2.4998(5)	2.4911(8)
	M3×2	2.6058(6)	2.6098(5)	2.6075(5)	2.6085(4)	2.5577(6)
	M3×2	2.6902(8)	2.6917(6)	2.6858(6)	2.6887(5)	2.6321(7)
	M4	2.9125(9)	2.9206(7)	2.9247(7)	2.9255(6)	2.8663(9)
	M2	2.6336(11)	2.6356(8)	2.6369(7)	2.6379(7)	2.6291(11)
	M2×4	2.6568(7)	2.6598(5)	2.6588(5)	2.6598(5)	2.6548(7)
M3	M3×2	2.6766(5)	2.6776(4)	2.6752(5)	2.6781(4)	2.6284(8)
	M3	2.6954(10)	2.6973(7)	2.6950(7)	2.6895(6)	2.6618(6)
	M4	2.9154(9)	2.9167(7)	2.9133(6)	2.9134(6)	2.8821(8)
M4	M4	2.690(3)	2.709(2)	2.7183(18)	2.7269(17)	2.593(3)

Appendix 5. (Continued)

(b) Bond lengths [Å] for **(6)** ~ **(9)**.

		(6)	**(7)**	**(8)**	**(9)**
A1	A3×2	2.975(7)	2.984(5)	2.991(7)	2.976(6)
	M1×2	3.183(5)	3.126(6)	3.126(7)	3.106(4)
	M3×4	3.015(5)	2.984(9)	2.992(11)	2.983(4)
	M3×4	3.0345(18)	3.021(2)	3.014(2)	3.0065(14)
	M4×1	2.899(9)	2.860(11)	2.872(13)	2.857(7)
	M4×2	3.083(8)	3.093(10)	3.080(11)	3.086(6)
A2	A2	3.053(15)	2.997(18)	3.00(2)	2.976(12)
	A3×3	3.226(5)	3.229(6)	3.223(7)	3.223(4)
	M1×3	3.1535(16)	3.1534(18)	3.154(2)	3.1548(12)
	M2×3	2.972(7)	2.972(8)	2.970(10)	2.970(5)
	M3×3	3.060(4)	3.041(4)	3.042(5)	3.035(3)
	M3×3	3.093(4)	3.075(5)	3.075(6)	3.066(3)
A3	A3	3.368(12)	3.285(15)	3.270(17)	3.288(9)
	M1×2	2.989(3)	2.958(8)	2.947(10)	2.950(5)
	M1×1	3.218(6)	3.239(8)	3.239(9)	3.236(5)
	M2×1	2.970(6)	2.953(7)	2.938(8)	2.948(4)
	M2×2	2.992(5)	3.034(7)	2.992(10)	2.976(6)
	M3×2	3.019(5)	3.034(7)	3.043(8)	3.030(4)
	M3×2	3.083(3)	3.229(6)	3.079(5)	3.062(2)
	M4×2	3.503(6)	3.470(7)	3.474(9)	3.463(5)
M1	M2	2.4947(10)	2.4972(11)	2.4990(12)	2.5000(7)
	M3×2	2.5888(8)	2.5668(6)	2.5646(7)	2.5569(4)
	M3×2	2.6807(9)	2.6510(7)	2.6453(9)	2.6386(5)
	M4	2.8797(10)	2.8551(10)	2.8517(11)	2.8417(7)
M2	M2	2.6292(14)	2.6274(15)	2.6255(18)	2.6272(10)
	M2×4	2.6580(9)	2.6593(9)	2.6612(10)	2.6598(6)
M3	M3×2	2.6449(11)	2.6188(9)	2.6151(10)	2.6108(6)
	M3	2.6720(7)	2.6668(5)	2.6670(6)	2.6640(4)
	M4	2.9052(9)	2.8871(9)	2.8851(10)	2.8802(6)
M4	M4	2.670(2)	2.654(3)	2.650(4)	2.640(2)

Appendix 6. The temperature-dependent magnetic susceptibility measurements for $Li_{0.88}Mg_{0.75}Zn_{1.13}Al_{2.24}$ (empty circle) and $Li_{1.63}Zn_{1.50}Al_{1.87}$ (filled circle).

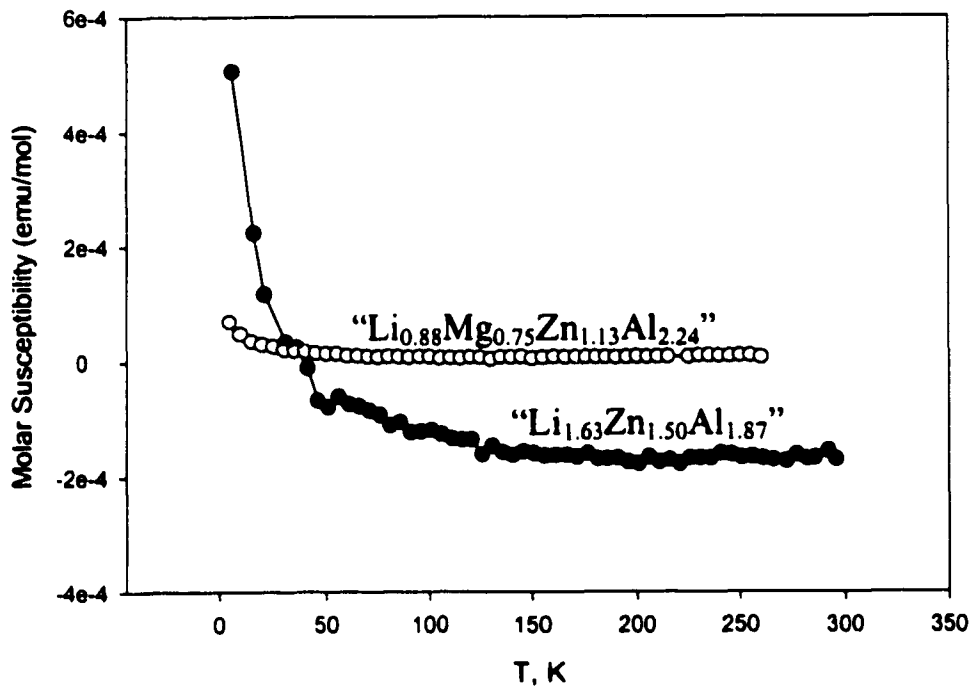

CHAPTER 5

SITE-PREFERENCE STUDY OF TERNARY ALKALINE EARTH-ZINC-ALUMINIDES SYSTEM FORMING STRUCTURAL VARIANTS Of $BaAl_4$

A paper to be submitted to *Inorg. Chem.*
Chi-Shen Lee and Gordon J. Miller

Abstract

A series of intermetallic compounds with $BaAl_4$-type structure (*I4/mmm*) in the $AeZn_xAl_{4-x}$ (Ae = Ca-Ba, $0<x<2$) systems have been synthesized and characterized by single crystal X-ray analyses. Single phase of $CaZn_xAl_{4-x}$ exists when $x \sim 2.0$. The Sr- and $BaZn_xAl_{4-x}$ phases exhibit a phase width of $0.0 \leq x \leq 2.0$. The site preference for Zn and Al atoms is affected by the alkaline earth metal.

Introduction

The $BaAl_4$ structure is a popular structure among solid state compounds: more than 800 intermetallic compounds with this structure type have been reported to date.[1] Using the average valence electron number per atom (*vec*) as an index (e.g., the *vec* of $BaAl_4$ is (3*4+2)/4 = 3.5, Ba is treated as electron donor), the $BaAl_4$-type intermetallic phases exist in the *vec* range between 2.75 and 3.5 e^-/atom when Al is replaced by other main group metals.[1-4] Extensive theoretical studies have been done during the last decade to understand the electronic structure, chemical bonding, and physical properties for this particular structure.[3,5-7] The $BaAl_4$ structure features a body-centered tetragonal unit cell (space group *I4/mmm*, No. 139). The Ba atoms occupy the corner and center positions and the Al atoms form a $^3_\infty[Al_4]^{2-}$ network. The $^3_\infty[Al_4]^{2-}$ net contains two independent sites: the M2 sites form two-dimensional

square nets and the M1 sites cap the square net alternatively above and below the plane (see Figure 1).

When the $^{3}_{\infty}[Al_4]^{2-}$ network contains two or more types of atoms on M1 and M2 sites, three different structure types were observed. These $BaAl_4$-type derivatives are shown in Figure 2 for $ThCr_2Si_2$[8] (I4/mmm, centrosymmetric), $CaBe_2Ge_2$[9] (P4/nmm, noncenterosymmetric) and $BaNiSn_3$[10] (I4mm, noncentrosymmetric), respectively. Previous theoretical studies based on a Mulliken population analyses suggest that elements with grater electronegativity prefer to occupy the M1 site (five coordinate) than the M2 sites (four coordinate).[5,11] However, the experimental results show some exceptions such as $CaBe_2Ge_2$, in which the Ge (more electronegative element) atoms occupy not only M1 but also M2 sites between two adjacent $^{2}_{\infty}[Be_2Ge_2]^{2-}$ slabs.[12,13] The factor(s) controlling the site preference of M1 and M2 sites in the $BaAl_4$ structure attracted our attention during the investigation of the Ln-Au-Al system (Ln: rare earth elements).[11] A previous study in Eu-Au-Al system revealed a variant of $BaAl_4$-type compounds, $EuAu_{0.75}Al_{3.25}$, with space group of I4/mmm.[11] Au and Al atoms occupy M1 site (39% Au / 61% Al) and 100% Al on the M2 site. On the other hand, two noncentrosymmetric structure types were identified by powder X-ray diffraction studies from $LnAu_xAl_{4-x}$ compounds (x = 1.0-2.0, Ln = La-Tb): The $BaNiSn_3$ structure (space group I4mm) is observed at low x ($1.0 < x < 1.5$) and the $CaBe_2Ge_2$ structure (space group P4/nmm) is formed when x is between 1.5 and 2.0. Therefore, the structure of $LnAu_xAl_{4-x}$ may be controlled by the relative mole ratio of Au to Al.[9,10] The structural studies also suggest that Au atoms avoid forming Au-Au contacts.[11]

Based on the results from the ternary Ln-Au-Al studies, we decided to explore compounds with the $BaAl_4$ structure type in alkaline earth (Ae)-zinc-aluminum system using single crystal X-ray analyses to elucidate the site preference of M1 and M2 as well as the effect(s) of different alkaline earth elements. In this chapter, the investigations of ternary intermetallics, $AeZn_xAl_{4-x}$ (Ae = Mg-Ba, x = 1-3), will be presented.

Experimental

Synthesis

All materials were handled in an Ar-filled glovebox in which the concentration of O_2 is kept lower than 10 ppm. Starting materials were Mg turnings (Johnson-Matthey, 99.9 %), Ca turnings (Johnson-Matthey, 99.9 %), Sr rod (Johnson-Matthey, 99.9 %), Ba rod (Johnson-Matthey, 99.9 %), Zn powder (Alfa, 99.9%), Al ingot (Alfa, 99.9999%), and Al foil. Detailed procedures for reaction preparations were described in chapter 2. Stoichiometric amounts of alkaline earth, Zn and Al metals with total weight near 500 mg for each reaction are prepared based on the formula of $AeZn_xAl_{4-x}$ (Ae = Mg, Ca, Sr and Ba; x= 1.0, 2.0 and 3.0) in Ta containers (3/8 in. diameter). The weighing error for each elemental reagent is less than 0.5 % wt. Ta tubes were heated either in an evacuated sealed silica tube or under dynamic vacuum (pressure < 10^{-3} torr). For $AeZn_2Al_2$ reactions, the tubes were first heated to 850 °C over 24 hours to melt each reagent, then cooled to 475 °C at the rate of 5 °C/hour, annealed at 475 °C for 4 weeks, and finally quickly cooled to room temperature. $AeZnAl_3$ and $AeZn_3Al$ reactions were carried out by heating elemental mixtures at 850 °C for 6 hr, slowly cooled to 400 °C at the rate of 5 °C/hr and finally cooled to room temperature. Quenching experiments

on $AeZn_2Al_2$ (Ae = Mg, Ca, Sr and Ba) were also carried out by putting the heated sample into liquid N_2 and identifying phases by powder X-ray diffraction study.

Products were opened in the Ar-filled glovebox. All products show brittle, silvery lustrous chunks of metal that are mildly air-sensitive (decomposed to metal oxides after 2 weeks). X-ray powder patterns were obtained using an Enraf-Nonius Guinier camera (λ = 1.540562 Å) and silicon powder as internal standard. The identified phases from powder X-ray diffraction on each reaction are listed in Table 1.

Structural Determination

Needle-shaped crystals were selected from the crushed products in a glovebox and mounted on glass fibers for X-ray structural analyses. For each specimen, the crystal quality was first checked by a rotational photograph on a Siemens P4 or a Rigaku AFC6R diffractometer with monochromated Mo Kα radiation (λ= 0.71073Å). The lattice constants were indexed from 20-30 reflections from diffraction points measured on the rotational photo or from a random search in the 2θ range 25~ 35°. At least two independent intensity data sets from product of $AeZn_xAl_{4-x}$ reactions were collected using the ω-2θ scan mode. Three standard reflections were checked every 100 reflections collected and used to calibrate the intensity data. Lorentz and polarization effects plus an absorption correction with the aid of the average of ψ scans of three reflections at different 2θ values were applied to each data collection. The space group was chosen on the basis of systematic absences, intensity statistics, the Wilson plot test, as well as the Hamilton test. The structures were solved by direct methods and refined by full-matrix least-squares refinement of F^2 with SHELXTL program (ver 5.12).[14,15] Some details of the data collection and refinement are listed in Table

2. The cell constants of each compound were calculated from powder X-ray diffraction patterns based on the refined positional parameters of AZn_xAl_{4-x}.

Magnetic susceptibilities measurements:

About 30 mg of powdered sample were packed to a sealed silica tube. Temperature-dependent magnetic susceptibility measurements at field strength of 3 Tesla over the temperature range 6 - 300K were performed using a Quantum Design MPMS SQUID magnetometer. Data were corrected for the diamagnetic contributions of the constituent atomic cores and the sample holder.[16]

Electronic Structure Calculation

The theoretical investigations were performed using Extended-Hückel tight-binding band calculations on a hypothetical formula, $[Zn_xAl_{4-x}]^{2-}$ (x = 0, 1, 2), with several model structures presenting different "colorings" of Zn and Al on $[Zn_xAl_{4-x}]^{2-}$ network.[17-20] The appropriate *vec* for $[Zn_2Al_2]^{2-}$ (*vec* = 3.0), $[Zn_1Al_3]^{2-}$ (*vec* = 3.25) and $[Al_4]^{2-}$ (*vec* = 3.5) were used to calculated the relative Mulliken populations and total energies.[21,22] Detailed computational procedures were described in previous chapters. Atomic orbital parameters are as follows. Al: $H_{ii}(3s)$ = -12.3 eV, Hii(3p) = -6.5 eV, $\zeta(3s) = \zeta(3p) = 1.167$), Zn: $H_{ii}(4s)$ = -12.41 eV, $H_{ii}(4p)$ = -6.53 eV, $\zeta(4s) = 2.01$, $\zeta(4p) = 1.70$.

Results

Structure Determination

The site preferences of ternary AZn_xAl_{4-x} compounds were studied by changing the alkaline earth elements as well as the relative mole ratio of Zn to Al (Ae = Mg, Ca, Sr and

Ba, x = 1-3). The following results are separated into three parts for $AeZnAl_3$, $AeZn_2Al_2$, and $AeZn_3Al$ reactions.

1. $AZnAl_3$ (A = Ca-Ba): Reactions in the $AZnAl_3$ system were carried out using Ca, Sr and Ba metals. X-ray powder diffraction patterns indicate that only Sr and Ba reactions gave nearly pure phases of $BaAl_4$-type compounds (space group I4/mmm), whereas the products from the $CaZnAl_3$ reactions contain mixtures of $CaZn_2$, $CaAl_2$, $CaZn_3$ and $BaAl_4$-type compounds ($CaZn_xAl_{4-x}$: a = 4.133(4), c = 11.51(1), V = 196.6(3)). Attempts to pick a single crystal from the $CaZnAl_3$ reactions failed.

Single crystal data were collected from products of Sr- and $BaZnAl_3$ reactions. For each single crystal study, the tetragonal unit cell was indexed during the random search of reflections. Systematic absence conditions of the data set gave 11 possible tetragonal I-centered space groups. Previous studies in Ln-Au-Al systems suggest that *I4mm* (noncentrosymmetric) and *I4/mmm* (centrosymmetric) are two possible space groups for $LnAu_xAl_{4-x}$ phases. In this study, both space groups (*I4mm* and *I4/mmm*) were used for structural analyses. The statistical methods of Wilson plots and Hamilton tests were employed to determine the best structural model.[23-25]

The Wilson plot for each single crystal data set was generated by plotting the fraction of normalized intensity data (f(I)) as a function of normalized intensity from 0.0 to 1.0. The results are shown in Figure 3a. Solid and dashed lines in Figure 3a represent the theoretical fraction of intensity f(I) for centrosymmetric (solid line) and noncentrosymmetric (dashed line) structures. The results indicate that the structure of Sr- and $BaZnAl_3$ are

centrosymmetric because these distribution lines are closer to the ideal centrosymmetric curve than the noncentrosymmetric curve.

The Hamilton test was used to compare the results of structural refinements from two models (space groups *I4mm* and *I4/mmm*). The results of each single crystal data shown in Table 4 indicate that the space group *I4/mmm* is better than the space group *I4mm* in 99 % significant level. The final results are listed in Table 3-5. The refined formula are $SrZn_{0.98(2)}Al_{3.02(3)}$ and $BaZn_{1.18(6)}Al_{2.82(6)}$, respectively.

2. $AeZn_2Al_2$ (Ae = Mg-Ba): X-ray powder patterns for AZn_2Al_2 reactions (A = Mg-Ba) indicate that the reactions of Ca-, Sr- and $BaZn_2Al_2$ gave nearly pure $BaAl_4$-type compounds (space group I4/mmm) with trace amounts of Al. The product of the Mg-Zn-Al (1:2:2) reaction contains a mixture of the Laves phase, $MgZn_2$ (a = 5.218(2) Å, c = 8.538(5) Å, V = 201.3(1) $Å^3$, β = 120°), and Al with no evidence of a $BaAl_4$-type compound. Quenching reactions of $AeZn_2Al_2$ (Ae = Mg-Ba) was performed to synthesize possible ternary phases. X-ray powder patterns indicate that the product from the $MgZn_2Al_2$ reaction contains mixtures of $MgZn_2$ + Al, the product from the Ca- and $SrZn_2Al_2$ reactions single phase. The product from $BaZn_2Al_2$ quenching reaction contains binary phases of $BaZn_5$, a $BaAl_4$-type phase ($BaZn_xAl_{4-x}$, a = 4.182(1) Å, c = 11.436(8) Å, V = 229.7(2) $Å^3$) and trace amount of Al.

Single crystals from the Ca-, Sr and $BaZn_2Al_2$ reactions were selected for structure characterization. The Wilson plots for crystal data on $CaZn_2Al_2$, $SrZn_2Al_2$ and $BaZn_2Al_2$ (two independent data sets) are shown in Figure 3b. The results indicate that the single crystal data of $CaZn_2Al_2$ and $SrZn_2Al_2$ favor centrosymmetric structure. However, the Wilson plot from

two independent $BaZn_2Al_2$ single crystal data suggest different structural models. There are six independent $BaZn_2Al_2$ single crystal data set were collected in this study, the Wilson plots for each data indicate that three data prefer *I4mm* and the other three prefer *I4/mmm* space group. On the other hand, the Hamilton test on these single crystal data favored the centrosymmetric space group I4/mmm.

The crystal data of $AeZn_2Al_2$ (Ae = Ca- Ba) are listed in Table 3-5. The refined compositions are $CaZn_{2.0(1)}Al_{2.0(1)}$, $SrZn_{1.94(3)}Al_{2.06(3)}$ and $BaZn_{1.84(4)}Al_{2.16(4)}$, respectively.

3. AZn_3Al: Reactions of Ae:Zn:Al =1:3:1 (Ae = Ca, Sr, Ba) gave mixtures of $BaAl_4$-type ($AeZn_xAl_{4-x}$, x = 0.0-1.0), binary and elemental phases. Attempts to pick single crystals suitable for structural analyses failed. The unit cell constants of possible $AeZn_xAl_{4-x}$ phases in each Ae-Zn-Al (Ae:Zn:Al =1:3:1) reaction were refined by diffraction lines from Guinier powder patterns. These results are listed in Table 7 together with the refined cell constants from other $AeZn_xAl_{4-x}$ compounds. The cell constants from Ae-Zn-Al reactions (Ae:Zn:Al =1:3:1, Ae = Ca-Ba) are essentially between $AeZnAl_3$ and $AeZn_2Al_2$. The results suggest that the possible ternary $AeZn_xAl_{4-x}$ phase in each Ae-Zn-Al reaction (Ae:Zn:Al =1:3:1) contains Zn/Al composition between 0.33 ($AZnAl_3$) and 1.0 (AZn_2Al_2).

Discussion

1. Structure of AZn_xAl_{4-x} (A = Ca-Ba, x = 1, 2): The structure of $AeZnAl_3$ and $AeZn_2Al_2$ are $BaAl_4$-type (space group I4/mmm). A perspective view of AZn_xAl_{4-x} along the [100] direction is shown in Figure 2a and the two unique positions of M1 (Wycoff site 4e) and M2

(Wycoff site 4d) are labeled. Two significant factors controlling the site preference of Zn on the $^{3}_{\infty}[Zn_xAl_{4-x}]^{2-}$ network were discovered.

According to the results of theoretical studies, the M1 site is more negatively polarized than M2 based on relative Mulliken populations over the *vec* range between 2.75 and 3.5 e/atom. Therefore, a more electronegative element prefers to occupy the M1 site than the M2 site.[11,26] The results of single crystal analyses on $AeZnAl_3$ and $AeZn_2Al_2$ (Ae = Ca-Ba) indicates a similar trend as the theoretical calculations that the M1 and M2 sites favor Zn and Al, respectively.

The effects of relative Zn/Al mole ratio and the effect of the alkaline earth metal on site preference of M1 and M2 sites and structures (distance and angle) are listed in Table 8. When small amounts of Al in the $AeAl_4$ (Ae = Sr, Ba) are replaced by Zn to form $AeZnAl_3$, the M1 site (see results of $SrZnAl_3$ and $BaZnAl_3$ data in Table 3-5) is mixed occupied by Zn and Al closed to 1:1 ratio. The M1-M1 contacts could be a combination of Zn-Al (100%), Zn-Zn(50%) + Al-Al (50%), or some combination of these. Although the ordered structure of Zn and Al on the M1 site was not observed, Extended-Hückel calculations on the model formula of $[ZnAl_3]^{2-}$ (excluding alkaline earth atoms) containing Zn-Al contacts along the *c* axis is more stable than model with Zn-Zn and Al-Al pairs on M1-M1 contacts.[26] The result suggest that the M1-M1 contacts prefer heteroatomic Zn-Al pairs.[11] As more Zn atoms are added into $Ae(Zn_xAl_{4-x})$ to form $AeZn_2Al_2$, the M1 site is nearly 100% occupied by Zn. At this point, the M1 and M2 sites are occupied by two kinds of elements (the ideal composition is AZn_2Al_2 with 100% Zn on M1 and 100% Al on M2 sites). When x is larger than 2 for $AeZn_xAl_{4-x}$, the additional Zn atoms will occupy M2 site to generate Zn-Zn contacts on the

ab plane. However, the Zn-rich phases, such as $AeZn_3Al$, were not observed. The results indicate that both Zn and Al can occupy the M1 sites. On the other hand, the M2 site is always Al rich (> 75 at%). According to the experiments, a phase width is observed in Sr- and $BaZn_xAl_{4-x}$ ($0 \leq x \leq 2$) systems and the *vec* range is between 3.0 ($AeZn_2Al_2$) and 3.5 ($AeAl_4$) e⁻/atom. For $CaZn_xAl_{4-x}$ system, only $CaZn_2Al_2$ (*vec* = 3.0 e/atom) exists.

Size Effect on Alkaline Earth Atom

The second factor controlling the site preference is the size effect of the alkaline earth atoms. According to the crystal data in Table 7, the cell constants and cell volumes of AZn_2Al_2 increase as the size of the alkaline earth elements increase from Ca to Ba. The site preference of M1 and M2 sites for Zn and interatomic distances from Ca-, Sr and $BaZn_2Al_2$ crystal data are shown in Figure 5. As we can see from Figure 5a, M1 and M2 sites become more "disordered" when the atom size is increased from Ca to Ba. The Zn occupancy on the M1 site decreases from 92% to 66% and the M2 site is increases from 5% to 25% as alkaline earth metals in $AeZn_2Al_2$ changes from Ca to Ba. The interatomic distances from Ca- to $BaZn_2Al_2$ are shown in Figure 5b. For contacts between the alkaline earth atom and the $[Zn_2Al_2]^{2-}$ network, the A-M1 distance increases 8.5 % from Ca to Ba. On the other hand, the interatomic distances in the $[Zn_2Al_2]^{2-}$ network show several interesting features. First of all, the M1-M2 distance is only slightly changed (increased by 2.2%). The M1-M1 and M2-M2 distances are increased by 8.2% and the M1-M2-M1 angle (α) increases by 4.9%. The overall effects increase the *a/c* ratio and unit cell volumes. Second, the distance range of M2-M2 contact is between 2.9 and 3.2 Å. On the other hand, the M1-M1 distance varies from 2.49 to 2.71 Å.[27] The M1-M2 distance is essentially fixed between 2.63 and 2.69 Å. The results

indicate that the size of the alkaline earth atom affect the M1-M1 and M2-M2 distances more than M1-M2 distances. The interatomic distance may play a role to the site preference of Zn and Al atoms. Similar trends were also found in the $AZnAl_3$ system. Although only $SrZnAl_3$ and $BaZnAl_3$ were observed, only $BaZnAl_3$ allowed partial occupancy of Zn on the M2 site.

Physical properties

Magnetic susceptibility measurements at 3T for the $AeZnAl_3$ and $AeZn_2Al_2$ samples show temperature-independent magnetic behavior over the range 50-273 K. After the diamagnetic core correction, all samples show paramagnetic behavior and the results are illustrated in Figure 7. For $AZnAl_3$ systems, the average susceptibility of $SrZnAl_3$ and $BaZnAl_3$ are $6.1x10^{-5}$ and $7.7x10^{-5}$ emu/mole, values that are on the order of Pauli paramagnetic behavior. For $AeZn_2Al_2$ (Ae = Ca-Ba), the results for $SrZn_2Al_2$ and $BaZn_2Al_2$ show similar temperature-independent molar susceptibilities as the $AeZnAl_3$ ($5.1\ x10^{-5}$ for $SrZn_2Al_2$ and $3.5\ x10^{-5}$ for $BaZn_2Al_2$). The magnetic susceptibility of Sr- and $BaZn_xAl_{4-x}$ (x = 1, 2) decreases when the Zn composition increases. The magnetic behavior of $CaZn_2Al_2$ is quite different than that of Sr- and $BaZn_2Al_2$ samples. The molar susceptibility of $CaZn_2Al_2$ gradually decreases from $1.0x10^{-3}$ to $5.0x10^{-4}$ emu/mol when the temperature is increased from 50 to 300K. The magnetic susceptibility is significantly larger than Sr- and $BaZn_2Al_2$ samples for the whole temperature range (50-300K). Below 50 K, the susceptibility of $CaZn_2Al_2$ increases due to the contributions of impurities.

Conclusions

Ternary $AeZn_xAl_{4-x}$ systems were characterized to study the effects of alkaline earth elements and the Zn/Al ratio on the site preference problem in $BaAl_4$-type structures. All compounds show centrosymmetric structure types (space group I4/mmm). The site preference for Zn and Al atoms is affected by the size of alkaline earth element and by the electronegativity of Zn and Al. The phase width in AZn_xAl_{4-x} was observed in Sr- and $BaZn_xAl_{4-x}$ systems ($0.0 \leq x \leq 2.0$).

References

1) Villars, P.; Calvert, L. D. *Pearson's Handbook of Crystallographic Data for Intermetallic Phases*; 2nd ed ed.; ASM International, Metals Park OH:, 1991.

2) Note, The vec value of $BaZn_xAl_4$ is calculated from the total number of valence electrons divided by the total number of atoms per formula unit. Ba is excluded because its electronegativity is much smaller than Al.

3) Hulliger, F. *Helv. Phys. Acta* **1985**, *58*, 216-25.

4) Pearson, W. B. *J. Solid State Chem.* **1985**, *56*, 278-87.

5) Burdett, J. K.; Miller, G. J. *Chem. Mater.* **1990**, *2*, 12-26.

6) Zheng, C.; Hoffmann, R. *Z. Naturforsch., B: Anorg. Chem., Org. Chem.* **1986**, *41B*, 292-320.

7) Zheng, C.; Hoffmann, R. *J. Am. Chem. Soc.* **1986**, *108*, 3078-88.

8) Hoffmann, R.; Zheng, C. *J. Phys. Chem.* **1985**, *89*, 4175-81.

9) Ban, Z.; Sikirica, M. *Acta Cryst* **1965**, *18*, 594.

10) Hulliger, F.; Nissen, H.-U.; Wessicken, R. *J. Alloys Compd.* **1994**, *206*, 263-6.

11) Hulliger, F. *J. Alloys Compd.* **1995**, *218*, 255-8.

12) Nordell, K. J. *Exploring Aluminum-Rich Intermetallics with Experiment and Theory*; Iowa Stata University: Ames, 1997.

13) Eisenmann, B.; May, N.; Mueller, W.; Schaefer, H. *Z. Naturforsch. B* **1972**, *27*, 1155-7.

14) Grin, Y. N.; Rogl, P.; Hiebl, K.; Wagner, F. E.; Noël, H. *J. Solid State Chem.* **1987**, *70*, 168.

15) Sheldrick, G. M. *Crystallographic Computing 3*; Sheldrick, G. M., Kruger, C. and Goddard, R., Ed.; Oxford University Press: Oxford,, 1985, pp 175.

16) Sheldrick, G. M. *SHELXTL. Structure Determination Programs*; Version 5.12 ed.; Siemens Analytical X-ray Instruments Inc.: Madison, WI., 1995.

17) Mulay, L. N.; Boudreaux. , E. A. *Theory and applications of molecular diamagnetism*; Wiley: New York, 1976.

18) Hoffmann, R.; Lipscomb, W. N. *J. Chem. Phys.* **1962**, *36*, 2179, 3489.

19) Hoffmann, R. *J. Chem. Phys* **1963**, *39*, 1397.

20) Ammeter, J. H.; Buergi, H. B.; Thibeault, J. C.; Hoffmann, R. *J. Am. Chem. Soc.* **1978**, *100*, 3686-92.

21) Whangbo, M.-H.; Hoffmann, R.; Woodward, R. B. *Proc. R. Soc. London, Ser. A* **1979**, *366*, 23-46.

22) Hughbanks, T.; Hoffmann, R. *J. Am. Chem. Soc.* **1983**, *105*, 3528-37.

23) Wijeyesekera, S. D.; Hoffmann, R. *Organometallics* **1984**, *3*, 949-61.

24) Stout, G. H.; Jensen, L. H. *X-ray Structure Determination: A Practical Guide*; 2nd ed.; John Wiley & Sons, Inc.: New York, 1989.

25) Wilson, A. J. C. *Nature* **1942**, *150*, 151.

26) Hamilton, W. C. *Acta Cryst* **1965**, *18*, 502.

27) Lee, C.-S., Mulliken population analyses of $[Al_4]^{2-}$ network (vec = 11-14) based on extended Hückel tight-binding methods. Unpublished results.

28) Huheey, J. E. *Inorganic Chemistry. 3rd Ed*; Harper and Row, New York, N. Y.:, 1983.

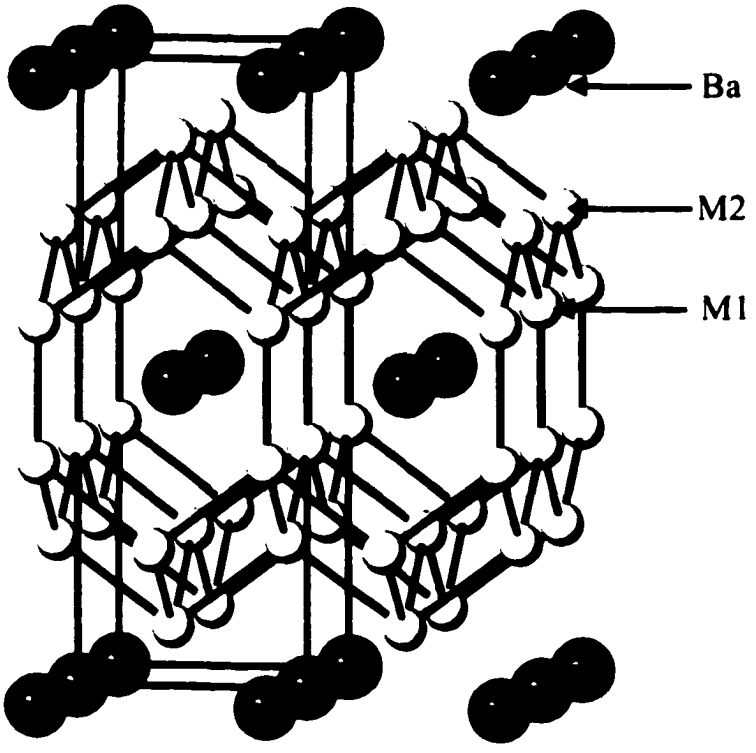

Figure 1. The crystal structure of $BaAl_4$ projected along [100]. The Ba atoms are drawn in big filled black ball and Al atoms (both M1 and M2) are white balls. Two independent positions on $^{3}_{\infty}[Al_4]^{2-}$ network (M1 and M2) are labeled.

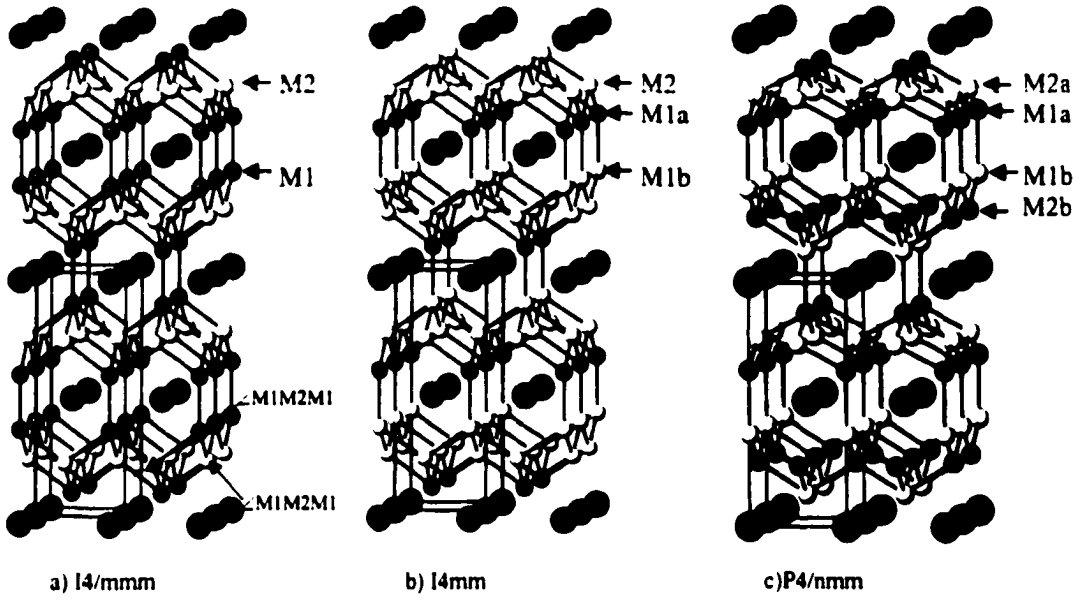

Figure 2. $BaAl_4$-type derivatives. a) $BaAl_4$ structure: Au and Al mixed occupy on M1 sites. b) $BaZnSn_3$-type structure: Au and Al are ordered in M1a (black, Au) and M1b (white, Al). c) $CaBe_2Ge_2$-type structure: both M1 and M2 sites from $BaAl_4$ structure are seperated to M1a, M2b(black, Be) and M1b, M2a (Ge) sites.

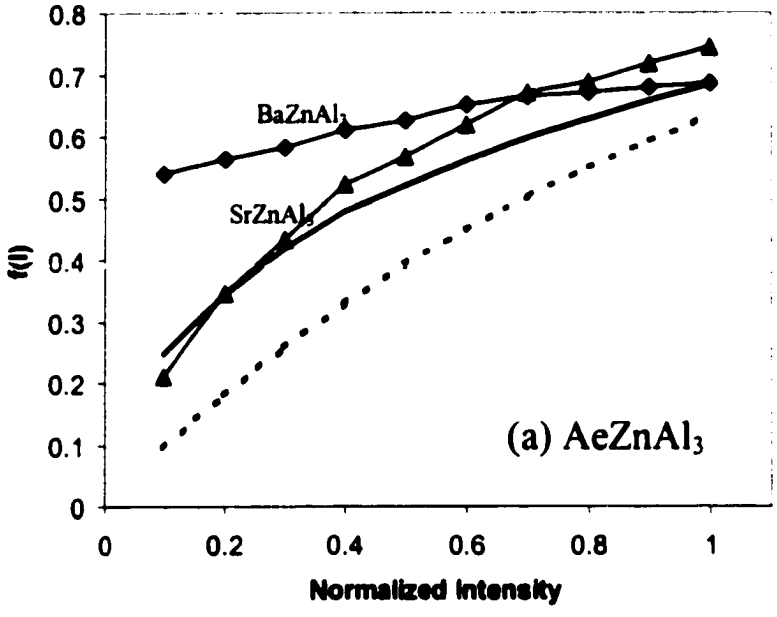

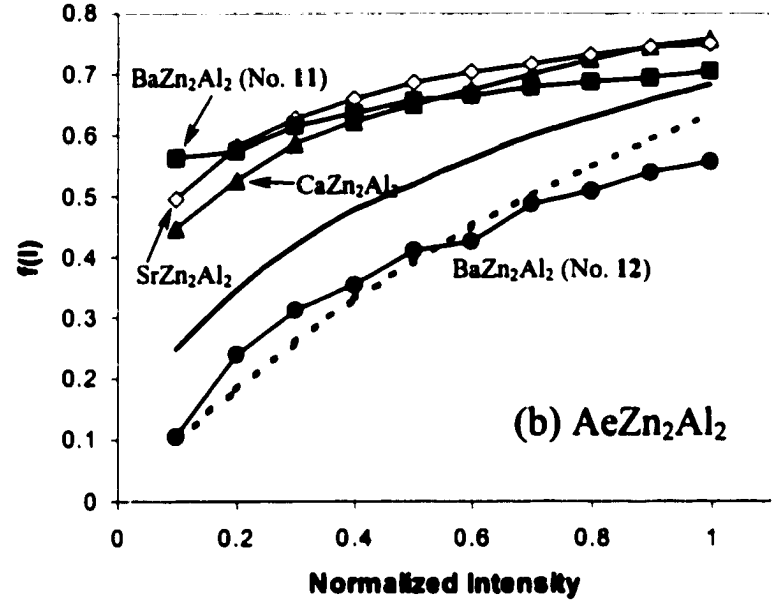

Figure 3. Wilson plot of single crystal data for a) $AZnAl_3$ and b) AZn_2Al_2 (A = Ca, Sr, Zn). The solid and dashed lines represent the theoretical curves for centro- (black) and noncentrosymmetric (dashed) structures.

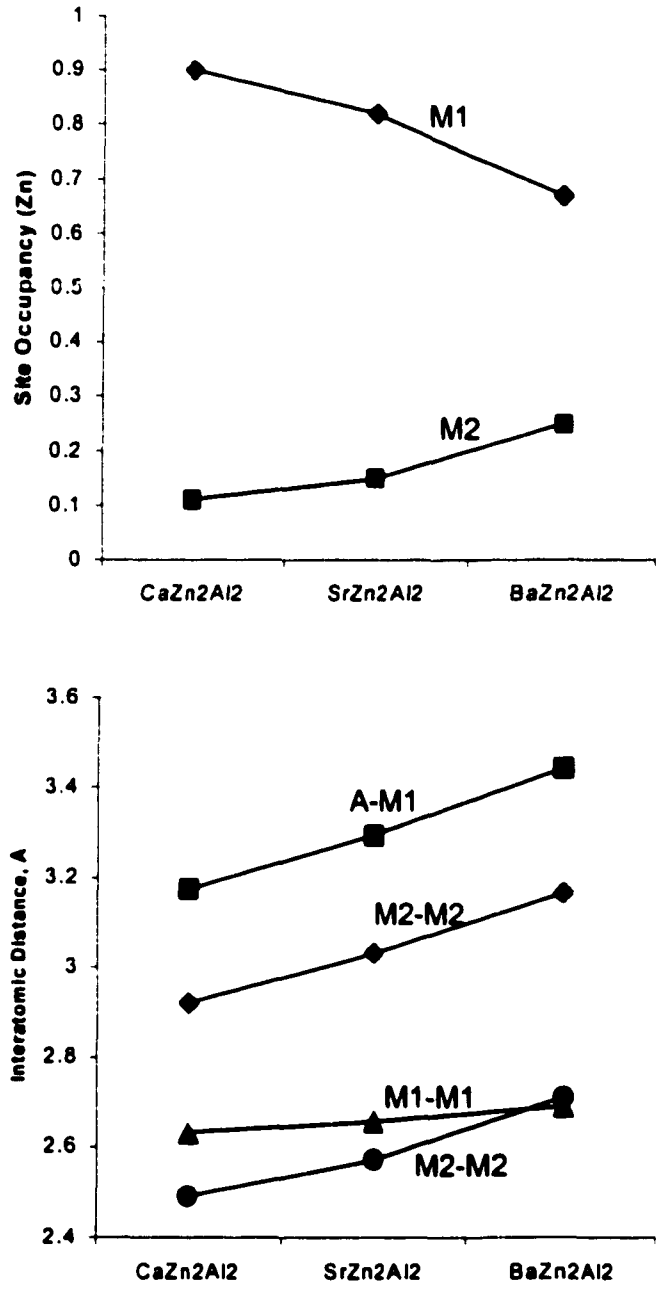

Figure 4. Effect of alkaline earth metal on Ca-, Sr- and $BaZn_2Al_2$ structure. a) Zn occupany , b) Interatomic distance (Å).

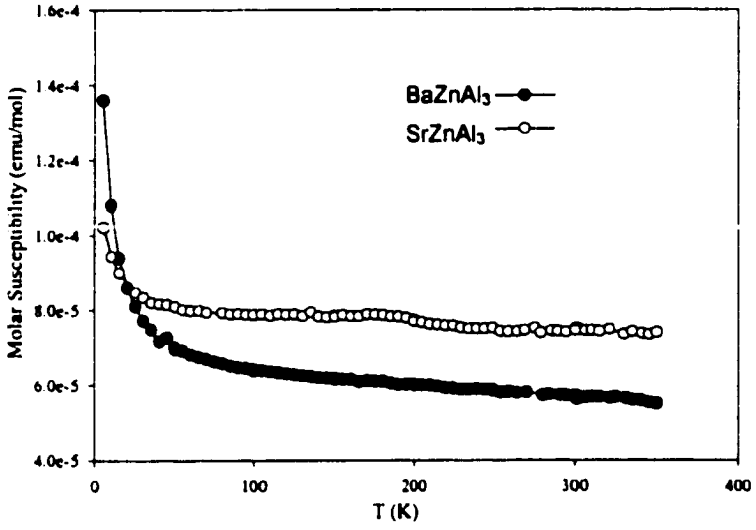

a)

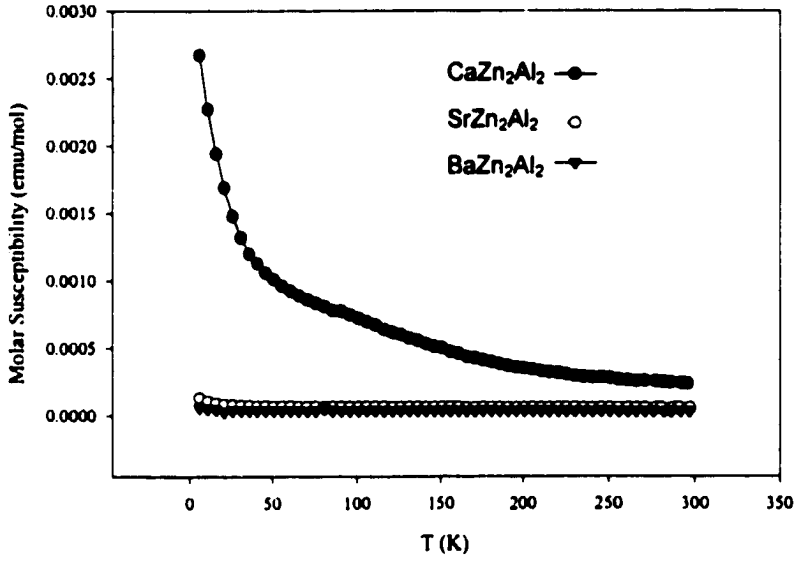

b)

Figure 5. The molar magnetic susceptibilities of a) $SrZnAl_3$ (filled circle) and $BaZnAl_3$ (empty circle). b) $CaZn_2Al_2$ (filled circle), $SrZn_2Al_2$ (empty circle) and $BaZn_2Al_2$ (filled triangle).

Table 1. Summary of reaction compositions and products identification for various AZn_xAl_{4-x} reactions (A = Mg, Ca, Sr, Ba; x = 1-3).

Reactions	Identified Phase	Comment
1. x=1		
$CaZnAl_3$	$CaZn_xAl_{4-x}$ + CaZn2 + $CaAl_2$ + $CaZn_3$	powder
$SrZnAl_3$	$SrZnAl_3$ (M) + Al(t)	powder, single crystal
$BaZnAl_3$	$BaZnAl_3$ (M)	powder, single crystal
2. x=2		
$MgZn_2Al_2$	$MgZn_2$ (M) + Al	powder, single crystal
$CaZn_2Al_2$	$CaZn_2Al_2$ (M) + Al (t)	powder, single crystal
$SrZn_2Al_2$	$SrZn_2Al_2$ (M) + Al (t)	powder, single crystal
$BaZn_2Al_2$	$BaZn_2Al_2$ (M)	powder, single crystal
3. x=3		
$CaZn_3Al$	$CaZn_xAl_{4-x}$ + $CaZn_5$	powder
$SrZn_3Al$	$SrZn_xAl_{4-x}$ + $SrZn_5$ + Al (t) + Zn (t)	powder
$BaZn_3Al$	$BaZn_xAl_{4-x}$ + $BaZn_5$ (M)	powder

[a] M = major phase; t = trace amounts.

Table 2. Summary of Single Crystal refinements on ternary $BaAl_4$-type compounds in various AZn_xAl_{4-x} (A = Ca, Sr, Ba; x = 1-3) reactions.

No.	Reactions Refined Formula	*a*, Å	*c*, Å	Volume, Å^3	R1/wR2(%);GOF	$2\theta_{max}$	totl/uniq reflns
	x=1						
1	$SrZn_{0.98(2)}Al_{3.02(3)}$	4.2988(4)	11.538(2)	213.21(5)	2.91/8.83; 1.193	60	418/114
2	$SrZn_{1.04(2)}Al_{2.96(2)}$	4.2912(7)	11.517(2)	212.08(6)	2.38/6.28; 1.228	60	790/112
3	$BaZn_{1.23(4)}Al_{2.77(4)}$	4.4751(8)	11.425(2)	227.89(6)	1.90/5.06; 1.234	60	802/126
4	$BaZn_{1.18(6)}Al_{2.82(6)}$	4.4677(7)	11.416(2)	227.89(6)	1.75/4.33; 1.023	60	1500/126
	x = 2						
5	$CaZn_{2.0(1)}Al_{2.0(1)}$	4.1243(8)	11.560(2)	196.6(2)	3.51/7.67; 1.030	60	728/103
6	$CaZn_{2.0(1)}Al_{2.0(1)}$	4.1281(9)	11.525(2)	196.39(7)	1.49/4.02; 1.022	52	1140/62
7	$SrZn_{0.98(2)}Al_{3.02(3)}$	4.2889(8)	11.423(2)	210.13(6)	1.51/4.15; 1.051	120	2740/113
8	$SrZn_{2.21(4)}Al_{1.89(4)}$	4.2832(6)	11.384(2)	208.56(5)	2.74/6.3; 1.13	55	509/94
9	$SrZn_{2.24(1)}Al_{1.86(1)}$	4.2856(5)	11.379(2)	208.99(6)	1.91/4.90; 1.174	55	622/94
10	$SrZn_{2.16(3)}Al_{1.84(3)}$	4.2840(4)	11.392(2)	209.07(3)	3.54/9.56; 1.075	75	1375/196
11	$BaZn_{1.85(8)}Al_{2.15(8)}$	4.472(1)	11.430(4)	228.6(1)	2.87/6.64; 1.042	55	340/100
12	$BaZn_{1.84(4)}Al_{2.16(4)}$	4.4768(6)	11.403(2)	228.54(6)	1.36/3.19; 1.077	60	1409/118
13	$BaZn_{1.78(4)}Al_{2.22(4)}$	4.4712(6)	11.436(2)	228.63(6)	1.79/2.89; 1.124	60	1500/119
14	$BaZn_{1.68(8)}Al_{2.32(8)}$	4.4584(3)	11.402(3)	226.6(2)	2.47/6.74; 1.077	70	316/80
15	$BaZn_{1.76(8)}Al_{2.24(8)}$	4.4568(2)	11.378(7)	226.0(2)	1.94/5.27; 1.083	60	410/121
16	$BaZn_{1.66(8)}Al_{2.34(8)}$	4.458(2)	11.404(4)	226.6(2)	3.49/8.04; 1.089	75	1432/211

Table 3. Crystal Data and Conditions of Data Collection.

a) $AZnAl_3$ (A = Sr, Ba)

Refined Composition	$SrZn_{0.98(2)}Al_{3.02(3)}$	$BaZn_{1.18(6)}Al_{2.82(6)}$
Instrument	Siemens P4	Regaku AFC6R
form wt (g/mol)	233.93	283.65
Crystal size, mm		
Space group , Z	I4/mmm, 2	
a(Å)	4.298(2)	4.496(2)
c(Å)	11.534(9)	11.49(1)
V(Å^3)	213.1(2)	232.4(2)
d_{calc} (g/cm^3)	1.822	2.067
Abs coeff (mm^{-1})	18.523	14.215
Transmission range	0.537-0.966	0.751-1.0
Temperature, K	293(2)	293(2)
R1, wR2 (all data)	0.0301, 0.0883	0.0189, 0.0433
Goodness-of-fit on F^2	1.193	1.023
Extinction coefficient	0.000(11)	0.008(2)
($\Delta\rho$) max, min (e/Å^3)	1.567, -0.850	0.832, -0.723

[a] $R1 = \sum \| F_o | - | F_c \| \Big/ \sum | F_o |$; $wR2 = \left[\sum \left[w\left(F_o^2 - F_c^2 \right)^2 \right] \Big/ \sum \left[w\left(F_o^2 \right)^2 \right] \right]^{1/2}$, $w = \sigma_F^{-2}$

Table 3. (Continued)

b) AZn_2Al_2 (A = Ca, Sr, Ba)

Refined Composition	$CaZn_{2.0(1)}Al_{2.0(1)}$	$SrZn_{0.98(2)}Al_{3.02(3)}$	$BaZn_{1.84(4)}Al_{2.16(4)}$
Instrument	Rigaku AFC6R	Rigaku AFC6R	Rigaku AFC6R
Form. wt. (g/mol)	225.74	269.63	284.21
Crystal size, mm	0.075x0.075x0.075	0.075x0.1x0.125	0.15x0.175x0.225
Space group , Z		I4/mmm, 2	
a(Å)	4.1281(6)	4.2889(6)	4.4768(6)
c(Å)	11.525(2)	11.423(2)	11.403(2)
V(Å^3)	196.39(6)	210.13(6)	228.54(6)
d_{calc} (g/cm^3)	1.909	2.131	2.297
Abs coeff (mm^{-1})	6.929	11.890	9.169
Transmission range	0.8939-1.0	0.8519-1.0	0.6065-1.0
Temperature, K		293(2)	
R1, wR2 (all data)	0.0204, 0.0402	0.0294, 0.0415	0.0137, 0.0319
Goodness-of-fit on F^2	1.022	1.051	1.077
Extinction coefficient	0.007(4)	0.005(4)	0.0117(15)
($\Delta\rho$) max, min (e/Å^3)	0.440, -0.394	0.546, -0.527	0.475, -1.005

[a] $R1 = \sum \| F_o | - | F_c \| \Big/ \sum | F_o |$; $wR2 = \left[\sum \left[w\left(F_o^2 - F_c^2\right)^2 \right] \Big/ \sum \left[w\left(F_o^2\right)^2 \right] \right]^{1/2}$, $w = \sigma_F^{-2}$

Table 4. Atomic coordinates and equivalent isotropic displacement parameters ($Å^2$) for a) $AeZnAl_3$ (Ae = Sr, Ba) and b) $AeZn_2Al_2$ (Ae = Ca, Sr, Ba). U(eq) is defined as one third of the trace of the orthogonalized U^{ij} tensor.

a) $AeZnAl_3$ (Ae = Sr, Ba)

atom	site	x	y	z	U(eq)		site occ.
$SrZn_{0.98(2)}Al_{3.02(3)}$							
Sr	*2a*	0	0	0	0.015(1)	Sr	1.00
M1	*4e*	0	0	0.3888(2)	0.015(1)	Al	0.51(1)
						Zn	0.49(1)
M2	*4d*	0	0.5000	0.2500	0.015(1)	Al	1.00(1)
$BaZn_{1.18(6)}Al_{2.82(6)}$							
Ba	*2a*	0	0	0	0.010(1)	Ba	1.00
M1	*4e*	0	0	0.3826(1)	0.014(1)	Al	0.52(1)
						Zn	0.48(1)
M2	*4d*	0	0.5000	0.2500	0.014(1)	Al	0.89(2)
						Zn	0.11(2)

Table 4. (Continued)

b) $AeZn_2Al_2$ (Ae = Ca, Sr, Ba)

atom	site	x	y	z	U(eq)		Site occ.
$CaZn_{2.0(1)}Al_{2.0(1)}$							
Ca	*2a*	0	0	0	0.012(1)	Ca	1.00
M1	*4e*	0	0	0.3919(1)	0.011(1)	Al	0.10(3)
						Zn	0.90(3)
M2	*4d*	0	0.5000	0.2500	0.013(1)	Al	0.89(2)
						Zn	0.11(2)
$SrZn_{1.94(3)}Al_{2.06(3)}$							
Sr	*2a*	0	0	0	0.010(1)	Sr	1.00
M1	*4e*	0	0	0.3874(1)	0.011(1)	Al	0.18(1)
						Zn	0.82(1)
M2	*4d*	0	0.5000	0.2500	0.014(1)	Al	0.850(6)
						Zn	0.150(6)
$BaZn_{1.84(4)}Al_{2.16(4)}$							
Ba	*2a*	0	0	0	0.011(1)	Ba	1.00
M1	*4e*	0	0	0.3812(1)	0.015(1)	Al	0.33(1)
						Zn	0.67(1)
M2	*4d*	0	0.5000	0.2500	0.017(1)	Al	0.75(1)
						Zn	0.25(1)

Table 5. Selected Bond lengths [Å] for $AeZn_xAl_{4-x}$ (Ae = Ca, Sr, Ba; x = 1.0-2.2).

	A-M1	M1-M1	M1-M2	M2-M2
$SrZn_{0.98(2)}Al_{3.02(3)}$	3.2992(7)	2.565(4)	2.681(1)	3.0397(3)
$BaZn_{1.18(6)}Al_{2.82(6)}$	3.4318(5)	2.680(2)	2.6986(6)	3.1593(4)
$CaZn_{2.0(1)}Al_{2.0(1)}$	3.1737(5)	2.491(2)	2.6334(7)	2.9190(4)
$SrZn_{1.94(3)}Al_{2.06(3)}$	3.2943(5)	2.573(1)	2.6574(5)	3.0327(4)
$BaZn_{1.84(4)}Al_{2.16(4)}$	3.4434(5)	2.710(2)	2.6922(5)	3.1656(4)

Table 6. Results of Wilson plot and Hamilton tests.

No.	Data	Wilson Plot	Hamilton Test
1	SrZnAl3	I4/mmm	I4/mmm
2	SrZnAl3	I4/mmm	I4/mmm
3	BaZnAl3	I4/mmm	I4/mmm
4	BaZnAl3	I4/mmm	I4/mmm
11	$BaZn_2Al_2$	I4mm	I4mm[a]
12	$BaZn_2Al_2$	I4/mmm	I4/mmm
13	$BaZn_2Al_2$	I4/mmm	I4/mmm
14	$BaZn_2Al_2$	I4mm	I4mm[b]
15	$BaZn_2Al_2$	I4mm	I4/mmm
16	$BaZn_2Al_2$	I4/mmm	I4/mmm

[a]Significant level > 25%. [b]Significant level > 99%.

Table 7. Summary of calculated cell constants for $BaAl_4$-type compounds from $AeZn_xAl_{4-x}$ (Ae = Ca-Ba, x = 1.0 - 3.0) reactions.

Reactions		Ca	Sr	Ba
AZn_3Al[a]	a (Å)	4.122(3)	4.301(3)	4.487(3)
	c (Å)	11.51(1)	11.37(2)	11.47(1)
	a/c	0.36	0.38	0.39
	V ($Å^3$)	195.5(2)	210.3(3)	231.0(3)
AZn_2Al_2	a (Å)	4.122(1)	4.2172(9)	4.4602(9)
	c (Å)	11.512(8)	11.417(4)	11.376(5)
	a/c	0.36	0.37	0.39
	V ($Å^3$)	195.6(1)	208.28(9)	226.3(1)
$AZnAl_3$[b]	a (Å)	4.133(4)	4.298(2)	4.496(2)
	c (Å)	11.51(1)	11.534(9)	11.49(1)
	a/c	0.36	0.37	0.39
	V ($Å^3$)	196.6(3)	213.1(2)	232.4(2)
AAl_4[c]				
	a (Å)	4.35	4.46	4.539(3)
	c (Å)	11.07	11.12	11.16(1)
	a/c	0.39	0.39	0.41
	V ($Å^3$)	209.8	221.3	229.92

[a] Product contains mixtures of binary (A-Zn and A-Al) and $BaAl_4$-type compounds.

[b] $CaZnAl_3$ product contains mixtures of binary (A-Zn and A-Al) and $BaAl_4$-type compounds.

[c] Pearson Handbook of Crystallographic Data for intermetallic phases (1991).

Table 8. Crystal data of $AeZn_xAl_{4-x}$ (Ae = Ca-Ba, x = 1.0, 2.0).

		Ca	Sr	Ba
x = 2	a (Å)	4.122(1)	4.2172(9)	4.4602(9)
	c (Å)	11.512(8)	11.417(4)	11.376(5)
	a/c	0.36	0.37	0.39
	V ($Å^3$)	195.6(1)	208.28(9)	226.3(1)
	M1-M1	2.491(2)	2.573(2)	2.710(2)
	M1-M2	2.6334(7)	2.6574(5)	2.6922(5)
	M2-M2	2.9190(4)	3.0327(4)	3.1656(4)
	M1 (Zn %)	90(3)	82(1)	67(1)
	M2 (Zn %)	11(2)	15.0(6)	25(1)
	∠M1M2M1(α)	103.22(3)	107.60(3)	107.98(1)
	∠M1M2M1(β)	112.69(2)	110.41(1)	112.49(3)
x = 1	a (Å)		4.298(2)	4.496(2)
	c (Å)		11.534(9)	11.49(1)
	a/c		0.37	0.39
	V ($Å^3$)		213.1(2)	232.4(2)
	M1-M1		2.565(4)	2.680(2)
	M1-M2		2.681(1)	2.6986(6)
	M2-M2		3.0397(3)	3.1593(4)
	M1 (Zn %)		49(1)	48(1)
	M2 (Zn %)		0	11(2)
	∠M1M2M1(α)		106.61(6)	108.34(2)
	∠M1M2M1(β)		110.92(3)	111.75(3)

CHAPTER 6

$Ba_{14}Zn_5Al_{22}$: A NEW TERNARY INTERMETALLIC COMPOUND WITH A NOVEL 2D NETWORK

A paper to be submitted To *J. Solid State Chem.*
Chi-Shen Lee and Gordon J. Miller

Abstract

A new ternary intermetallic compound $Ba_{14}Zn_5Al_{22}$ was synthesized by heating the pure elements at 800 °C followed by slow cooling in a sealed Ta tube. The compound crystallizes in the monoclinic space group *I2/m*, Z = 2, with a = 10.474(2) Å, b = 6.0834(14) Å, c = 34.697(8) Å and β = 90.814(4)°. The crystal structure of $Ba_{14}Zn_5Al_{22}$ contains slabs of Zn-Al networks that contain a novel two dimensional (2D) network. Extended-Hückel Band calculations have been performed to understand the relationship between the composition and orbital interactions for Zn-Al contacts.

Introduction

Synthetic efforts on Ae-Zn-Al systems (Ae = Mg, Ca, Sr, Ba) have identified several intermetallic compounds that are intermediate between Hume-Rothery type and Zintl type , e.g., $BaZn_{10}Al_2$ (*vec* = 2.33), $(Mg_xLi_{1-x})_{2-z}(Zn_yAl_{1-y})_{3+z}$ (*vec* = 2.0-2.5) and $AeZn_xAl_{4-x}$ (Ae = Ca, Sr, Ba; x = 0-2; *vec* = 3.0-3.5).[1-4] These compounds show different Zn-Al networks with *vec* ranges between 2.0 and 3.25. Like Hume-Rothery phases, compounds with phase widths were observed in $(Mg_xLi_{1-x})_{2-z}(Zn_yAl_{1-y})_{3+z}$ and $AeZn_xAl_{4-x}$ systems. On the other hand, $BaZn_{10}Al_2$ (*vec* = 2.33) shows a fixed composition, similar to Zintl phases. Theoretical calculations of the electronic structure indicate that the bonding character of the Zn-Al

framework has an important influence on the phase width and chemical composition.[2,3] Furthermore, the atomic site preferences for Zn and Al atoms in these various structures is affected by coordination environment and the atom size of alkaline earth metals.[2,3,5]

During investigation of the $Ba(Zn_xAl_{1-x})_2$ (x = 0.0-1.0; *vec* = 3.0-4.0) system, a new ternary compound, $Ba_{14}Zn_5Al_{22}$, was synthesized. In this chapter, the structural characterization and theoretical calculations of the title compound are presented.

Experimental

Synthesis and Characterization

All reactions were prepared in an Ar-filled glovebox with the concentration of O_2 lower than 10 ppm. Starting materials included Ba turnings (Johnson-Matthey, 99.9 %), Zn powder (Alfa, 99.9%), Al ingot (Alfa, 99.9999%), and Al foil. The exploratory reactions of $Ba(Zn_xAl_{1-x})_2$, x varying from 1.0 to 1.0, were carried out in Ta ampoules. Reactant mixtures were heated to 900 °C under dynamic vacuum for 6 hours, then cooled to 400 °C at the rate of 5°C/hour and finally rapidly cooled to room temperature. Each product appears as brittle, silver colored ingots that are both air and moisture sensitive. The surfaces of all products turned from silver to dark black in 2 days inside the glovebox. Guinier powder X-ray diffraction patterns (Enraf-Nonius Guinier camera, Cu $K\alpha_1$ radiation (λ = 1.54056 Å), internal standard = Si powder) were used for preliminary characterizations (see Table 1). The observed diffraction patterns usually gave weak diffraction intensities. For the products from Zn-rich reactions, the X-ray powder patterns identified mixtures of known binary phases. On the other hand, interesting results were observed for products from the Zn-poor region. Powder patterns from products of two Zn-poor reactions (Ba:Zn:Al = 1:0.4:1.6 and 1:0.5:1.5)

show positions of diffraction lines similar to those of the theoretical pattern of Ba_7Al_{13}. However, there is a weak line at 2θ ~10° that cannot be identified which suggests this product to be a new phase with a structure type similar to Ba_7Al_{13}. A quench experiment was performed by using liquid N_2 for one Zn-poor reaction (Ba:Zn:Al = 1:0.5:1.75) and the result (based on the Guinier powder pattern) is the same as the product obtained from slow cooling process. The preliminary single crystal characterizations (see below) suggest a possible composition of $Ba_7Zn_3Al_{10}$.

Attempts to synthesize new ternary phase based on the stoichiometries of Ba:Zn:Al = 7:3:10 were performed using the same heating procedures. Single crystal X-ray diffraction was carried out and the best result gave the refined formula, $Ba_{14}Zn_5Al_{22}$. Subsequent reactions based on the final refined composition gave nearly pure phase of the title compound with trace amounts of Al.

Single Crystal X-ray Analysis and Structure Determination

Needle- and plate-shaped single crystals were selected from crushed products in an Ar-filled glovebox, mounted and sealed inside a glass capillary, and the quality was checked by means of rotation photographs on Siemens P4 or Rigaku AFC6R diffractometers. Several single crystal data sets were collected on a Bruker Smart CCD diffractometer both at room and low temperature (-163 (2) °C). Unfortunately, most of the samples were twinned crystals that could be used for structural analyses. Procedures for intensity data collection and structure determination were described in Chapter 3.[6-8] Several structural models have been used for different single crystal data sets and are discussed below. Table 2 lists some important data and refined formula based on three independent single crystal data collections.

1. **Model A (Hexagonal):** The first single crystal data were collected on a Siemens P4 diffractometer (Mo Kα radiation, λ=0.71073 Å). The unit cell indexed from 25 random-search reflections ($15° \leq 2\theta \leq 40°$) gave a hexagonal unit cell (a = 6.0686(8) Å, c = 17.224(5) Å), which is close to Ba_7Al_{13} (a = 6.099(2) Å, c = 17.269(6) Å, space group $P\bar{3}m1$). The fractional search routine and axial photos along each axis were performed, but supercell reflections were detected. A single crystal data set was then collected based on the hexagonal unit cell and the structure was solved by direct methods. The crystal structure shows features similar to Ba_7Al_{13}, and the refined composition is $Ba_7Zn_3Al_{10}$ (R1/wR2 = 5.83/14.07, Goodness of Fit (GOF) = 1.095, Table 2). The structure of the **Model A** is shown in Figure 2. The Zn atoms are located at the center of the unit cell (z ~ 0.5) and the layer of trigonal bipyramids is 100 %Al. The central layer contains two inequivalent sites at (-0.076(2), 0.462(1), 0.4848(5)) (70% Zn) and (0.27(2), 0.637(8), 0.527(3)) (30% Zn) to form a puckered network. The atomic position and thermal displacement parameters for Ba and Al atoms are reasonable except for the Zn atoms in the central region of Zn-Al network. Interatomic M-M contacts in the central layer are less than 0.9 Å. These results indicate that the structure solution is not complete and superstructure may exist.

2. **Model B (Monoclinic):** The second single crystal data set was collected on a Siemens Smart CCD single crystal diffractometer (Mo Kα radiation, λ=0.71073 Å). More than 30 single crystal samples were checked and they all showed poor diffraction peaks or twining. To avoid reflections from a twinned crystal, very small crystals were selected for X-ray study. One single crystal data set was successfully

measured at room temperature (25(2) °C) over a hemisphere of reciprocal space. (0.04×0.07×0.08 mm^3). The monoclinic unit cell constants were indexed by the observed reflections with $I/\sigma > 20$ from the intensity data to be a = 10.541(4) Å, b = 6.086(3) Å, c = 17.431(7) Å, β = 90.317(11)°. This unit cell is close to an orthorhombic supercell ($\sqrt{3}a$, b, c) of Ba_7Al_{13} (a, b, c are corresponding to the hexagonal cell). Since the β angle is very close to 90°, zone photos of [0kl], [h0l] and [hk0] planes were taken to check their reflection symmetry and the results confirmed the monoclinic model. The statistical analyses (Wilson test) indicate a centrosymmetric structure with Laue group *2/m*. The unconventional space group *I2/m* was selected to compare with the Ba_7Al_{13}-type structure. The structure was then solved by the direct methods and the possible atom positions were selected with the aid of Atoms 5.0 software.[9] The crystal structure of **Model B** is shown in Figure 3. This model is still not correct because the thermal displacement parameters of u_{11} and u_{33} on M6 and interatomic distance of M7-M7 are not reasonable. Some results of the refinements are listed in Table 2.

3. **Model C (Monoclinic):** A single crystal sample from the product of the $Ba_7Zn_3Al_{10}$ reaction was used for single crystal data collection on a Siemens Smart CCD single crystal diffractometer (Mo Kα radiation, λ=0.71073 Å). The intensity data were collected from the whole sphere of reciprocal space at room temperature 25(2) °C. Attempts to index the unit cell from the intensity data gave an even larger monoclinic unit cell than **Model B** which is close to ($\sqrt{3}$a, b, 2c) of the hexagonal cell of

Ba_7Al_{13}. Least-squares refinement of the intensity data gave the best fit with a monoclinic cell, a = 10.474(2) Å, b = 6.0834(14) Å, c = 34.697(8) Å, β = 90.814(4) °. The space group was determined by the same procedures as 2.2.1 and the unconventional space group *12/m* was selected. The structure was solved by direct methods and the initial electron density map showed 7 large peaks (assigned as Ba) atoms and 11 smaller peaks (assigned as Al). Initial least-squares refinements using Ba and Al atoms were performed with fixed isotropic thermal displacement parameters. After a few refinement cycles, the R-factor significantly decreased to less than 20%. The site occupancies were then refined to identify the relative electron density at each site. The Ba sites are 100% occupied and the four Al sites are mix-occupied by both Zn and Al atoms. Subsequent refinements were able to refine anisotropic thermal displacement parameters on each site. The final structural refinement gave R-factors of R1/ wR2 = 0.0649/0.1667 for all data and the highest residual electron density is 4.911 e/Å^3 (0.80 Å from Ba2). Important crystal data, positional, thermal displacement parameters (iso- and anisotropic) and selected interatomic distances for $Ba_{14}Zn_5Al_{22}$ (crystal No 5) are listed in Table 3-6. The calculated pattern based on the **Model C** ($Ba_{14}Zn_5Al_{22}$) was generated and compared with Ba_7Al_{13} (see Figure 4). The calculated powder pattern for **Model C** ($Ba_{14}Zn_5Al_{22}$, Figure 4b) shows similar positions of diffraction lines to the calculated powder pattern for Ba_7Al_{13} pattern (Figure 4a) in 2θ ranges between 10 and 50°. There are two positions ([002] and [004]) on the calculated $Ba_{14}Zn_5Al_{22}$ pattern in

low 2θ region (2θ < 10°) that are not shown on the calculated Ba_7Al_{13} pattern. The Guinier powder pattern for $Ba_{14}Zn_5Al_{22}$ sample only found the [004] line.

4. **Model D (Monoclinic):** Models with unit cell constants larger than **Model C** could be indexed by supercell reflections. These peaks are weak ($10 \le I/\sigma \le 15$) and broad, and therefore, difficult to locate the positions of these reflections. One of these possible supercell models has a monoclinic unit cell close to ($2\sqrt{3}$ a, 2b, 2c) of the hexagonal cell with $\beta = 90.805(6)°$ (see Table 2 No 6). However, attempts to solve the crystal structure failed (R-factors > 20 %). Some results are listed in Table 2.

5. **Other Models:** During the structure refinement of a data set for **Model C**, there were about 4% of all reflections that could not be indexed and refined due to significant differences between the observed and calculated intensities. These reflections are located at high 2θ region (≥ 30°), and are assigned to the minor contribution of a twin crystal. The orientation matrix between the refined model and the twin crystal is:

$$\begin{pmatrix} a' \\ b' \\ c' \end{pmatrix} = \begin{bmatrix} 1-2\times\sin(90-\beta) & 0 & 0 \\ 0 & 1 & 0 \\ 0 & 0 & -1 \end{bmatrix} \begin{pmatrix} a \\ b \\ c \end{pmatrix}, \beta=90.8°$$

The diffraction points between the main crystal and twin crystal are very close because the β angle is near 90°. According to the image data, overlapping diffraction peaks do not split until 2θ is larger than 30°. The other poorly fit reflections (~ 6%) show narrow peak widths along the a^* and b^* axes ($\Delta\theta < 0.8°$) and wide peak widths along the c^* axis ($\Delta\theta > 0.8°$). Therefore, a superstructure with large unit cell constants along the *c*-axis may exist.

Electronic Structure Calculations

Extended-Hückel tight-binding band calculations were carried out on a hypothetical formula, $[Al_{27}]^{28-}$, to understand the bonding character of the anionic network in $Ba_{14}Zn_5Al_{22}$.[10-13] Atoms from barium atom were excluded from the calculations and only Al parameters were used in the anionic Zn-Al network. Detailed procedures are described in Chapter 3.[14-16] Atomic orbital parameters are as follows. Al: $H_{ii}(3s) = -12.3$ eV, $H_{ii}(3p) = -6.5$ eV, $\zeta(3s) = \zeta(3p) = 1.167$).

Results and Discussion

Structure Description

In the binary phases, $BaZn_2$[17] adopts the $CeCu_2$ structure type with a three-dimensional network (*vec* = 3.0). Ba_7Al_{13}[18,19] shows a two-dimensional network (*vec* = 4.1). The *vec* of the title compound $Ba_{14}Zn_5Al_{22}$ (*vec* = 3.85) is close to Ba_7Al_{13}. The general view of $Ba_{14}Zn_5Al_{22}$ (99% probability thermal ellipsoids) along [100] direction is shown in Figure 5. The structure contains discrete Zn-Al slabs with Ba atoms in the vacancies (interstitial region). The Zn-Al slab can be described as $^2_\infty\{[Al_5][MAl_4]\}$-$^2_\infty[M_7]$-$^2_\infty\{[Al_5][MAl_4]\}$ (M= Zn+Al). The arrangement of barium atoms (represented by light gray ellipsoids) forms two types of stacking structures, shown in Figure 6. One stacking pattern is a distorted cubic close-pack (*ccp*) structure (Ba4, Ba5 and Ba7) and the second type is a distorted cubic-diamond structure (Ba1, Ba2, Ba3 and Ba6). The stacking of Ba atoms in $Ba_{14}Zn_5Al_{22}$ is essentially the same as the Ba stacking in Ba_7Al_{13} except that the structure is distorted from trigonal to monoclinic symmetry. The average distance between two Ba atoms is 3.8(1) Å.

The Zn-Al network in $Ba_{14}Zn_5Al_{22}$ is similar to the Al substructure of Ba_7Al_{13}. However, two unique features were found in the ionic network of $Ba_{14}Zn_5Al_{22}$. The Zn-Al network forms a combination of two $^2_\infty[M_5]$ layers surrounding a novel 2D network of $^2_\infty[M_7]$. Furthermore, Zn atoms are found only on atomic positions in the central region, especially in the central 2D layer and all Zn/Al mixed occupied sites are four coordinate (d(M-M) < 3.0 Å). A single slab of the Zn-Al network is drawn in Figure 7 (Ba atoms are omitted for clarity). The outer layers of the slab are $^2_\infty[M_5]$ sheets built up of trigonal bipyramidal clusters, and one of the axial positions is partially occupied by Zn ($^2_\infty[Al_5]$ (*tbp*-1) and $^2_\infty[MAl_4]$ (*tbp*-2) units, see the shaded clusters in Figure 7). The M10 site in tbp-2 has a Zn/Al ratio of 0.214(4)/0.786(4). The average interatomic distance between two *tbp* units is 2.86 Å, which is shorter than the intra-atomic distances within each *tbp* cluster (3.06 Å). The electronic structure of the $^2_\infty[Al_5]$ layer has been studied, the results based on the bonding character (overlap populations) indicate that the interaction between two *tbp* clusters is stronger than intra-cluster bonding on the equatorial edge of a *tpb* cluster. Therefore, the intercluster distances are shorter than the intracluster distances. The observed distances in $Ba_{14}Zn_5Al_{22}$ are consistent with the structure data of Ba_7Al_{13}, Ba_3Al_5 and Ba_4Al_5.[19-22]

The title compound contains a novel 2D network $^2_\infty[M_7]$ in the center of the Zn-Al slab. The refined formula for this net ($^2_\infty[M_7]$) is close to $^2_\infty[Zn_{4.3}Al_{2.7}]$. There are seven atoms per unit cell (M8x4, M9 and M11x2) and each atom is mixed-occupied by Zn and Al. The M8 site forms alternating short-long contacts of M8-M8 pairs (2.524(5) and 3.559(5) Å) along *b* axis, and its coordination environment is close to tetrahedral (see Figure 7). The M9

site is connected to four M8 atoms (d(M8-M9) = 2.662(2) Å) lying on a plane and two Al16 atoms (3.262 (7) Å) from top and bottom to form a corner-sharing tetrahedral clusters. The local structure around M9 atom can be considered as a partial structure of Ba_7Al_{13} (or $MgCu_2$ type structure). The M11 site generates M11-M11 pairs (2.66 Å) along the *a* axis. Each M11-M11 pair is coordinated to four M8 and two M10 atoms to form a fragment similar to staggered ethane, see Figure 7. Such local structure around the M11-M11 pair is similar to the coordination environment of a Zn-Zn pair in the structure of $BaZn_2$ (see Figure 1 for the structure of $BaZn_2$). Combining the local structure of M9 and M11, the local structure in the central region of Zn-Al slab contains two types of fragments resembling the partial structure of Ba_7Al_{13} and $BaZn_2$.[17,19] Detailed comparison between $Ba_{14}Zn_5Al_{22}$ and other binary phases are described later in this section.

Another way to describe the structure of the $^2_\infty[M_7]$ sheet is based on two types of octagons (*oct-1* and *oct-2*), shown in Figure 8a. The *oct-1* units are made up of two M8-M8 pairs and two M11-M11 dimers connected along the *b*-axis by sharing edges (M11-M11 pair). The *oct-2* units are made up of four M8, two M9 and two M10 atoms linked along the *b*-axis by sharing a corner (a M9 atom). These two types of octagonal rings are alternately connected by sharing M8(x2) and M11 atoms. The structure of the $^2_\infty[M_7]$ layer, therefore, can be written $(3838)(38^3)(8^3)$ based on the number of triangular face (3) or octagon ring (8) generated on each individual position (M8 = 38^2, M9 = 3838, M11 = 8^3).[23] Comparing with Ba_7Al_{13}, the corresponding 2D layer (Kagomé net) can be written as a (3636) network (see Figure 8b).

There are four types of Zn-Al polyhedra centered by Ba atoms compared to one type of Friauf polyhedron for Ba_7Al_{13}. These polyhedra are shown in Figure 9. As we can see in Figure 9a, the Friauf polyhedron contains 12 Zn/Al atoms to form a truncated tetrahedron. Additional Ba atoms cap each hexagonal face. Therefore, the Al framework in Ba_7Al_{13} is made up of fused Friauf polyhedra sharing three hexagonal faces to form 2D slabs.[19] The polyhedra in $Ba_{14}Zn_5Al_{22}$ are quite different due to the $(3838)(38^3)(8^3)$ network in the center of the Zn-Al network. The Zn-Al polyhedra in $Ba_{14}Zn_5Al_{22}$ (radii < 4.0 Å of Ba) are irregular shaped with 12, 13 (two types) and 14 vertices (see Figure 9b-e). Ba atoms cap distorted hexagonal faces or irregular shapes of 6, 7 and 8 membered Zn-Al rings. (Note: the structure of Ba_7Al_{13} may need to be reinvestigated because the Al atom on the Kagomé network gave an unreasonable isotropic thermal parameter).[19]

The structure of $Ba_{14}Zn_5Al_{22}$ may be considered as an intermediate structure type between $BaAl_2$ (H. P. phase, 3D structure) and Ba_7Al_{13} (2D structure).[20-22] The comparison is shown in Figure 10. The $BaAl_2$- and $MgZn_2$-type structures represent two types of fused Friauf polyhedral networks (Figure 10a).[18,24,25] When the Ba concentration is increased, the Zn-Al networks are transformed from 3D structures ($BaAl_2$, $BaZn_2$) to 2D slabs (Ba_7Al_{13}, $Ba_{14}Zn_5Al_{22}$). The partial structure of Ba_7Al_{13} contains combinations of $MgCu_2$- and $MgZn_2$-type structures (Figure 10c). On the other hand, the similar slabs in $Ba_{14}Zn_5Al_{22}$ preserve the $MgZn_2$-type fragment, but the central region contain fragments similar to both $MgCu_2$ (or Ba_7Al_{13} partial structure) and $BaZn_2$ structure types (Figure 10b). Finally, only the 2D layer of trigonal bipyramidal clusters exists in the structures of Ba_3Al_5 and Ba_4Al_5 (Figure 10c).

The structural transition for the $Ba(Zn,Al)_{1+x}$ system indicates that the dimensionality of the Zn-Al network is reduced as the concentration of Ba increased.[26-28]

Is $Ba_{14}Zn_5Al_{22}$ a Zintl phase?

The formal charges of Zn and Al atoms in the $Ba_{14}Zn_5Al_{22}$ (*vec* = 3.85) were examined to see if the Zintl concept can be applied. If Ba is a two-electrons donor, the formal charge on the Zn-Al network should be -28, i.e. $[Zn_5Al_{22}]^{28-}$. Using the shortest interatomic contacts (< 3.0 A) in the Zn-Al framework as the index for "bonding" interactions, the coordination numbers on each (Zn, Al) atom can be grouped into (1)three-bonded trigonal pyramid (Al12-13), (2) four-bonded tetrahedral (Al14-15, Al17-18, M9-M11), (3) four-bonded planar (M9) and (4) five-bonded (Al16). The formal charge of an atomic site is calculated by the difference between the number of valence electrons and the number of bonding electrons. For example, the M11 site contains 38.6(4)/61.4(4) at% Zn/Al and each M11 is coordinated to four atoms (M8×2 + M10 + M11). The formal charge of M11 is,

$$(0.386\times2 + 0.614\times3) - 4.0 = -1.386$$

The total charge of the Zn-Al slab according to this prescription is $[Zn_5Al_{22}]^{35.8-}$. Clearly the calculated formal charge is too large for electrons from 14 Ba atoms (28 e^-).

The second attempt to assign the formal charge was carried out using the average covalent bonding scheme. The number of electron pairs, two-center two-electron (2c,2e) and three-center two-electron (3c,2e) bonds were considered to calculate the number of bonding electrons. For atoms with three interatomic contacts (Al12, Al13), each is involved in three 2c,2e bonds plus one electron pair. Therefore, the formal charge is

3 - (3 + 2) = -2.

On the other hand, Al11 and Al14 are four coordinated, with two 2c, 2e bonds (perpendicular to plane) and two 3c,2e bonds (parallel to plane).[29] The other four coordinate positions were assigned to four 2c, 2e bonds (M8, M10). The five coordinated atom Al16 is assigned as three 2c,2e bonds to two Al15 and one Al17 atoms, and one 3c2e bond with M8 atoms. The bonding scheme for M9 is assigned as one electron pair (perpendicular to the plane) plus two 2c,2e and one 3c,2e bonds along the plane to four M8 atoms. The summary for bonding on each atom is listed in Table 8. The total charge of this model is $[Zn_5Al_{22}]^{25.65-}$. The total charges of $[Zn_5Al_{22}]^{n-}$ are close to the electrons of 14 Ba (28 e^-), however, the charge difference between Ba and (Zn,Al) atoms is still not balanced.

The third attempt was carried out by theoretical band calculations on the model $[Al_{27}]^{28-}$. The effect of orbital interactions on each atom were analyzed to determine the site-preference as well as the optimal composition in terms of maximum overlap populations from all Zn-Al contacts.[4,5,30] Detailed procedures are described in Chapter 2 and 3. The densities of states (DOS) curves are shown in Figure 11a. The dashed line indicates the Fermi level appropriate to $Ba_{14}Zn_5Al_{22}$ (*vec* = 3.85). Partial DOS for $^2_\infty[Al_5]$ and $^2_\infty[Al_7]$ contributions are shown in gray and black shaded areas. The Fermi level at *vec* = 3.85 is located inside a big band (mostly contributed by Al(3p) orbitals) at -6.4 eV. The contributions of electronic states near the Fermi level are from both atoms on $^2_\infty[M_7]$ and $^2_\infty[M_5]$ layers.

The COOP curves for Al-Al contacts within the $^{2}_{\infty}[Al_5]$ (solid), and $^{2}_{\infty}[Al_7]$ (long dashed) layers, as well as between layers ($^{2}_{\infty}[Al_5]$- $^{2}_{\infty}[Al_7]$, round dot) are shown in Figure 11b. The overlap populations (OP) for all Al-Al contacts are close to the optimized values when *vec* is between 3.8 and 4.0 ($\Delta OP < 2\%$). The transition from bonding to antibonding character exists in a narrow region of *vec*. If optimized bonding on the Zn-Al network is a requirement for the stable composition, the phase width of this system should be narrow due to the sharp transition from bonding to antibonding character in the DOS.

Conclusions

The structure of a new ternary intermetallic $Ba_{14}Zn_5Al_{22}$ was determined in this study. Theoretical calculations on the bonding characters of Zn-Al framework show a sharp transition within a narrow range of *vec* and the result parallels the experiments (narrow phase width).

References

1)Lee, C.-S.; Miller, G. J. *J. Am. Chem. Soc.* **2000**, *122*, 4937-4947.

2)Lee, C.-S.; Miller, G. J. *manuscript in preparation* **2000**.

3)Lee, C.-S.; Miller, G. J. *manuscript in preparation* **2000**.

4)Lee, C.-S.; Miller, G. J. *manuscript in preparation* **2000**.

5)Miller, G. J. *Eur. J. Inorg. Chem.* **1998**, 523-536.

6)*SAINT*; Version 4 ed.; Siemens Analytical X-ray Instruments Inc.: Madison, WI., 1995.

7)Sheldrick, G. M. *SHELXTL. Structure Determination Programs*; Version 5.12 ed.; Siemens Analytical X-ray Instruments Inc.: Madison, WI., 1995.

8)Sheldrick, G. M. *Crystallographic Computing 3*; Sheldrick, G. M., Kruger, C. and Goddard, R., Ed.; Oxford University Press: Oxford,, 1985, pp 175.

9)Dowty, E. *Atoms*; 4.0 ed., 1997.

10)Hoffmann, R.; Lipscomb, W. N. *J. Chem. Phys.* **1962**, *36*, 2179, 3489.

11)Hoffmann, R. *J. Chem. Phys* **1963**, *39*, 1397.

12)Ammeter, J. H.; Buergi, H. B.; Thibeault, J. C.; Hoffmann, R. *J. Am. Chem. Soc.* **1978**, *100*, 3686-92.

13)Whangbo, M.-H.; Hoffmann, R.; Woodward, R. B. *Proc. R. Soc. London, Ser. A* **1979**, *366*, 23-46.

14)Hughbanks, T.; Hoffmann, R. *J. Am. Chem. Soc.* **1983**, *105*, 3528-37.

15)Wijeyesekera, S. D.; Hoffmann, R. *Organometallics* **1984**, *3*, 949-61.

16)Chadi, D. J.; Cohen, M. L. *Phys. Rev. B* **1973**, *8*, 5474.

17)Bruzzone, G.; Ferretti, M.; Merlo, F. *J. Solid State Chem.* **1985**, *114*, 305.

18)Cordier, G.; Czech, E.; Schäfer, H. *Z. Naturforsch., B: Anorg. Chem., Org. Chem.* **1984**, *39B*, 421.

19)Fornasini, M. L.; Bruzzone, G. *J. Less-Common Metals* **1975**, *40*, 335.

20)Fornasini, M. L. *Acta Crystallogr., Sect. C: Cryst. Struct. Commun.* **1988**, *44C*, 1355.

21)Fornasini, M. L. *Acta Crystallogr., Sect. B* **1975**, *31B*, 2551.

22)Corbett, J. D. *Unpublished result* **1999**.

23)Pearson, W. B. *The Crystal Chemistry and Physics of metals and alloys*; Wieley-Interscience: New York, 1972.

24)Villars, P.; Calvert, L. D. *Pearson's Handbook of Crystallographic Data for Intermetallic Phases*; 2nd ed ed.; ASM International, Metals Park OH:, 1991.

25)Pearson, W. B. *The Crystal Chemistry and Physics of Metals and Alloy*; Wiley - Interscience, New York:, 1972.

26)Schaefer, H. *Annu. Rev. Mater. Sci.* **1985**, *15*, 1-41.

27)Schaefer, H.; Eisenmann, B.; Mueller, W. *Angew. Chem.* **1973**, *85*, 742-60.

28)Nesper, R. *Angew. Chem.* **1991**, *103*, 805-34 (See also Angew. Chem., Int. Ed. Engl., 1991, 30(7), 789-817).

29)Miller, G. J. *Structure and bonding at the Zintl border*; Kauzlarich, S. M., Ed.; VCH, New York, N, 1996, pp 1-59.

30)Nordell, K. J. *Exploring Aluminum-Rich Intermetallics with Experiment and Theory*; Iowa Stata University: Ames, 1997.

31)Nesper, R.; Miller, G. J. *J. Alloys Compd.* **1993**, *197*, 109-21.

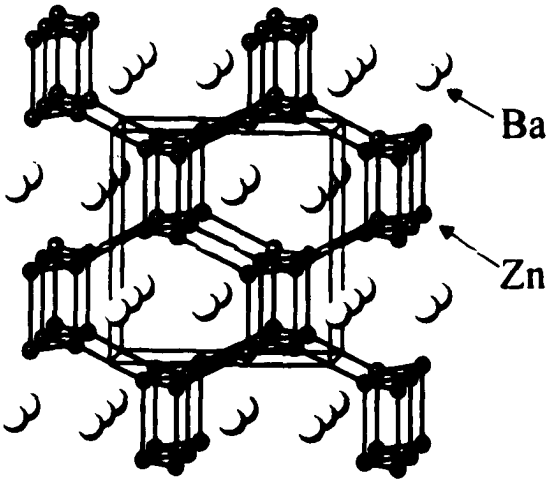

(a) $BaZn_2$

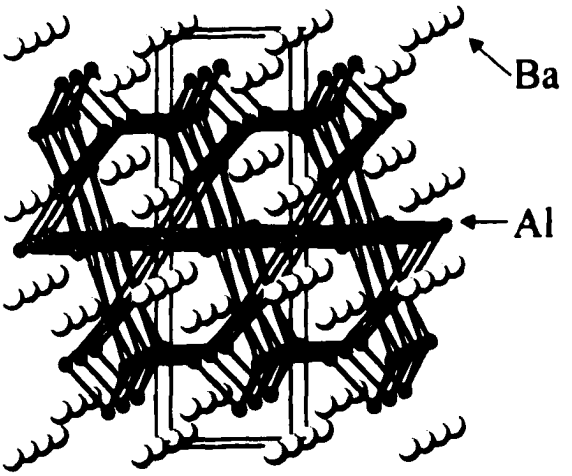

(b) B_7Al_{13}

Figure 1. Gernaral views of (a) $BaZn_2$-type structure and 9b) Ba_7Al_{13} type structure. Black sticks are used to present the ionic framework on each structure and the unit cell is outlined.

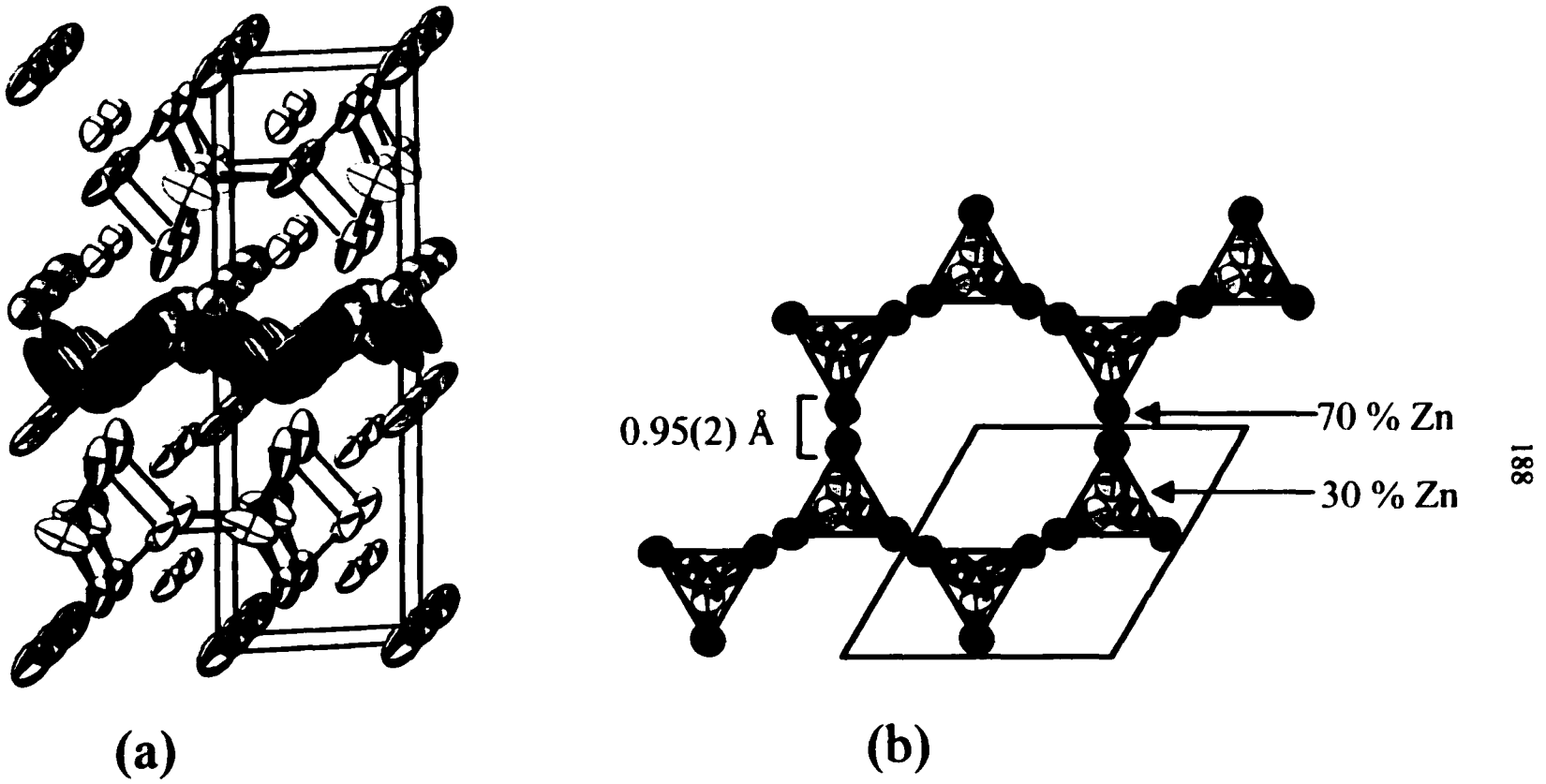

Figure 2. (a) The structure of **Model A** viewed along [100]. The thermal ellipsoid parameters are drawn with 99% probability size. (b) The Zn network near z = 0.5 (50% probability size). The unreasonable interatomic distances are labeled.

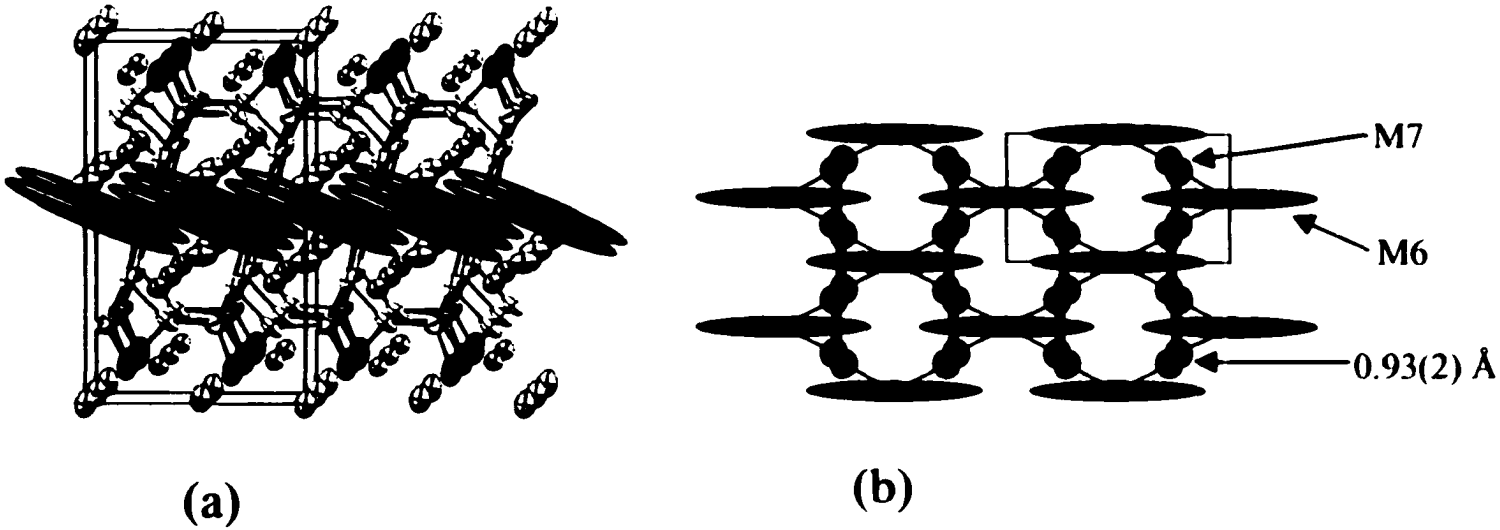

Figure 3. The structure of **Model B** with 99% probability size of thermal ellipsoid parameters. (a) A general view near [100]. (b) The Zn network near z = 0.5 showing the unreasonable thermal displacement parameters and interatomic distances.

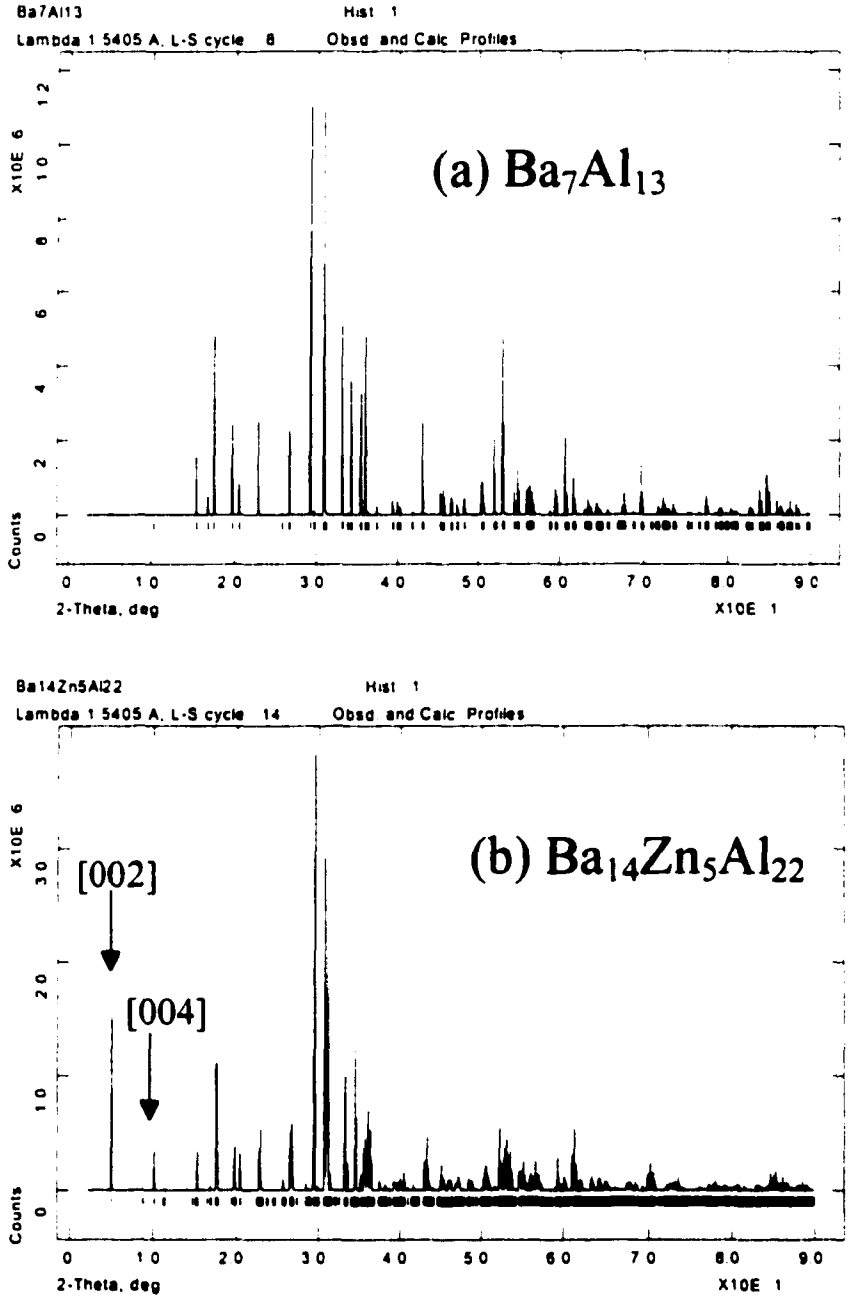

Figure 4. Theoretical powder patterns of (a) Ba_7Al_{13} and (b) $Ba_{14}Zn_5Al_{22}$. The graphs were generated by GSAS software package.[32]

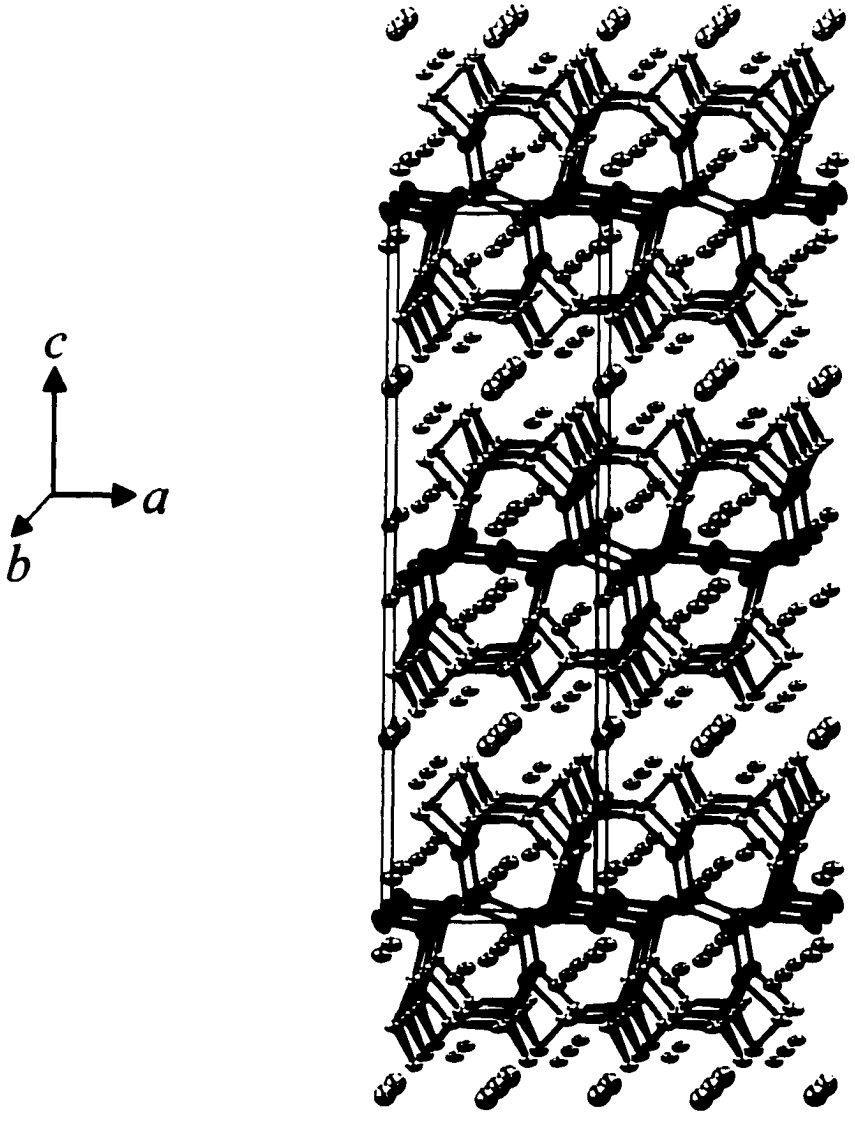

Figure 5. The crystal structure of $Ba_{14}Zn_5Al_{22}$ projected along [100] (**Model C**). Ba atoms are drawn in isolated light gray spheres and Zn/Al atoms are white and dark gray spheres connected by black sticks (d < 2.9 Å). The thermal ellipsoid parameters are drawn with 99% probability size.

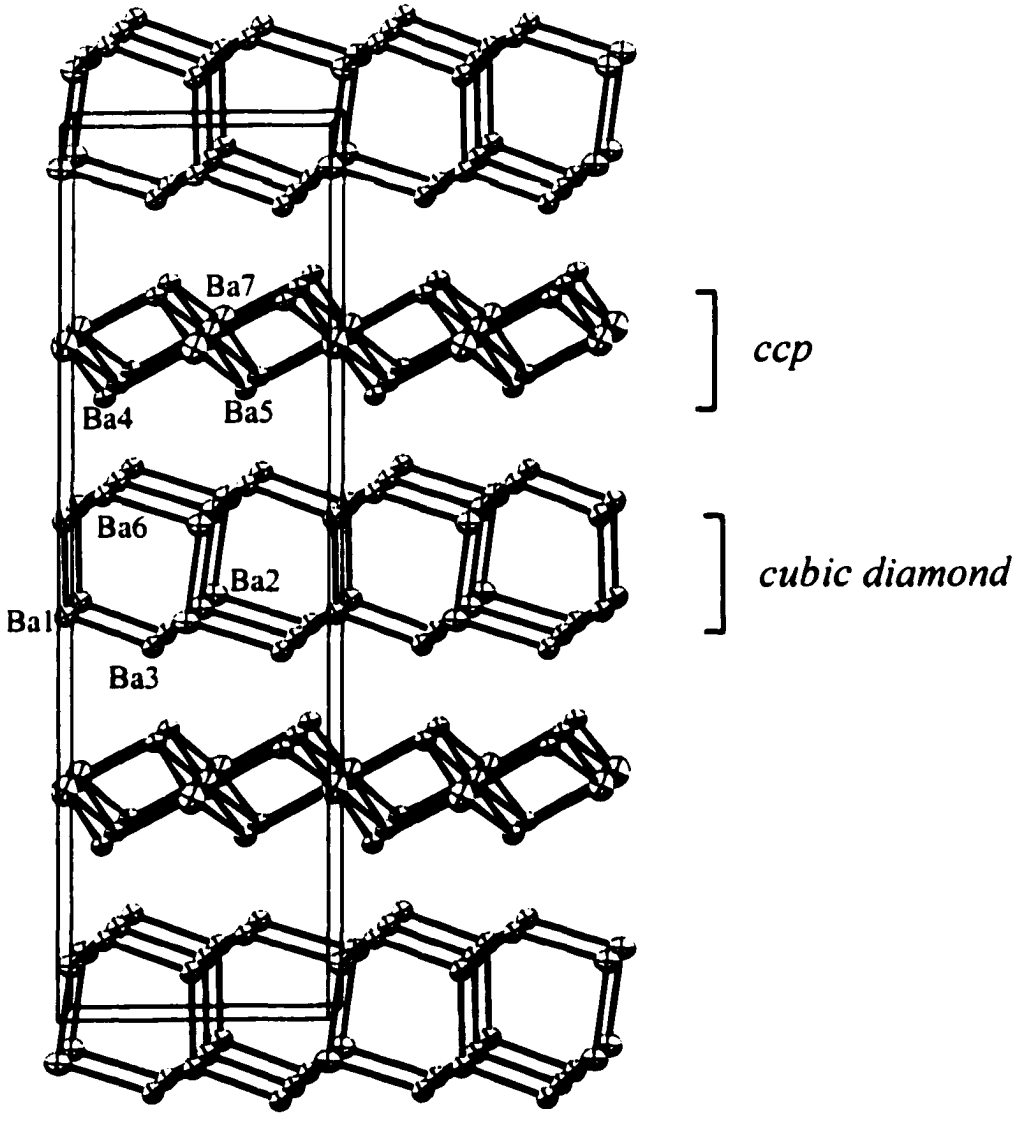

Figure 6. The Ba substructures in $Ba_{14}Zn_5Al_{22}$. The Ba-Ba contacts within each sub structure (d < 3.9 Å) are connected but omit the contacts between substructures. (a) distorted cubic close pack (ccp) on Ba4, Ba5 and Ba7 atoms (2) distorted cubic diamond structure on Ba1, Ba2, Ba3 and Ba6 atoms.

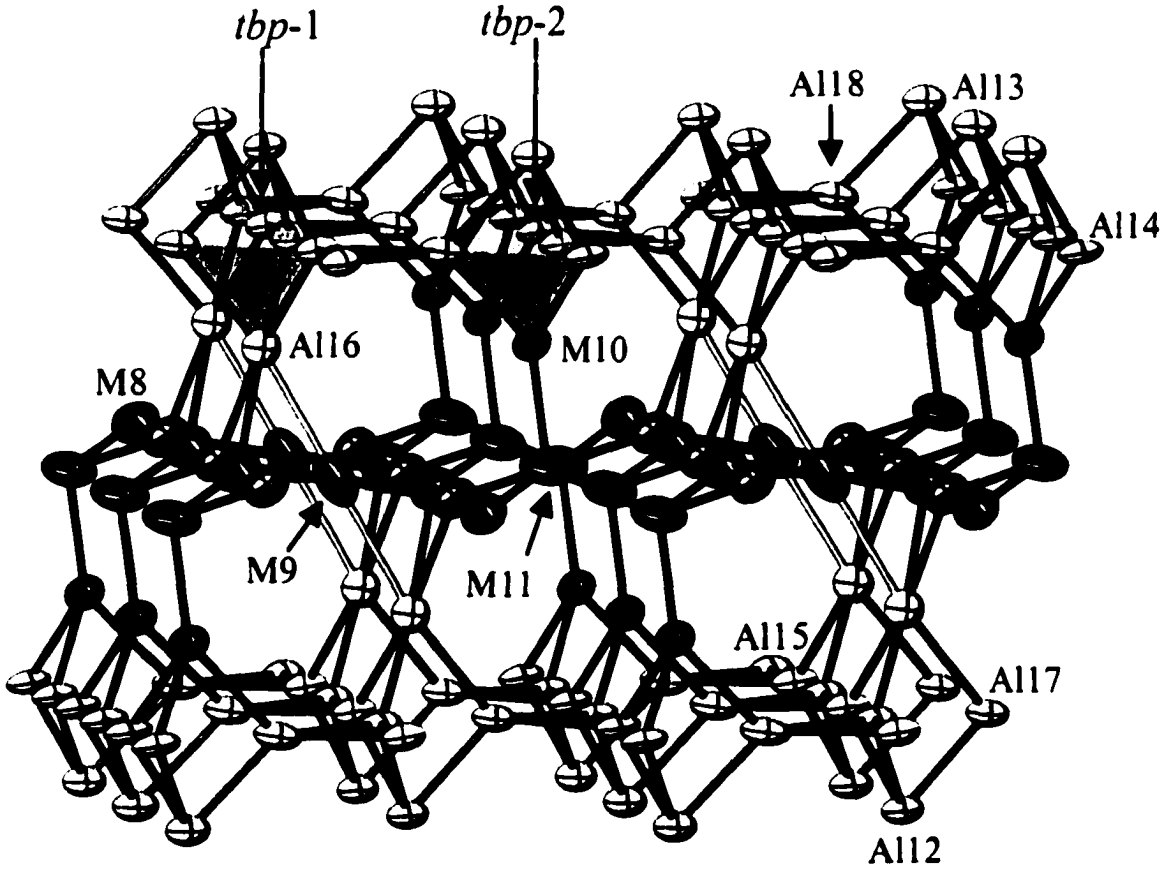

Figure 7. A single slab of $^{2}_{\infty}\{[MAl_4][Al_5]\}$-$^{2}_{\infty}[M_7]$-$^{2}_{\infty}\{[MAl_4][Al_5]\}$ (M = Zn + Al). M8-M11 atoms are drawn in dark gray color and the other Al atoms are white. Ba atoms are omit for clarity.

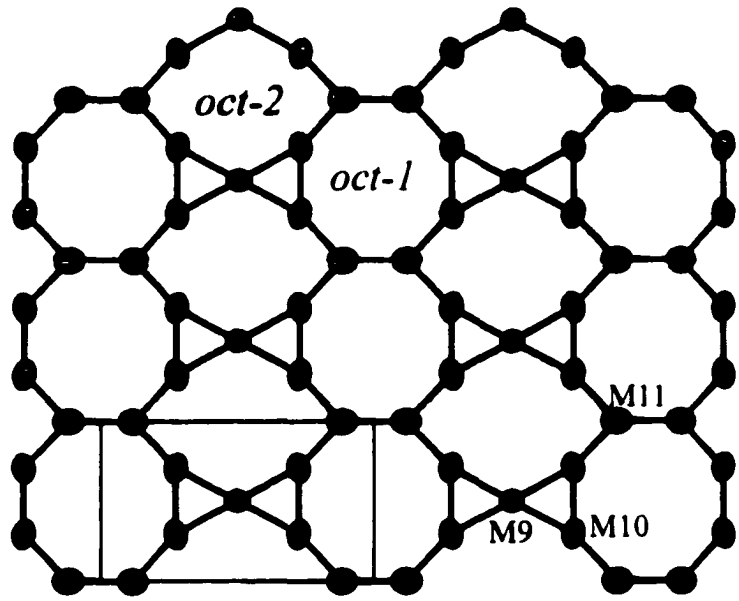

(a) (3838)(38^2)(8^3) network ($Ba_{14}Zn_5Al_{22}$)

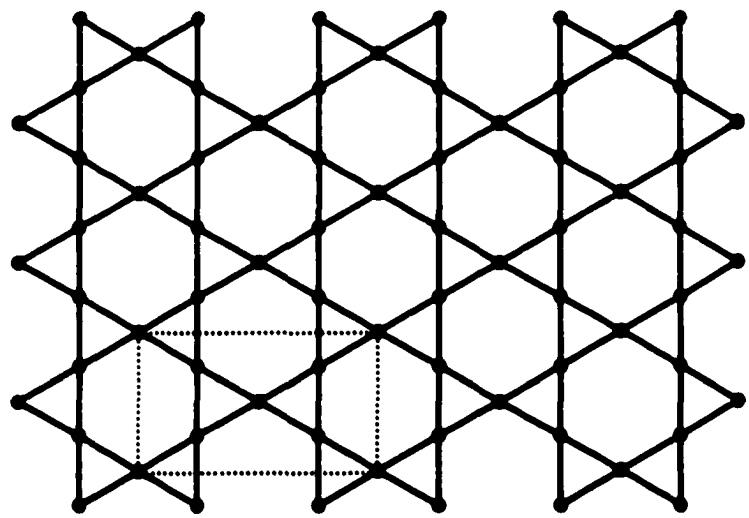

(b) (3636) network (Ba_7Al_{13})

Figure 8. (a) The (3838)(38^3)(8^3) network from $Ba_{14}Zn_5Al_{22}$.(b) The (3636) network from Ba_7Al_{13}. The dashed rectangles in both (a) and (b) represent the similar building unit from Kagomé net.

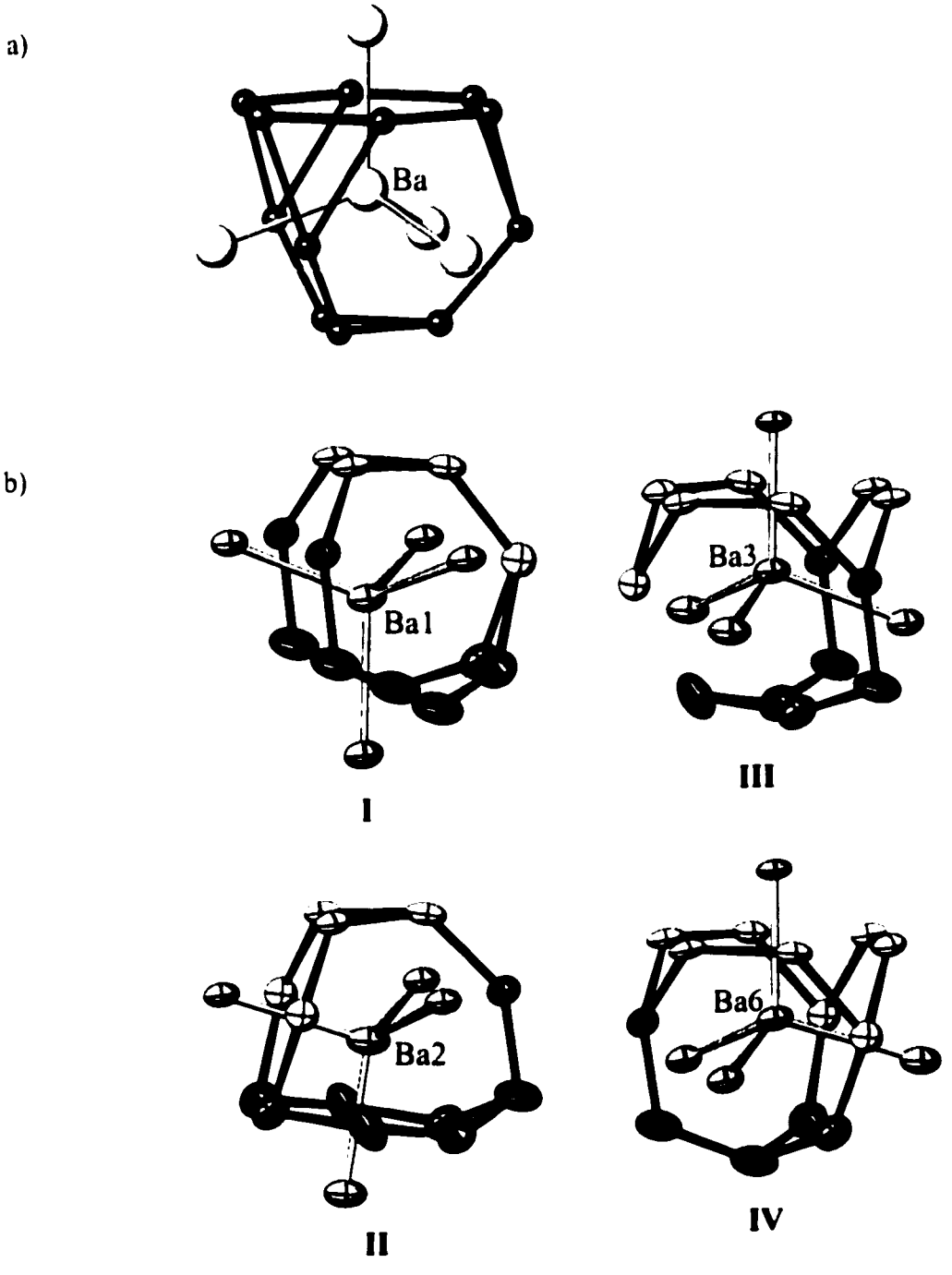

Figure 9. (a) The regular Frauf polyhedron from Ba_7Al_{13}. (b) The polyhedra units for $Ba_{14}Zn_5Al_{22}$ centered by Ba1(**I**), Ba2 (**II**), Ba3 (**III**) and Ba6 (**IV**).

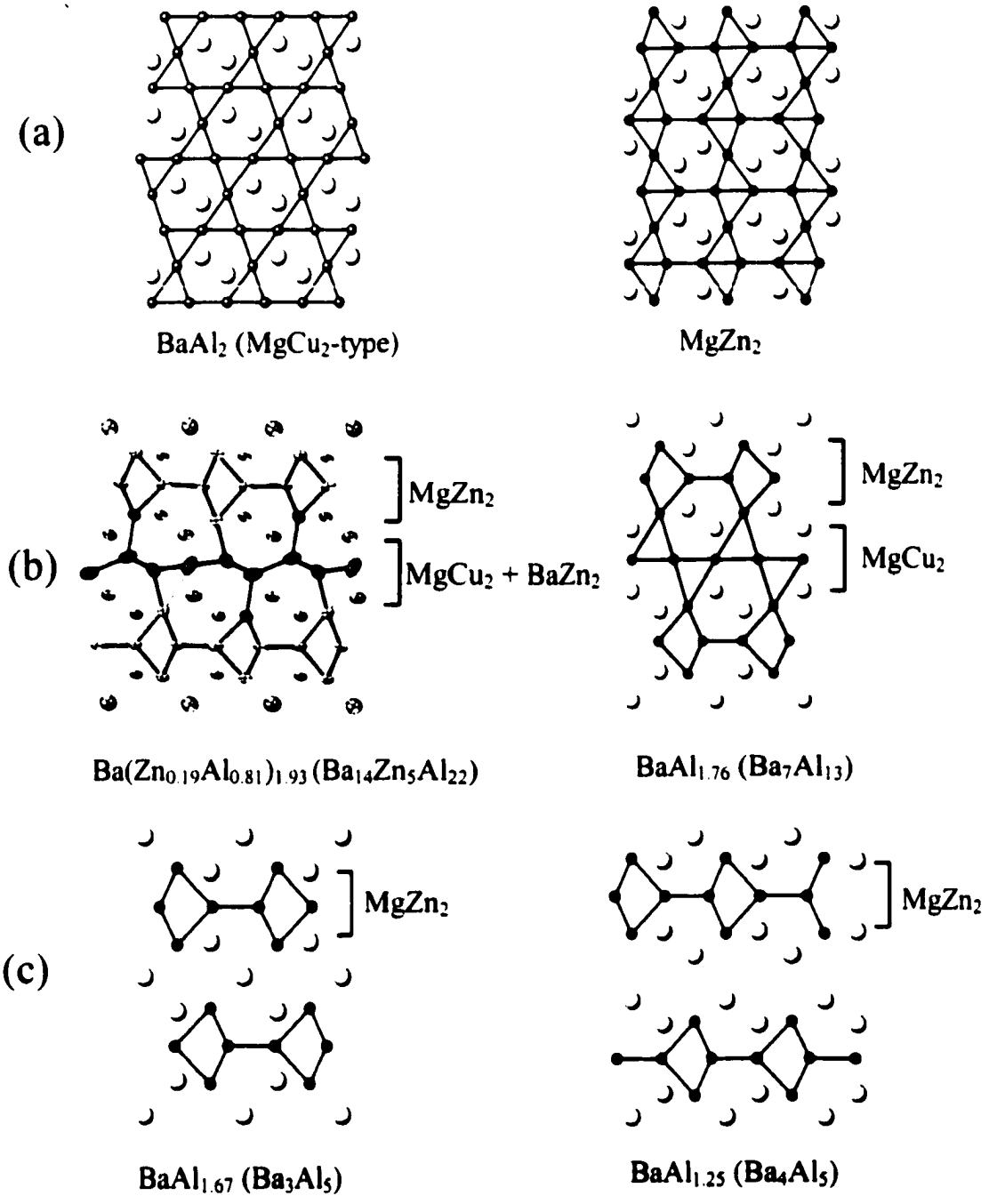

Figure 10. Projection of the structures presenting the structure transition in various Ba-Al and Ba-Zn-Al phases. Gray spheres are Ba atoms and small circles connected by black sticks are Zn/Al atoms. Partial structure(s) is labeled on right side of each figure. The $MgZn_2$ structure is presented for comparison. (a) 3D structures: $MgCu_2$- and $MgZn_2$-type. (b) 2D framwork: $Ba_{14}Zn_5Al_{22}$ and Ba_7Al_{13} structures. (c) 2D framework: Ba_3Al_5 and Ba_4Al_5 structures.

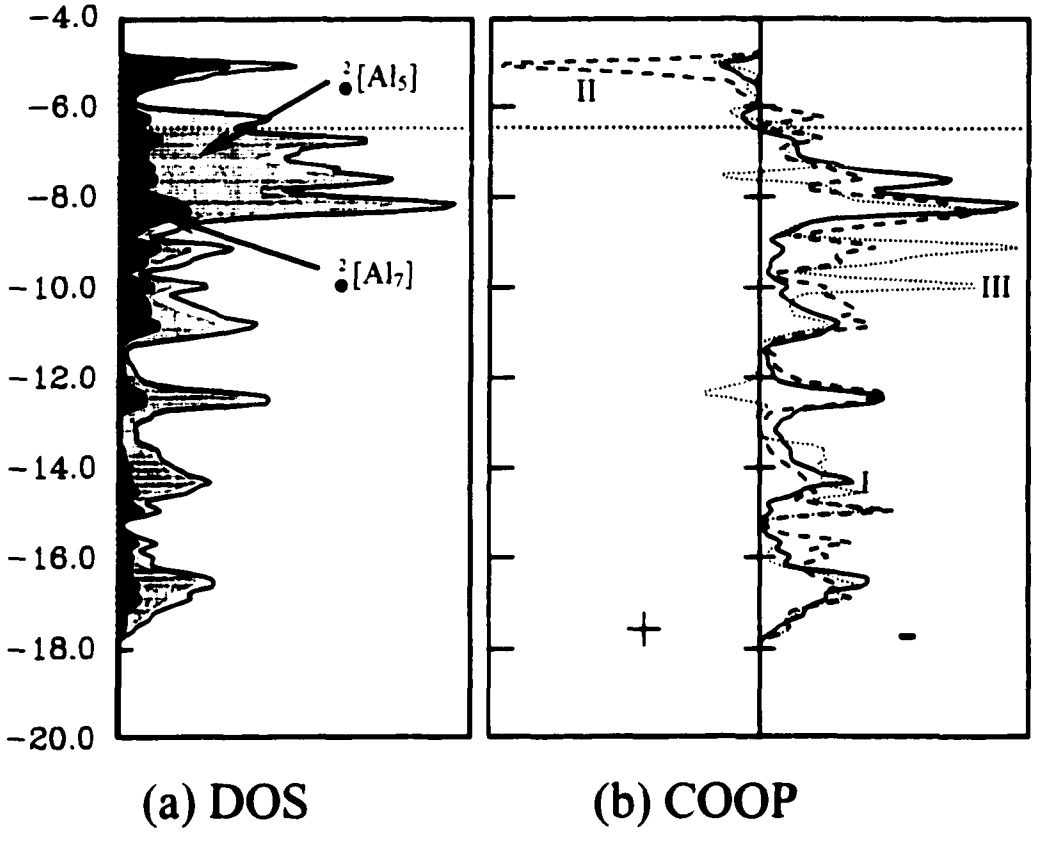

Figure 11. The DOS and COOP curves from the theoretical calculations of $[Al_{27}]^{28-}$. Dashed lines denote the Fermi energy of *vec* = 104 e⁻. (a) Total DOS (solid line), PDOS of $^{2}_{\infty}[Al_7]$ (black shadow) and $^{2}_{\infty}[Al_5]$ layers (gray shadow). (b) COOP curves for three types of Zn-Al contacts in $^{2}_{\infty}[Al_5]$(I, solid), $^{2}_{\infty}[Al_7]$ (II, long dashed), and between $^{2}_{\infty}[Al_5]$ and $^{2}_{\infty}[Al_7]$ layers (III, round dot).

Table 1. Summary of reaction compositions and products identification for various ternary Ba-Zn-Al reactions

Reactions	Identified Phase	Comment
I. $Ba(Zn_xAl_{1-x})_2$		
$BaZn_{0.4}Al_{1.6}$	$Ba_{14}Zn_5Al_{22}$(M) + Al(t)	powder, single crystal
$BaZn_{0.5}Al_{1.5}$	$Ba_{14}Zn_5Al_{22}$(M) + Al(t)	powder, single crystal
$BaZn_{0.8}Al_{1.2}$	$BaAl_4$(M) + Ba_7Al_{13}(m)	powder
$BaZn_{1.2}Al_{0.8}$	$BaZn_5$(M) + Ba_7Al_{13}(m)	powder
$BaZn_{1.25}Al_{0.75}$	$BaZn_5$(M) + Ba_7Al_{13}(m) + $BaAl_4$(m)	powder
$BaZn_{1.4}Al_{0.6}$	$BaZn_5$(M) + $BaZn_2$(m) + Ba_7Al_{13}(m) + $BaAl_5$(m)	powder
$BaZn_{1.5}Al_{0.5}$	$BaZn_2$(M) + Al(m)	powder
$BaZn_2$	$BaZn_2$(M) + BaZn(m) + $BaZn_5$(m)	powder
II. $Ba_7(Zn_xAl_{1-x})_{13}$		
$Ba_7(Zn_{0.23}Al_{0.77})_{13}$	$Ba_{14}Zn_5Al_{22}$(M) + Al (t)	powder, single crystal
$Ba_7(Zn_{0.46}Al_{0.54})_{13}$	$BaZn_5$ (M) + Ba_3Al_5(m) + Al(t)	powder
$Ba_7(Zn_{0.62}Al_{0.38})_{13}$	$BaZn_{4.5}Al_{0.5}$ (M) + Ba_3Al_5(m) + Al(t)	powder, single crystal
III. $Ba_{14}Zn_5Al_{22}$		
$Ba_{14}Zn_5Al_{22}$	$Ba_{14}Zn_5Al_{22}$(M) + Al (t)	powder

[a] M = major phase; m = minor phase, t = trace amounts.

Table 2. Summary of Single Crystal Refinements on ternary $Ba_{14}Zn_5Al_{22}$ compounds.

No.	Refined Formula	*a*, Å	*b*, Å	*c*, Å	Volume, Å^3	R1/wR2(%);GOF	$2\theta_{max}$	totl/uniq reflns
	Model A							
1	$Ba_7Zn_3Al_{10}$ [a]	6.071(2)	10.510(2)	17.224(5)	549.33(18)	0.0583/0.1407/1.095	50.0	1408/425
	Model B							
2	$Ba_{14}Zn_{3.0}Al_{27.0}$ [b]	10.541(4)	6.086(3)	17.431(7)	1118.2(8)	0.101/0.301; 1.76	56.7	3100/1323
	Model C							
3	$Ba_{14}Zn_{4.76(5)}Al_{22.24(5)}$ [b]	10.474(2)	6.0834(14)	34.697(8)	2210.5(9)	0.0585/0.1651; 1.165	56.7	9495/1785
4	$Ba_{14}Zn_{5.0}Al_{22.0}$ [c]	10.451(2)	6.075(1)	34.687(7)	2201.8(8)	0.0761/0.2322; 1.53	56.7	7072/2781
5	$Ba_{14}Zn_{5.0}Al_{22.0}$ [b]	10.540(6)	6.083(3)	34.84(2)	2234(2)	0.0967/0.2746;1.058	56.7	6330/2782
6	**Model D**							
	$Ba_{14}Zn_4Al_{23}$ [b]	20.979(5)	12.179(3)	69.50(2)	1.17(3)×10^3	NA	56.7	22576/6919

[a] Room temperature Siemens P4 data. [b] Room temperature CCD data. [c] Low temperature (163(2) K) CCD data.

Table 3. Crystal Data and Conditions of Data Collection for $Ba_{14}Zn_{4.76(5)}Al_{22.24(5)}$[a]

Refined Composition	$Ba_{14}Zn_{4.76(5)}Al_{22.24(5)}$
Instrument	Smart CCD
form wt (g/mol)	5676.36
Crystal size, mm	0.05×0.08×0.3
Space group , Z	*I2/m*, 2
a(Å)	10.474(2)
b(Å)	6.0834(14)
c(Å)	34.697(8)
β, °	90.814(4)
V(Å^3)	2210.5(9)
d_{calc} (g/cm^3)	4.264
Abs coeff (mm^{-1})	15.264
Transmission range	0.455-1.000
Temperature, K	298(2)
R1, wR2 (all data)[b]	0.0585, 0.1651
Goodness-of-fit on F^2	1.165
Extinction coefficient	0.00004(4)
(Δρ) max, min (e/Å^3)	4.196, -2.323

[a] from **Model C** (No. 3)

[b] $R1 = \sum \| F_o | - | F_c \| \Big/ \sum | F_o |$; $wR2 = \left[\sum \left[w\left(F_o^2 - F_c^2 \right)^2 \right] \Big/ \sum \left[w\left(F_o^2 \right)^2 \right] \right]^{1/2}$, $w = \sigma_F^{-2}$

Table 4. Atomic coordinates, site occupancy and isotropic displacement parameters ($Å^2$) for $Ba_{14}Zn_{4.76(5)}Al_{22.24(5)}$. U_{eq} is defined as one third of the trace of the orthogonalized U_{ij} tensor.

atom	site	x	y	z	U_{eq}		Site occ.
Ba1	4i	0.5032(1)	0	0.0535(1)	0.016(1)		
Ba2	4i	0.9748(1)	½	0.0544(1)	0.018(1)		
Ba3	4i	0.8253(1)	0	0.0898(1)	0.013(1)		
Ba4	4i	0.8337(1)	0	0.1966(1).	0.013(1)		
Ba5	4i	0.3296(1)	½	0.1971(1)	0.013(1)		
Ba6	4i	0.3294(1)	½	0.0882(1)	0.013(1)		
Ba7	4i	0.5026(1)	0	0.2486(1)	0.024(1)		
M8	8j	0.2223(2)	0.2074(4)	0.0087(1)	0.022(1)	Zn	0.842(4)
						Al	0.158(4)
M9	2a	0	0	0	0.018(2)	Zn	0.191(4)
						Al	0.809(4)
M10	4i	0.6573(5)	-½	0.0895(1)	0.014(1)	Zn	0.214(4)
						Al	0.786(4)
M11	4i	0.6184(4)	½	0.0144(1)	0.023(1)	Zn	0.386(4)
						Al	0.614(4)
Al12	4i	0.11648(6)	0	0.2018(2)	0.014(1)		
Al13	4i	0.8346(7)	0	0.2975(2)	0.014(2)		
Al14	8j	0.5720(4)	0.2311(8)	0.1458(1)	0.015(1)		
Al15	8j	0.10778(4)	-0.7396(8)	0.1430(1)	0.015(1)		
Al16	4i	0.1616(6)	0	0.811(2)	0.013(1)		
Al17	4i	0.3360(6)	0	0.1434(2)	0.015(2)		
Al18	4i	0.8428(6)	½	0.1454(2)	0.015(2)		

Table 5. Selected Bond length [Å] for $Ba_{14}Zn_5Al_{22}$.

Ba1	-Ba1	3.709(3)	Ba6	-M8 ×2	3.456(2)
	-Ba3	3.585(2)		-M10	3.434(5)
	-Ba6 ×2	3.7521(12)		-M11	3.992(5)
	-M8 ×2	3.540(2)		-M11	3.608(4)
	-M8 ×2	3.832(2)		-Al14 ×2	3.604(5)
	-M10 ×2	3.656(3)		-Al15 ×2	3.583(5)
	-M11 ×2	3.548(2)		-Al16 ×2	3.520(3)
	-M11 ×2	4.041(3)		-Al17 ×2	3.596(4)
	-Al14 ×2	3.563(5)			
	-Al16 ×1	3.717(6)	Ba7	-Al12	3.872(7)
	-Al17 ×1	3.601(6)		-Al12 ×2	3.921(4)
				-Al13 ×2	3.846(4)
Ba2	-Ba2	3.816(3)		-Al13	3.849(7)
	-Ba3 ×2	3.6432(12)		-Al14 ×2	3.911(5)
	-Ba6	3.879(2)		-Al15 ×2	4.132(5)
	-M8 ×2	3.476(2)		-Al17	4.022(7)
	-M8 ×2	3.538(2)		-Al18	3.999(7)
	-M9 ×2	3.5907(10)			
	-M10	3.558(5)	M8	-M8	2.524(5)
	-M11	3.963(5)		-M8	3.559(5)
	-Al15 ×2	3.558(5)		-M9	2.662(2)
	-Al16 ×2	3.727(4)		-M10	4.061(5)
	-Al18	3.466(6)		-M11	2.575(4)
				-Al16	2.889(6)
Ba3	-Ba4	3.704(2)			
	-M8 ×2	3.672(2)	M9	-Al16	3.262(7)
	-M9	3.6368(14)			
	-M10 ×2	3.514(2)	M10	-M11	2.633(7)
	-Al14 ×2	3.596(5)		-Al14 ×2	2.708(6)

Table 5. (Continued)

	-Al15 ×2	3.573(5)		-Al18	2.724(8)
	-Al16	3.540(6)			
	-Al18 ×2	3.604(4)	M11	-M11	2.661(9)
Ba4	-Ba7 ×1	3.932(2)	Al12	-Al15	2.728(7)
	-Ba7 ×2	3.9649(13)		-Al17	2.724(9)
	-Al12	3.469(7)			
	-Al13	3.502(7)	Al13	-Al14	2.729(7)
	-Al13 ×2	3.523(4)		-Al18	2.736(9)
	-Al14 ×2	3.530(5)			
	-Al15 ×2	3.554(5)	Al14	-Al14	2.811(10)
	-Al18 ×2	3.525(3)		-Al14	3.272(10)
				-Al17	2.844(7)
Ba5	-Ba6	3.781(2)		-Al18	3.274(8)
	-Ba7 ×2	3.9530(13)			
	-Ba7	3.980(2)	Al15	-Al15	2.915(10)
	-Al12 ×2	3.503(3)		-Al15	3.169(10)
	-Al12	3.507(7)		-Al16	2.819(7)
	-Al13	3.518(7)		-Al17	3.134(7)
	-Al14 ×2	3.525(5)		-Al18	2.863(7)
	-Al15 ×2	3.531(5)			
	-Al17 ×2	3.568(3)	Al16	-Al17	2.812(9)

Table 6: Anisotropic displacement parameters ($Å^2 x\ 10^3$) for $Ba_{14}Zn_5Al_{22}$.

	U_{11}	U_{22}	U_{33}	U_{23}	U_{13}	U_{12}
Ba1	0.019(1)	0.014(1)	0.016(1)	0	-0.002(1)	0
Ba2	0.026(1)	0.010(1)	0.017(1)	0	0.001(1)	0
Ba3	0.016(1)	0.008(1)	0.015(1)	0	-0.001(1)	0
Ba4	0.017(1)	0.009(1)	0.012(1)	0	-0.001(1)	0
Ba5	0.017(1)	0.009(1)	0.012(1)	0	-0.001(1)	0
Ba6	0.017(1)	0.007(1)	0.015(1)	0	-0.002(1)	0
Ba7	0.026(1)	0.016(1)	0.032(1)	0	-0.003(1)	0
M8	0.018(1)	0.020(1)	0.024(1)	-0.004(1)	-0.004(1)	-0.002(1)
M9	0.042(4)	0.018(4)	0.056(5)	0	0.017(4)	0
M10	0.029(3)	0.021(3)	0.031(3)	0	-0.004(2)	0
M11	0.036(3)	0.011(2)	0.021(2)	0	0.008(2)	0
Al12	0.020(4)	0.009(4)	0.012(3)	0	-0.001(3)	0
Al13	0.020(4)	0.011(4)	0.012(3)	0	0.000(3)	0
Al14	0.020(2)	0.013(3)	0.012(2)	0.000(2)	0.001(2)	0.001(2)
Al15	0.018(2)	0.012(3)	0.014(2)	0.000(2)	0.000(2)	0.001(2)
Al16	0.014(3)	0.007(3)	0.018(3)	0	0.000(3)	0
Al17	0.022(4)	0.010(4)	0.012(3)	0	0.003(3)	0
Al18	0.024(4)	0.009(4)	0.012(3)	0	0.004(3)	0

$U_{ij} = \exp(-2\pi^2(a^{*2}U_{11}h^2 + b^{*2}U_{22}k^2 + c^{*2}U_{33}l^2 + 2a^*b^*U_{12}hk + 2a^*c^*U_{13}hl + 2b^*c^*U_{23}kl)$

Table 7. Formal charges of (Zn/Al) sites for $Ba_{14}Zn_5Al_{22}$

Atom	Al/Zn occp.	e⁻ pair	2c2e	3c2e	# e^a	Formal charge
$^2_\infty[Al_5]$						
Al12	1.00/0.00	1	3	0	5	-2
Al15 ×2	1.00/0.00	0	2	2	3.33	-0.33
Al16	1.00/0.00	0	3	1	3.67	-0.67
Al17	1.00/0.00	0	2	2	3.33	-0.33
					Total Charge:	-3.67
$^2_\infty[MAl_4]$						
M10	0.77/0.23	0	4	0	4	-1.23[b]
Al13	1.00/0.00	1	3	0	5	-2
Al14 ×2	1.00/0.00	0	2	2	3.33	-0.33
Al18	1.00/0.00	0	2	2	3.33	-0.33
					Total Charge:	-4.23
$^2_\infty[M_7]$						
M8a ×2	0.18/0.82	0	3	1	3.67	-0.67[b]
M8b ×2	0.18/0.82	0	2	2	3.33	-1.15[b]
M9	0.81/0.19	1	2	1	4.67	-1.83[b]
M11 ×2	0.67/0.33	0	4	0	4	-1.37[b]
					Total Charge:	-9.85
	Total charge: ($^2_\infty[Al_5]$) ×2 + ($^2_\infty[MAl_4]$) ×2 + $^2_\infty[M_7]$ =					-25.65

[a] # e = bonding electrons

[b] Formal charge = [(Al occp)*3 + (Zn occp.)*2] – (# e).

CHAPTER 7

GENERAL CONCLUSIONS

The structure and properties of intermetallic compounds in Ae-Zn-Al systems are presented in this thesis. The studies of ternary Ae-Zn-Al intermetallic compounds offer a better understanding for the effects of *vec* on crystal structure, atomic site preference, and phase width of solid-state compounds. General conclusions are summarized below:

1. What factors affect the phase width?

Figure 1 illustrates the relationship between the *vec*, average coordination number (ave. C.N.) and the intermetallic compounds synthesized and characterized in this thesis. The observed compounds essentially cover the whole range of *vec* from 2.0 to 4.0. The coordination numbers of these sites are flexible, which can vary from 7 (*vec* < 3) to 3 (*vec* > 3). Compounds over a wide range of *vec* are obtained in the R-phase (Li-Mg-Zn-Al system, $2.0 \leq vec \leq 2.5$) and $AeZn_xAl_{4-x}$ ($3.0 \leq vec \leq 3.5$, Ae = Sr, Ba) systems. On the other hand, compounds with nearly precise *vec* exist in the $BaZn_{10}Al_2$ (*vec* = 2.33) and $Ba_{14}Zn_5Al_{22}$ (*vec* = 3.85) phases. There is no definitive correlation between *vec* value and the occurrence of a phase width.

Theoretical studies on these compounds revealed the effects of Zn-Al bonding to the phase width. For system with wide phase widths (e.g., R-phase system), the orbitals near the Fermi level contain a range of Zn-Al non-bonding character (from COOP curves, near zero overlap coefficient) but non-zero contributions to the electronic states (from DOS curves). Such an electronic structure allows the system to be flexible within a range of *vec* and

maintain bonding among Zn-Al contacts. According to the theoretical studies for R-phase system, the calculated *vec* range is consistent with the X-ray and neutron studies. Similar results are also found in the $AeZn_xAl_{4-x}$ system. Moreover, the observed *vec* for $BaZn_{10}Al_2$ and $BaZn_{0.34(5)}Al_{1.59(5)}$ systems are close to the optimized bonding of Zn-Al contacts. The COOP curve from average Zn-Al contacts presents a sharp transition from bonding to antibonding character at the Fermi level. These results indicate that the Zn-Al bonding is stable in a narrow range of *vec*. The stable composition contains filled bonding levels and empty antibonding levels in the COOP curves.

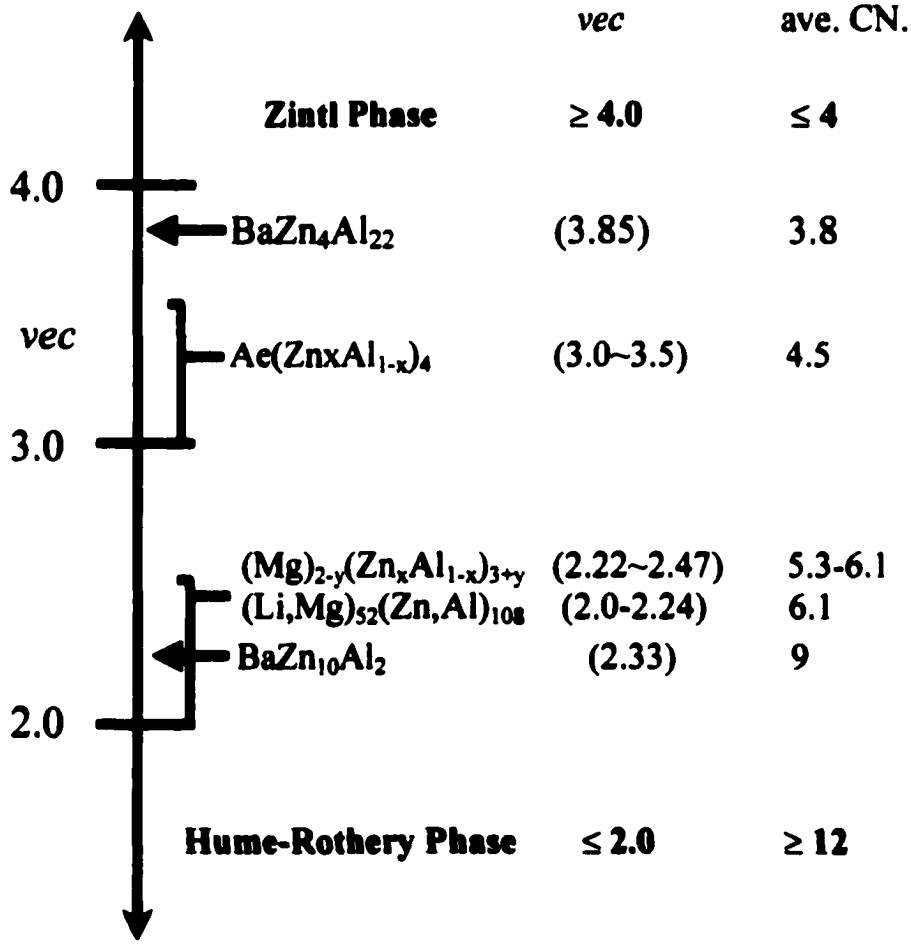

Figure 1. Summary of the identified intermetallic phases vs. *vec*.

2. What factors affect the site preference?

The site preference for electropositive (alkaline earth metal) and electronegative elements (Zn and Al) were identified by single crystal X-ray and neutron diffraction analyses for series of Ae-Zn-Al intermetallic compounds. Structural analyses show that the positions of alkaline earth metals always locate on the positions with long interatomic distances (usually > 3.0 Å) and are fully occupied. On the other hand, atomic positions for Zn and Al have short interatomic contacts (2.5 < d < 2.8 Å) between two (Zn/Al) sites and could be mix-occupied by different Zn/Al ratios. Theoretical studies on the intermetallic systems with *vec* < 3 e^-/atom indicate that the electropositive atom (e.g. Mg and Li) prefers to occupy the positively polarized sites and the electronegative atom (e.g. Zn and Al) favors the negatively polarized sites. The results are consistent with the relative electronegativities between (Li, Mg) and (Zn, Al). The other factor affect the atomic sites site preferences is the relative Zn:Al compositions. The results from the R-phase studies show that the Zn- and Al-rich sites with nearly fixed Zn/Al ratios exist in both Zn-rich (low *vec*) and Al-rich R-phases (high *vec*). Beside these sites with fixed composition, there are atomic sites that allow a range of Zn/Al ratios. These atomic sites are responsible for the phase width of some intermetallic systems (e.g., M1, M3 site in R-phase system). In $AeZn_xAl_{4-x}$ phases, Zn and Al atoms prefer to occupy different atomic sites (M1 and M2). The effect of alkaline earth elements to the site preferences in Zn-Al networks is observed in the $AeZn_xAl_{4-x}$ system. The interatomic distance were affected by alkaline earth metal that the large cation tends to increase the degree of Zn/Al disorder on the Zn-Al network.

The relative atomic site potential could be compared by relative Mulliken population analyses from extended-Hückel band calculations. This analysis is able to distinguish the electropositive from electronegative elements in systems with *vec* lower than 3.

3. What factors affect the crystal structure?

The relationship between the *vec* to crystal structure (ave. C.N.) is shown in Figure 1. For Zn-rich phase (low *vec*), the structures of the Zn-Al network are complex and each atom contains more than four interatomic contacts. A special building unit, the icosahedral M_{12} clusters, is observed not only in $BaZn_{10}Al_2$ but also in the R-phase system. The coordination number for Zn/Al sites gradually decreases as the *vec* increases. This trend shows a transition from Hume-Rothery type (low *vec*, high C.N.) to Zintl type (high *vec*, low C.N.).

The compound with the highest *vec* is $BaZn_{0.34(5)}Al_{1.59(5)}$ (*vec* = 3.85) with a Zn-Al network that resembles a Zintl phases (C.N. $\leq$ 4). However, the formal charge of each Zn/Al sites in $BaZn_{0.34(5)}Al_{1.59(5)}$ cannot be assigned clearly by the Zintl-Klemm concept. Although the most stable composition is consistent between the theoretical calculations and experiments, detailed theoretical studies are necessary to clarify the correlation between the site preference and relative site potential in different Zn/Al sites.

APPENDIX A.

REACTION COMPOSITION AND PRODUCT IDENTIFICATION

No.	Reaction Stoichiometry	Heating Method	Reaction Products (powder X-ray Diffraction
	I. $Ba(M_xAl_{1-x})_{13}$		
1	$BaZn_{10}Al_3$	furnace	$BaZn_{10}Al_2$(M) + Al(t)
2	$BaZn_8Al_5$	furnace	$BaZn_5$(M) + $Ba(Zn,Al)_{13}$(m) + Al(t)
3	$BaZn_5Al_8$	furnace	$BaZn_5$(M) + $Ba(Zn,Al)_{13}$(m) + Al(t)
4	$BaZn_{10}Al_2$	furnace	$BaZn_{10}Al_2$(M)
5	$BaZn_{12}Co$	furnace	$BaZn_{12}Co$(M)
6	$BaZn_{12}Fe$	furnace	$BaZn_{12}Fe$(M)
7	$BaZn_{12}$	furnace	$BaZn_{12.77}$(M)
8	$BaFeCu_5Al_7$	arc welder	$Ba(Fe,Cu,Al)_{13}$(M) + Al(t)
9	$BaFe_2CuAl_8$	arc welder	$Ba(Fe,Cu,Al)_{13}$(M) + Al(t) + unknown lines
10	$BaFeCu_{4.5}Al_{7.5}$	arc welder	$Ba(Fe,Cu,Al)_{13}$(M) + $BaFe_2Al_9$(m) + Al(t)
11	$BaCoCu_5Al_7$	arc welder	$Ba(Co,Cu,Al)_{13}$(M) + $BaCo_2Al_9$(m) + Al(t)
12	$BaCoCu_3Al_9$	arc welder	$Ba(Co,Cu,Al)_{13}$(M) + $BaCo_2Al_9$(m) + Al(t)
13	$BaCo_2CuAl_8$	arc welder	$Ba(Co,Cu)_2Al_9$(M) + Al(t) + Unknown lines
14	$BaNiCu_5Al_7$	arc welder	$Ba(Ni,Cu,Al)_{13}$(M) + Al(t) + unknown lines
15	$BaNi_2CuAl_8$	arc welder	$Ba(Co,Cu)_2Al_9$(M) + Al(t) + Unknown lines
16	$LaCu_6Al_7$-$LaFe_6Al_7$	arc,anneal	$La(Cu, Fe, Al)_{13}$(M) + Al(t)
17	$BaCo_6Al_7$	arc,anneal	$BaCo_2Al_9$(m) + unknown lines
	II. R-phases		
28	Mg_2Zn_3	furnace	$MgZn_2$(M) + Al(t)
29	Mg_2ZnAl_2	furnace	R-phase(M) + Al(t)
30	Mg_2Zn_2Al	furnace	R-phase(M) + Zn(t)
31	Mg_2Al_3	furnace	Mg_2Al_3(m) + Al(m) + unknown lines
32	$Mg_{52}Al_{108}$	furnace	$Mg_{17}Al_{12}$ (M) + unknown lines
33	$Mg_{52}Zn_{20}Al_{88}$	furnace	R-Phase(M) + $Mg_{17}Al_{12}$(m)

APPENDIX A. (Continued)

34	$Mg_{52}Zn_{40}Al_{68}$	furnace	R-phase(M) + Al(tr)
35	$Mg_{52}Zn_{44}Al_{64}$	furnace	R-Phase(M)
36	$Mg_{52}Zn_{54}Al_{54}$	furnace	R-Phase(M)
37	$Mg_{52}Zn_{68}Al_{40}$	furnace	R-Phase(M)
38	$Mg_{52}Zn_{88}Al_{20}$	furnace	$MgZn_2$(M) + Zn(m) + R-phase(m)
39	$Mg_{52}Zn_{108}$	furnace	$MgZn_2$(M) + Zn(m)
40	$Li_{20}Mg_{32}Zn_{39}Al_{69}$	furnace	R-phase(M)
41	$Li_{20}Mg_{32}Zn_{85}Al_{23}$	furnace	R-phase(M) + $MgZn_2$(t) + Al(t) + Mg_2Zn_{11}(t)
42	$Li_{24}Mg_{28}Zn_{36}Al_{72}$	furnace	R-phase(M)
43	$Li_{32}Mg_{20}Zn_{39}Al_{69}$	furnace	R-phase(M) + $MgZn_2$(t) + Mg_2Zn_{11}(t)
44	$Li_{32}Mg_{20}Zn_{85}Al_{23}$	furnace	R-phase(M) + $MgZn_2$(t) + Mg_2Zn_{11}(t)
45	$Li_{52}Zn_{32}Al_{76}$	furnace	R-phase(M) + LiZn(t) + LiAl(t)
46	$Li_{52}Zn_{39}Al_{69}$	furnace	R-phase(M) + Zn(t)
47	$Li_{52}Zn_{48}Al_{60}$	furnace	R-phase(M) + Zn(t)
48	$Li_{52}Zn_{76}Al_{32}$	furnace	R-phase(M)
49	$Mg_{28}Eu_{24}Zn_{36}Al_{72}$	furnace	$Eu(Zn,Al)_4$(M) + $MgZn_2$(m) + R-phase(t) + Al (t) + Zn (t)
50	$Mg_{28}Ca_{24}Zn_{36}Al_{72}$	furnace	$Ca(Zn,Al)_4$(M) + $MgZn_2$(m) + R-phase(t) + Al (t) + Zn (t)
	IV. $Ae(Zn_xAl_{1-x})_4$		
51	$CaZnAl_3$	furnace	$CaZn_xAl_{4-x}$(m) + $CaZn_2$(m) + $CaAl_2$(m) + $CaZn_3$(m)
52	$SrZnAl_3$	furnace	$SrZnAl_3$ (M) + Al(t)
53	$BaZnAl_3$	furnace	$BaZnAl_3$ (M)
54	$MgZn_2Al_2$	furnace	$MgZn_2$ (M) + Al(m)
55	$CaZn_2Al_2$	furnace	$CaZn_2Al_2$ (M) + Al (t)
56	$SrZn_2Al_2$	furnace	$SrZn_2Al_2$ (M) + Al (t)
57	$BaZn_2Al_2$	furnace	$BaZn_2Al_2$ (M)
58	$CaZn_3Al$	furnace	$CaZn_xAl_{4-x}$(m) + $CaZn_5$(M)

APPENDIX A. (Continued)

59	$SrZn_3Al$	furnace	$SrZn_xAl_{4-x}$(m) + $SrZn_5$(M) + Al (t) + Zn (t)
60	$BaZn_3Al$	furnace	$BaZn_xAl_{4-x}$(m) + $BaZn_5$(M)
	V. $Ba(Zn_xAl_{1-x})_2$		
61	$BaZn_{0.4}Al_{1.6}$	furnace	$Ba_{14}Zn_5Al_{22}$(M) + Al (t)
62	$BaZn_{0.5}Al_{1.5}$	furnace	$Ba_{14}Zn_5Al_{22}$(M) + Al (t)
63	$BaZn_{0.8}Al_{1.2}$	furnace	$BaAl_4$(M) + Ba_7Al_{13}(m)
64	$BaZn_{1.2}Al_{0.8}$	furnace	$BaZn_5$(M) + Ba_7Al_{13}(m)
65	$BaZn_{1.25}Al_{0.75}$	furnace	$BaZn_5$(M) + Ba_7Al_{13}(m) + $BaAl_4$(m)
66	$BaZn_{1.4}Al_{0.6}$	furnace	$BaZn_5$(M) + $BaZn_2$(m) + Ba_7Al_{13}(m) + $BaAl_5$(m)
67	$BaZn_{1.5}Al_{0.5}$	furnace	$BaZn_2$(M) + Al + unknown lines
68	$BaZn_2$	furnace	$BaZn_2$ (M) + BaZn(m) + $BaZn_5$(m)
69	$Ba_7(Zn_{0.23}Al_{0.77})_{13}$	furnace	$Ba_{14}Zn_5Al_{22}$(M) + Al (t)
70	$Ba_7(Zn_{0.46}Al_{0.54})_{13}$	furnace	$BaZn_5$ (M) + Ba_3Al_5(m) + unknown lines
71	$Ba_7(Zn_{0.62}Al_{0.38})_{13}$	furnace	$BaZn_{4.5}Al_{0.5}$ (M) + Ba_3Al_5(m) + unknown lines
72	$Ba_{14}Zn_5Al_{22}$	furnace	$Ba_{14}Zn_5Al_{22}$ (M)
	VI. Other reactions		
73	$MnAl_6$	arc welder	$MnAl_6$(m) + Al(m) + unknown lines
74	$MnAl_4$	arc welder	Al (m) + unknown lines
75	$MnAl_3$	arc welder	Al (m) + unknown lines
76	$BaMnAl_6$	arc welder	Al (m) + unknown lines
77	$LaMnAl_7$	arc welder	Al (m) + unknown lines
78	$Ba_3Cu_2Al_7$	arc welder	$Ba(Cu,Al)_4$ (M) + unknown lines
79	$Ba_3Ag_2Al_7$	arc welder	$Ba(Ag,Al)_4$ (M) + unknown lines
80	$Ba_3Au_2Al_7$	arc welder	$Ba(Au,Al)_4$ (M) + unknown lines
81	$Mg_6Zn_5Al_8$	arc welder	$MgZn_2$(M) + R-phase(m) + unknown lines
82	$Mg_6Ag_5Al_8$	arc welder	Mg_2Zn_{11} (?) + unknown lines
83	$Mg_2Cu_6Al_5$	arc welder	$Mg_2Cu_6Al_5$ (?) + Cu
84	$Mg_3Zn_{13}Al_3$	arc welder	$MgZn_2$ (M) + Mg_2Zn_{11} (?) + unknown lines

Note: M = major, m = minor, t = trace.

APPENDIX B.

SUMMARY OF SINGLE CRYSTAL REFINEMENTS ON VARIOUS ALUMINIDES

I. $Ba(M_xAl_{1-x})_{13}$ (space group, $Fm\bar{3}c$, no. 226)

No.	Reactions	Refined Comp.	a (Å)	R1/ wR2(%); GOF	$2\theta_{max}$	totl/uniq reflns	Filename
1	$BaZn_{10}Al_3$	$BaZn_{10.1}Al_{1.9}$	12.243(1)	2.14/5.60/1.049	55	3927/107	971113
2	$BaZn_{10}Al_3$	$BaZn_{11.0}Al_{1.0}$	12.2300(10)	2.57/8.09/1.082	55	733/107	980123
3	$BaZn_{10}Al_2$	$BaZn_{10.7}Al_{1.3}$	12.2483(11)	2.32/5.82/1.052	60	1496/133	980909
4	$BaZn_{10}Al_2$	$BaZn_{10.6}Al_{1.4}$	12.2425(15)	3.88/9.07/1.064	70	463/191	980913
5	$BaZn_{12}$	$BaZn_{12.77}$	12.337(2)	2.05/5.31/1.149	56	799/116	Mil40
6	$BaZn_{12.77}$	$BaZn_{12.75(1)}$	12.3220(4)	1.77/4.74/1.22	60	953/139	990112
7	$BaZn_{12}Fe$	$BaZn_{12}Fe$	12.330(2)	2.95/7.18/1.241	60	881/138	990113
8	$BaZn_{12}Co$	$BaZn_{12}Co$	12.3434(8)	2.00/6.43/0.998	60	1548/139	980911
9	$BaZn_{12}Co$	$BaZn_{12}Co$	12.333(3)	4.21/11.93/1.085	70	486/199	980914
10	$Ba(Ni,Cu)_5Al_8$	$Ba(Ni,Cu)_5Al_8$	12.243(1)	3.92/11.14/1.023	54	3821/497	971117

II. R-phases: Mg-Zn-AL (space group, $Im\bar{3}$, no. 204)

No.	Reactions Mg:Zn:Al	Refined Formula[d]	a (Å)	Volume (Å^3)	R1/wR2(%);GOF	$2\theta_{max}$	Totl/Uniq Reflns	Filename
11	Mg_2ZnAl_2	$Mg_{52}Zn_{43.7(4)}Al_{64.3(4)}$	14.3324(9)	2944.1(3)	2.62/3.03;0.924	56[a]	6350/675	mil01
12	Mg_2ZnAl_2	$Mg_{52}Zn_{44.4(9)}Al_{63.6(9)}$	14.3656(8)	2964.6(3)	3.89/5.54;1.075	45[c]	3938/362	980511
13	Mg_2ZnAl_2	$Mg_{52}Zn_{42.5(3)}Al_{65.5(3)}$	14.364(2)	2963.9(6)	3.26/5.95;0.928	55[c]	893/566	980513
14	Mg_2ZnAl_2	$Mg_{52}Zn_{42(2)}Al_{66(2)}$	14.341(2)	2949.2(6)	3.21/6.64;0.959	50[c]	777/492	980802

APPENDIX B. (Continued)

15	Mg_2ZnAl_2	$Mg_{52}Zn_{42.3(4)}Al_{65.7(4)}$	14.347(2)	2952.9(6)	3.58/8.61;1.055	50 [c]	778/490	980801a
16	Mg_2ZnAl_2	$Mg_{52}Zn_{39.8(4)}Al_{68.2(4)}$	14.395(1)	2982.9(4)	3.16/5.87;1.068	56 [b]	5171/684	mil30
17	Mg_2Zn2Al	$Mg_{52}Zn_{75.5(6)}Al_{33.5(6)}$	14.168(1)	2843.7(4)	4.17/3.11;0.986	56 [b]	9324/677	mil05
18	Mg_2Zn2Al	$Mg_{52}Zn_{64.3(4)}Al_{43.7(4)}$	14.157(2)	2837.1(6)	3.31/6.15;1.028	45 [b]	839/281	980514
19	Mg_2Zn2Al	$Mg_{52}Zn_{64.8(4)}Al_{43.2(4)}$	14.126(2)	2818.5(6)	4.46/9.76;1.002	50 [c]	748/473	980817
20	Mg_2Zn2Al	$Mg_{52}Zn_{63.5(3)}Al_{44.5(3)}$	14.126(2)	2818.5(6)	5.88/9.19;1.015	75 [c]	7907/1362	980818
21	$Mg_{52}Zn_{20}Al_{88}$	$Mg_{52}Zn_{34.6(3)}Al_{73.4(3)}$	14.3939(4)	2982.2(1)	2.08/7.26;1.064	40 [c]	1052/268	981119
22	$Mg_{52}Zn_{20}Al_{88}$	$Mg_{52}Zn_{33.0(3)}Al_{75.0(3)}$	14.412(1)	2993.3(4)	2.11/4.01;1.003	56 [b]	5476/692	mil19
23	$Mg_{52}Zn_{20}Al_{88}$	$Mg_{52}Zn_{32.1(5)}Al_{75.9(5)}$	14.416(2)	2995.7(8)	6.71/3.53;0.808	56 [b]	2760/686	mil22
24	$Mg_{52}Zn_{44}Al_{64}$	$Mg_{52}Zn_{53.2(3)}Zn_{54.8(3)}$	14.2827(9)	2913.6(3)	2.01/6.91;1.064	50 [c]	2798/683	981012
25	$Mg_{52}Zn_{44}Al_{64}$	$Mg_{52}Zn_{49.3(3)}Al_{58.7(3)}$	14.338(1)	2947.8(5)	2.86/8.79;1.068	45 [c]	1391/375	981013
26	$Mg_{52}Zn_{44}Al_{64}$	$Mg_{52}Zn_{52.7(2)}Al_{55.3(2)}$	14.297(1)	2922.4(4)	2.42/3.19;1.071	56 [b]	8958/680	mil15
27	$Mg_{52}Zn_{54}Al_{54}$	$Mg_{52}Zn_{55.3(4)}Al_{52.7(4)}$	14.283(1)	2914.0(4)	1.68/3.64;1.087	56 [b]	5356/679	mil23
28	$Mg_{52}Zn_{54}Al_{54}$	$Mg_{52}Zn_{54.3(3)}Al_{53.7(3)}$	14.303(1)	2926.1(4)	2.27/3.40;1.012	56 [b]	5450/681	mil13
29	$Mg_{52}Zn_{68}Al_{40}$	$Mg_{52}Zn_{70.1(7)}Al_{37.9(7)}$	14.138(1)	2825.9(4)	2.34/3.72;1.001	56 [b]	4925/648	mil20
30	$Mg_{52}Zn_{68}Al_{40}$	$Mg_{52}Zn_{62.6(5)}Al_{45.4(5)}$	14.224(5)	2877.6(2)	4.13/5.60;1.005	108 [b]	16594/2916	mil18a

APPENDIX B. (Continued)

III. R-phases: Li-Mg-Zn-Al (space group, $Im\bar{3}$, no. 204)

No.	Reactions / Refined Formula	*a*, Å	Volume, Å^3	R1/wR2(%);GOF	$2\theta_{max}$	totl/uniq reflns	Filename
	$Li_{28}Mg_{24}Zn_{:5}Al_{72}$, I						
31	$Li_{20.4}Mg_{31.6}Zn_{85.4}Al_{22.6}$	14.1109(17)	2809.7(6)	2.91/5.00;1.077	57	2695/645	mil21
32	$Li_{20.0}Mg_{32.0}Zn_{88.1}Al_{19.9}$	14.1063(11)	2807.0(4)	3.03/5.20;	57	3346/643	mil29
33	$Li_{19.5}Mg_{32.5}Zn_{87.0}Al_{21.0}$	14.084(2)	2793.6(4)	3.52/9.58;1.091	60	2321/767	981208
	$Li_{28}Mg_{24}Zn_{36}Al_{72}$, II						
34	$Li_{32.2}Mg_{19.8}Zn_{39.2}Al_{68.8}$	14.0929(15)	2799.0(5)	3.81/3.22;0.947	57	2641/645	mil28
35	$Li_{31.6}Mg_{20.4}Zn_{39.3}Al_{68.3}$	14.101(7)	2804(2)	5.77/7.89;1.074	57	2350/652	mil31
36	$Li_{34.6}Mg_{17.4}Zn_{36.5}Al_{71.5}$	14.081(2)	2791.8(5)	3.77/8.21/0.928	60	2281/767	981207
	$Li_{52}Zn_{48}Al_{60}$						
37	$Li_{52}Zn_{51.2}Al_{56.8}$	13.9544(18)	2717(3)	4.21/4.74;1.058	57	2520/610	mil41
38	$Li_{52}Zn_{50.7}Al_{57.3}$	13.933(2)	2704.6(5)	3.01/9.68/1.151	60	778/772	990114
39	$Li_{52}Zn_{50.7}Al_{57.3}$	13.9328(18)	2704.7(6)	3.27/9.68;1.151	60	2422/778	990117

APPENDIX B. (Continued)

IV. $AeZn_xAl_{4-x}$ (space group, *I4/mmm*, no. 139)

No.	Reactions Refined Formula	*a,c* Å	Volume, Å3	R1/wR2(%);GOF	$2\theta_{max}$	totl/uniq reflns	Filename
	x=1						
40	$SrZn_{0.98(2)}Al_{3.02(3)}$	4.2988(4) 11.538(2)	213.21(5)	2.91/8.83; 1.193	60	418/114	990515
41	$SrZn_{1.04(2)}Al_{2.96(2)}$	4.2912(7) 11.517(2)	212.08(6)	2.38/6.28; 1.228	60	790/112	990516
42	$BaZn_{1.23(4)}Al_{2.77(4)}$	4.4751(8) 11.425(2)	227.89(6)	1.90/5.06; 1.234	60	802/126	990517-1
43	$BaZn_{1.18(6)}Al_{2.82(6)}$	4.4677(7) 11.416(2)	227.89(6)	1.75/4.33; 1.023	60	1500/126	990517-2
	x = 2						
44	$CaZn_{2.0(1)}Al_{2.0(1)}$	4.1243(8) 11.560(2)	196.6(2)	3.51/7.67; 1.030	60	728/103	980216
45	$CaZn_{2.0(1)}Al_{2.0(1)}$	4.1281(9) 11.525(2)	196.39(7)	1.49/4.02; 1.022	52	1140/62	980215
46	$SrZn_{0.98(2)}Al_{3.02(3)}$	4.2889(8) 11.423(2)	210.13(6)	1.51/4.15; 1.051	120	2740/113	980218

APPENDIX B. (Continued)

47	$SrZn_{2.21(4)}Al_{1.89(4)}$	4.2832(6) 11.384(2)	208.56(5)	2.74/6.3; 1.13	55	509/94	980215
48	$SrZn_{2.24(1)}Al_{1.86(1)}$	4.2856(5) 11.379(2)	208.99(6)	1.91/4.90; 1.174	55	622/94	980817a
49	$SrZn_{2.16(3)}Al_{1.84(3)}$	4.2840(4) 11.392(2)	209.07(3)	3.54/9.56; 1.075	75	1375/196	980908
50	$BaZn_{1.85(8)}Al_{2.15(8)}$	4.472(1) 11.430(4)	228.6(1)	2.87/6.64; 1.042	55	340/100	980129
51	$BaZn_{1.84(4)}Al_{2.16(4)}$	4.4768(6) 11.403(2)	228.54(6)	1.36/3.19; 1.077	60	1409/118	980213
52	$BaZn_{1.78(4)}Al_{2.22(4)}$	4.4712(6) 11.436(2)	228.63(6)	1.79/2.89; 1.124	60	1500/119	980214
53	$BaZn_{1.68(8)}Al_{2.32(8)}$	4.4584(3) 11.402(3)	226.6(2)	2.47/6.74; 1.077	70	316/80	980823
54	$BaZn_{1.76(8)}Al_{2.24(8)}$	4.4568(2) 11.378(7)	226.0(2)	1.94/5.27; 1.083	60	410/121	980824
55	$BaZn_{1.66(8)}Al_{2.34(8)}$	4.458(2) 11.404(4)	226.6(2)	3.49/8.04; 1.089	75	1432/211	980825a

APPENDIX B. (Continued)

V. $Ba(Zn_xAl_{1-x})_2$ (space group, $I2/m$, no. 12)

No.	Refined Formula	*a*, *b*, *c* Å	Volume, Å^3	R1/wR2(%);GOF	$2\theta_{max}$	totl/uniq reflns	Filename
	Model A						
56	$Ba_7Zn_3Al_{10}$	6.071(2)	549.33(18)	5.83/14.07/1.095	50.0	1408/425	c2
		10.510(2)					
		17.224(5)					
	Model B						
57	$Ba_{14}Zn_{3.0}Al_{27.0}$	10.541(4)	1118.2(8)	10.1/30.1; 1.76	56.7	3100/1323	mil39
		6.086(3)					
		17.431(7)					
	Model C						
58	$Ba_{14}Zn_{4.76(5)}Al_{22.24(5)}$	10.474(2)	2210.5(9)	5.85/16.51; 1.165	56.7	9495/1785	mil06b
		6.0834(14)					
		34.697(8)					
59	$Ba_{14}Zn_{5.0}Al_{22.0}$	10.451(2)	2201.8(8)	7.61/23.22; 1.53	56.7	7072/2781	mil08a
		6.075(1)					
		34.687(7)					

APPENDIX B. (Continued)

60	$Ba_{14}Zn_{5.0}Al_{22.0}$	10.540(6) 6.083(3) 34.84(2)	2234(2)	9.67/27.46; 1.058	56.7	6330/2782	mil46
	Model D						
61	$Ba_{14}Zn_4Al_{23}$ [b]	20.979(5) 12.179(3) 69.50(2)	1.17(3)×10^{3}NA		56.7	22576/6919	mil46

VI. Other Single Crystal Data

No.	Refined Comp.	Cell	Space Group	R1/ wR2(%); GOF	$2\theta_{max}$	totl/uniq reflns	Filename
62	$MgZn_2$	5.2306(4)	*P6$_3$/mmc*	2.01/2.59/1.221	132	2602/141	980220
63	$BaZn_5$	10.832(2) 8.457(3) 5.353(1)	*Cmcm*	9.25/22.85/1.172	65	1058/502	980912a
64	$EuAl_4$	4.4109 11.4252	*I4/mmm*	1.47/3.58;1.06	60	739/125	981212

APPENDIX B. (Continued)

65	$EuZn_{11}$	10.705(4) 10.700(7) 6.873(3)	*I4/mmm*	2.28/4.99;1.091	60	1356/322	981211
66	$Mg_{17}Al_{12}$	10.455(9)	$I\bar{4}3m$	2.03/3.36/1.036	58	4234/291	mil09a

APPENDIX C.

ELECTRONIC STRUCTURE STUDIES OF Ba_2PdP_3 AND RELATED COMPOUNDS

Abstract

The effect of valence electron count per formula unit (*VEC*) on the anionic substructure of Ba_2PdP_3 and related compounds, which are related to AlB_2 structure type, is studied by the semiempirical Extended-Hückel tight-binding (EHTB) method. The calculations include molecular, one dimensional (1D) chains and two dimensional (2D) sheets to examine the relative stability between different structures. The results suggest that the transition from low to high-dimensional structure is affected by the *VEC*.

Introduction

Solid-state compounds containing layered structures with hexagons as a building unit exist not only in planar (e.g. graphite and AlB_2) but also in puckered forms (e.g. α-As and SnP_3).[1] The structural feature of these compounds is the 6^3-type two-dimensional (2D) network. Many ternary compounds M_xAB_3 with such 2D network have been synthesized (M=alkali, alkaline earth or rare earth element; A = late or post transition metal; B = group 14-15 elements; x = 2). A few examples of AlB_2-type derivatives are listed in Table 1.[2-7] Compounds with distorted AlB_2- or α-As-type structures have been reported that contain 1D chains. The first example is Ba_2PdP_3 (*VEC* = 29 e^-), which contains $^1_\infty[PdP_3^{4-}]$ planar zigzag chains.[6] The second example is K_3SnSb_3 (*VEC* = 32 e^-) with puckered polyacene type 1D-chains.[2] In these compounds, the 6^3-net (planar or puckered) is broke to form discrete 1D

chains. The relationship between *VEC* and structural trends in these compounds is similar to the 3D to 2D transitions along the sequence PdP_2-PdPS-PdS_2 (*VEC* = 20-22 e^-).[8-10] The 3D structure is not stable when the additional electrons fill high-lying antibonding orbitals of the 3D structure, therefore, the structure favors a lower dimensional network.[11] In this study, the effect of the electronic configuration on structural stability was examined theoretically by a series of models.

Structures of M_xAB_3 Materials

Figure 1 shows the structure of AlB_2 and two ternary derivatives, U_2RuSi_3 and Ba_2PdP_3.[5-7] U_2RuSi_3 contains planar $^2_\infty[RuSi_3^{6-}]$ sheets (*VEC* = 26 e^-) separated by U atoms. Ru can be replaced by Rh or Pd and each gives a $^2_\infty[TSi_3^{6-}]$ sheet with a different superstructure of the AlB2 structure type.[5,7] As the *VEC* increases to 29 e^-/formula unit, an interesting compound, Ba_2PdP_3, was reported,[6] which contains a pseudo layer structure with discrete zigzag $^1_\infty[PdP_3^{4-}]$ chains (Fig. 1c) made up of three P_3 units coordinated to each Pd atom in a planar manner. Both Pd and P_3 units propagate along the chain by a 2_1 screw-axis. According to the Zintl concept, the formal charge on P_3 unit can be assigned as P^{1-} (terminal, one connection) and P^{2-} (central, two connections).[12] This assignment implies that the formal charge of Pd is +1 (d^9) in a planar environment. The other assignment may be $[Ba^{2+}]_2[Pd^0][P_3^{4-}]$ based on the known binary phase of K_4P_3 (contains P_3^{4-} unit).[13] The average P-P bond distance in Ba_2PdP_3 is 2.203(3) Å, which is less than the P-P distance in black phosphorous (2.228 Å, Bond order = 1.0)[12] but longer than P-P distance in K_4P_3 (2.183 Å; Bond order = 1.25). This result indicates that the bond order of P-P in Ba_2PdP_3 is slightly

larger than a single bond but not as strong as the P-P bond in K_4P_3. The above assignments show that the formal charge of Pd and P cannot be clearly defined. The odd number of *VEC* (29 e^-/PdP_3^{4-}) suggests that Ba_2PdP_3 contains a half-filled band, which may lead to metallic and/or magnetic properties or structural distortions to form a stable superstructure. However, no physical measurements of this compound have been reported.

Compounds with puckered 6^3-sheets and 1D chains are observed in α-As, SnP_3 and K_3SnSb_3 (see Figure 2).[1-3] The building unit for these materials is the chair hexagonal unit. In this system, the *VEC* range is between 29 and 32 e^-/formula. The structure of SnP_3 (*VEC* = 29 e^-) features Sn in a trigonal pyramidal coordination to three P atoms and chair form of P_6 rings. The average bond angle within the layer is 100°. The K_3SnSb_3 (*VEC* = 32 e^-) contains polyacene-type $^1_\infty[SnSb_3^{-3}]$ chains with the same average bond angle as SnP_3.

Electronic Structure of 1D Chains

1. Ba_2PdP_3: The electronic structure of Ba_2PdP_3 was studied by Extended-Hückel tight-binding (EHTB) calculations.[14-20] Parameters for all theoretical calculations are given in Table 2. In this study, a planar molecular unit $Pd(P_3)_3^{n-}$ **(1)** and an ideal 1D chain $^1_\infty[PdP_3^{4-}]$ **(2)** were used to understand the formation of the zigzag 1D chain. The MO diagram of **1** is shown in Figure 3a. The orbital energies indicate an energy gap between MO No. 35 and 36 (ΔE = 7.5 eV). Therefore, a possible highest occupied molecular orbital (HOMO) is No. 35 ($Pd(P_3)_3^{15-}$). The interaction between Pd and the P_3 units in the HOMO is antibonding in character.

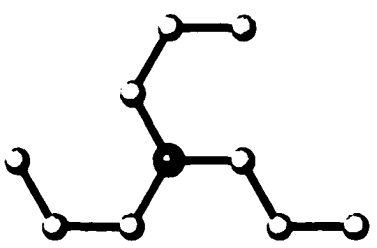

1

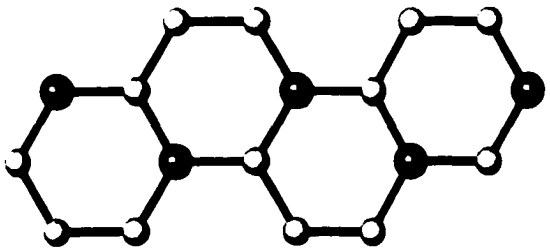

2

A similar feature of the electronic states also observed in the density of states (DOS) curve for the 1D chain, $^{1}_{\infty}[PdP_3^{4-}]$ (**2**). The bonding characters of Pd-P and P-P contacts were evaluated by crystal orbital overlap population (COOP) curves, which illustrate bonding (positive, right side) or antibonding (negative, left side) character for an interatomic interaction as a function of energy. The results, shown in Figure 3b and 3c, indicates that P-P contacts show bonding interactions below -16 eV, and bonding interactions for Pd-P and P-P contacts between -9 and -15 eV. The Fermi level of **2** at *VEC* = 29 e/formula ($Pd(P_3)_3^{4-}$, E_f = -10.2 eV) lies near the top of a large peak that shows weakly antibonding character for the Pd-P and P-P contacts. The result suggests that the Ba_2PdP_3 is a metallic compound. The Pd 4d band (shaded area in Fig. 5a) is essentially below the Fermi level (Mulliken population of Pd(4d) = 9.80). The maximum VEC of **2** is 30 e^-/formula (E_f = -9.8 eV) and additional electrons (VEC >30) will fill high-lying bands with strong P-P antibonding character. The d band of Pd atom is nearly filled and s, p orbitals contribute to higher-lying states near the Fermi level. The formal charge of Pd and P may be written as $^{1}_{\infty}[Pd^{-\delta}P_3^{-4+\delta}]$ at VEC = 29 e^-/atom.

The DOS curve of $^{1}_{\infty}[PdP_3]$ suggests a possible configuration of 30 e/formula. On the other hand, COOP curves of Pd-P and P-P contacts show antibonding character that prefer to have lower *VEC*. To address the effect of the interatomic interaction, the band structure of **2** was analysized (two $[PdP_3]$ per unit cell, 42 orbitals/cell). The bands No 27-30 for **2** are shown in Figure 4 with their orbital diagrams. These bands are degenerate at X(0.5, 0, 0) due to the two symmetry related $[PdP_3]$ units (2_1 symmetry) for each unit cell. Bands No 27-30 can be grouped into two categories, Φ(x,y) (No. 27-28) and Φ(z) (No. 29-30). When *VEC* = 29 e^-, the Fermi level is located at the degenerate point of Φ(z) (No. 29, 30) at X(0.5, 0, 0). The bandwidth of Φ(29) is ~0.5 eV. The energy of Φ(29) at Γ(0, 0, 0) is lower than at X(0, 0, 0) because of the long-range P-P π-bonding interactions. The band Φ(30) (E ~ -10.3 eV) is a combination of $P(p_z)$ and $Pd(d_{xz}, d_{yz})$ orbitals with a very narrow bandwidth (~ 0.1 eV), which is responsible for the sharp peak in the DOS curve near −10.0 eV. The other two bands, Φ(27) and Φ(28), contain orbital interactions in the (x,y) plane. The average bandwidth of Φ(27) and Φ(28) is 0.7 eV. The bonding character of Pd-P and P-P contacts at *VEC* = 29 e is π-antibonding (see Figure 4).

Four distorted models were constructed to study the effects of structural distortions to the stability of the 1D chain. Structural distortions may occur in some solid-state systems with partially occupied bands (second John-Teller theorem).[21] The distorted structure (intra- or intercell interactions) may change the electronic structure near the Fermi level to stabilized the system and the partially filled band may split to form a energy gap. The calculated band structures of distorted 1D chains are shown in Figure 5. The first and second distorted structures (**2A** and **2B**) contain compressed Pd-P and P-P distances (2.1 Å). Both **2A** and **2B**

contain crossing bands Φ(28) and Φ(30) near the Γ point (0.0, 0.0, 0.0). The Fermi levels in these models are equal or higher than the ideal structure **2** when *VEC* = 29 e^-/formula. The third and fourth models (**2C** and **2D**) contain short P-P contacts and alternate short-long distance of Pd-P and P-P bonds. These models show band gaps at the X point (ΔE ~ 0.7 eV). The highest occupied band for both models at *VEC* = 29 e^-/formula is Φ(28), which is different with the ideal chain at Φ(29). For model **2D**, the compressed $[Pd_2P_6]$ unit stabilizes the intra-atomic interaction (bonding characters) while the expanded intercell distance decrease the inter-cell interactions (antibonding characters). The net effect stabilizes Φ(28) at Γ point and Φ(29) at X point (band gap ΔE = 0.6 eV). The analyses suggest that the distorted Pd-P and P-P contacts may open a energy gap and stabilize the 1D chain.

2. Polyacene-Type Chain: If each atom in the P_3 unit coordinates to Pd to form 1D chain, the result forms a polyacene type 1D structure. This polyacene-type chain exists in $Ca_3Al_2Si_2$ as $^1_\infty[Si_{2/1}Al_{4/2}^{6-}]$.[22,23]

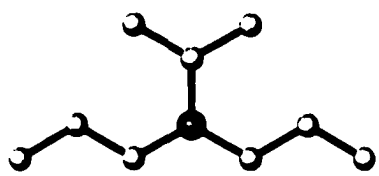

3

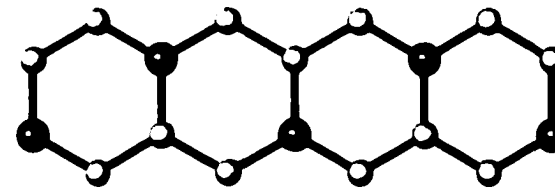

4

Theoretical calculations for this polyacene 1D chain were carried out to study their electronic structures and stabilities. The results of a MO diagram (based on fragment **3**), as well as DOS

and COOP curves for **4** are similar to the results of **1** and **2**. The band structure of **4** shows bands (No. 27-30) contains the similar Φ(x,y) and Φ(z) bands as **2** (see Figure 4). However, the dispersion of these bands is different. Energies of Φ(x,y) and Φ(z) bands are lower at Γ(0, 0, 0) than at X(0.5, 0.0, 0.0). The Φ(z) and Φ(x,y) bands are partially fill when *VEC* = 29 e^-/formula. The orbitals near the Fermi level are Pd-P and P-P antibonding.

Band structure calculations of the four distorted structures were performed to study the effect of distortion to the stability of this 1D chain, and are shown in Figure 7. The results indicate that the decreased Pd-P and P-P distances not only stabilize band Φ(28) at X, but also destabilize Φ(29) at the Γ point. The net effect gives a small energy change of Fermi level for each model. Three distorted models (**4B**, **4C** and **4D**) generate a band gap and their Fermi levels are higher than **4** at *VEC* = 29 e^-/formula.

3. Puckered 1D Chain: Another type of 1D structure containing cyclohexane-type rings (chair form) as building units. The K_3SnSb_3[2] (*VEC* = 32 e^-) contains the isolated 1D $^1_\infty[SnSb_3^{-3}]$ chains with such distorted hexagon units. The formation of this puckered chain may be driven by the nature of the Sn atom. The inert pair effect from the Sn *5s* valence electrons affects the bonding interaction between Sn and Sb. At the same time, the group 15 elements (Sb) also prefer to form trigonal-pyramidal units.

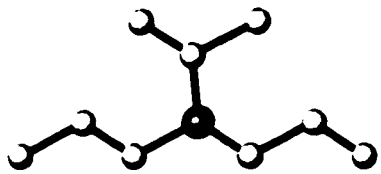

5

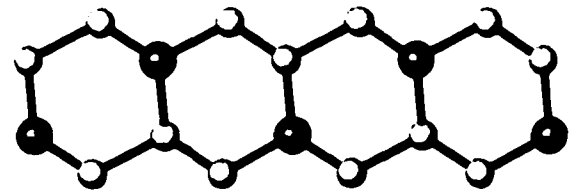

6

Puckered 1D chains were studied to evaluate their electronic structure and stability. The results of MO diagram and DOS curve for **5** and **6** are shown in Figure 8 (A modified Pd' parameter containing inert 5s parameter was used and listed in Appendix). According to the MO diagram, the HOMO (No. 36) shows Pd'-P and P-P antibonding character. The DOS curve indicates that the VEC_{MAX} is 32 e^-/formula, which is more than in the planar 1D chain (**2** and **4**, 30 e/ formula) due to a low-lying 5s orbital in Pd'. The theoretical calculations for another puckered model (**7** and **8**) show similar results and are not shown.

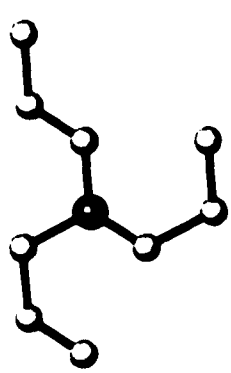

7

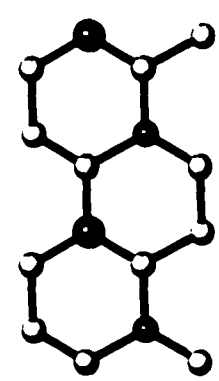

8

4. Relative Stability of Planar and Puckered Chains: According to the observed 1D structures (Table 1), the zigzag planar chain **2** exists in Ba_2PdP_3 while the puckered chain **6** exists in K_3SnSb_3. A question may arise: Why the planar and puckered chains form different kinds of structural connections? In this section, the relative stability for planar (**2** and **4**) and puckered (**6** and **8**) 1D chain isomers was studied to examine the structural preference between zigzag and polyacene type models. The total energy of the top four bands (No. 27-30 for planar and No. 29-32 for puckered structures) for each model were used to calculate the relative stability between zigzag and polyacene type 1D chains. Based on the frontier orbital theory, these bands near the highest occupied crystal orbital are important for the formation of the respective 1D structures. The relative energy of the planar and puckered chains are depicted in Figure 9. The results indicate that: 1) the relative stability between **2** and **4** shows W-shaped curve. The zigzag type, **2**, is energetically favored when $VEC \geq 29$. The stability of the planar chain depends on the *VEC*. Comparing with the experiment, the observed zigzag chain **2** (from Ba_2PdP_3) is more stable than polyacene-type chain **4**. 2) The energy stability between **6** and **8** also gives a W-shaped curve. The 1D chain **8** (same as the K_3SnSb_3) is more stable than **6** for $VEC \geq 30$ e$^-$. The trend from the calculations is consistent with experiments.

The electronic structure of 6^3-sheet

Following the theoretical studies of various 1-D chains, extended Pd-P and P-P 2D frameworks are discussed in this section. These models contain planar (**9** and **10**) and puckered 6^3-sheet (**11** and **12**). The study was focused on the effect of *VEC* toward the stability between 1D and 2D structures.

1. Planar 2D sheet: The 2D planar structure **9** is made up of interconnected 1D chains **2**. The 2D space group of **9** is *P2gg* that contains 2_1 screw-axes along x- and y-axes. The structure of **9** is similar to the "pseudo 2D layer" of Ba_2PdP_3 (Figure 1c). A branched phosphide $^{1}_{\infty}[P_6]$ polymer is formed between two connected 1D chains (see middle part of **9**). Compared with the 1D structure **2**, the 2D sheet **9** creates inter chain P-P contacts between two 1D chains (P1-P1 and P2-P2). Figure 10 is the calculated DOS (shaded area is Pd d band) and COOP curves (intra- and interchain P-P contacts) for **9**, with the Fermi levels at VEC = 24, 28 (U_2PdSi_3) and 29 (Ba_2PdP_3) e^-/formula. A band gap forms (–5.5 to -8.5 eV) at *VEC* = 28 e^-/formula (Fermi level = -8.5 eV). The COOP curves for Pd-P and P-P contacts indicates that these bonds are optimized at *VEC* ~ 24 e^-.

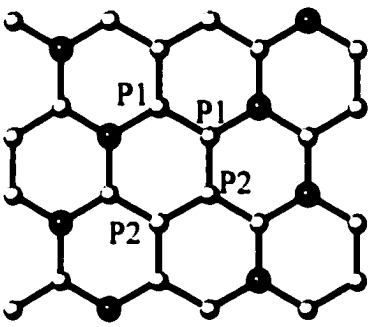

9

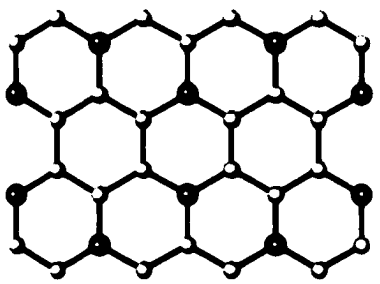

10

The structure of **10** is constructed by connecting **6** to form a 2D structure with a hexagonal unit cell (2D space group *P6m*). This 2D network is observed in U_2RuSi_3.[7] The results of band calculations for **10** show similar trends as **9**.

The stability between 1D and 2D structures can be understood by the concept of frontier orbital interactions.[21] When two 1D chains are connected to form a 2D sheet, a σ-

type interaction is formed between Φ(28) bands (see Figure 4). The orbital interaction of Φ(28) bands is illustrated in **11**. Since the Φ(28) band is filled in 1D chain at *VEC* = 29, this interchain interaction is not stable.

The projected DOS curves (P1($3p_y$) band) for **2** and **9** are shown in Figure 12 to illustrate the effect of the interchain interaction to crystal orbital distribution. For the 1D model, the P1($3p_y$) band is mostly below the Fermi level, which is like an electron pair localized on P1. On the other hand, the PDOS of P1($3p_z$) band is separated into two regions of low (-10.0 ~ -25.0 eV) and high energy (-5.0 ~0.0 eV) in the 2D model. The Fermi levels for **9** at VEC = 29 is filled to the high-energy band (E_f = -3.2 eV) with P-P antibonding character.

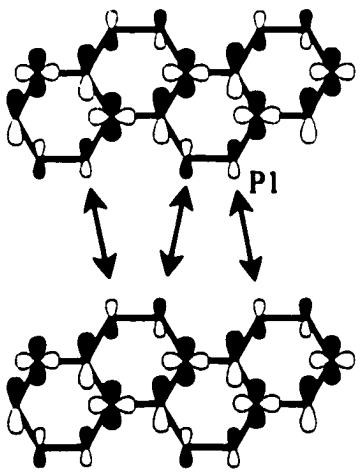

11

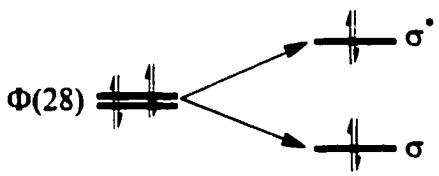

At this point, the theoretical studies indicate that an antibonding interaction for the 2D systems at *VEC* = 29 e^-/formula. The COOP curves for Pd-P, P-P contacts are optimized at

VEC = 24 e^-/formula. The result suggests that the 2D framework would be stable at lower *VEC*. The effect of *VEC* on Fermi levels of 1-D and 2-D structures is examined and shown in Figure 12, which clearly indicates that the Fermi levels of 2D sheets (**9** and **10**) increase dramatically when the *VEC* is higher than 28 e^-/formula. The value is lower than *VEC* for the 1D chains (**2** and **4**, *VEC* > 30). The experiments show that the *VEC* of Ba_2PdP_3 is 29 e^- and the *VEC* range of the AlB_2-type phases (with M_2AB_3) is between 22 and 28 e.[1] The theoretical results in this study are consistent to the observed data.

2. Puckered 2D Sheet: 12 and **13** are models with puckered 6^3-sheet (interconnected 1-D chains of **6** and **8**). Note both Pd and P atoms are coordinated by three atoms in a C_{3v}-like environment. The puckered structure **12** contains a branched $^1_\infty[P^{1-}]$ 1D polymer (2-D space group P2). There is no observed compound similar to the 2-D framework in **12**. Another 2-D network **13** contains 3m symmetry prependicular to the plane (2-D space group is *P3m1*). This particular layer structure is found in the crystal structure of InP_3 and SnP_3.

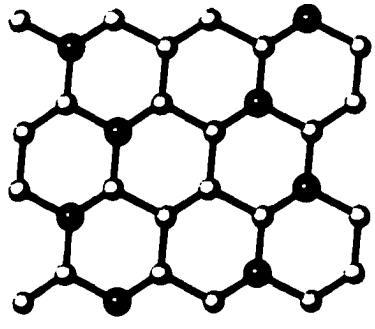

12

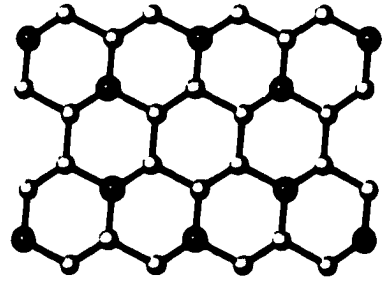

13

The electronic structure of **12** and **13** are studied to analyze the bonding character of

Pd-P and P-P contacts. The same bond distances and angles as in the puckered 1D chains (**6** and **8**) are used in this study. The results from DOS and COOP curves show similar features as **9** and **10**. The maximum *VEC's* of puckered 2D sheets are 30 e^-, which is two electrons less than for puckered 1D chains due to the inert 5s band from the post-transition metal. The observed compounds K_3SnSb_3 (*VEC* = 32 e, $^1_\infty[SnSb_3^{3-}]$) and SnP_3 (*VEC* = 29 e, $^2_\infty[SnP_3]$) show a similar trend as the theoretical study.

3. Relative stability of planar and puckered sheets: The relative stability between planar (**10**) and puckered (**12**) 2D models is depicted in Figure 13.. The same atomic parameters of Pd and P were used for both models. The results indicate that the puckered structure is more stable than the planar structure at high *VEC* region (> 27). The comparison between planar and puckered sheets is similar to the trigonal planar to pyramidal distortion of AH_3 (D_{3h} → C_{3v}) molecules.[21] The puckered structure is more stable than the planar at high *VEC* region due to the additional electron in nonbonding orbitals.

Conclusions

The effect of *VEC* and the electronic configuration on the structural stability of Ba_2PdP_3 and related structures are discussed. This study demonstrated the effect of *VEC* to the stability of 1D vs. 2D as well as planar vs. puckered structures. The 1D chain is more stable than the 2D sheet at high *VEC* because the electrons fill nonbonding states of the 1D chain. The formation of a puckered structure is affected by the geometry as well as the nature of post-transition metal.

Computational Details

All electronic structure studies of 1-D and 2-D models were calculated by the extended Hückel tight-binding method. [14-20] Densities of states (DOS) and crystal orbital overlap population (COOP) curves were calculated from 100 k-points in the first Brillouin zone. The program developed by Dr. G. J. Miller was used for theoretical calculations. The atomic parameters used in this paper are shown in Table 2. A modified Pd' with an inert 5s orbital was used in the calculations of puckered models to simulate the post transition metal. The bond distances and bond angles have been modified as described below: The regular bond distances of Pd-P and P-P are 2.33 Å, which are obtained from the average bond distances in Ba_2PdP_3. The bond angles of P-P-P or P-Pd-P in the planar model is 120° for planar and 110° for puckered models. The distorted models in the band structure study contain P-P distances of 2.1, 2.33, 2.6 Å.

References

1)Villars, P.; Calvert, L. D. *Pearson's Handbook of Crystallographic Data for Intermetallic Phases*; 2nd ed ed.; ASM International, Metals Park OH:, 1991.

2)M.Asbrand; Eisenmann, B. *Z. Anorg. Allgem. Chem* **1997**, *623*, 561.

3)Olofsson, O. *Acta. Chem. Scand.* **1970**, *24*, 3.

4)Kinomura, N.; Terao, K.; Kikkawa, S.; Horiuchi, H.; Koizumi, M. *Mat. Res. Bull.* **1983**, *18*, 53.

5)Chevalier, B.; Pottgen, R.; Darriet, B.; Gravereau, P.; Etourneau, J. *J. Alloy. Comp.* **1996**, *233*, 150.

6)Johrendt, D.; Mewis, A. *J. Alloys Comp.* **1994**, *205*, 183.

7)Pottgen, R.; Gravereau, P.; Dariet, B.; Chevalier, B.; Hickey, E.; Etoureau, J. *J. Mater. Chem.* **1994**, *4*, 463.

8)Zachariasen, W. H. *Acta Crystallogr.* **1963**, *16*, 2653.

9)Jeitschko, W. *Acta Crystallogr., Sect. B* **1974**, *30B*, 2565.

10)Gronvold, F.; Rose, E. *Acta Crystallogr.* **1957**, *10*, 329.

11)Burdett, J. K.; Coddens, B. A. *Inorg. Chem.* **1988**, *27*, 418-21.

12)Schnering, H. G.; Honle, W. *Chem. Rev.* **1988**, *88*, 243.

13)Schnering, H. G. v.; Hartweg, M.; Hartweg, U.; Honle, W. *Angew. Chem., Int. Ed. Engl.* **1989**, *28*, 56.

14)Hoffmann, R.; Lipscomb, W. N. *J. Chem. Phys.* **1962**, *36*, 2179, 3489.

15)Hoffmann, R. *J. Chem. Phys* **1963**, *39*, 1397.

16)Ammeter, J. H.; Buergi, H. B.; Thibeault, J. C.; Hoffmann, R. *J. Am. Chem. Soc.* **1978**, *100*, 3686-92.

17)Whangbo, M.-H.; Hoffmann, R.; Woodward, R. B. *Proc. R. Soc. London, Ser. A* **1979**, *366*, 23-46.

18)Hughbanks, T.; Hoffmann, R. *J. Am. Chem. Soc.* **1983**, *105*, 3528-37.

19)Wijeyesekera, S. D.; Hoffmann, R. *Organometallics* **1984**, *3*, 949-61.

20)Chadi, D. J.; Cohen, M. L. *Phys. Rev. B* **1973**, *8*, 5474.

21)Burdett, J. K. *Molecular Shapes: Theoretical Models of Inorganic Stereochemistry*; Wiley, New York, N. Y.:, 1980.

22)Widera, A.; Schäfer, H. *Z. Naturforsch. B* **1977**, *92*, 887.

23)Li, J.; Hoffmann, R. *J. Phys. Chem.* **1988**, *92*, 487-93.

Table 1. Ternary phases with the formula A_xBC_3

Formula	VEC	structure type	Ionic network	Ref.
K_3SnSb_3	32†	SnP_3 derivative	$^1_\infty[SnSb_3^{3-}]$ 1D chain, puckered	2
SnP_3	29†	α-arsenic	$^1_\infty[SnP_3]$ 6^3 sheet, puckered	3
Ba_2PdP_3	29	AlB_2 derivative	$[PdP_3^{4-}]^1_\infty$, zigzag planar 1D chain	6
U_2PdSi_3	28	AlB_2	6^3 sheet, planar	5
U_2RhSi_3	27	AlB_2	**6^3 sheet, planar**	5
U_2RuSi_3	26	AlB_2	6^3 sheet, planar	7

† : The d electrons of Sn and In are included.

Table 2. Atomic Parameters for Extended Hückel Calculations

	Orbital	H(ii)	ζ	C_1	ζ_2	C_2
P	3s	-18.6	1.88			
	3p	-12.5	1.63			
Pd	5s	-8.64	2.19			
	5p	-2.68	2.15			
	4d	-12.65	5.98	0.5265	2.61	0.6374
Pd'‡	5s	**-16.16**	**9.99**			
	5p	-2.68	2.15			
	4d	-12.65	5.98	0.5265	2.61	0.6374

‡ : The H_{ii} of Pd(5s) is replaced by Sn(5s).

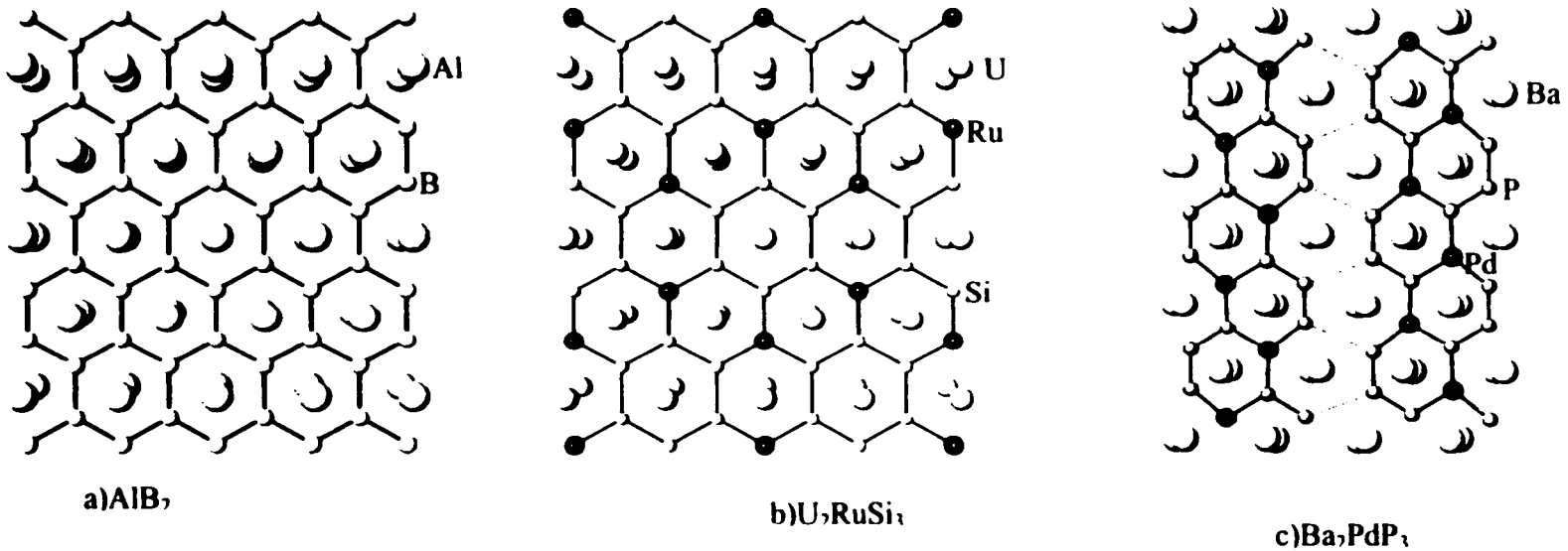

a)AlB_2 b)U_2RuSi_3 c)Ba_2PdP_3

Figure 1. The AlB_2-type structures: a) AlB_2. b) U_2RuSi_3 and c) Ba_2PdP_3.

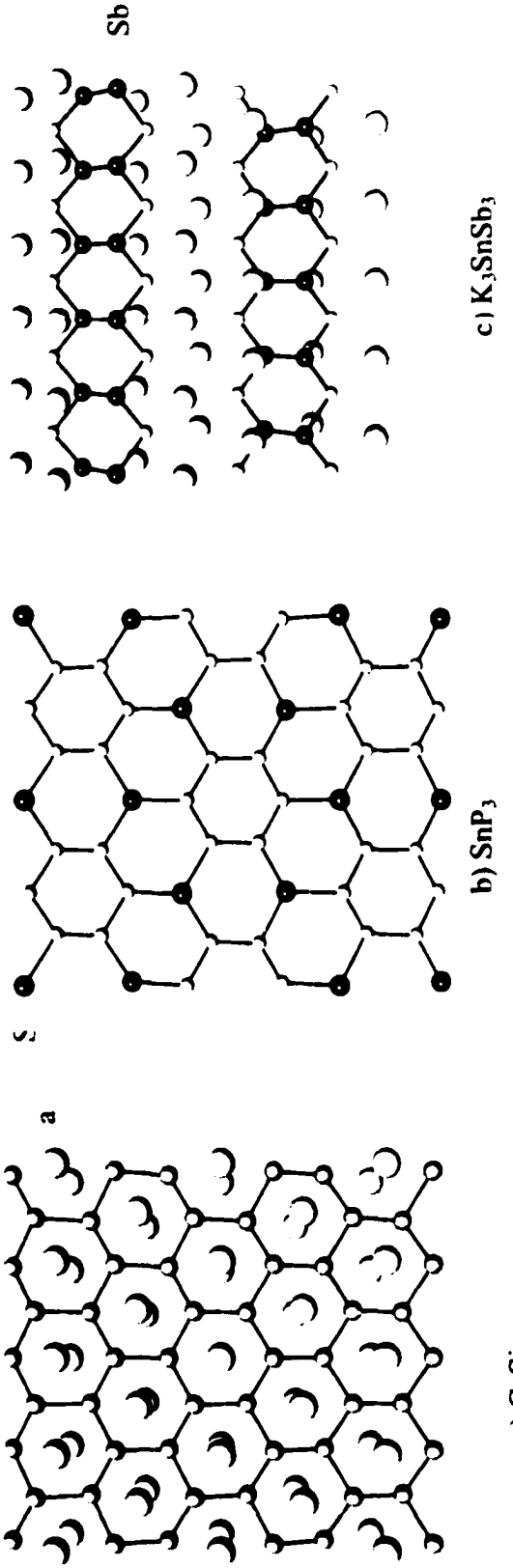
Sb
a
a) $CaSi_2$
b) SnP_3
c) K_3SnSb_3

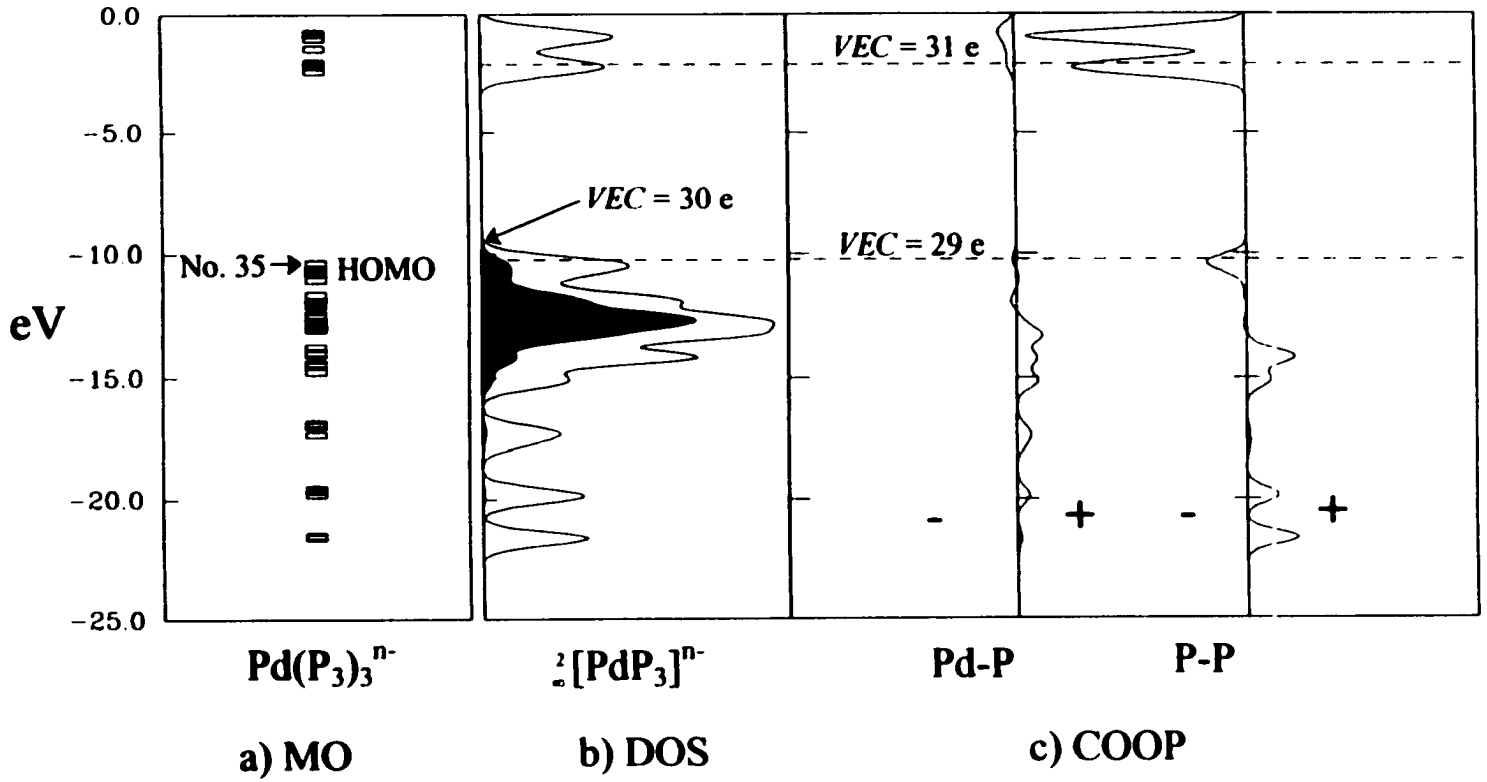
0.0
-5.0
-10.0
-15.0
-20.0
-25.0
eV
No. 35 → HOMO
VEC = 31 e
VEC = 30 e
VEC = 29 e
-
+
-
+
Pd(P3)3n-
∞2[PdP3]n-
Pd-P
P-P
a) MO
b) DOS
c) COOP

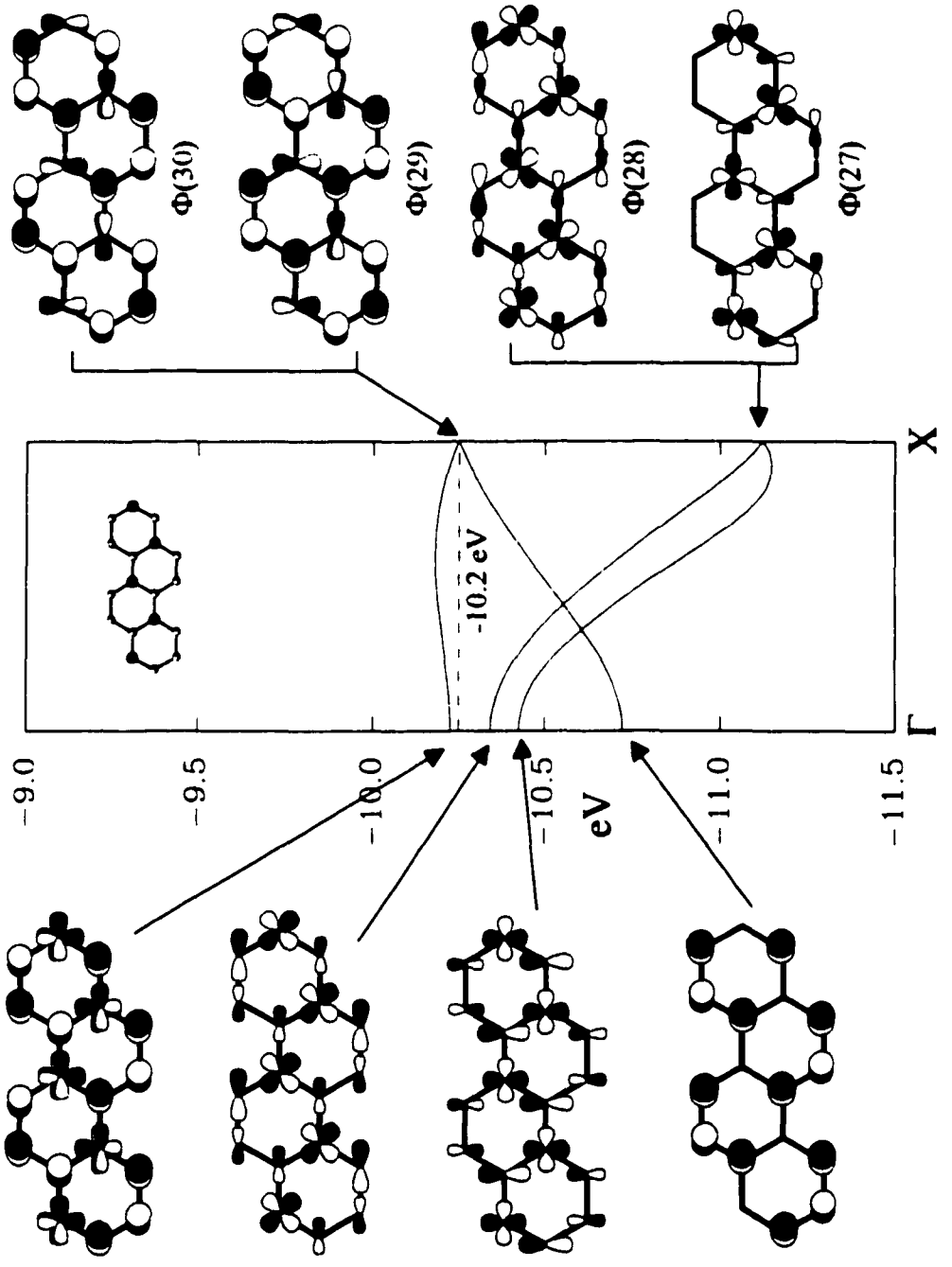
Φ(30)
Φ(29)
Φ(28)
Φ(27)
-10.2 eV
X
Γ
−9.0
−9.5
−10.0
−10.5
eV
−11.0
−11.5

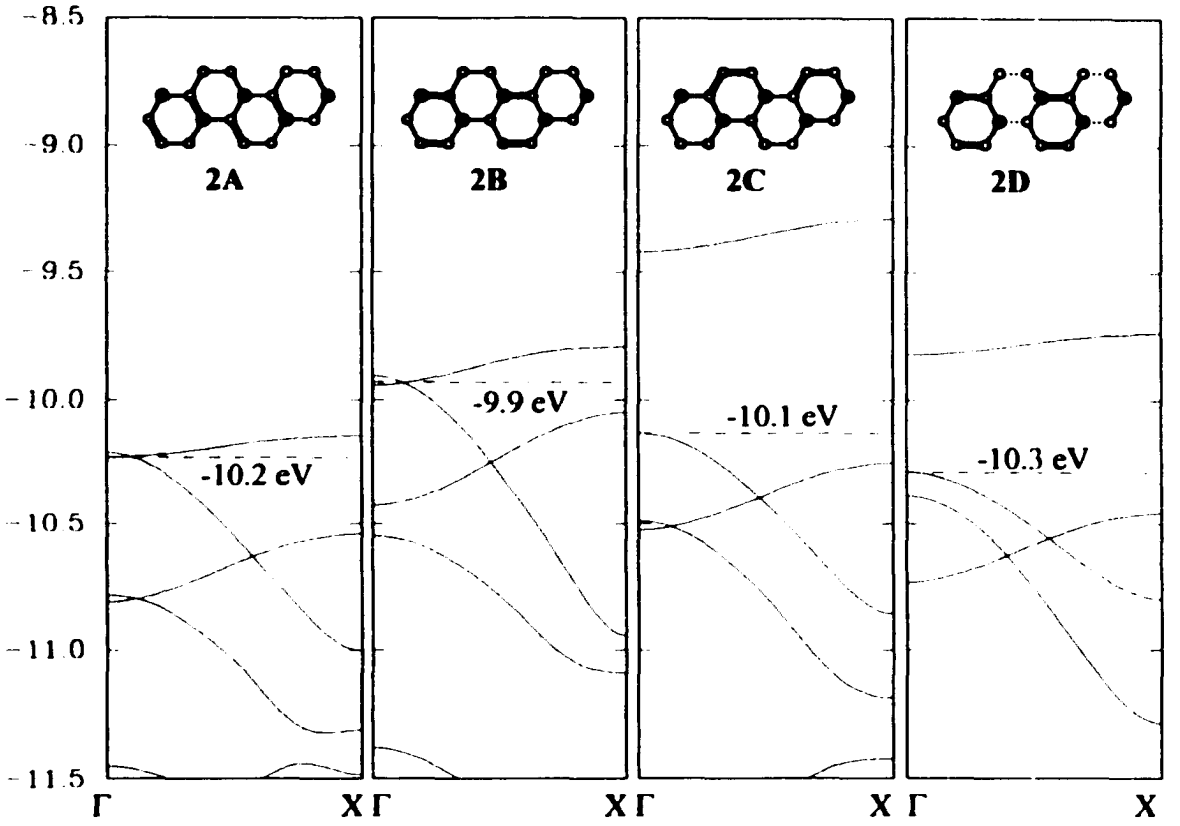

Figure 5. Calculated band structures of distorted $^{1}_{\infty}[PdP_3]^{n-}$ (**2**). The distorted structure is drawn on top of each diagram. Black and gray circles are Pd and P atoms. Thick, regular and dash sticks represent short (2.1 Å), middle and long (2.6 Å) interatomic distances. Dash line on each band structure is the Fermi level at *VEC* = 29 e.

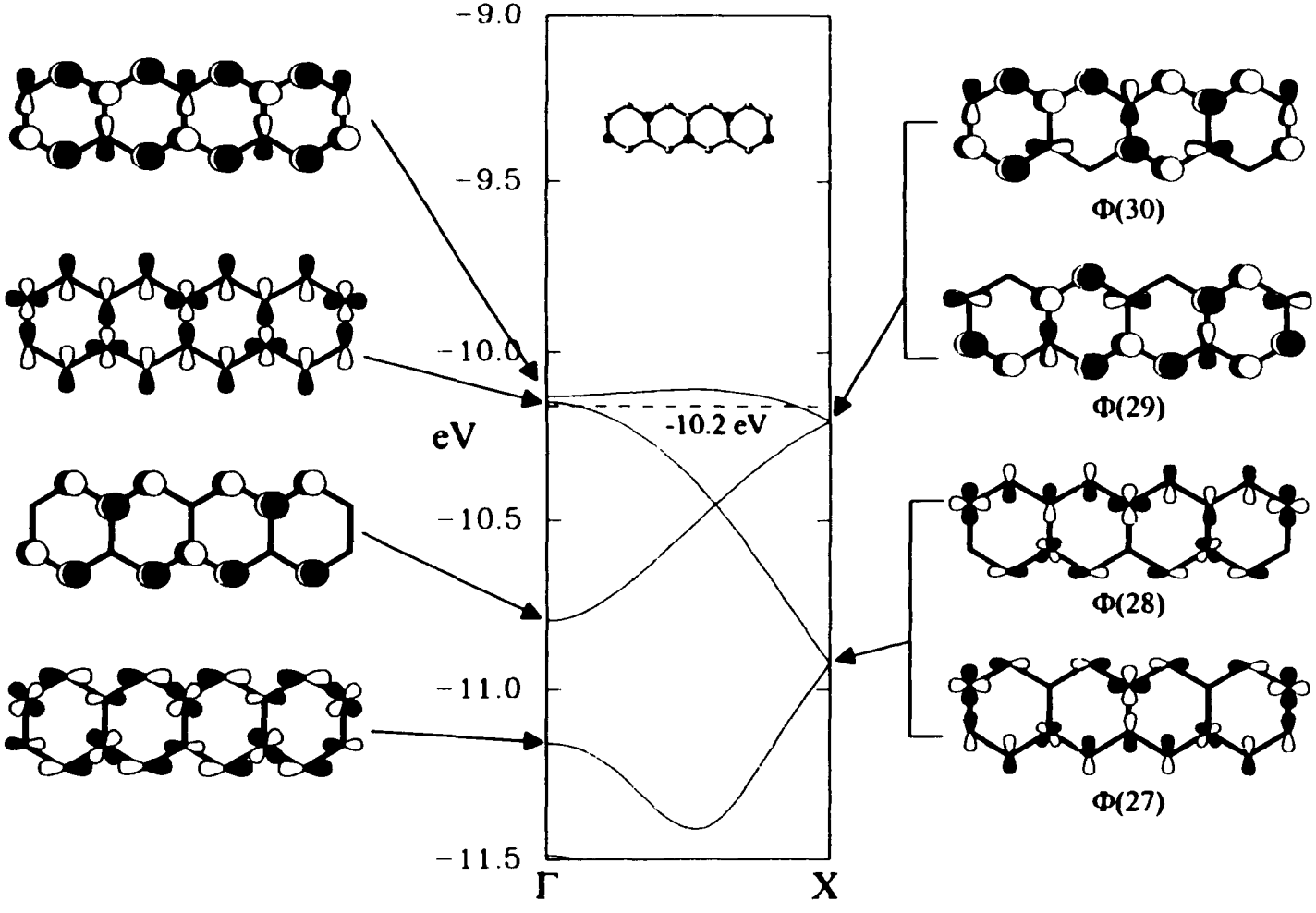
-9.0
-9.5
-10.0
-10.5
-11.0
-11.5
eV
-10.2 eV
Γ
X
Φ(30)
Φ(29)
Φ(28)
Φ(27)

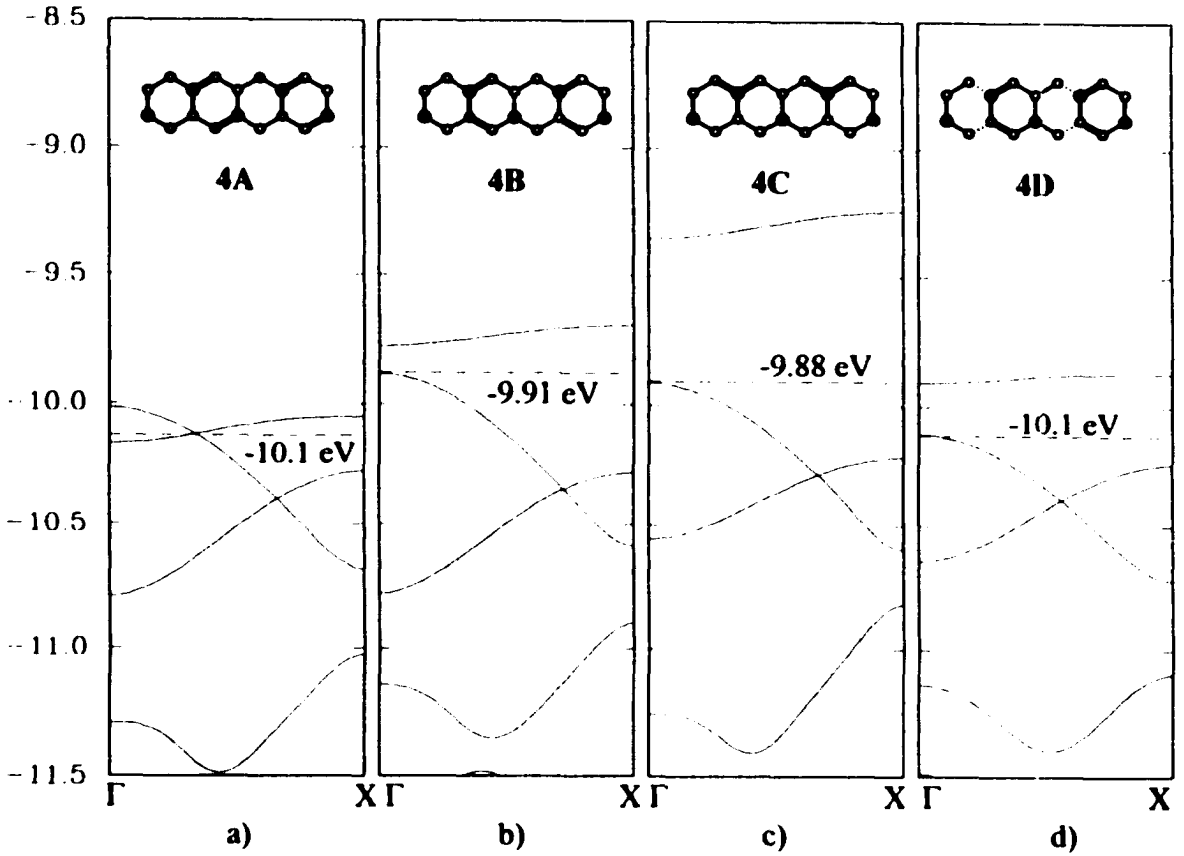

Figure 7. Calculated band structures of distorted polyacene 1D chain (**4**). The distorted structure is drawn on top of each diagram. Black and gray circles are Pd and P atoms. Thick, regular and dash sticks represent short (2.1Å), middle and long (2.6 Å) interatomic distances. Dash line for each band structure is the Fermi level at *VEC* = 29 e.

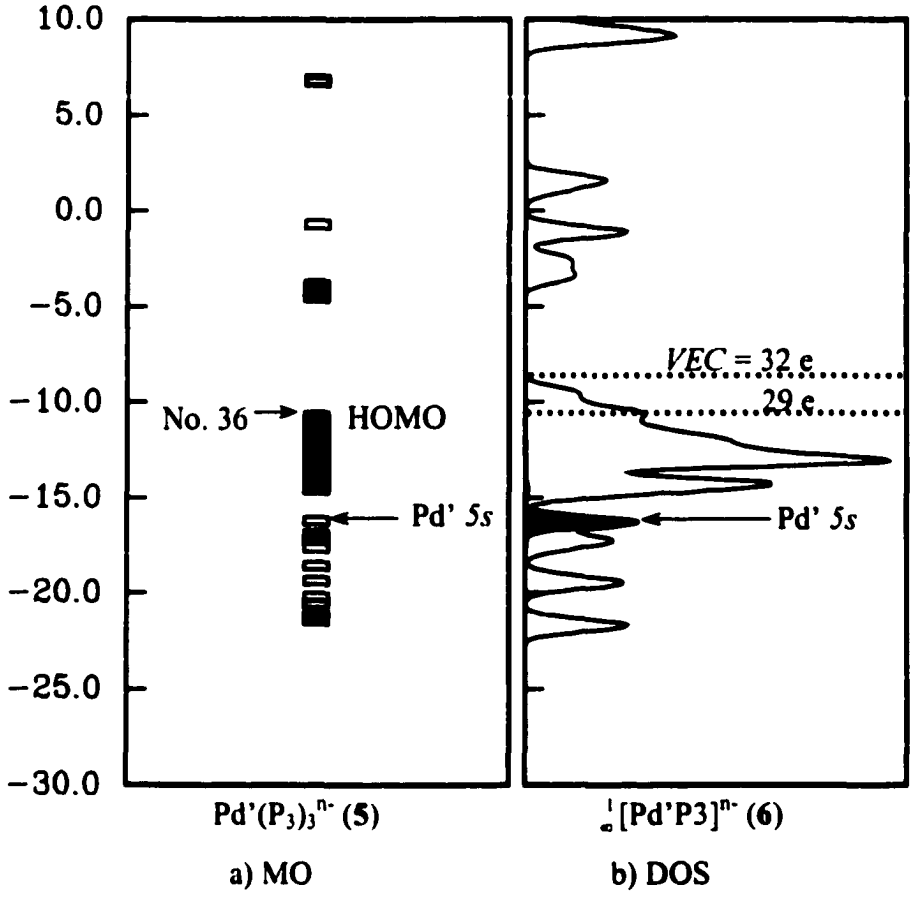

Figure 8. a) MO diagram for puckered molecular unit **5**, b) DOS curve for puckered polyacene 1D chain **6**. The horizontal dashed lines indicate the position of the Fermi level at *VEC* = 29 and 32 e⁻; the shaded area in the DOS curve is the projected Pd' 5s band. See appendix for the modified parameters of Pd'.

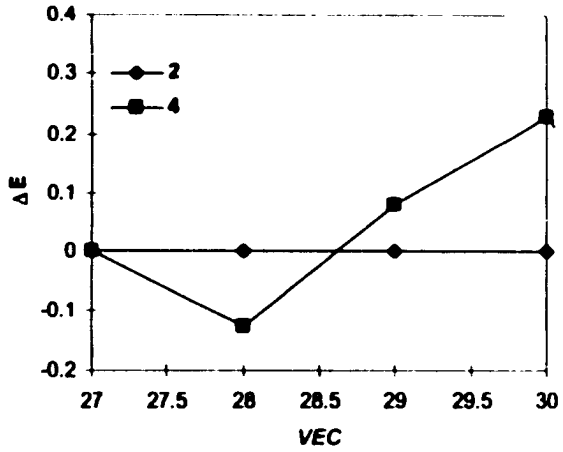

a) Planar 1D chain: **2** vs. **4**

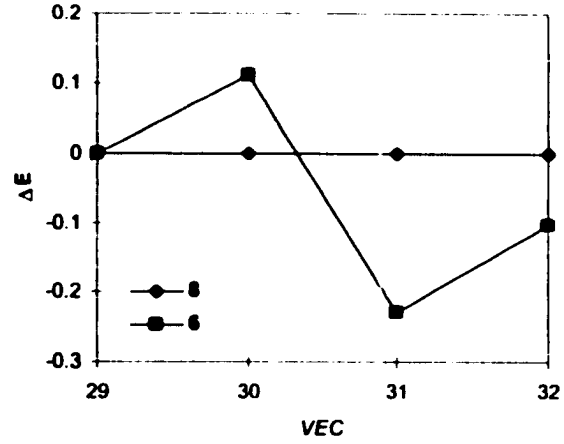

b) Puckered 1D chain: **6** vs. **8**

Figure 9. The relative stability for a) planar (**2** vs. **4**) and b) puckered (**6** vs. **8**) 1-D chains. The models **2** and **7** are used as the reference. For each *VEC*, the model with lower energy is more stable.

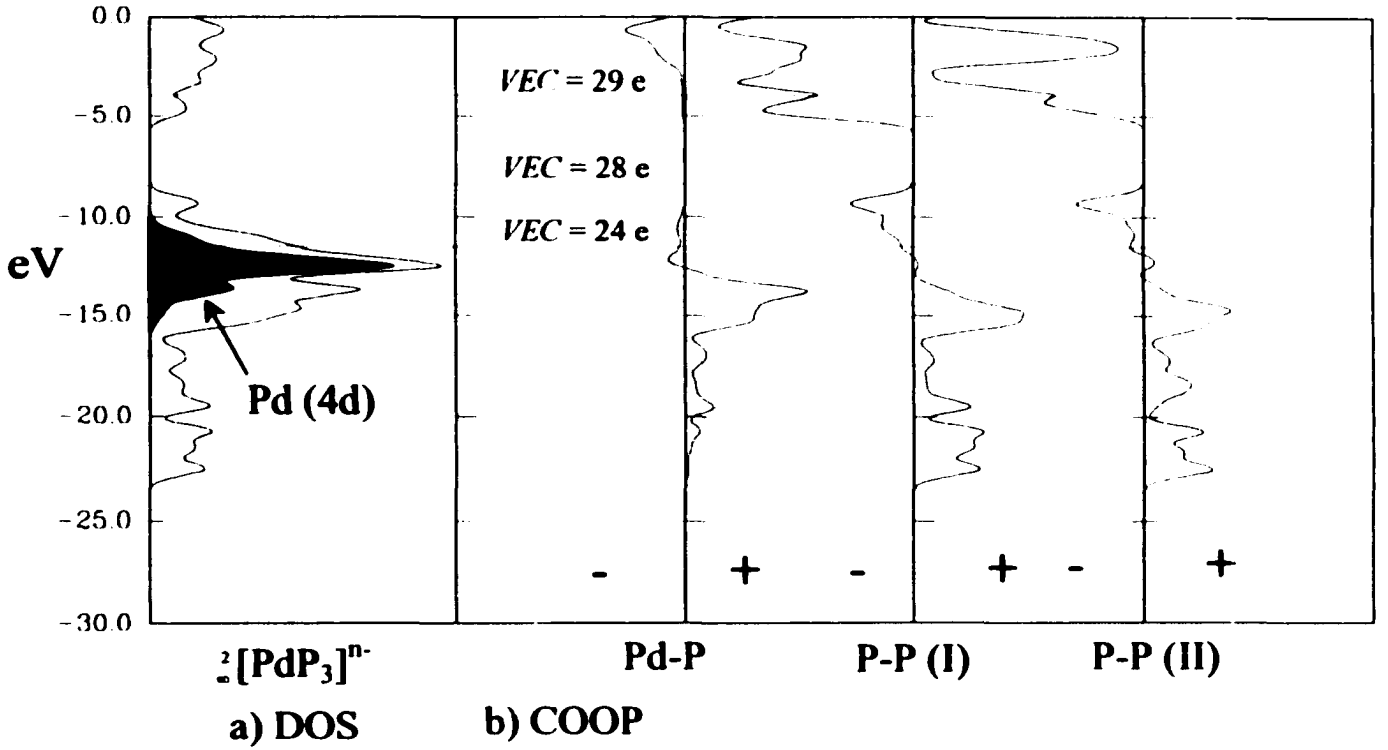

Figure 10. a) The DOS curve of **9** with the projection of Pd 4d orbitals (shaded area). b) The COOP curves of Pd-P bonds, intrachain P-P (I), and interchain P-P(II) contacts. The dash lines indicate the position of Fermi energy at VEC = 24, 28 and 29 e^-.

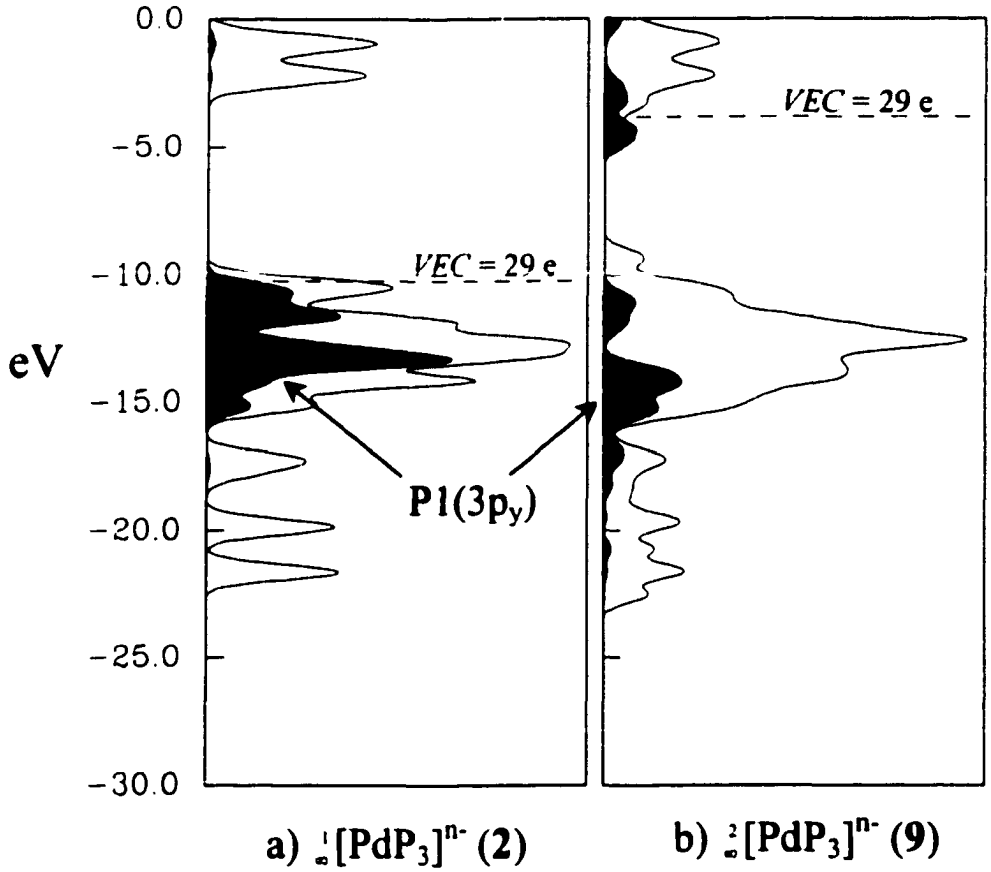

Figure 11. The DOS curves of a) 1D chain (**2**), and b) 2D sheet (**9**) with their PDOS curves of P1($3p_y$) bands (shaded area). The contribution of each PDOS curve was multiplied by three times as their original value. Dash line on each curve is the position of Fermi level at *VEC* = 29 e.

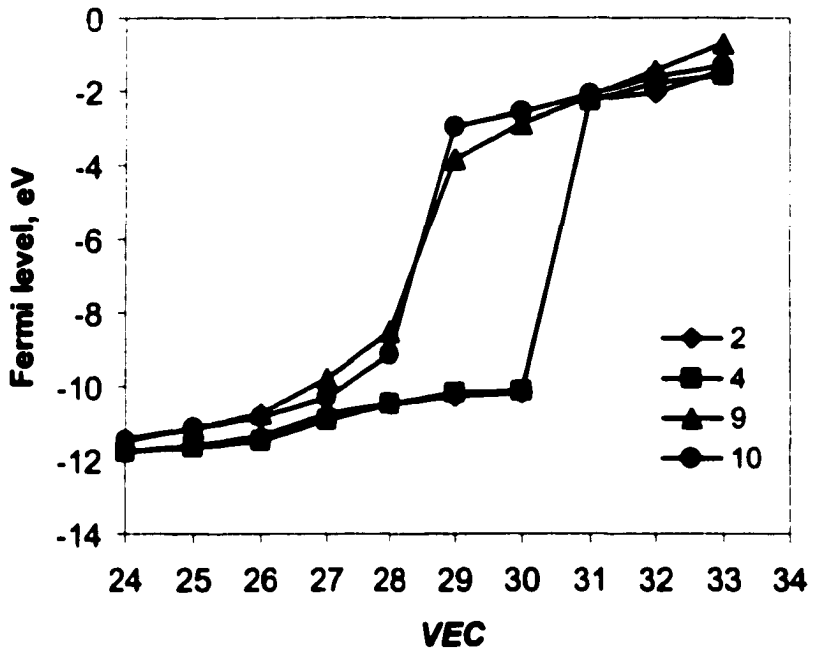

Figure 12. The Fermi levels for 1-D (**2**, **4**) and 2-D (**9**, **10**) models as a function of *VEC*.

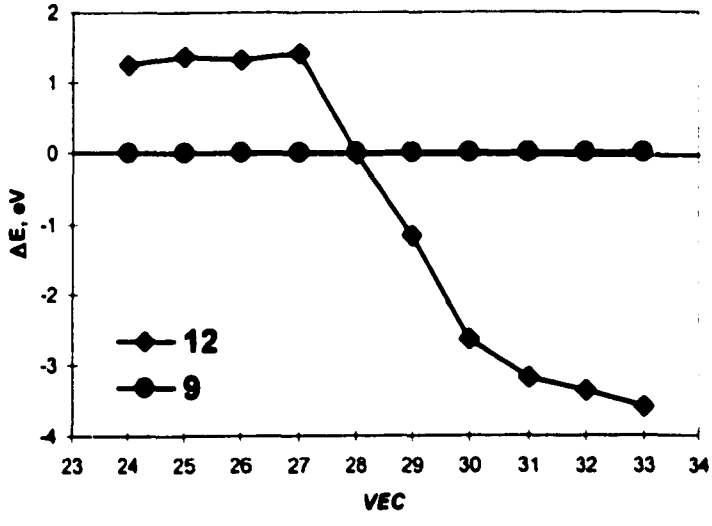

Figure 13. The relative total energy between planar (**9**) and puckered (**12**) 2D sheets as a function of *VEC*. The model with lower energy is more stable.

ACKNOWLEDGMENTS

"謙謙君子 卑以自牧"

-易經 謙卦 初爻 象辭

"The noble man is characterized by the utmost Modesty. He uses his humility to shepherd himself."

- I-Ching, Qian (No. 15), First Yin, Commentary on the images (Translated by Richard John Lynn)

I want to sincerely thank my advisor, Professor Gordon J Miller for his patience and encouragement during my graduate studies. It has been a great experience for me to do research with my advisor and learn chemistry at Iowa State University.

I want to express my appreciation to many people whose help was invaluable to my research. Thanks to Professor Bob Jacobson for helpful suggestions regarding crystallography, Jerry Ostenson for magnetic measurements, Jim Anderegg for XPS measurements and X-ray support, Warren for help with the EDS, Dr. Ian Fisher for conductivity measurement, Dr. Ilia Guzei for CCD diffractometer training, and my group members for their helpful discussions. I also want to thank many of the chemistry and Ames lab faculty members for their helpful discussions about my research.

Many thanks to my wife Wen, who always supports me unconditionally. Finally, thanks to my parents, for their love and support throughout my education.